UNIVERSIDAD NACIONAL AUTÓNOMA DE MÉXICO
PROGRAMA DE POSGRADO EN ASTROFÍSICA

Instituto de Astronomía

EFECTOS DE LA ACRECIÓN DE SATÉLITES PEQUEÑOS EN INDUCIR FLUJOS DE GAS HACIA EL CENTRO DE UNA GALAXIA DE DISCO

TESIS

QUE PARA OPTAR POR EL GRADO DE:
MAESTRO EN CIENCIAS (ASTROFÍSICA)

PRESENTA:
FELIPE GERARDO RAMÓN FOX

TUTOR
DR. HÉCTOR ACEVES CAMPOS, INSTITUTO DE ASTRONOMÍA-UNAM

ENSENADA, BAJA CALIFORNIA
MÉXICO
AGOSTO 2014

UNIVERSIDAD NACIONAL AUTÓNOMA DE MÉXICO
PROGRAMA DE POSGRADO EN ASTROFÍSICA

Instituto de Astronomía

EFFECTS OF THE ACCRETION OF SMALL SATELLITES IN INDUCING GAS FLOWS TO THE CENTRE OF A DISC GALAXY

THESIS

SUBMITTED FOR THE DEGREE OF:
MASTER IN SCIENCE (ASTROPHYSICS)

PRESENTED BY:
FELIPE GERARDO RAMÓN FOX

SUPERVISOR
DR. HÉCTOR ACEVES CAMPOS, INSTITUTO DE ASTRONOMÍA-UNAM

ENSENADA, BAJA CALIFORNIA
MÉXICO
AUGUST 2014

Abstract

Interactions play an important role in the evolution of galaxies as they can reshape their morphology as well as trigger nuclear and star formation activity (e. g. Benson 2010, Alexander & Hickox 2012, and references within). According to the current scenario of galaxy formation in the context of the ΛCDM cosmology, initial perturbations in the dark matter density of the early universe merge to form larger structures that eventually lead to the massive haloes that host galaxies in the present epoch (e. g White & Rees 1978, Mo et al. 2010). Galaxies form as the gas settles and stars form in a disc within the growing halo, and they interact and merge with others to form larger systems (e. g. Benson 2010). The current cosmological models predict that a significant population of satellites with masses in the range of $10^9 M_\odot$ exists around galaxies similar to the Milky Way (e. g. Klypin et al. 1999, Bullock et al. 2010, Sawala et al. 2012). These small satellites can still have noticeable effects in inducing morphological effects such as lopsidedness and in disturbing the gas disc to produce inflows.

The present work explores the effect of small satellites with mass ratios of ≈1:100 in inducing gas flows to the central regions of a disc galaxy. The primary galaxy consists of a stellar disc with an exponential density profile, a bulge with a Hernquist (1990) profile, and a gaseous disc residing in a Navarro et al. (1996) dark matter halo with physical parameters corresponding to the Milky Way models of Klypin et al. (2002). The N-body models of the galaxy are generated using the method developed by McMillan & Dehnen (2007). The halo has a total mass of $M_h = 10^{12} M_\odot$ and a scale radius $r_s = 21$ kpc; the stellar disc has a mass of $M_d = 4.167 \times 10^{10} M_\odot$ and a scale radius of $R_D = 3.5$ kpc; the gas disc gas a mass $M_g = 0.1 M_d$; and the central bulge has a $M_b = 8.33 \times 10^9 M_\odot$ and a scale radius of 0.7 kpc. The number of particles for the halo is $N_h = 10^6$, for the stellar and gas discs it is $N_s = N_d = 500\,000$, and for the bulge it is $N_b = 10\,000$. Two model galaxies are considered: a non-barred model and a barred model. The first has a Toomre parameter of $Q = 1.5$, and the second has $Q = 3.0$. In both models, the Toomre parameter is constant as a function of radius. Because bars produce steady flows of gas in an isolated galaxy, a model galaxy that avoids the formation of a bar motivates the use of Model A in order to isolate the effects of an external perturber.

The satellite galaxy is modelled by a Plummer density profile. Two models are used: one has $M = 6 \times 10^9 M_\odot$ (Satellite 1) and a scale radius of $a = 1.0$ kpc; the second one has $M = 1.2 \times 10^{10} M_\odot$ (Satellite 2) and a scale radius of $a = 1.3$ kpc. These corresponds to mass ratios of approximately 6:1000 and 3:265, respectively. The following three orbits are explored: a circular orbit with initial radius $R_i = 3R_D$ and inclination $i = 30°$ (Orbit 1),

a second circular orbit with $R_i = 6R_D$ and the same inclination (Orbit 2), and a coplanar orbit with $R_{peri} = R_D$ and $R_{apo} = 6R_D$ (Orbit 3). Both prograde and retrograde cases are explored. It is noted that Mihos & Hernquist (1994) and Hernquist & Mihos (1995) have only explored the prograde case of Orbit 2, and their primary galaxy resides in a core-like halo. These orbits are chosen because they represent extreme cases that provide a measure of the probable upper limits of the induced gas flows in the disc. Additionally, the results of the simulations of Orbit 2 can be compared with previous works.

The results of this work show that satellites with such small mass ratios can still produce observable distortions in the gas and stellar components of the galaxy, indicating that these minor interactions can be a mechanism that produces lopsidedness. In terms of gas flows, the prograde circular orbits are more favourable for producing gas flows. The most extreme case is that of Orbit 2. The final gas mass distribution shows that the satellite with $M = 1.2 \times 10^{10} M_\odot$ can drive an amount of up to $\approx 60\%$ of the total gas mass to a region within $R = R_D$. In the case of the coplanar orbit, both the prograde and retrograde orbits produce final mass distributions where $\approx 50\%$ of the gas mass of the galaxy is within $R = R_D$. In terms of gas flows, the prograde circular orbits produce rather sudden flows of gas whereas the coplanar orbits produce a more gradual flow. A representative case is the simulation with Satellite 2 in prograde Orbit 2 and Model A shows, where $\approx 35\%$ of the total gas mass passes through $R = R_D$ in a timescale of ≈ 400 Myr. In the coplanar prograde orbit with Satellite 2 and Model A, approximately 15% of the gas passes through $R = R_D$ during the simulation. The results are described in detail in Chapter 4.

This work shows that small satellites can induce significant gas flows to the central regions of a disc galaxy, which is relevant in the context of fuelling active galactic nuclei. In the present work, a limited sample of the orbital parameter space and the satellite range has been explored. However, an interesting continuation of this work would be to make similar simulations with infalling satellites having initial conditions derived from cosmological simulations in order to asses their impact in terms of gas flows.

Acknowledgements

For all their support in my education, and for helping me with moving to Ensenada to begin my master studies, and encouraging me to reach my goals, I am very grateful to my parents. I also want to give special thanks to my sister Caroline for her encouragement to finish this work.

I am particularly grateful to my advisor Dr. Héctor Aceves for his support, motivation, and patience during my studies. He has always motivated me to keep learning about astronomy, and to review my work from a critical perspective. I thank him very much for his guidance, advice, and insightful discussions that have led to the completion of this work.

I also want to thank the other members of my thesis committee: Dr. Gilberto Gómez, Dr. Leonel Gutiérrez, Dr. Ivânio Puerari, and Dr. Mauricio Reyes Ruiz for their help, patience, insightful comments and discussions, and for their suggestions for improving the present work.

I would also like to give special thanks to Dr. Takamitsu Miyaji for giving me useful references and comments in the context of AGNs, to Dr. Reyes Ruiz for stimulating discussion in computational hydrodynamics, to Dr. Luis Aguilar for his insightful discussions in galactic dynamics, and to Dr. Héctor Velázquez for sharing his experience in high performance computing.

I would also like to thank María Elena Jímenez and the people at the library at IA-UNAM, Ensenada, for their help in the use of scientific databases. I would also like to thank Dr. Lester Fox, Dr. Raúl Michel, Dr. Davide Ricci, and Dr. Héctor Oti for their teachings in observational astronomy, and introducing me to the instrumentation at the San Pedro Mártir Observatory. I also want to thank friends and colleagues in Ensenada for their support.

Finally, I wish to acknowledge the support from a CONACYT scholarship for master studies, and the financial support from PAPIIT (UNAM) (IN108914), CONACYT (179662), and Coordinación de Estudios de Posgrado (UNAM) grants, which have provided funding for computer hardware as well as for travel to schools and conferences that have been useful for the completion of this work, and a valuable complement for my academic formation.

Contents

List of Figures

List of Tables

Resumen

Introducción

De acuerdo con el esquema de Hubble, existen tres tipos principales de galaxias en términos de su morfología: elípticas, lenticulares S0 y espirales. Éstas últimas también se dividen dependiendo de si presentan una barra central o no. En cuanto a su actividad, se pueden clasificar por la presencia de actividad nuclear o de brotes de formación estelar que se determina por la presencia y anchura de ciertas líneas espectrales. Por una parte, los brotes formación estelar pueden darse en diversas partes de la galaxia, pero la actividad nuclear se remite a una zona central en una escala del orden de 10^2 parsecs (pc), alrededor de un núcleo con masa $\sim 10^8 M_\odot$ y con una escala de tiempo del orden de 10^8 años; ver por ejemplo Woltjer (1959) y Beckmann & Shrader (2012). Actualmente, el modelo unificado del Núcleo Galáctico Activo (NGA) propone que en el centro de una galaxia reside un hoyo negro rodeado por un disco de acreción de gas, un toroide de polvo y un chorro de gas perpendicular. Alrededor de este núcleo, también pueden existir algunos núcleos de formación estelar. La inclinación de la línea de visión con respecto al plano del disco de acreción permite explicar las diferencias entre galaxias Seyfert 1 ó 2, quásares o blazares Beckmann & Shrader (2012).

Para alimentar un núcleo activo, se necesitan mecanismos que lleven gas hacia las regiones centrales de una galaxia para que éste sea eventualmente acretado por el agujero negro supermasivo. Se ha mostrado que las interacciones y fusiones mayores (donde la razón de masas entre las galaxias es $M_1/M_2 \sim 1$) pueden llevar cantidades de gas significativas hacia las regiones centrales de una galaxia, por lo que su estudio es importante en el contexto de los NGAs (ver por ejemplo Alexander & Hickox (2012)). Si bien, se ha estudiado el efecto de la acreción de satélites pequeños en una galaxia, se ha tratado poco el efecto que tienen en la componente gaseosa. Algunos primeros trabajos en esta dirección son los de Mihos & Hernquist (1994) y Hernquist & Mihos (1995), donde se explora el efecto que tiene un satélite en una órbita circular prograda con radio inicial de seis escalas radiales del disco, con una razón de masas del orden de 1:60 sobre una galaxia primaria de disco en un halo que tiene un perfil de densidad de una esfera isoterma. Por otro lado, trabajos recientes en simulaciones cosmológicas muestran que, de acuerdo con el modelo ΛCDM, alrededor de una galaxia puede existir una población de satélites de baja masa $\sim 10^9 M_\odot$, que posiblemente pueden albergar gas y estrellas. Para un halo como el de la Vía Láctea $M \sim 10^{12} M_\odot$, esto corresponde a una razón de masas del orden de 1:100 - 1:1000. Este rango de masas ha sido poco explorado y estos satélites aún pueden tener un efecto significativo en el disco de la galaxia primaria en términos de la morfología y de la dinámica de la componente gaseosa.

En este trabajo, se estudia el efecto que tienen satélites en el rango de masas de 1:100 para inducir flujos de gas hacia las regiones centrales del disco. Se considera una galaxia de disco en un halo de materia oscura con un perfil de densidad de Navarro-Frenk-White (Navarro et al. 1996) con parámetros físicos comparables a la Vía Láctea. Se utilizan dos modelos de galaxia, uno sin barra y otro con barra, ya que el primero permite aislar los efectos del satélite del de otras estructuras en el disco. Se utilizán satélites con masas de $M = 6 \times 10^9 M_\odot$ y $M = 1.2 \times 10^{10} M_\odot$ y tienen un perfil de densidad de Plummer. Para el satélite, se consideran algunas órbitas en casos progrados como retrogrados.

Este resumen se divide en las siguientes partes. En la sección Metodología se describe brevemente el código numérico, los modelos de galaxia primaria y satélite utilizados, así como las condiciones iniciales. En la sección de Resultados, se resumen los principales resultados del trabajo. En la última sección, se presentan las conclusiones y comentarios finales.

Metodología

Código Numérico

Para el desarrollo de las simulaciones, se utiliza la versión pública del código GADGET-2 (Springel 2005). Es un código de N-cuerpos que se utiliza tanto para integraciones de simulaciones cosmológicas, donde el factor de escala $a(t)$ varía de acuerdo a un modelo cosmológico, así como para integraciones de N-cuerpos sin considerar un universo en expansión $[a(t) = 1]$. También, este programa permite incluir una componente gaseosa simulada con el método de Hidrodinámica de Partículas Suavizadas (en inglés, Smoothed Particle Hydrodynamics, SPH) (Gingold & Monaghan 1977, Monaghan 1992, Springel 2010). Para todas las partículas, la fuerza gravitacional se calcula utilizando una versión optimizada del código de árbol (Barnes & Hut 1986), que es útil para calcular la fuerza de gravedad a grandes distancias con un costo computacional que crece como $N \log N$, donde N es el número de partículas. En este esquema, la caja de simulación se va dividiendo en cubos más pequeños cuyos lados son un factor de 2 de los lados de la caja original. Esta división se repite hasta que cada partícula quede en una caja. En el siguiente paso, se calcula la fuerza para una partícula. Para distribuciones de partículas alejadas, la fuerza se calcula a partir de una expansión multipolar mientras que para las partículas cercanas, la fuerza se obtiene de la ley de gravitación suavizada en un radio de suavizamiento ϵ.

Las ecuaciones de movimiento se integran utilizandoo un esquema tipo Kick-Drift-Kick (KDK, por sus siglas en inglés). El paso de tiempo se determina a partir de $\Delta t \propto (\epsilon/a)^{1/2}$, donde ϵ es el radio de suavizamiento y a es la magnitud de la aceleración de la partícula.

En la parte de hidrodinámica, se integran las ecuaciones de continuidad, movimiento y energía siguiendo la formulación de SPH de Springel & Hernquist (2002) que conserva la entropía del gas. Esta formulación es una aproximación consistente con la representación Lagrangiana de las ecuaciones de dinámica de fluidos. Para la modelación de choques, se introduce un factor de viscosidad artificial siguiendo el formalismo de Balsara (1995), Monaghan & Gingold (1983) con algunas modificaciones y es consistente con la conservación del momento (Springel 2005). Los cálculos también consideran la fuerza gravitacional producida por el gas. El paso de tiempo de las partículas se determina a partir de una versión modificada de la condición de Courant. Todos los pasos de tiempo de la simulación están acotados entre un máximo y mínimo determinados por el usuario.

En el código GADGET-2 se puede modelar un gas ya sea con la ecuación de estado isoterma o con una ecuación de estado adiabática. Sin embargo, cabe aclarar que la versión pública del código no considera mecanismos de enfriamiento y calentamiento del gas, así como otros mecanismos físicos en el medio interestelar como retroalimentación por supernovas y vientos estelares.

Construcción de Modelos de Galaxias

En el estudio de galaxias en interacción por medio de simulaciones de N-cuerpos, se requieren modelos de galaxias que sean estables por al menos unos cuatro períodos orbitales de la galaxia y que además representen los perfiles de densidad y cinemáticos adecuadamente. Para una galaxia como la Vía Láctea, el período de rotación a un radio solar $R_\odot = 8$ kpc es $\tau \approx 250$ millones de años. Entonces, se necesita un modelo que sea estable por al menos unos $\approx 10^9$ años. Dado que las galaxias son colecciones de estrellas con por lo menos 10^{11} partículas, el tiempo de relajación o la escala de tiempo en la que las colisiones (interacciones muy cercanas entre partículas que desvíen su trayectoria significativamente) modifican sustancialmente las órbitas de las estrellas es varios órdenes de magnitud mayor al período orbital de la galaxia. Por esta razón, la órbita de una estrella individual se puede aproximar por la que resultaría si la galaxia se tratara como un sistema continuo y el sistema se puede tratar como si fuera no colisional.

En esta aproximación, la distribución de espacio fase $f(\mathbf{q}, \mathbf{p}; t)$, donde $\mathbf{q}$ y $\mathbf{p}$ son las posiciones y momentos generalizados, satisface la ecuación no colisional de Boltzmann. Si se asume un estado estable, entonces la distribución en equilibrio depende sólo de las posiciones y velocidades. La ecuación de Boltzmann también depende del potencial gravitacional del sistema. A su vez, el potencial se obtiene de la densidad de materia ρ a partir de la ecuación de Poisson. La densidad ρ está conectada con la distribución de espacio fase. Entonces, si la distribución de espacio fase f satisface simultáneamente la ecuación de Poisson y la de Boltzmann, se dice que el sistema es autoconsistente. En el contexto de simulaciones de galaxias, el objetivo de obtener una distribución de espacio fase de manera autoconsistente y en estado estable es para obtener un modelo en equilibrio de una galaxia que se pueda utilizar como condición inicial.

Existen varias aproximaciones para inicializar modelos de galaxias que tienen un halo de materia oscura, un disco y un bulbo central. Una de ellas es el método de los momentos de la ecuación de Boltzmann. Se obtienen los primeros momentos de la ecuación, de los que se obtienen ecuaciones análogas a las de fluidos, que dependen de la densidad de materia y la dispersión local de velocidades. Dado un perfil de densidad, se pueden obtener las dispersiones de velocidades del sistema. Por ejemplo, Hernquist (1993) utiliza este método asumiendo que las distribuciones de velocidad locales son Gaussianas. Otra aproximación, es utilizar funciones de distribución que dependan de integrales de movimiento asociadas al potencial de la galaxia. Por el teorema de Jeans, una función de distribución que depende únicamente de las integrales de movimiento es una solución de estado estable a la ecuación no colisional de Boltzmann. En este principio, se basan diversos métodos como los de Kuijken & Dubinski (1995), Widrow & Dubinski (2005) y McMillan & Dehnen (2007), por mencionar algunos ejemplos.

Modelos de la Galaxia Primaria

Los modelos de galaxias se construyen utilizando el método de McMillan & Dehnen (2007) implementado en el paquete de herramientas para dinámica de sistemas estelares NEMO (Teuben 1995). Dicho esquema genera modelos de galaxias de disco autoconsistentes con componentes no gaseosas que incluyen un halo de materia oscura, un disco estelar y un bulbo. Las componentes esferoidales, se inicializan muestreando una función de densidad esféricamente simétrica. Posteriormente, se dejan relajar en el potencial producido por el término monopolar del potencial del disco. Después, la componente estelar se va poblando adiabáticamente. Una ventaja de los modelos de McMillan & Dehnen (2007) es que pueden generar discos donde el parámetro Q de Toomre (1964) sea una función del radio galactocéntrico o sea constante para toda la galaxia.

Para agregar la componente gaseosa del disco, se sigue un esquema similar al de Springel (2000) y Dobbs et al. (2010), donde el gas inicialmente se distribuye con un perfil de densidad similar al de la componente estelar y se establece en equilibrio rotacional. Después, se deja relajar en el potencial de la galaxia por unos cuatro períodos orbitales.

En el presente trabajo, se utiliza una galaxia primaria de disco con parámetros físicos similares a los de la Vía Láctea basados en los de (Klypin et al. 2002, McMillan & Dehnen 2007) que incluye una componente de materia oscura, un disco estelar y uno gaseoso, y un bulbo central. El halo de materia oscura tiene un perfil de densidad que sigue el modelo de Navarro-Frenk-White (Navarro et al. 1996), una masa total de $M_h = 10^{12} M_\odot$ y un radio de escala de 21 kpc. El disco estelar tiene una masa de $M_d = 4.167 \times 10^{10} M_\odot$, una escala radial de $R_D = 3.5$ kpc, y una escala vertical $z_d = 0.35$ kpc. El bulbo central tiene un perfil de densidad de Hernquist (Hernquist 1990), tiene una masa de $M_b = 8.333 \times 10^9 M_\odot$, y una escala radial de 0.700 kpc. Por último, la componente gaseosa se distribuye con un perfil de densidad similar al de la component estelar. El gas tiene una temperatura de $T = 8 \times 10^3$ K y se trata como un gas ideal isotermo. La masa del gas es $M_g = 0.1 M_d$. Por su curva de rotación, esta galaxia tiene un período orbital $\tau \approx 240 \times 10^6$ años en $R = 8$ kpc.

Se realizan simulaciones con dos modelos de galaxia: una sin barra (Modelo A) y otra con barra (Modelo B). En términos de los número de partículas de las componentes, el halo de materia oscura tiene un total de $N_h = 10^6$, los discos estelar y gaseoso contienen $N_d = N_g = 500000$, y el bulbo central se integra de $N_b = 10000$ partículas. Los radios de suavizamiento de la fuerza gravitacional utilizados son: $\epsilon_h = 0.121$ kpc para el halo,

$\epsilon_d = \epsilon_g = 0.035$ kpc para el disco estelar y el gaseoso, y $\epsilon_b = 0.110$ kpc para el bulbo. Es importante comentar que en una galaxia con barra, ésta estructura genera flujos hacia las regiones centrales en evolución aislada (ver por ejemplo Athanassoula (1994)). Por esta razón, el propósito del Modelo A es construir una galaxia donde se elimine la influencia de una barra para cuantificar los efectos que introduce la interacción con el satélite. Con el Modelo B, se busca cuantificar dichos efectos en una galaxia barrada. Cabe agregar que para el Modelo A se utiliza un parámetro de Toomre $Q = 3.0$ y para el Modelo B, $Q = 1.5$; en ambos modelos se ha definido que Q sea constante en toda la galaxia.

Modelos de la Galaxia Satélite

El satélite se construye, utilizando el programa `mkplummer` del paquete de herramientas NEMO (Teuben 1995), con un perfil densidad de Plummer con masas de $M_1 = 6 \times 10^9 M_\odot$ (Satélite 1) y $M_2 = 1.2 \times 10^{10} M_\odot$ (Satélite 2). La escala radial del satélite se define de modo que la densidad central sea aproximadamente igual a la densidad promedio del disco. De esto se obtiene que la escala radial del primer satélite es $a \approx 1.0$ kpc, y la del segundo es $a \approx 1.3$ kpc. El satélite se compone de $N_s = 72000$ partículas y el radio de suavizamiento es de $\epsilon = 0.035$ kpc, como en el disco de la primaria.

Parámetros Órbitales del Satélite

Se consideran tres tipos de órbitas para la galaxia satélite: la Órbita 1 es circular con radio inicial $R_i = 3R_D$ e inclinación inicial de $i = 30°$; la Órbita 2 es circular con radio inicial $R_i = 6R_D$ y la misma inclinación; la tercera es una órbita coplanar con pericentro $R_p = R_D$ y apocentro de $6R_D$. En todas se consideran casos progrados y retrogrados. Hernquist & Mihos (1995) han explorado sólo el caso progrado de la Órbita 1 en el contexto de flujos de gas en galaxias de disco. Cabe comentar que en este trabajo se exploran los casos retrogrados de las órbitas mencionadas para determinar hasta qué punto tienen efecto en los flujos de gas de la galaxia primaria. Este tipo de órbitas son típicamente poco explorados ya que su velocidad relativa con respecto a la rotación del disco es alta por lo que se espera menos daño en el disco durante su interacción.

Con los dos modelos de galaxias, los dos modelos de satélites definidos y las tres órbitas, en sus casos progrado y retrogrado, resulta en un total de 24 simulaciones. Todos los casos se dejan evolucionar por 4 períodos orbitales de la primaria ($\approx 10^9$ años).

Resultados

Morfología

Debido a la interacción del satélite, se producen perturbaciones en la galaxia que se reflejan en cambios en su morfología. Los casos más impactantes, son los del satélite en las órbitas circulares progradas. En el caso de la Órbita 2 ($R_i = 6R_D, i = 30°$) con el Satélite 1 ($M = 6.0 \times 10^9 M_\odot$), después de dos cruces por el plano del disco, se produce una galaxia con un marcado patrón espiral que se asemeja a una de gran diseño. Como ejemplo, éste se muestra en la Figura 1.

Con el Satélite 2 ($M = 1.2 \times 10^{10} M_\odot$) en la misma órbita, se produce una perturbación muy significativa, pero el disco de la galaxia aún sobrevive. Los casos progrados de la Órbita 1 ($R_i = 3R_D, i = 30°$) también reflejan perturbaciones en el mapa de densidad. En los casos retrogrados, es interesante el de la Órbita 1 debido a que tanto el Satélite 1 como el 2, producen efectos en la morfología de la galaxia al final de la simulación. Las simulaciones con la Órbita 3 ($R_{peri} = R_D, i = 0°$) también muestran perturbaciones en la morfología tanto en la órbita prograda como en la retrograda.

Las figuras y resultados detallados se muestran en la sección 4.1 de este trabajo.

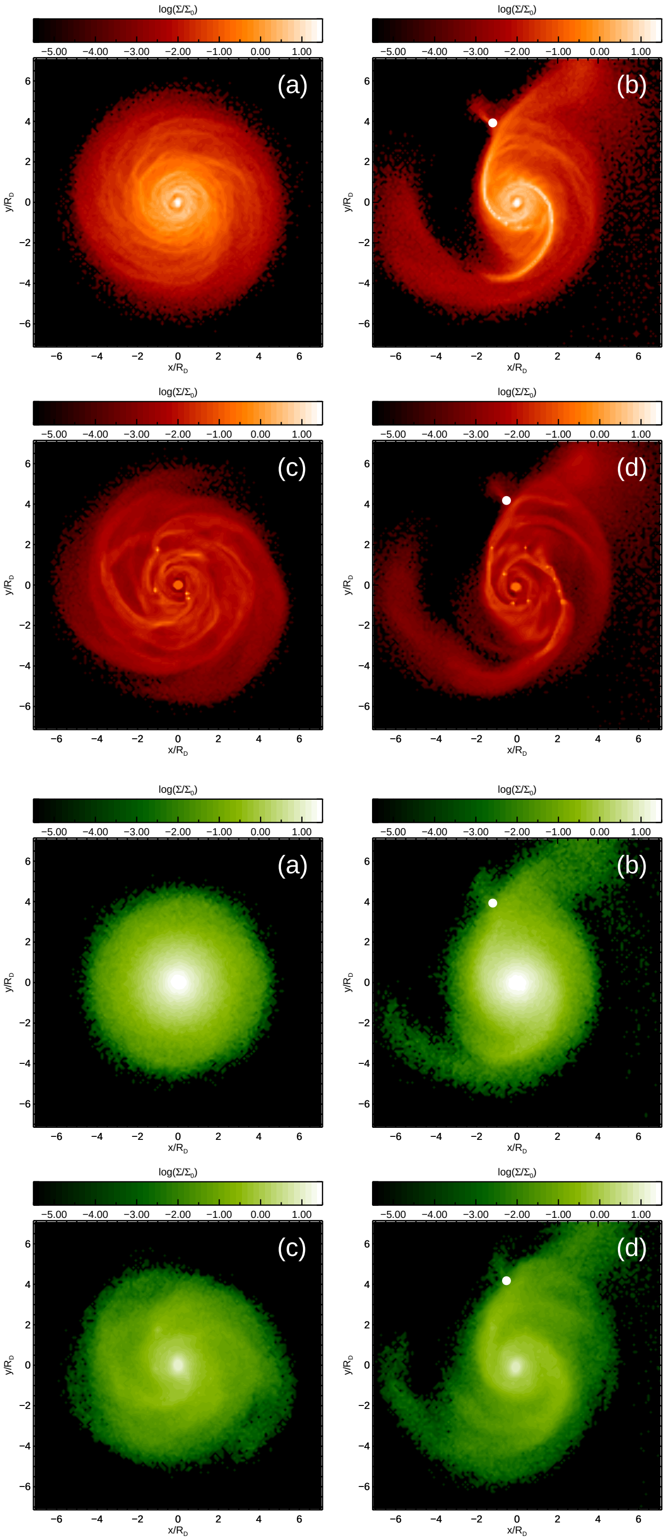

Figura 1: Ejemplo de la morfología generada en las componentes gaseosa (rojo) y estelar (verde) con el satélite de $M = 6.0 \times 10^9 M_\odot$ en la Órbita 2 prograda ($R_i = 6R_D, i = 30^\circ$). Los cuadros (a) y (b) corresponden al Modelo A en el caso aislado y en interacción, respectivamente. Los cuadros (c) y (d) muestran la misma información para el modelo B.

Distribución de la Masa de Gas

Una medida de la distribución de la masa de gas de la galaxia es la función de masa integrada o masa acumulada $M(< R)$. Si hay gas que está migrando hacia el interior a través de un anillo de radio R, la cantidad $M(< R)$ tiene que crecer con el tiempo. Formalmente, la masa acumulada se obtiene al integrar la densidad superficial hasta cierto radio. En el caso numérico, la galaxia simulada se divide en anillos y se suma la masa en cada uno de estos hasta un radio dado. La estimación de la cantidad de gas que migra hacia las zonas centrales se obtiene de la diferencia entre la masa integrada del gas en función del radio al final y al inicio de la simulación. Debido a que en evolución aislada existen flujos debido a la presencia de barras, es mejor comparar la distribución final después de la interacción con la que se obtiene de la evolución aislada de la galaxia en el mismo intervalo de tiempo.

En las simulaciones de la Órbita 1 prograda con el Modelo A (galaxia no barrada) se obtiene que al final de la simulación la zona central tiene aproximadamente 30 % de la masa de gas de la galaxia, aunque no se observa una dependencia clara con la masa del satélite (ver sección 4.2 y Figura 4.25 para más detalle). En el caso retrogrado (ver Figura 4.25 en la sección 4.2), con el Satélite 1 no se observa mucha diferencia con respecto al caso aisaldo. En el caso del Satélite 2, se observa que cierta cantidad de gas en regiones externas migra a radios menores, pero no es muy efectivo el transporte hacia el centro. Sin embargo, este efecto es consistente con la morfología que muestra la galaxia al final de esta simulación. En las simulaciones con el Modelo B (galaxia con barra), se muestran tendencias similares, pero al comparar con la distribución de gas en evolución aislada, la diferencia no es tan significativa. Los resultados se muestran en la Figura 4.28 de la sección 4.2.

Respecto a las simulaciones con la Órbita 2, en el caso progrado se observan efectos importantes tanto en el Modelo A (Figura 2,cuadro izquierdo) como en el Modelo B (Figura 2, cuadro derecho). Las simulaciones con el Satélite 1 muestran que a $R = R_D$ la masa integrada es aproximadamente 40 % de la masa total de gas. Con el satélite más masivo (Satélite 2), se obtiene que a $R = R_D$, la masa integrada alcanza cerca del 60 % de la total. En este caso, se encuentra que duplicar la masa del satélite aumenta significativamente los efectos observados en la primaria. En los casos retrogrados, no se observan cambios importantes en la distribución de gas final en comparación con la que resulta de la evolución aislada.

En los casos con la Órbita 3, las distribuciones de masa de gas finales muestran que se producen flujos de gas con las dos masas de satélites, con las órbitas tanto progradas como retrogradas, y en los dos modelos de galaxias. Los resultados se describen con más detalle en la sección 4.2.

Flujos de Gas Inducidos

Al visualizar la distribución de masa de gas final, queda poco clara la evolución temporal de los flujos de gas. En esta sección, se eligen dos radios fijos: $R = 0.28R_D$ y $R = R_D$, que corresponden a 1 kpc y 3.5 kpc, respectivamente y se obtiene la masa integrada hasta ese punto como función del tiempo. Entonces, si $M(< R)$ es la masa integrada hasta cierto radio, cuando el gas migra desde radios mayores, $M(< R)$ va a crecer en función del tiempo. En cambio, si se mueve desde el interior, está funcion decrece. Cualquier redistribución de gas dentro dentro del anillo R no afecta al valor de $M(< R)$ mientras éste no cruce el anillo. Por esta razón, es un buen indicador del flujo a través del anillo.

Los resultados de las simulaciones con la Órbita 1 y el Modelo A, en el caso progrado (ver Figura 4.31, cuadro izquierdo en la §4.2), muestran que hay una diferencia en la respuesta de los flujos según la masa del satélite. También, la respuesta varía en distintos puntos de la galaxia. Para los dos satélites, los flujos en $R = 0.28R_D$ muestran que ambos satélites logran llevar una fracción de gas de ≈ 15 a $\approx 20\,\%$ hacia el centro de la galaxia. Sin embargo, la tasa es más lenta con el satélite menos masivo. Los flujos en $R = R_D$, a pesar de ciertas oscilaciones, muestran que una pequeña fracción de gas migra al interior de este punto. Es interesante ver que en el caso retrogrado (ver Figura 4.31, cuadro izquierdo en la §4.2), el Satélite 2 produce ciertos flujos en $R = R_D$. Sin embargo, ninguno de los satélites produce flujos que lleguen a la zona central. Con el Modelo B, se observan tendencias similares (Figura 4.34 de la §4.2).

En el caso de la órbita 2, la respuesta del gas es más significativa en los casos progrados. Con ambos satélites, se produce cierta perturbación en el Modelo A, a partir de $t \approx 1.5\tau$ (como ejemplo, se incluye en esta sección en la Figura 2, cuadro izquierdo inferior). Con el Satélite 1, el flujo aumenta hacia el final de la simulación en $R = R_D$. Sin embargo, no hay flujos significativos en el interior del disco. Los resultados del Satélite 2 muestran que hay una respuesta importante en $R = R_D$. Se estima que una cantidad equivalente al $35\,\%$ del gas total de la galaxia pasó hacia el interior po este punto. Aproximadamente 1.5τ después, se observa un aumento importante en el flujo en $R = 0.28R_D$ y se observa que una cantidad importante de gas se movió al interior. En el Modelo B, se observan tendencias similares (Figura 2 de esta sección, cuadro inferior derecho). Con el Satélite 1, la diferencia de los flujos con respecto a la evolución aislada no es significativa. Sin embargo, con el Satélite 2 hay una respuesta importante. El mayor cambio ocurre a partir de $t \approx 2\tau$. También, se observa que hay flujos tanto en $R = R_D$ como en $R = 0.28R_D$. En el primer punto, se estima que $\approx 15\,\%$ de la masa total de gas migró hacia el interior. En el segundo, se estima que esta cantidad es de $\approx 10\,\%$. En los casos retrogrados, no se observa diferencia con respecto a la evolución aislada con cualquiera de las dos masas y en ambos modelos.

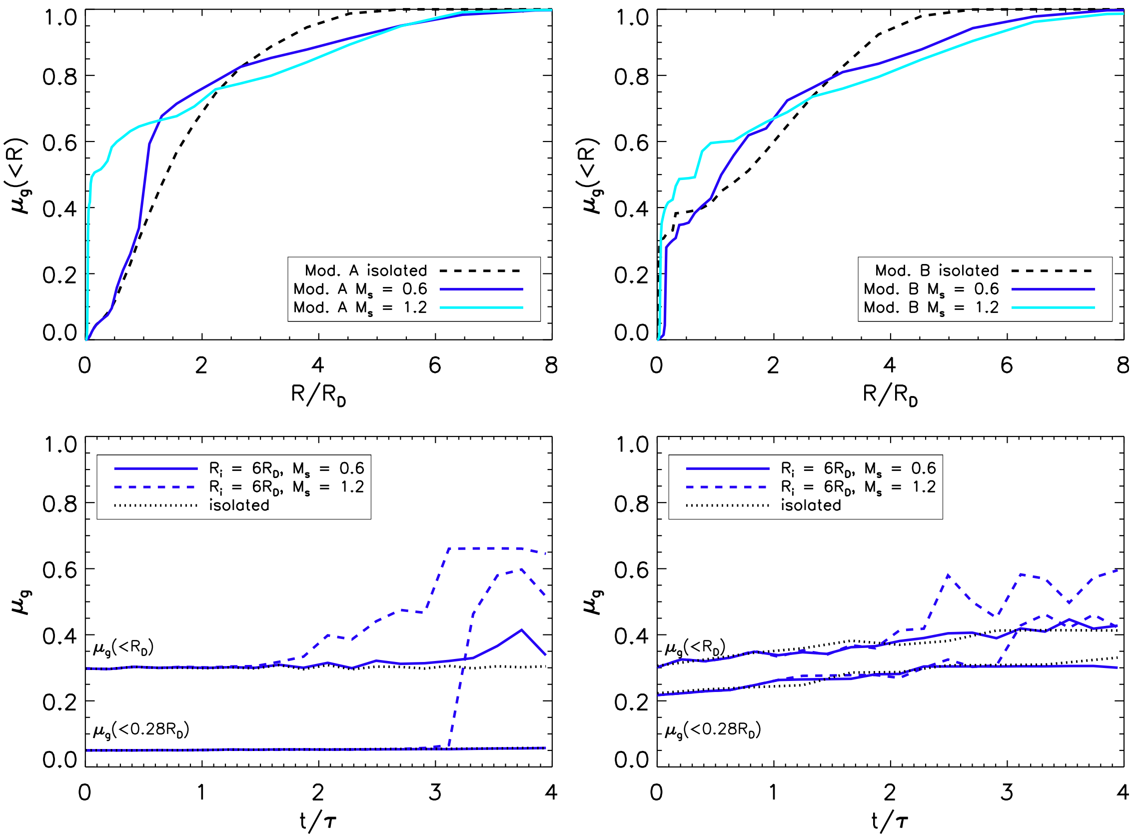

Figura 2: El cuadro superior izquierdo muestra la función de masa integrada final para la simulación con los satélites en la Órbita 2 prograda ($R_i = 6R_D, i = 30°$) y el Modelo A. El cuadro superior derecho muestra la misma información para el Modelo B. El cuadro inferior izquierdo muestra los flujos de gas para la misma simulación con el Modelo A, y el cuadro inferior derecho, con el Modelo B.

En los casos de la órbita coplanar (Órbita 3), se observan efectos tanto en los casos progrados como retrogrados y en ambos modelos de galaxia. En el Modelo A, es evidente que el Satélite 2 lleva más masa hacia el interor que el Satélite 1. En la Figura 4.33 de la §4.2, se muestran los resultados para el Modelo A como un ejemplo del caso coplanar. En el Modelo B, si bien se produce una respuesta en términos de flujos, parece no ser tan sensible a la masa del satélite.

Discusión

En este trabajo, se ha explorado el efecto de satélites con masas tales que están en una razón de masas de $\approx$ 1:100 con respecto a la masa total de la galaxia. Los resultados muestran que satélites en este rango de masas aún tienen la capacidad de producir efectos significativos en el disco. Se esperaría que al incrementar la masa del satélite, se aumente el efecto de la perturbación. Dentro del error introducido por efectos numéricos, se observa que esta tendencia se cumple en muchos casos, especialmente en los encuentros progrados que inician a $R = 6R_D$ con $i = 30°$.

En términos de morfología, estos satélites aún producen efectos observables en la distribución de densidad de la galaxia primaria. La morfología de los brazos espirales en la componente estelar es similar a la que obtienen, por ejemplo, Velazquez & White (1999) y Kazantzidis et al. (2008, 2009). En un trabajo reciente de Chakrabarti et al. (2011), se realizan simulaciones con satélites con razones de masa entre $\approx$1:3 y $\approx$1:100 para explorar los efectos en los mapas de gas de galaxias en interacción, pero no exploran los efectos en términos de flujos de gas. La morfología obtenida en el presente trabajo es cualitativamente similar a la de Chakrabarti et al. (2011). Bournaud et al. (2005) muestran que satélites con razones de masa en el orden de 1:10 producen asimetrías con modos $m = 1$ y $m = 2$. En este sentido, el presente trabajo muestra que satélites en el rango de 1:100 aún producen estos efectos.

Se muestra que estos satélites pueden generar flujos significativos en la galaxia primaria. En el caso de la Órbita 1 ($R_i = 3R_D, i = 30°$), si bien se muestra que la interacción con el satélite lleva una fracción no despreciable de gas al centro, de aproximadamente 25 % del gas de toda la galaxia, no se observa una clara dependencia con la masa del satélite. Cabe tener en cuenta que, como este satélite interactúa con las partes más internas y ligadas del disco, su órbita decae rápidamente y es acretado. El hecho de que la función de masa acumulada, en el Modelo A, crece en la región central muestra que la perturbación del satélite está provocando la redistribución de gas. En el caso del Modelo B, la presencia de la barra ya ha redistribuido material en esa región, por lo que la aportación del satélite en esta órbita a los flujos parece ser poco significativa. En el caso retrogrado, es interesante que el satélite más masivo produce una redistribución del material en toda la galaxia. Sin embargo, no es tan eficiente para llevarlo al centro.

Respecto a las simulaciones con la Órbita 2 ($R_i = 3R_D, i = 30°$), existe una respuesta importante en los casos progrados. En esta órbita, el satélite primero perturba las regiones externas, menos densas y poco ligadas. En las primeras interacciones, se producen colas que mueven cierta cantidad de gas a regiones más externas, lo que explica que la función de masa acumulada de gas cae, con respecto al caso aislado, en zonas externas. También, se producen flujos significativos hacia la región central. El flujo estimado a través de un anillo en $R = R_D$ muestra que una gran cantidad de gas migra desde radios externos. Aproximadamente 60 % del gas de la galaxia se encuentra dentro de este radio al final de la simulación. La perturbación eventualmente llega, en una escala de tiempo de $\approx \tau$, a la región interior. La galaxia barrada también muestra una respuesta significativa en flujos. Dado que la barra afecta a las regiones interiores y la perturbación del satélte a las exteriores, existe suficiente gas en las regiones exteriores que puede ser dirigido al centro. Los resultados muestran que la interacción del satélite masivo en la Órbita 2 tiene la capacidad de producir flujos mayores a los que produce la barra en evolución aislada, pues al final de la simulación se obtiene aproximadamente 10 % más gas que en evolución aislada. En estos casos, es claro que al aumentar la masa del satélite, aumenta la respuesta del disco en términos de flujos de gas.

Los resultados de la Órbita 3 muestran que tanto los casos prograrados como los retrogrados mueven cierta fracción de gas hacia la región central. En radios externos hay un cierto intervalo donde existe una mayor tasa de flujo y después se reduce. En regiones interiores, el flujo de gas es más gradual. El hecho de que en $R = 0.28R_D$ se mantiene una tasa de flujo relativamente constante muestra que la perturbacioń está afectando a las regiones interiores del disco. Es interesante que en los casos retrogrados también se observan flujos.

En los casos estudiados, se muestra que estos satélites tienen la capacidad de inducir flujos en la galaxia. El Modelo A permite distinguir los efectos del satélite en la galaxia. Como la distribución de gas es muy estable en evolución aislada, las simulaciones han permitido estimar en qué medida se redistribuye el gas de la galaxia por el efecto del satélite. En el Modelo B, la presencia de una barra genera flujos de gas hacia el centro en evolución aislada. Por esta razón, las simulaciones muestran que el efecto del satélite se manifiesta en los flujos de gas cuando perturba regiones alejadas de la barra donde exista suficiente gas que pueda ser dirigido al centro. En el caso de una galaxia barrada, si el satélite perturba las regiones interiores tiempo después de que la barra se ha formado, es posible que no aporte mucho a los flujos ya que la barra habrá desplazado cierta cantidad previamente. Los resultados también muestran que los flujos no son necesariamente graduales. Hay momentos donde la tasa es alta y después decae rápidamente. La morfología inducida también juega cierto papel en los flujos de gas. El gas tiende a concentrarse en los brazos espirales y estas estructuras también redistribuyen el material debido a los torques que producen.

Existen ejemplos de galaxias aisladas, como en el catálogo de galaxias aisladas de Karachentsev, que muestran asimetrías en sus mapas de densidad, pero no hay evidencia de galaxias compañeras similares en su vecindad. Es difícil determinar observacionalmente la población de satélites pequeñas en galaxias fuera de la Vía Láctea, sin embargo los escenarios esándar de formación de galaxias, ver por ejemplo Mo et al. (2010), predicen una población significativa de satélites pequeños alrededor de halos de materia oscura similares al de la Vía Láctea. El presente trabajo muestra que estos satélites aún pueden tener un impacto apreciable en la morfología de discos albergados por estos halos.

Los resultados del presente trabajo también tienen implicaciones en el contexto de los Núcleos Galácticos Activos. Se acepta que las fusiones entre galaxias pueden ser un mecanismo para iniciar la actividad nuclear, ver por ejemplo Alexander & Hickox (2012). Sin enbargo, no es posible determinar hasta qué punto las fusiones menores impactan en la actividad nuclear. Cabe mencionar que no hay una correlación clara entre la presencia de un NGA y una barra en la galaxia anfitriona. Las simulaciones con el Modelo A indican un mecanismo potencial en el que se desplaza una cantidad importante de gas con la interacción del satélite. En el caso de una galaxia sin barra o con una barra débil, estas perturbaciones pueden llevar suficiente gas a la región central de la galaxia. En una galaxia con barra, estas simulaciones muestran que estas perturbaciones pueden producir flujos mientras la barra no haya desplazado suficiente gas. Los casos que mayor cantidad de gas desplazan son las órbitas progradas y logran llevar gas hasta regiones al interior de 1 kpc. Cuando el satélite perturba las regiones más externas, el gas alcanza las regiones interiores en una escala de tiempo de $\approx \tau \approx 240$ Maños, un período orbital a $R = 8$ kpc. Los efectos de estas interacciones también pueden ser relevantes en términos de brotes de formación estelar, ver por ejemplo R. C. Kennicutt (1998).

Conclusiones y trabajo futuro

Los resultados de este trabajo se resumen a continuación:

- En términos de morfología, las órbitas circulares progradas pueden inducir perturbaciones significativas en las componentes gaseosa y estelar de la galaxia primaria. En los casos retrogrados, el satélite más masivo porduce una distribución de densidad asimétrica. Tanto la órbita prograda coplanar como la retrograda coplanar introducen perturbaciones observables en la densidad de la galaxia primaria. Dadas las razones de masa de los satélites, es un resultado interesante que estos satélites pequeños aún producen efectos observables en el disco de la primaria.

- Los satélites en el rango de masa considerado produce flujos de gas significativos en el disco de la primaria. Sin embargo, depende de la orientación de la órbita, si es prograda o retrograda, y la masa del satélite. Las simulaciones con la galaxia sin barra (Modelo A) muestran que las perturbaciones inducidas y los flujos de gas inducidos son una consecuencia del satélite en acreción. Las simulaciones de la galaxia con barra (Modelo B) muestran que los satélites en este rango de masas pueden producir aún flujos de gas en este tipo de galaxias. Las simulaciones con ambos modelos muestran que los flujos más altos se producen por la órbita con $R_i = 6R_D$, $i = 30°$, donde $\approx 60\,\%$ del gas de la galaxia es llevado a una región dentro de $R = R_D$. La órbita circular retrograda no introduce flujos significativos. Tanto la órbita coplanar prograda como la retrograda pueden introducir flujos a la región $R < R_D$. En estas simulaciones, una fracción de $\approx 50\,\%$ del gas de la galaxia alcanza esta región.

- La masa integrada hasta $R = 0.28R_D$ y $R = R_D$ muestra que los flujos no son graduales y son sensibles a la órbita y la masa del satélite. En el caso de las órbitas circulares, con $R_i = 3R_D$, se producen flujos graduales que no son muy sensibles a la masa del satélite. La órbita con $R_i = 6R_D$ produce flujos muy rápidos y la respuesta del gas se incrementa al aumentar la masa del satélite. La mayoría de los flujos de gas ocurre en una escala de tiempo de aproximadamente el período orbital de la galaxia. Dado que esta órbita perturba las regiones más externas de la galaxia, se observan flujos a través de anillos con $R = R_D$ y $R = 0.28R_D$. El gas llega a $R = R_D$ y después de $\approx \tau$ llega a la zona más interna. La respuesta de la galaxia al satélite en esta órbita es similar tanto en el modelo sin barra como en el modelo con barra, y es más sensible a la masa del satélite. Las simulaciones con la órbita coplanar muestran que ambos satélites producen flujos graduales independientemente del sentido de la rotación de la órbita, y que no dependen tanto de la masa del satélite o de la presencia de una barra.

- Se muestra que pequeños satélites con una razón de masas de $\approx 1 : 100$ producen distorsiones observables en el gas y la componente estelar de la galaxia primaria. Estas interacciones menores pueden ser mecanismos viables para inducir asimetrías en las galaxias.
- Estas interacciones también puede inducir flujos de gas imporantes hacia al región central de la galaxia primaria, que es relevante en el contexto de la actividad nuclear.

Simulaciones cosmológicas, consistentes con el modelo ΛCDM, han mostrado que pueden existir muchos de estos pequeños satélites alrededor de galaxias con masa similar a la Vía Láctea. En trabajos futuros, será interesante evaluar el efecto de estas estructuras en inducir flujos de gas considerando condiciones iniciales orbitales derivades de simulaciones cosmológicas. También, será adecuado realizar simulaciones similares incluyendo efectos de formación estelar y retroalimentación de supernovas para evaluar su impacto en los flujos finales.

Chapter 1

Introduction

Galaxies are large collections of stars, dust, gas, and dark matter showing a broad variety of shapes and morphological features. Since the times of Messier and Herschel, significant efforts have been made to study them systematically from an astronomical point of view. These objects are classified in terms of their morphology or of their spectra. The presence of certain lines and spectral features indicate the presence of enhanced star formation or nuclear activity. Galaxies gradually change with time, and their mutual interaction with others plays an important role in their evolution. Interactions can trigger star formation bursts, nuclear activity, and significantly reshape the morphology of the galaxy (see for example Mo et al. (2010), Benson (2010), Binney & Tremaine (2008), Bertin (2000)), and references within).

A first approach in the study of galaxies was the classification in terms of their morphological appearance. Around 1936, Hubble introduced a classification system that divides galaxies in three main morphological categories: elliptical, lenticular, and spiral. The third group is further subdivided into barred and non-barred spirals, and a fourth category was introduced to include irregular galaxies. de Vaucouleurs (1959) further refined this scheme in subsequent studies. Sandage et al. (1975), Sandage & Bedke (1988), and Sandage & Bedke (1994) compiled several photographic atlases which show the wide variety of morphological features that is identified in spiral and elliptical galaxies.

In the case of many spiral galaxies, several observational studies have shown that their stellar and gaseous components show morphological disturbances or asymmetries (e. g. Beale & Davies 1969), more commonly referred as *lopsidedness* (e. g. Baldwin et al. 1979). The interaction with a satellite galaxy has been suggested as a possible mechanism for producing these perturbations, as reviewed by Jog & Combes (2009). The galaxy UGC 7989, shown in Figure 1.1, is an example that shows some lopsidedness in its gas distribution. Other works, such as the Atlas of Peculiar Galaxies (Arp 1966), give many examples of galaxies that are interacting with nearby companions. Many of these objects show noticeable disturbances in their morphology, which suggests current or past interactions. In many cases, bridges and tidal tails are present indicating that the systems are interacting. Famous examples of interacting galaxies in the Arp catalogue are the *The Mice* (NGC 4676), shown in Figure 1.2), and *The Tadpole* (Arp 188), shown in Figure 1.3.

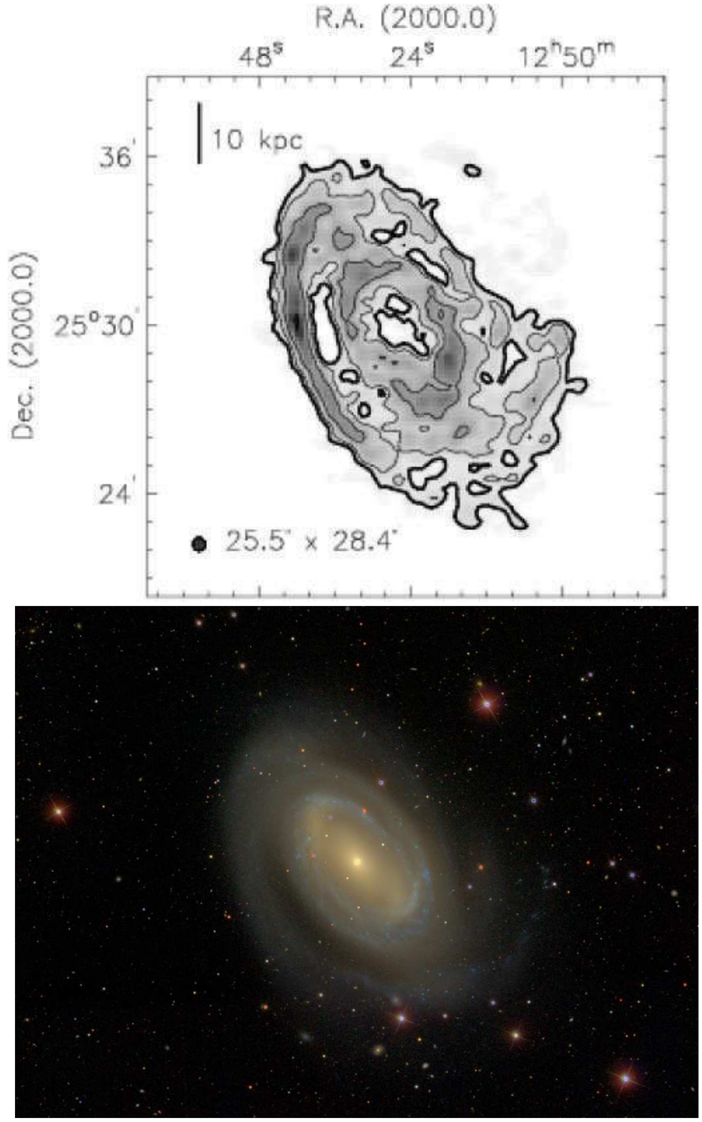

Figure 1.1: UGC 7989: an example of a galaxy with a lopsided gas HI distribution (upper panel) observed with the Very Large Array (Phookun & Mundy 1995). The composite optical image of the galaxy in the SDSS gri bands is shown in the lower panel. Image Credit: M. R. Blanton & D. W. Hogg (2006); Image obtained from the NED database.

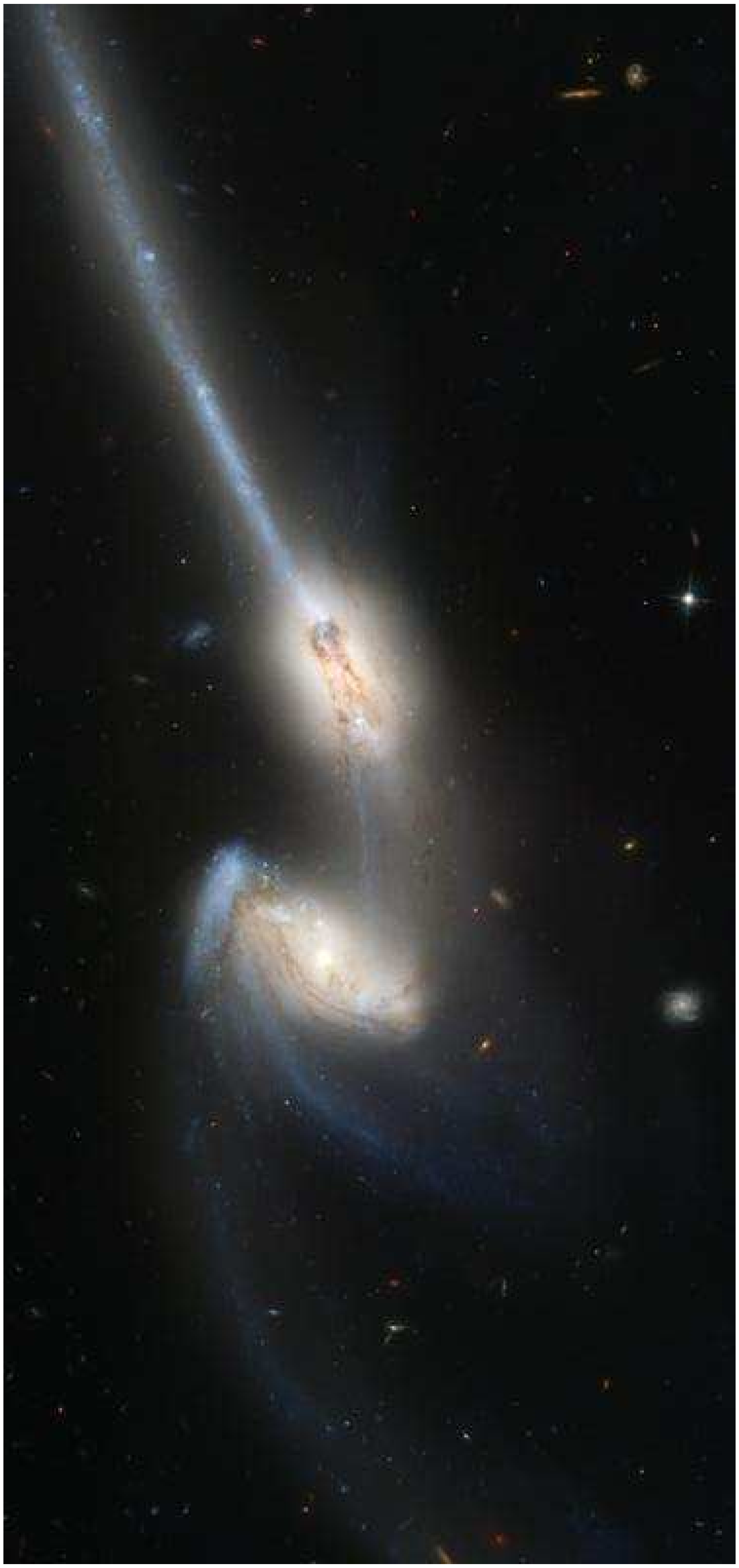

Figure 1.2: NGC 4676: an interacting pair of galaxies of comparable size. Image Credit: ACS Science & Engineering Team, Hubble Space Telescope, and NASA.

Figure 1.3: UGC 10214: a disc galaxy showing signs of an interaction with a satellite. Image Credit: ACS Science & Engineering Team, Hubble Space Telescope, and NASA.

Galaxies can also be studied from the point of view of spectroscopy as spectroscopic observations can provide information about the dominating stellar populations, chemical abundances, and whether nuclear activity is present or not. Seyfert (1943) presented evidence of high-excitation emission from the nuclear regions of some spiral galaxies. These galaxies were classified according to the strength and broadness of their spectral lines (e. g. Weedman 1970). Seyfert's work shows that important activity can exist within the nuclear region of a galaxy. Woltjer (1959) improved the picture of nuclear activity showing that nuclear emission must emerge from gas in a compact region within the inner 100 pc of a galaxy, and gravitationally bound to an object with a mass of $\sim 10^8 M_\odot$. This work gives a timescale for the activity of at least 10^8 yr.

The nature of the massive central object became a matter of debate. Hoyle & Fowler (1963) first suggested that it should be of stellar nature, but the picture of a supermassive black hole was eventually accepted (Salpeter 1964, Zel'Dovich & Novikov 1964). The nuclear region may present other forms of activity such as radio and X-ray emission that is linked to a small region surrounding the central supermassive black hole. Recent works have introduced a unified model for Active Galactic Nuclei (AGN), which consists of a supermassive black hole, encircled by a gas accretion disc, a dust torus, and two perpendicular jets that emerge from the centre. At larger distances, it can be surrounded by regions of star formation. With this model, differences in the spectra and type of radiation from nuclear regions are attributed to the angle of the line of sight with respect to the disc (see Beckmann & Shrader (2012), Alexander & Hickox (2012) and references therein).

Observations in the IR bands show that some active galaxies have very strong IR luminosities and enhanced star formation. These objects have been classified as Luminous and Ultra-Luminous Infrared Galaxies (LIRGS and ULIRGS respectively) due to their intense infrared radiation. These objects can have star formation rates reaching as high as $\sim 10^3 M_\odot\,\mathrm{yr}^{-1}$. Several observational studies have found that these galaxies show evidence of very strong interactions (see for example R. C. Kennicutt (1998) and references within), supporting the idea that interactions are important mechanisms for triggering activity in galaxies.

However, large amounts of gas have to be funnelled to the nuclear regions of a galaxy in order to trigger nuclear activity. Thus, it is necessary to understand and identify mechanisms that effectively transport gas to the central regions of the galaxy (e. g. Shlosman et al. 1990). Bars, gas instabilities, and spiral structure are internal large-scale mechanisms that can produce gas flows in galaxies (Alexander & Hickox 2012). Simulations by Athanassoula (1990) and Athanassoula (1994) have shown that bars can produce steady gas flows. Spiral features can also induce significant gas flows, as shown in the simulations of Kim & Kim

(2014).

On the other hand, galaxy interactions and mergers are external processes that can produce large-scale gas motions in a galaxy (Alexander & Hickox 2012). It has been shown that major galaxy interactions and mergers, those with a mass ratio $M_1/M_3 \approx 1$, can produce significant gas flows to the central regions of a galaxy (see for example Noguchi (1988), Barnes & Hernquist (1991), Barnes & Hernquist (1996)). A recent study by Montuori et al. (2010) shows that equal mass mergers and fly-by encounters can drive gas amounts up to $\sim 5 \times 10^9 M_\odot$ to a region within a radius of $\approx$ 2 kpc. These works favour the idea that mergers and interactions of roughly equal mass galaxies are important in delivering sufficient amounts of gas to trigger nuclear activity.

From a cosmological perspective, the current galaxy formation theory states that galaxies are formed by a hierarchical accretion process (e. g. White & Rees 1978). In this scenario, initial small-scale fluctuations of the dark matter distribution form the earliest haloes. Larger structures are formed as these haloes merge, leading to the formation of more massive haloes. In the gas that concentrates in the potential well of these haloes, star formation proceeds, and the first galaxies are formed. Eventually, these small galaxies follow the merging process to form larger systems. A more detailed discussion of current theories of galaxy formation is provided in Mo et al. (2010), Benson (2010), and references therein. The halo mass distribution or mass function is a fundamental concept in galaxy formation theory. This function describes the number of haloes of a given mass range per unit volume and characterises the halo population. Press & Schechter (1974) derived a an analytic form of the halo mass function from assuming an initial random Gaussian density perturbation. Cosmological simulations by Jenkins et al. (2001) show that the halo mass function follows the prediction of the Press-Shechter model.

The Press-Shechter model already predicts a significant abundance of dark matter haloes in the low-mass end of the distribution. Analytic calculations by Kauffman et al. (1993) predicted that the number of satellites around a typical galaxy should be larger than that obtained from observations. This is corroborated in cosmological N-body simulations by, for example, Klypin et al. (1999), Moore et al. (1999), and Guo et al. (2011). These works predict a significant fraction of satellites with a mass in the range $M < 10^{10} M_\odot$. Sawala et al. (2012) find, in simulations consistent with the ΛCDM, that satellites as small as $M \approx 5 \times 10^9 M_\odot$ are able to retain a gas fraction of a few percent at $z = 0$. For a galaxy-sized halo $M_h \sim 10^{12} M_\odot$, the predicted populations imply that satellites with a mass ratio in the range of ≈1:100 - 1:1000 are expected. On a timescale of 10^9 years, disc will have experience a large number of interactions leading to dynamical effects such as impulsive shocks and resonant heating Moore et al. (1999).

The dynamical effects of the accretion of small satellites has been studied in previous works (e. g. Velazquez & White (1999), Kazantzidis et al. (2008), and Kazantzidis et al. (2009)), but their effect on the gaseous component of a galaxy has been relatively unexplored. Some first works in this direction are those of Mihos & Hernquist (1994) and Hernquist & Mihos (1995), where the effect of a satellite with a mass ratio of 1:60 to that of the host is explored. In these works, the primary galaxy is assumed to have physical parameters similar to the Milky Way, and the disc resides in a cored pseudo-isothermal dark matter halo. However, the effect of satellites with mass ratios in the range of ≈1:100 in terms of induced gas flows has been unexplored.

The present work explores the effect of small satellites with mass ratios in the order of 1 : 100 in inducing gas flows to the central regions of a disc galaxy. The primary galaxy consists of a stellar disc, a bulge, and a gaseous disc residing in a dark matter halo following a Navarro-Frenk-White density profile, and the physical parameters correspond to a Milky Way type galaxy. Two model galaxies are considered: a non-barred and a barred galaxy. The first model is motivated by the fact that a barred galaxy in isolated evolution produces steady gas flows to its centre. It is then adequate to test a model where the effects of the satellite can be isolated. These results are compared with the effects on the barred galaxy. Two satellites with different masses, but in the range of mass ratios of 1:100 are chosen. These are placed on some inclined and coplanar orbits, considering both prograde and retrograde encounters. The aim of this study is to understand the dynamics of gas flows under the effect of such small satellites, and determine if these are relevant in producing observable morphological features and in the fuelling AGN activity in some galaxies.

In Chapter 2 fundamental concepts behind the simulations in this work are presented. Chapter 3 describes the code used, the methods for generating initial conditions, and tests of the stability of the galaxy models in isolated evolution. Then, Chapter 4 describes the results of the simulations in terms of the morphological features induced by the satellite, the gas mass distribution, and the induced flows. Chapter 5 presents the discussion and implications of this work. Conclusions and final remarks are presented in Chapter 6.

Chapter 2

Fundamental Concepts

In this chapter, the basic concepts of N-body systems and hydrodynamics applied to an astrophysical context as well as a description of the numerical methods relevant to the present work are introduced.

2.1. N-body Systems and Model Galaxies

A solution to the N-body problem describes the position as a function of time of N particles subject to their mutual attractions. The exact nature of the problem depends on the type of interaction between the particles. In a non-relativistic and gravitational astrophysical context, Newton's law of gravitation is assumed. In the case of $N = 2$, the problem has an exact solution given by conic sections, and it leads to Kepler's laws of planetary motion. For $N = 3$, some solutions can be obtained under certain approximations; see for example Heggie & Hut (2003), Mikkola (1989), and Mikkola & Hietarinta (1989). However, for a system with a large number of particles, as in modelling a galaxy, a numerical approach is necessary. In this section, basic concepts about N-body systems in the context of galaxy interactions are reviewed. The numerical schemes used for modelling the gravitational interaction in large N-body systems such as galaxies are emphasised.

2.1.1. The Gravitational N-body Problem

A galaxy is an example of a self-gravitating system that follows Newton's law of gravitation. Thus, the equation of motion for the i-th particle is given by:

$$\frac{\mathrm{d}^2\mathbf{r}_i}{\mathrm{d}t^2} = -\sum_{j\neq i}^{N} G m_j \frac{\mathbf{r}_i - \mathbf{r}_j}{|\mathbf{r}_i - \mathbf{r}_j|^3} \,, \tag{2.1}$$

which is typically expressed in the form:

$$\frac{\mathrm{d}\mathbf{r}_i}{\mathrm{d}t} = \mathbf{v}_i \,, \quad \frac{\mathrm{d}\mathbf{v}_i}{\mathrm{d}t} = \mathbf{a}_i(\mathbf{r}_i) \,, \tag{2.2}$$

where $\mathbf{r}_i$ is the velocity, and $\mathbf{a}_i$ is the acceleration of the i-th particle, which is given by the summation of the rest of the particles on the right-hand side of equation (2.1). Due to the non-linear dependence of this equation on particle separation, an analytical solution to the particle positions for a system where $N > 2$ is not, in general, attainable (e. g. (Heggie & Hut 2003), (Aguilar 1991)). For this reason, a numerical approach is necessary in order to find a solution. The formulation in terms of $\mathbf{r}$ and $\mathbf{v}$ is the basis for developing a scheme, as in Hamiltonian dynamics. Although equation (2.1) provides a general description for a self-gravitating system in many contexts, it is not a practical approach for simulating systems in the scale of galaxies and groups of galaxies since the summation requires N^2 operations to calculate the force. The numerical methods and approximations for solving the gravitational N-body problem are reviewed in works such as Aarseth (2003), Heggie & Hut (2003), Barnes (1994).

2.1.2. The Collisionless Boltzmann Equation and Constructing Model Galaxies

The Relaxation Time and the Collsionless Limit

Due to the large number of stars in a galaxy, it is possible to assume that an individual star moves in an orbit given by the smoothed potential of the entire distribution. The effect of the individual interactions with other nearby stars gradually changes the orbit. The timescale of this effect depends on the number of particles and is measured by the *relaxation time*. For a galaxy, it is typically orders of magnitude longer than its age (see for example King (1989), Binney & Tremaine (2008)). A complete description of the dynamical state of a system of particles is given by its coordinates in phase-space $(\mathbf{q}, \mathbf{p})$, where $\mathbf{q}$ and $\mathbf{p}$ are the generalised coordinates and momentum, at a given instant. A sufficiently large self-gravitating system of can be described by its distribution function in phase-space $f(\mathbf{q}, \mathbf{p}; t)$. The behaviour of this function is given by the Boltzmann equation (e. g. Binney & Tremaine 2008).

Before introducing the Boltzmann equation, it is necessary to clarify the difference between collisional and collisionless N-body systems. For a self-gravitating system represented by a finite number of particles, the force on a given particle can be expressed in the following terms (e. g Aguilar (1991), Binney & Tremaine (2008)):

$$\mathbf{F}_i = \mathbf{F}_{\text{short range}} + \mathbf{F}_{\text{long range}} \,. \tag{2.3}$$

The first term corresponds to the force exerted by the nearby neighbours, and it is affected by the statistical fluctuations in the neighbourhood. The second term is given by the mass distribution of the system as a whole and is not affected by the local fluctuations of distant particles (Aguilar 1991). This difference is illustrated in Figure 2.1. The close-up shows the discrete particle representation of the system. The short-range term of the force on a given particle is determined by these neighbours. As the separation between the particle and other regions of the system increases, local fluctuations of the particle distribution in those regions become less apparent, and the long-range term of the force is then given by the overall density distribution.

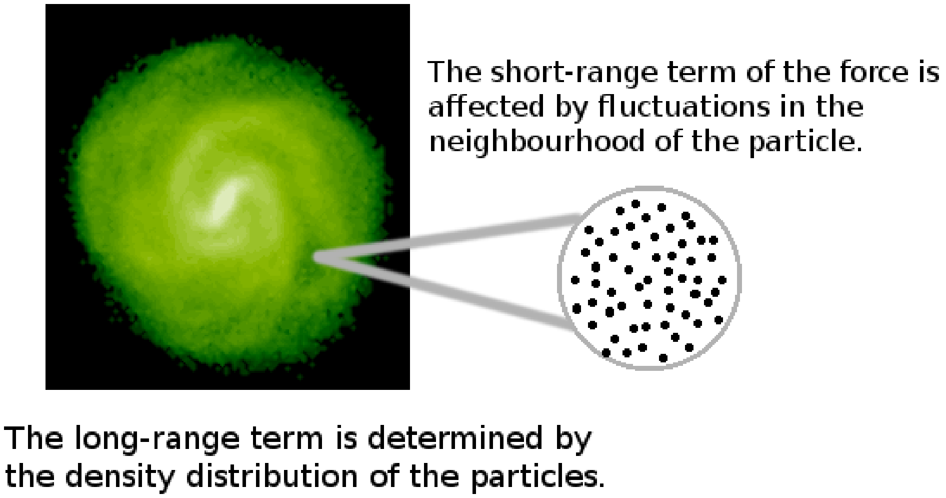

Figure 2.1: The force on a given particle is determined by a short-range term which is affected by statistical fluctuations in the neighbourhood of the particle, and by a long-range term which is determined by the overall density distribution of the system.

For example, the force on a particle at the centre of a spherical mass distribution is, by symmetry, zero. However, the discrete nature of the N-body representation introduces fluctuations that arise due to the coarseness of the gravitational potential. Thus, the force on a particle at the centre of an N-body representation of this distribution can be slightly different from zero, but momentum conservation is satisfied if the force is calculated with equation (2.1). If the mass distribution is divided in cubes in order to estimate the force of each cube on the central particle, then the number of particles in each cube needs to grow as

$N \propto r^2$ (r is the separation between the particle and the cube) to maintain the magnitude of the force exerted by each cube constant. If the average fluctuation of the number of particles follows a Poisson distribution, then (Aguilar 1991):

$$\frac{\Delta N}{N} = \frac{1}{\sqrt{N}} \propto \frac{1}{r} \tag{2.4}$$

This result shows that statistical fluctuations affect only the force exerted by nearby particles.

The first term in equation (2.3) is associated to collisions, which are understood as the interaction between two particles that produces a 90° deflection in their relative path. The importance of this effect can be understood in terms of the collisional timescale t_c, which is defined as the timescale for a strong interaction between two particles. It is possible to derive t_c from estimating the probability of collision between two particles. From Aguilar (1991), this is written as:

$$t_c = \frac{v^3}{4\pi G^2 m^2 n}\,, \tag{2.5}$$

in terms of local quantities, where v and m are the velocity and the mass of the particle, and n is the number density. In terms of global quantities such as the scale length R, the root mean square (RMS) speed v_{rms} and the number of particles N, it is (Aguilar 1991):

$$t_c \propto \left(\frac{R}{v_{rms}}\right) N\,, \tag{2.6}$$

this means that for small systems, or for those with a high characteristic velocity, collisional effects are significant. However, as the number of particles in the system increases, the collisional effects becomes less important. For a detailed derivation of equations (2.5) and (2.6), please refer to (Aguilar 1991).

The second term in equation (2.3) is associated to the crossing time t_{cross}. This is defined as the travel time for a particle to cross the characteristic scale of the system at the RMS speed v_{RMS}:

$$t_{\mathrm{cross}} = \frac{R}{v_{rms}}\,, \tag{2.7}$$

Thus, it can be seen that:

$$t_c \propto N t_{\mathrm{cross}}\,, \tag{2.8}$$

The crossing time is also known as the dynamical timescale, and in some contexts it is expressed as (e. g. Barnes 1994):

$$t_{\mathrm{cross}} \sim \sqrt{\frac{1}{G\rho_h}}\,, \tag{2.9}$$

According to Binney & Tremaine (2008), another derivation of a relation similar to equation (2.8) yields:

$$t_c \approx \frac{0.1N}{\ln N} t_{\mathrm{cross}} \,, \tag{2.10}$$

These results show that the importance of collisions decreases as the number of particles increases. Therefore, the distinction between a collisional and a non-collisional system is essentially established by the number of particles in the system. For a typical galaxy, where $N \sim 10^{11}$ or higher, the relaxation time is several orders of magnitude higher than the dynamical time. In this case, it is reasonable to use a collisionless description for this system.

The Collisionless Boltzmann Equation and Self-Consistent Systems

The phase space distribution $f(\mathbf{q}, \mathbf{p})$ is defined such that the number of particles δN in an element of volume of phase-space is:

$$\delta N = f(\mathbf{q}, \mathbf{p}) d^3\mathbf{q} d^3\mathbf{p} \,. \tag{2.11}$$

If this is multiplied by the mass of the particles, it becomes the amount of mass enclosed in the volume of phase-space. Consequently, the mass density can be obtained by integrating with respect to momentum:

$$\rho(\mathbf{r}) = \int m f(\mathbf{q}, \mathbf{p}) d^3\mathbf{p} \,. \tag{2.12}$$

The large number of stars and dark matter particles in a galaxy, and the large relaxation time with respect to the dynamical time, make the concept of a distribution function f very useful for modelling these systems.

In order to find an equation that describes the evolution of f, it is necessary to find the rate of change of the number of particles within an element of volume of phase-space. Ignoring collisions and assuming mass conservation, it can be shown that the distribution function satisfies the following (e .g Barnes 1996, Binney & Tremaine 2008):

$$\frac{\partial f}{\partial t} + \nabla_{\mathbf{X}} \cdot (f \dot{\mathbf{X}}) = 0 \,, \tag{2.13}$$

where $\mathbf{X} = (\mathbf{q}, \mathbf{p})$ is the state vector. This is a form of the *Collisionless Boltzmann Equation* (CBE). When collisions are not neglected, the right hand side should be equal to a source minus a sink function, as particles can be created or destroyed by some process (for example, stars are born and die in a galaxy). Expanding the divergence in equation (2.13), and using the Lagrangian derivative (see equation (2.41) in §2.2.1), it can be shown that:

$$\frac{Df}{Dt} + f(\nabla_{\mathbf{X}} \cdot \dot{\mathbf{X}}) = 0 \,, \tag{2.14}$$

If the system is Hamiltonian, the particle paths are given by Hamilton's equations:

$$\dot{\mathbf{p}} = -\frac{\partial H}{\partial \mathbf{q}}, \quad \dot{\mathbf{q}} = \frac{\partial H}{\partial \mathbf{p}}\,, \tag{2.15}$$

and the second term in equation (2.14) can be written as:

$$\nabla_{\mathbf{X}} \cdot \dot{\mathbf{X}} = \nabla_{\mathbf{q}} \cdot \dot{\mathbf{q}} + \nabla_{\mathbf{p}} \cdot \dot{\mathbf{p}} = \frac{\partial}{\partial \mathbf{q}}\frac{\partial H}{\partial \mathbf{p}} - \frac{\partial}{\partial \mathbf{p}}\frac{\partial H}{\partial \mathbf{q}} = 0\,. \tag{2.16}$$

This result implies that $Df/Dt = 0$, which means that the distribution function is constant in a volume moving with a given particle, or equivalently, the particle number is conserved in a phase-space volume.

Since $\dot{\mathbf{X}} = (\dot{\mathbf{q}}, \dot{\mathbf{p}}) = (\dot{\mathbf{q}}, -\nabla_{\mathbf{q}}\Phi)$, where Φ is the gravitational potential, equation (2.14) can be rewritten as:

$$\frac{Df}{Dt} = \frac{\partial f}{\partial t} + \dot{\mathbf{q}} \cdot \left(\frac{\partial f}{\partial \mathbf{q}}\right) - \left(\frac{\partial \Phi}{\partial \mathbf{q}}\right) \cdot \left(\frac{\partial f}{\partial \mathbf{p}}\right) = 0\,. \tag{2.17}$$

In a Cartesian coordinate frame, more commonly used in N-body simulations, the CBE is typically written as (e. g. Binney & Tremaine 2008):

$$\frac{\partial f}{\partial t} + \mathbf{v} \cdot \left(\frac{\partial f}{\partial \mathbf{r}}\right) - \left(\frac{\partial \Phi}{\partial \mathbf{r}}\right) \cdot \left(\frac{\partial f}{\partial \mathbf{v}}\right) = 0\,. \tag{2.18}$$

This equation is coupled to the Poisson equation for the gravitational potential:

$$\nabla^2 \Phi = 4\pi G(\rho + \rho_{\mathrm{ext}})\,, \tag{2.19}$$

where ρ corresponds to the mass density of the system, and it depends on the distribution function f through equation (2.12). The term ρ_{ext} corresponds to the contribution of any external influence on the system not described by the system's distribution function. This decomposition of the density is the conceptual basis for simulations that, for example, use N-body constructions within fixed dark matter haloes. In the context of N-body models of galaxies, the distribution function is the contribution of those of the halo, the disc, the bulge, and other components: $f = f_h + f_d + f_b$. The system is said to be self-gravitating if the dynamics of all the particles sampling the different components of a galaxy is affected by their mutual attraction. The system is said to be *self-consistent* if the density function and the potential satisfy the Poisson and Boltzmann equations simultaneously.

The CBE is a linear first-order partial differential equation of the form (King 1989):

$$\sum_{i=1}^{n} C_i \frac{\partial f}{\partial x_i} = 0\,, \tag{2.20}$$

where C_i are functions of x_i, where, $i = 1, ..., n$. The general solution for this equation is obtained from a set of subsidiary equations:

$$\frac{dx_1}{C_1} = \frac{dx_2}{C_2} = ... = \frac{dx_n}{C_n}\,, \tag{2.21}$$

which give $n-1$ independent ordinary differential equations. The solution can be expressed in terms of $n-1$ independent integrals expressed as:

$$I_i(x_1, x_2, ..., x_n) = K_i, \quad i = 1, 2, ..., n-1\,, \tag{2.22}$$

where K_i is a constant. The general solution of equation (2.20) can then be expressed as:

$$f(x_1, x_2, ..., x_n) = F(I_1, I_2, ..., I_{n-1})\,, \tag{2.23}$$

where F is an arbitrary function of its arguments. This form of the solution states that the solution is restricted to a function of $n-1$ variables which are the integrals I_n (King 1989).

The CBE in a Cartesian coordinate system is written as:

$$\frac{\partial f}{\partial t} + v_x \frac{\partial f}{\partial x} + v_y \frac{\partial f}{\partial y} + v_z \frac{\partial f}{\partial z} - \frac{\partial \Phi}{\partial x}\frac{\partial f}{\partial v_x} - \frac{\partial \Phi}{\partial y}\frac{\partial f}{\partial v_y} - \frac{\partial \Phi}{\partial z}\frac{\partial f}{\partial v_z} = 0\,. \tag{2.24}$$

By applying the formalism described above, the following subsidiary equations are obtained:

$$\frac{dt}{1} = \frac{dx}{v_x} = \frac{dy}{v_y} = \frac{dy}{v_y} = \frac{dv_x}{-\Phi_x} = \frac{dv_y}{-\Phi_y} = \frac{dv_z}{-\Phi_z}\,, \tag{2.25}$$

where

$$\Phi_x = \frac{\partial \Phi}{\partial x}, \quad \Phi_y = \frac{\partial \Phi}{\partial y}, \quad \Phi_z = \frac{\partial \Phi}{\partial z}\,. \tag{2.26}$$

Then, from equation (2.25), the following equations are derived:

$$\frac{\mathrm{d}x}{\mathrm{d}t} = v_x, \quad \frac{\mathrm{d}y}{\mathrm{d}t} = v_y, \quad \frac{\mathrm{d}z}{\mathrm{d}t} = v_z\,,$$

$$\frac{\mathrm{d}v_x}{\mathrm{d}t} = -\frac{\partial \Phi}{\partial x}, \quad \frac{\mathrm{d}v_y}{\mathrm{d}t} = -\frac{\partial \Phi}{\partial y}, \quad \frac{\mathrm{d}v_z}{\mathrm{d}t} = -\frac{\partial \Phi}{\partial z}\,, \tag{2.27}$$

which are the equations of motion of a star in the potential of the galaxy.

Given the form of the solution to this type of partial differential equation, the distribution function that satisfies the CBE can be expressed in terms of the integrals of motion of the particle in the potential of the system. An integral of motion is a quantity $I(\mathbf{x}(t), \mathbf{v}(t))$, which is a function of phase-space coordinates, that is a constant as a function of time:

$$\frac{\mathrm{d}}{\mathrm{d}t} I(\mathbf{x}(t), \mathbf{v}(t)) = 0\,. \tag{2.28}$$

These integrals also restrict its path through phase-space, and are defined for the motion of an individual test particle in the potential of the system. These are not integrals of the whole system such as the total energy or momentum of the system (King 1989).

The CBE, as written in equation (2.24), corresponds to a general time-dependent situation. The result expressed in (2.27) shows that a solution of the CBE is obtained by following the paths of the particles of the system. Thus, for an arbitrary self-gravitating system with a time-dependent distribution function $f(\mathbf{x}, \mathbf{v}, t)$, the evolution of f can be followed by sampling the distribution at $t = 0$, and integrating the equations of motion of the particles as long as collisional effects can be neglected. The distribution can be calculated from the positions of the particles after a given integration interval.

Equilibrium Solutions of the Collisionless Boltzmann Equation

An important application of the CBE in the modelling of galaxies is in obtaining a distribution function that adequately represents a model galaxy in equilibrium. If a system has lived long enough to reach an equilibrium condition, and if the relaxation time is much longer than the dynamical time, then a steady-state ($\partial f/\partial t = 0$) approximation can be used (e. g King 1989, Binney & Tremaine 2008). In this case, the CBE becomes:

$$v_x \frac{\partial f}{\partial x} + v_y \frac{\partial f}{\partial y} + v_z \frac{\partial f}{\partial z} - \frac{\partial \Phi}{\partial x}\frac{\partial f}{\partial v_x} - \frac{\partial \Phi}{\partial y}\frac{\partial f}{\partial v_y} - \frac{\partial \Phi}{\partial z}\frac{\partial f}{\partial v_z} = 0\,, \tag{2.29}$$

and the subsidiary equations are:

$$\frac{dx}{v_x} = \frac{dy}{v_y} = \frac{dy}{v_y} = \frac{dv_x}{-\Phi_x} = \frac{dv_y}{-\Phi_y} = \frac{dv_z}{-\Phi_z}\,, \tag{2.30}$$

The distribution function is the unknown variable in this equation.

The concept of an integral of motion is particularly useful in seeking a steady-state distribution function that satisfies CBE. The derivative in equation (2.28) can be written as:

$$\frac{\partial I}{\partial t} = \frac{\partial I}{\partial \mathbf{x}} \cdot \frac{\mathrm{d}\mathbf{x}}{\mathrm{d}t} + \frac{\partial I}{\partial \mathbf{v}} \cdot \frac{\mathrm{d}\mathbf{v}}{\mathrm{d}t} = 0\,, \tag{2.31}$$

which becomes

$$\mathbf{v} \cdot \frac{\partial I}{\partial \mathbf{x}} - \frac{\partial \Phi}{\partial \mathbf{x}} \cdot \frac{\partial I}{\partial \mathbf{v}} = 0\,. \tag{2.32}$$

This result states that the condition for I to be an integral of motion is the same as that for I to be a steady-state solution of the collisionless Boltzmann equation (e. g. Binney & Tremaine 2008), which leads to the *Jeans Theorem*:

Any steady-state solution of the collisionless Boltzmann equation depends on the phase-space coordinates only through integrals of motion in the given potential, and any function of the integrals yields a steady-state solution of the collisionless Boltzmann equation.

This means that distribution functions depending on the integrals of motion of the potential can be used to find steady-state solutions to the CBE. This introduces a powerful tool for seeking distribution functions useful for building equilibrium N-body models. The gravitational potential is a conservative potential, therefore the orbital energy E of the particle is one of the integrals of motion:

$$I_1 = \frac{1}{2}(v_x^2 + v_y^2 + v_z^2) + \Phi(x, y, z) = E\,. \tag{2.33}$$

Additionally, depending on the properties of the potential, other integrals of motion appear. One example is the magnitude total angular momentum L, which is an integral of motion when the potential has spherical symmetry. The vertical component of angular momentum L_z is also an integral of motion if the potential has rotational symmetry around an axis as in the case of an axisymmetric disc.

The large relaxation time of a galaxy implies that the distribution function can be well approximated by a steady-state solution. The methods and approximations for obtaining equilibrium distribution functions for collisionless systems have been widely reviewed in the literature (see for example Binney & Tremaine 2008).

Summary of Methods for Modelling Galaxies

The problem is to obtain a distribution function that can properly represent the observed density and velocity distributions of a realistic galaxy. As mentioned previously, the distribution function must satisfy simultaneously the CBE and the Poisson equation. The fact that galaxies are systems composed of a dark matter halo, a disc, and a central bulge adds a complication to the problem because a self-consistent solution needs to be obtained considering the potential of the system as a whole. The construction of realistic equilibrium models is a difficult problem requiring a certain degree of approximation. Some methods are briefly reviewed in the following paragraphs.

As equilibrium distribution functions for spherical systems can be derived using methods based on the Jeans Theorem, it is possible to first construct an N-body representation of a spherical bulge and halo from equilibrium models. Consequently, these are allowed to evolve or relax in the potential of a disc, which is introduced adiabatically (e. g. Barnes & White 1984). However, a disadvantage of such models is that the disc dynamics cannot be followed adequately.

Hernquist (1993) introduced an approach to initialise multi-component disc galaxies based on the moments of the CBE. The mass density profiles of the disc and bulge are assumed from the observed profiles, and the dark matter halo is initialised as a truncated pseudo-isothermal sphere. The properties of the velocity dispersions are obtained from the moments of the CBE, and the particle velocities are sampled from a local Gaussian distribution. In these methods, the distribution function is not completely specified, but parameters such as the velocity dispersion and its anisotropy are well constrained (e.g Barnes 1996, Binney & Tremaine 2008). However, Kazantzidis et al. (2004) showed that spherical systems initialised using this scheme present non-equilibrium effects that introduce deviations from identical spherical models initialised using the Eddington inversion method (see Binney & Tremaine 2008). In spite of these effects, schemes using the moments of the CBE have also been implemented in the works of Springel & White (1999) and Springel (2000).

An alternate approach was introduced by Kuijken & Dubinski (1995), and Widrow & Dubinski (2005), in which self-consistent models are generated. In Kuijken & Dubinski (1995), the model galaxy consists of a spherical halo with a distribution function of a lowered Evans model that depends on E and L_z (the vertical component of angular momentum). The disc has a distribution function based on the planar models of Shu (1969) which depends on E, L_z, and $E_z = \frac{1}{2}v_z^2 + \Phi(R,z) - \Phi(R,0)$. A spherical bulge is included using a King (1966) profile, with a distribution function depending only on E. The three distributions are function of the potential of the combined system, and are used in the Poisson equation to obtain the potential self-consistently. However, a disadvantage of these models is that it is difficult to control parameters such as the concentration of the halo. A certain amount of trial and error attempts are necessary to obtain a suitable model [1].

Widrow & Dubinski (2005) follow a similar approach using a dark matter halo with a

---

[1] The author is grateful to H. Velázquez for illustrating discussions on methods for generating initial conditions.

Navarro-Frenk-White (Navarro et al. 1996) density profile, a bulge with a Hernquist (1990), and a disc with an exponential surface density profile. This method also allows to include the effect of a central supermassive black hole. Nevertheless, tests by Widrow & Dubinski (2005) show that the profiles of the final halo and bulge may be different from those expected from isolated evolution.

Alternate schemes such as orbit-based methods have been developed and used in the literature (e. g. Schwarzchild 1979, Schwarzchild 1993). In this methods, the density distribution of a large group of orbits in a fixed potential is first calculated. Then, the weight of each orbit is computed in order to produce a target final profile. Syer & Tremaine (1996) develop an algorithm for constructing an equilibrium stellar system using an orbit-based scheme. The system is constructed by integrating the N-body system, and the masses of the particles are slowly adjusted until the time-averaged density field as well as other properties converge to a desired value.

McMillan & Dehnen (2007) introduce a scheme to generate disc galaxies with a spherical halo and bulge. First, the spherical components are initialised following an Eddington inversion method in the presence of the monopole term of the desired disc potential. Then, the non-monopole terms are adiabatically introduced to allow for the relaxation of the spherical components in the disc's potential. Finally, the disc of particles is introduced. This method is used in the present work to initialise the model galaxies, and it is described in more detail in section §3.2.

2.1.3. Numerical approximations to the Gravitational N-body Problem

In an N-body simulation representing a system such as a galaxy, the particles in the simulation represent discrete samples of a continuous phase-space distribution function. The function $f(\mathbf{r}, \mathbf{v})$ can then be replaced with a series of δ functions (Barnes 1996):

$$f(\mathbf{r}, \mathbf{v}) = \sum_{i}^{N} m_i \delta(\mathbf{r} - \mathbf{r}_i)\delta(\mathbf{v} - \mathbf{v}_i) \,. \tag{2.34}$$

For this approximation to be acceptable, the integral of the distribution function over a given volume must correspond to the average of equation (2.34) over the same volume for several similar N-body representations. Any observable a of the system can be calculated by:

$$a = \int A(\mathbf{r}, \mathbf{v}) f(\mathbf{r}, \mathbf{v}) d^3\mathbf{r} d^3\mathbf{v} \,, \tag{2.35}$$

where $A(\mathbf{r},\mathbf{v})$ is a function of phase-space coordinates associated to the observable. Using equation (2.34), this becomes:

$$a \approx \sum_{i}^{N} m_i A(\mathbf{r}_i,\mathbf{v}_i)\,, \tag{2.36}$$

This equation can be interpreted as a Monte Carlo approximation of the observable. The fractional error in the calculation of a scales as $N^{-1/2}$. The entire sampling of the distribution function is also interpreted as a Monte Carlo sampling (see for example (Barnes 1994) and (Barnes 1996)).

To start an N-body simulation, the initial conditions are determined from sampling a valid distribution function at a given instant. Then, the dynamical evolution of the system is followed by integrating the system of equations given in equation (2.1). However, the $1/r^2$ dependence of the force produces strong accelerations when the particle separation tends to zero. From a computational point of view, this can increase the numerical error in the integration of the equations of motion for particles with small separations. To overcome this problem, the gravitational force is said to be "softened" such that when $r \to 0$, the force tends to a finite value. Thus, equation (2.1) is commonly expressed as:

$$\frac{\mathrm{d}^2\mathbf{r}_i}{\mathrm{d}t^2} = -\sum_{j\neq i}^{N} G m_j \frac{\mathbf{r}_i-\mathbf{r}_j}{(|\mathbf{r}_i-\mathbf{r}_j|^2+\epsilon^2)^{3/2}}\ ,, \tag{2.37}$$

where ϵ is the softening length. This form is known as a Plummer softening because the potential from which this force is derived corresponds to the Plummer potential. With this softening, the discrete particles are said to represent spheres with a density profile corresponding to the Plummer density profile. It is typically used in many N-body codes (see for example Aarseth (1963), Aarseth (2003), and Barnes & Hernquist (1992)). The parameter ϵ also introduces a limit in the spatial resolution of the simulation. In practice, any variation in the system with a scale length smaller than a few times ϵ cannot be properly represented. There is no particular method for defining the softening length, and its choice depends on the nature and scale of the system modelled. For example, a simulation of cosmological scales may have $\epsilon\ \sim$kpc. However, to resolve the dynamics of a disc galaxy ϵ should be several factors lower than the vertical scale length, which is ≈ 0.3 kpc for the Milky Way.

An important step in an N-body integration is the calculation of the forces, which can be costly in computational terms. Equation (2.37) is a direct summation method where the number of operations grows as N^2, thus making it impractical a large number of particles. However, it is appropriate for simulating small stellar systems where collisional effects are important. Other methods estimate the mass density in a mesh, and use Fourier methods to obtain the corresponding potential from the Poisson's equation. Then the force on each of the particles is obtained from $\mathbf{F} = -\nabla\Phi$ (Aguilar 1991, Binney & Tremaine 2008). Another approach is to expand the force in terms of harmonic functions or power series, which can be advantageous in particular configurations where some symmetry is preserved. A brief introduction to these methods can be reviewed in Aguilar (1991) or in Binney & Tremaine (2008), and a more thorough discussion is presented in Aarseth (2003). As it pertains for this work, the rest of the discussion will focus on the hierarchical tree code method.

Hierarchical methods work by grouping particles in a hierarchical tree structure. Because the high-order terms of the multipole expansion of the gravitational field decay rapidly, the long-range gravitational potential of a region can be approximated by a function $\propto 1/r$ (Barnes 1996). Therefore, the direct summation of equation (2.37) can be replaced by a sum over the subdivided regions where the number of operations scales as $\log N$. A version of this tree code was introduced by Barnes & Hut (1986), and it has been widely implemented in different codes; see for example Hernquist (1987), Hernquist & Katz (1985), Makino (1990), Carraro et al. (1998), Springel et al. (2001), Springel (2005), Merlin et al. (2010), Merlin et al. (2012).

The tree algorithm creates a root cell around the system of particles, which is recursively subdivided until each particle has been isolated in a cell, as shown in Figure 2.2. The next step is to calculate the gravitational force starting with the root cell and examining the cells it contains. In the Barnes & Hut (1986) algorithm, the potential is approximated with a single $1/r$ term if $d > l/\theta$, where d is the separation between the body and the cell's centre of mass, l is the length of the cell, and θ is called the opening angle. Tests show that values of θ in the range of 0.5 to 0.7 can produce relative force errors in the order of 10^{-3} (Barnes & Hut 1989, Hernquist 1987). In some circumstances, the opening criterion can fail when the offset between the cell's centre of mass and geometrical centre is significant. In that case, the criterion becomes $d > l/\theta + \delta$, where δ is the mentioned offset.

Once the force has been calculated, the next step is to advance the particles to updated positions and velocities. A simple scheme would be to use the leap-frog method as it is accurate to second order and time-reversible if the time step is constant for all the particles. This is a symplectic algorithm as it preserves the phase-space structure of the system (Binney & Tremaine 2008, Donnelly & Rogers 2005). A common version of the method is the

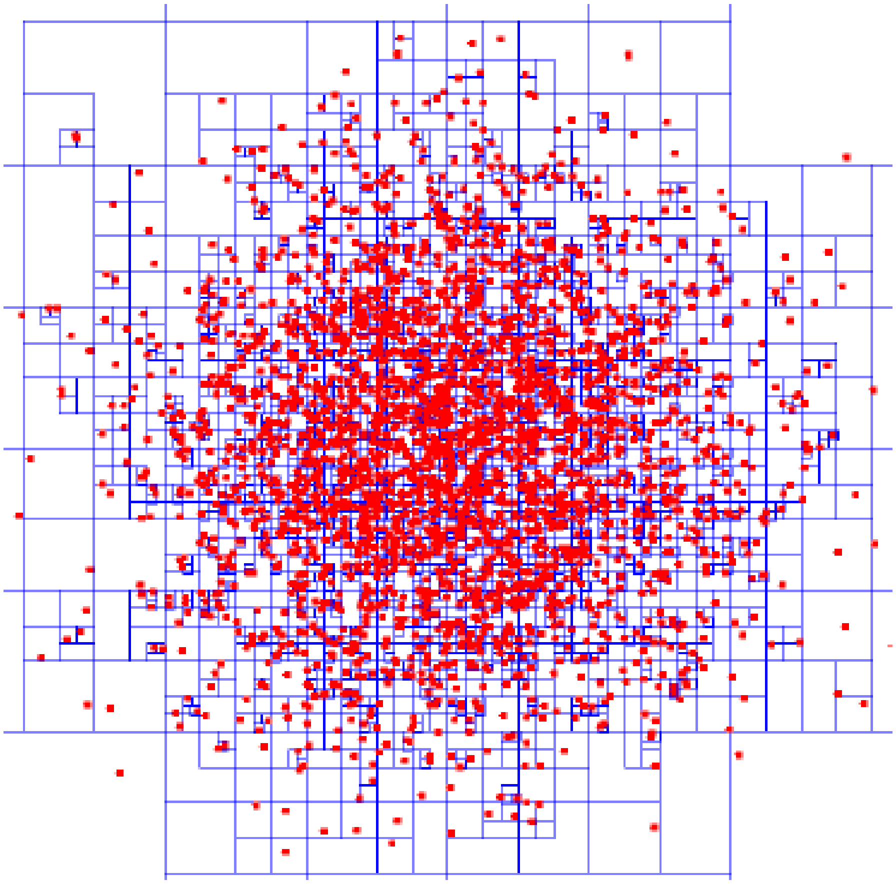

Figure 2.2: This diagram shows an example of cell division scheme in the Barnes and Hut Tree algorithm. Image Credit: H. Chan-Maestas. (`http://www.cs.rit.edu/~jrm3215/pc1/report.pdf`)

mapping:

$$\begin{aligned} \mathbf{v}_i^{[k+1/2]} &= \mathbf{v}_i^{[k]} + \frac{\Delta t}{2}\mathbf{a}_i^{[k]} \\ \mathbf{r}_i^{[k+1]} &= \mathbf{r}_i^{[k]} + \Delta t \mathbf{v}_i^{[k+1/2]} \\ \mathbf{v}_i^{[k+1]} &= \mathbf{v}_i^{[k+1/2]} + \frac{\Delta t}{2}\mathbf{a}_i^{[k+1]}, \end{aligned} \tag{2.38}$$

which is a Kick-Drift-Kick sequence because the particle is first advanced in velocity (kick), then in position (drift), and again in velocity (kick). Although higher order schemes can be derived, these require more steps, and more memory since the information from previous time steps needs to be saved (Kinoshita et al. 1990, Yoshida 1990). Due to its simplicity and symplectic nature, the leapfrog is very convenient for large N-body simulations (e. g. Binney & Tremaine 2008).

Typical collisionless simulations of galaxies have a large dynamical range of densities.

Regions of higher density have a lower dynamical time scale ($\tau_{dyn} \propto 1/\sqrt{G\rho}$) and require a smaller time step. Additionally, for a disc system, the time step should be a fraction of the smallest orbital period, or for a spherical system, it should be a fraction of the crossing time. For these reasons, some regions require a smaller time step than others in order to resolve the dynamics within a given accuracy. It is computationally inefficient to fix the time step to the smallest necessary for a given system as it significantly increases the computational time. For this reason, an algorithm using individual time steps for each particle is adequate in order to save computational time. A synchronisation scheme can be established and the particles that require smaller time steps are treated until they reach the common step. This saves computational time as the force calculations are repeated only for a reduced number of particles. A disadvantage is that the reversibility of the leap frog is lost (e. g. Barnes 1996). Several works have explored different individual time step schemes that preserve this property (e. g. Saha & Tremaine 1994, Hut et al. 1995, Quinn et al. 1997).

There are some errors and limitations that need to be taken into account when running and interpreting N-body simulations. In an N-body code, numerical errors are introduced by mathematical approximations, force-calculation algorithms, truncation introduced by finite time-steps, and round-off errors due to a finite computer word-length. The error in the integration of the equations of motion is estimated by monitoring laws such as the conservation of energy and momentum. Reducing the global time step of the simulation decreases errors in the conservation of energy. The errors in force calculations can be measured by running the same initial conditions with different parameters of the force-calculation algorithm. The maximum time step can be estimated from the dynamical time, or the local dynamical time of the region with the highest density. A fraction of this timescale is typically used as the maximum time step.

The discrete representation of the system with a finite number of bodies introduces noise in the calculation of the potential. These fluctuations may reach scales larger than the softening length, and produce deflections in the particles' orbits that would not be seen in a truly collisionless system (e. g. Barnes 1994). This affects the reliability of N-body simulations to study, for example, the detailed structure of orbit families in a galactic potential. Two-body relaxation introduces long-term effects and fluctuations, but are negligible as long as the relaxation time (equations (2.6) and (2.8)) is orders of magnitude higher than the crossing time. Relaxation effects can be reduced by increasing the number of particles in the system. Tests have shown that these fluctuations scale as $N^{-1/2}$ (Barnes 1996). Other fluctuations may be introduced by amplification mechanisms in discs, but these can be controlled by increasing the number of particles in the simulation (Barnes 1996). Depending on the force-calculation algorithm, it is also necessary to monitor the drift of the centre of mass of the system, specially if momentum is not strictly conserved by the algorithm. Barnes (1994) suggests that the fractional error in energy and force calculations should be at most $\sim N^{-1/2}$.

As in any numerical approximation, errors are introduced. However, collisionless N-body simulations can be trusted if, aside from not presenting an upper limit in conserving total mechanical energy, any feature is repeatedly observed in simulations of statistically equivalent samplings of the same initial conditions (Barnes 1994). Ideally, an ensemble of simulations, initialised with different seeds of a random number generator, of the same initial conditions should be run using the same parameters in order to obtain average results that can be interpreted from a statistical point of view (Aguilar 1991). However, this will depend on the computational power and time available for a given project. Also, an adequate choice of simulation parameters will depend on the nature of the system to be studied, the characteristic scales involved, and whether a gaseous component is present or not. A good computational astrophysics practice dictates that some tests, of energy conservation and force errors, are necessary before using a set of simulation parameters for a given algorithm.

2.2. Fundamentals of Gas Dynamics

In this section the basic equations of hydrodynamics are explained, followed by a brief review of how these equations are represented in the Smoothed Particle Hydrodynamics formulation (SPH). The SPH method is introduced because it is implemented in the code used in the present work.

2.2.1. Equations of hydrodynamics

One of the basic problems of hydrodynamics is to find a description of how the properties and motion of an element of fluid evolves in time. The basic equations of hydrodynamics emerge from applying principles such as mass continuity, Newton's second law of motion, and the laws of thermodynamics to an element of fluid. There are several mathematical approaches to derive the equations of hydrodynamics. In this case, the derivation described in Clarke & Carswell (2007) is followed as it takes a more conceptual approach.

Prior to discussing the equations of hydrodynamics, it is necessary to understand that there are two possible descriptions of fluid dynamics: the *Lagrangian* and the *Eulerian* description. The Lagrangian description follows the motion of individuals elements of fluid. Therefore, the properties of each element of fluid are followed as the element moves. In the Eulerian description, fluid properties are followed at a given position in a fixed frame, and different fluid elements can pass through that point. This approach finds solutions of how the fluid properties behave in that particular point.

It is possible to find a connection between the Lagrangian and Eulerian descriptions. A given quantity f of a fluid element can be defined as a function of position $\mathbf{r}$ and time t. The Lagrangian derivative is defined as:

$$\frac{Df}{Dt} = \lim_{\delta t \to 0} \frac{\delta f}{\delta t} = \lim_{\delta t \to 0} \left(\frac{f(\mathbf{r} + \delta \mathbf{r}, t + \delta t) - f(\mathbf{r}, t)}{\delta t} \right) . \tag{2.39}$$

The idea behind this equation is to follow how f changes for a displacement $\delta \mathbf{r}$ in an interval δt for a frame moving with the fluid. By expressing the numerator as a Taylor series and neglecting higher order terms, it can be expressed as:

$$\delta f = \frac{\partial f(\mathbf{r}, t)}{\partial t} \delta t + \delta \mathbf{r} \cdot \nabla f(\mathbf{r}, t) . \tag{2.40}$$

By substituting this in equation (2.39) and evaluating the limit, and with $\mathbf{v} = \lim_{\delta t \to 0} \frac{\delta \mathbf{r}}{\delta t}$, the Lagrangian derivative is finally expressed as:

$$\frac{Df}{Dt} = \frac{\partial f}{\partial t} + \mathbf{v} \cdot \nabla f . \tag{2.41}$$

This equation summarises the difference between the Lagrangian and Eulerian frames. In the left hand side, the rate of change is measured following the element of fluid. In the right hand side, the second term is known as the advection term. This term describes how the properties of the fluid at a given point change due to the motion of the individual fluid elements. The choice of the description will depend on the nature of the problem. In the context of N-body simulations, the Lagrangian description fits adequately as the gas can be modelled as a system of self-gravitating particles interacting with other components of the system. Each particle, carries information of the properties of the fluid. This will be reviewed in detail in §2.3. In the remainder of this section, the basic equations of hydrodynamics are described. For completeness, both the Lagrangian and Eulerian forms of the equations are presented.

Continuity Equation

First, the *continuity equation* is introduced. For a fluid volume of mass m, the rate of change of mass in this volume depends on the mass flow through its surface. In mathematical terms,

$$\frac{dm}{dt} = - \oint_S \rho \mathbf{v} \cdot d\mathbf{A} , \tag{2.42}$$

where ρ is the density, $\mathbf{v}$ is the velocity, $d\mathbf{A}$ is the differential element of area vector. Since,

$$m = \int_{\mathrm{V}} \rho dV \,, \tag{2.43}$$

the differential form of this equation is obtained by substituting this in the left side of equation (2.42), and using the divergence theorem on the right side:

$$\frac{\partial \rho}{\partial t} + \nabla \cdot (\rho \mathbf{v}) = 0 \,. \tag{2.44}$$

This is the Eulerian form of the continuity equation. Transformation to the Lagrangian form is achieved by substituting the identity $\nabla \cdot (\rho \mathbf{v}) = \rho \nabla \cdot \mathbf{v} + \mathbf{v} \cdot \nabla \rho$, and rearranging terms in order to substitute the Lagrangian derivative $D\rho/Dt = \partial \rho/\partial t + \mathbf{v} \cdot \nabla \rho$. After rearranging the terms, the resulting equation is:

$$\frac{D\rho}{Dt} + \rho(\nabla \cdot \mathbf{v}) = 0 \,. \tag{2.45}$$

Momentum Equation

The second equation is the *momentum equation* which states Newton's second law of motion for a fluid element. Following the formalism of Clarke & Carswell (2007),this can be written as:

$$\left(\frac{D}{Dt} \int_{\mathrm{V}} \rho \mathbf{v} dV \right) \cdot \mathbf{n} = - \int_{\mathrm{S}} P\mathbf{n} \cdot d\mathbf{A} + \int_{\mathrm{V}} \rho \mathbf{g} \cdot \mathbf{n} dV \,, \tag{2.46}$$

where P is the pressure, $\mathbf{g}$ is the external force, dV is the differential volume, and $\mathbf{n}$ is a unitary vector in an arbitrary direction. The left hand side corresponds to the rate of change of the momentum of the element of fluid. In the right hand side, the first term corresponds to pressure forces and the second to external forces ($\mathbf{g}$), also known as, body forces. Since the pressure term is a surface integral, using the divergence theorem, it can be rewritten as:

$$\int_{\mathrm{S}} P\mathbf{n} \cdot dA = \int_{\mathrm{V}} \nabla \cdot (P\mathbf{n}) dV \,. \tag{2.47}$$

Using the identity $\nabla \cdot (P\mathbf{n}) = \mathbf{n} \cdot \nabla P + P \nabla \cdot \mathbf{n} = \mathbf{n} \cdot \nabla P$, it becomes:

$$\int_{\mathrm{V}} \nabla \cdot (P\mathbf{n}) dV = \int_{\mathrm{V}} \nabla P \cdot \mathbf{n} dV \,. \tag{2.48}$$

With the substitution of this term in equation (2.46), and reducing the integration volume to a small element of fluid of volume δV, the momentum equation can be written as:

$$\frac{D(\rho \mathbf{v} \delta V)}{Dt} \cdot \mathbf{n} = (-\nabla P + \rho \mathbf{g}) \cdot \mathbf{n} \delta V \, . \tag{2.49}$$

The left hand side can be expanded as:

$$\frac{D(\rho \mathbf{v} \delta V)}{Dt} \cdot \mathbf{n} = \left(\frac{D(\rho \delta V)}{Dt} \mathbf{v} + \rho \delta V \frac{D\mathbf{v}}{Dt} \right) \cdot \mathbf{n} \, , \tag{2.50}$$

where the first term is zero because of the conservation of mass. Substitution of the second term of equation (2.50) in equation (2.49) and further simplification of terms leads to the momentum equation in Lagrangian form:

$$\rho \frac{D\mathbf{v}}{Dt} = -\nabla P + \rho \mathbf{g} \, . \tag{2.51}$$

This form of the equation leads to a very natural interpretation of the motion of an element of fluid resulting from the effect of pressure gradients and external body forces. Using the Lagrangian derivative applied to the velocity $\mathbf{v}$, the equation is transformed to the Eulerian form:

$$\rho \left(\frac{\partial \mathbf{v}}{\partial t} + \mathbf{v} \cdot \nabla \mathbf{v} \right) = -\nabla P + \rho \mathbf{g} \, . \tag{2.52}$$

Energy Equation

The third equation is the *energy equation* which is a statement of the conservation of the total energy of a fluid element. As described in Clarke & Carswell (2007), a starting point is to define the total energy per unit volume:

$$E = \rho \left(\frac{1}{2} |\mathbf{v}|^2 + \Phi + u \right) = \rho e \, , \tag{2.53}$$

where Φ is the gravitational potential, u is the specific internal energy of the gas, and e is the specific energy of the fluid. The first derivative with respect to time of this equation yields:

$$\frac{DE}{Dt} = \rho \frac{De}{Dt} + \frac{D\rho}{Dt} e \, . \tag{2.54}$$

The derivative in the first term is given by:

$$\frac{De}{Dt} = \mathbf{v} \cdot \frac{D\mathbf{v}}{Dt} + \frac{D\Phi}{Dt} + \frac{Du}{Dt} \, , \tag{2.55}$$

and because $e = E/\rho$, the second term is:

$$\frac{D\rho}{Dt}e = \frac{E}{\rho}\frac{D\rho}{Dt}\,. \tag{2.56}$$

The term Du/Dt in equation (2.55) is found from the first law of thermodynamics: $\delta u = \delta q - \delta w$, where u is the specific internal energy, q is the heat per unit mass, and w is the work per unit mass. It becomes:

$$\frac{Du}{Dt} = \dot{Q} - P\frac{D\mathrm{v}}{Dt}\,, \tag{2.57}$$

where $\dot{Q}$ is any heating or cooling mechanism that affects the element of fluid, and $\mathrm{v} = 1/\rho$ is the specific volume. The second term in this equation can be written in terms of the density as:

$$\frac{D(1/\rho)}{Dt} = -\frac{1}{\rho^2}\frac{D\rho}{Dt}\,, \tag{2.58}$$

thus,

$$\frac{Du}{Dt} = \dot{Q} + \frac{P}{\rho^2}\frac{D\rho}{Dt}\,. \tag{2.59}$$

The energy equation is obtained by substituting this and equation (2.55) in equation (2.54), which becomes:

$$\frac{DE}{Dt} = \frac{E}{\rho}\frac{D\rho}{Dt} + \rho\left(\mathbf{v}\cdot\frac{D\mathbf{v}}{Dt} + \frac{D\Phi}{Dt} + \dot{Q} + \frac{P}{\rho^2}\frac{D\rho}{Dt}\right)\,. \tag{2.60}$$

This is the energy equation in Lagrangian form. To convert to Eulerian form, the left hand side is substituted with the Lagrangian derivative. On the left hand side, it is convenient to substitute terms obtained from the continuity equation, the momentum equation, and the Lagrangian derivative of the potential (for a detailed derivation see Clarke & Carswell 2007). After substitution and rearrangement of terms, the energy equation becomes:

$$\frac{\partial E}{\partial t} + \nabla\cdot[(E+P)\mathbf{v}] = \rho(\dot{Q} + \frac{\partial\Phi}{\partial t})\,. \tag{2.61}$$

In order to close the system of hydrodynamic equations, it is necessary to define an equation of state for the gas: $P = P(\rho, T)$, depending on the physical properties of the gas.

2.3. The Smoothed Particle Hydrodynamics Method

In the previous section, the equations of hydrodynamics were discussed from a theoretical point of view. This section describes the fundamentals of a numerical method for obtaining an approximate solution to the equations of hydrodynamics. In an Eulerian description, mesh-based methods are adequate and commonly used. In the case of the Lagrangian description, a scheme that follows the evolution of individual fluid elements would be appropriate. Such a method could be easily coupled with N-body simulations. A numerical method with the aforementioned properties is Smoothed Particle Hydrodynamics (SPH), which is an approximation to a Lagrangian scheme. In this method, the particles sample the phase-space of the system, and the properties of an element of fluid at the position of a tracer particle are calculated in terms of the neighbouring particles that fall within a smoothing length. It was originally used in the study of stellar objects using polytropic models (Gingold & Monaghan 1977, Lucy 1977). It was further developed by Monaghan & Lattanzio (1985) for other astrophysical problems. Since then, it has been widely implemented in diverse astrophysical contexts, from modelling the formation of planets to cosmological simulations. In the following paragraphs, the hydrodynamic equations written in the SPH formulation are described.

2.3.1. SPH Interpolation

In the SPH method, all physical quantities f are interpolated at a point with the equation:

$$f(\mathbf{r}) = \int f(\mathbf{r}')W(\mathbf{r}-\mathbf{r}',h)dV' \,, \tag{2.62}$$

where the function W is called the interpolating kernel function, and the integration is carried with respect to $\mathbf{r}'$. The interpolating kernel must satisfy the property:

$$\int W(\mathbf{r}-\mathbf{r}',h)dV' = 1 \,. \tag{2.63}$$

This function W is characterised by the smoothing length h, and as $h \to 0$, $W \to \delta(\mathbf{r}-\mathbf{r}')$, where δ is the Dirac delta function. The interpolated quantity can be a scalar or a vector.

According to Monaghan & Lattanzio (1985), the interpolating kernel function cannot be just any mathematical function as it must be defined in terms of accuracy, smoothness, and computational cost. Interpolation errors should not exceed $O(h^2)$, and at least the first derivative should be continuous in all the integration domain. Some examples of functions satisfying this properties are the Gaussian kernel (Gingold & Monaghan 1977), and several spline functions described in (Monaghan 1992, Monaghan & Lattanzio 1985, Springel 2005), to cite some examples. The cubic spline is commonly used in SPH codes, which is defined as $W(\mathbf{r},h) = w(q)$:

$$w(q) = \frac{8}{\pi}\begin{cases} 1-6q^2+6q^3 & 0 \le q \le \frac{1}{2} \\ 2(1-q)^3 & \frac{1}{2} < q \le 1 \\ 0 & q > 1 \end{cases} \,. \tag{2.64}$$

where $q = |\mathbf{r}|/2h$ (see Springel (2010) and references within).

For a set of a finite number of particles used to approximately represent a fluid, equation (2.62) can be rewritten as

$$f(\mathbf{r}_i) = \sum_j^N f(\mathbf{r}_j) W(\mathbf{r}_i - \mathbf{r}_j, h) \delta V_j \,, \tag{2.65}$$

where f is being evaluated at the position $\mathbf{r}_i$, and the summation runs through all the neighbours of the particle at $\mathbf{r}_i$. Substituting $\delta V_j = \frac{m_j}{\rho_j}$, the previous equation becomes:

$$f(\mathbf{r}_i) = \sum_j^N f(\mathbf{r}_j) W(\mathbf{r}_i - \mathbf{r}_j, h) \frac{m_j}{\rho_j} \,. \tag{2.66}$$

If $f(\mathbf{r}_i) = \rho(\mathbf{r}_i)$, then:

$$\rho(\mathbf{r}_i) = \sum_j^N m_j W(\mathbf{r}_i - \mathbf{r}_j, h) \,. \tag{2.67}$$

The interpolation of the density depends on the mass of the individual particles and the form of the kernel.

In the case of gradients,

$$\nabla f(\mathbf{r}) = \nabla_i f(\mathbf{r}_i) = \sum_j^N f(\mathbf{r}_j) \nabla_i W(\mathbf{r}_i - \mathbf{r}_j, h) \,, \frac{m_j}{\rho_j} \tag{2.68}$$

and for quantities such as $\nabla \cdot \mathbf{v}$,

$$\nabla_i \cdot \mathbf{v}(\mathbf{r_i}) = \sum_j^N \mathbf{v}(\mathbf{r_j}) \cdot \nabla_i W(\mathbf{r}_i - \mathbf{r}_j, h) \frac{m_j}{\rho_j} \,. \tag{2.69}$$

Since $\nabla \cdot \mathbf{v}$ has derivatives with respect to $\mathbf{r}_i$, the operator affects only the kernel function inside the summation. However, as mentioned in Monaghan (1992), Springel (2010), higher accuracy can be obtained by calculating the divergence with the identity: $\rho \nabla \cdot \mathbf{v} = \nabla(\rho \mathbf{v}) - \mathbf{v} \cdot \nabla \rho$. Hence:

$$\nabla_i \cdot \mathbf{v}(\mathbf{r_i}) = \sum_j^N (\mathbf{v}_j - \mathbf{v}_i) \cdot \nabla_i W(\mathbf{r}_i - \mathbf{r}_j, h) \,. \tag{2.70}$$

2.3.2. Conventional SPH Formulation

In the conventional SPH formulation (Monaghan 1992), the continuity equation can be written as the kernel interpolating function in equation (2.67) or alternatively, as:

$$\frac{D\rho(\mathbf{r}_i)}{Dt} = \sum_j^N m_j(\mathbf{v}_i - \mathbf{v}_j)\nabla_i W(\mathbf{r}_i - \mathbf{r}_j, h)\,. \tag{2.71}$$

Since the momentum equation depends on pressure gradients, a better approximation is obtained by symmetrising the pressure gradient term $\nabla P/\rho$ with (Monaghan 1992):

$$\frac{\nabla P}{\rho} = \nabla\left(\frac{P}{\rho}\right) + \frac{P}{\rho^2}\nabla\rho\,, \tag{2.72}$$

thus, the momentum equation, becomes:

$$\frac{D\mathbf{v}_i}{Dt} = -\sum_j m_j\left(\frac{P_j}{\rho_j^2} + \frac{P_i}{\rho_i^2}\right)\nabla_i W(\mathbf{r}_i - \mathbf{r}_j, h) - \nabla_i\Phi(\mathbf{r}_i)\,, \tag{2.73}$$

in this equation Φ is the gravitational potential. This formulation has the advantage that makes the force of interaction between particles symmetric, ensuring the conservation of momentum. Furthermore, equation (2.73) can be derived from a variational principle for an adiabatic fluid (Monaghan 1992, Springel & Hernquist 2002), which makes it appropriate in studies of dynamics.

Combining equation (2.59) with Lagrangian form of the continuity equation (see equation (2.45)), results in:

$$\frac{Du}{Dt} = -\left(\frac{P}{\rho}\right)\nabla\cdot\mathbf{v}\,, \tag{2.74}$$

which is just a restatement of the first law of thermodynamics. In SPH form, it becomes:

$$\frac{Du_i}{Dt} = \left(\frac{P_i}{\rho_i^2}\right)\sum_j^N m_j(\mathbf{v}_i - \mathbf{v}j)\cdot\nabla_i W(\mathbf{r}_i - \mathbf{r}_j)\,, \tag{2.75}$$

It can also be written in the following form:

$$\frac{Du}{Dt} = -\nabla\left(\frac{P\mathbf{v}}{\rho}\right) + \mathbf{v}\cdot\nabla\left(\frac{P}{\rho}\right)\,, \tag{2.76}$$

which becomes

$$\frac{Du_i}{Dt} = \sum_j m_j\left(\frac{P_j}{\rho_j^2}\right)(\mathbf{v}_i - \mathbf{v}_j)\cdot\nabla_i W(\mathbf{r}_i - \mathbf{r}_j)\,. \tag{2.77}$$

Finally, by averaging these equations (see Monaghan 1992), a symmetrical version can be obtained:

$$\frac{Du_i}{Dt} = \frac{1}{2}\sum_j^N m_j \left(\frac{P_j}{\rho_j^2} + \frac{P_i}{\rho_i^2}\right)(\mathbf{r}_i - \mathbf{r}_j)\cdot\nabla_i W(\mathbf{r}_i - \mathbf{r}_j)\,. \tag{2.78}$$

In the previous discussion, all interpolated quantities and equations depend on the interpolating kernel W. This function is modulated by the smoothing length h, which determines the number of neighbouring particles that will be used to calculate the interpolated quantities. For this reason, h sets spatial resolution of the SPH method. For a better interpolation, the smoothing length should increase or decrease depending on the density of particles around a given particle. A simple scheme to modify h as the density varies is to assume that (Monaghan 1992):

$$h \propto \bar{\rho}^{\,-\frac{1}{3}}\,, \tag{2.79}$$

where $\bar{\rho}$ is the average density, given by

$$\bar{\rho} = \frac{1}{N}\sum_j^N \rho_j\,. \tag{2.80}$$

The time derivative of equation (2.79) is

$$\frac{dh_i}{dt} = -\left(\frac{h_i}{3\rho_i}\right)\frac{d\rho_i}{dt}\,. \tag{2.81}$$

In the SPH formalism, it becomes:

$$\frac{dh_i}{dt} = -\left(\frac{h_i}{3\rho_i}\right)\sum_j^N m_j(\mathbf{r}_i - \mathbf{r}_j)\cdot\nabla_i\tilde{W}_{ij}\,, \tag{2.82}$$

where $\tilde{W}_{ij} = 1/2[W(\mathbf{r}_i - \mathbf{r}_j, h_i) + W(\mathbf{r}_j - \mathbf{r}_i, h_j)]$. This is a symmetric version of the kernel function. Numerical experiments have shown that this formulation improves the conservation of momentum (Hernquist & Katz 1985, Monaghan 1992). Other SPH schemes determine the smoothing length by requiring that there is a fixed mass within the volume enclosed by h (Springel & Hernquist 2002).

Several formulations of the SPH equations consistent with the equations of hydrodynamics exist. The choice of the equation depends on the nature of the problem. In some cases, according to Monaghan (1992), equation (2.78) can generate spurious amounts of internal energy when particles approach each other. Experiments have shown that equation (2.75) can reduce this effect. If the thermal energy is integrated with any of these equations, and the density is calculated with the kernel interpolating function, the entropy is not accurately conserved (Monaghan 1992, Springel & Hernquist 2002). Furthermore, if the density is calculated using equation (2.71) and the energy is evolved with any of the above equations, the mass is not conserved (Monaghan 1992). Recent formulations of the SPH method include adequate conservation of entropy as described in, for example, Springel (2005, 2010), Springel & Hernquist (2002).

2.3.3. An entropy-conserving SPH method

Several versions of the SPH method formulate the dynamical equations in terms of the internal energy of the gas. However, a derivation in terms of the entropy is also possible. In this subsection, the SPH formulation of Springel & Hernquist (2002) is described as it is the method that is implemented in the code used for the simulations in the present work. The code is described in §3.1.

In the entropy formulation of Springel & Hernquist (2002), the specific entropy s of a fluid element can be characterised in terms of an entropic function $A(s)$, defined by

$$P = A(s)\rho^{\gamma}\,, \tag{2.83}$$

where γ is the adiabatic index. For an isentropic flow, the function $A(s)$ should be constant in time. If there are external sources or sinks of energy as, for example, radiative heating and cooling, the entropic function also becomes a function of time and it can be obtained from (Springel & Hernquist 2002):

$$\frac{DA}{Dt} = -\frac{\gamma-1}{\rho^{\gamma}}\mathcal{E}\,, \tag{2.84}$$

where $\mathcal{E}$ is the emissivity per unit volume. Since $P = (\gamma-1)\rho u$, then u is given by:

$$u = \frac{A(s)}{\gamma-1}\rho^{\gamma-1}\,. \tag{2.85}$$

In SPH form, equation (2.84) becomes

$$\frac{DA_i}{Dt} = -\frac{\gamma-1}{\rho_i^{\gamma}}\mathcal{E}_i\,. \tag{2.86}$$

As previously mentioned, the equations of hydrodynamics in SPH form can be derived from the principle of least action. The Lagrangian can be written in the following form

(Springel 2010):

$$L = \sum_{i}^{N} \left(\frac{1}{2} m_i \mathbf{v}_i^2 - m_i u_i \right) , \tag{2.87}$$

with the entropy formulation described above, this becomes

$$L = \sum_{i}^{N} \left(\frac{1}{2} m_i \mathbf{v}_i^2 - m_i \frac{A_i}{\gamma - 1} \rho_i^{\gamma-1} \right) . \tag{2.88}$$

The flow is assumed to be strictly adiabatic (Springel & Hernquist 2002).

In order to introduce a spatially varying resolution, the smoothing length is required to satisfy (Springel & Hernquist 2002):

$$\frac{4}{3} \pi h_i^3 \rho_i = \bar{m} N_{sph} , \tag{2.89}$$

where $\bar{m}$ is the average particle mass, and N_{sph} is the number of neighbouring particles. This equation also defines the N constraints on the coordinates of the Lagrangian. The resulting equation of motion is:

$$m_i \frac{D\mathbf{v}_i}{Dt} = - \sum_{j}^{N} m_j \frac{P_j}{\rho_j^2} \left[1 + \frac{h_j}{3\rho_j} \frac{\partial \rho_j}{\partial h_j} \right]^{-1} \nabla_i \rho_j , \tag{2.90}$$

where

$$\nabla_i \rho_j = m_i \nabla_i W_{ij}(h_j) + \delta_{ij} \sum_{k}^{N} m_k \nabla_i W_{ki}(h_i) . \tag{2.91}$$

Equation (2.90) reduces to

$$\frac{D\mathbf{v}_i}{Dt} = - \sum_{j}^{N} m_j \left[f_i \frac{P_i}{\rho_i^2} \nabla_i W_{ij}(h_i) + f_j \frac{P_j}{\rho_j^2} \nabla_i W_{ij}(h_j) \right] , \tag{2.92}$$

where

$$f_i = \left[1 + \frac{h_i}{3\rho_i} \frac{\partial \rho_i}{\partial h_i} \right]^{-1} . \tag{2.93}$$

In order to include gas self-gravity, the gravitational potential energy is added to the Lagrangian of equation (2.87). The gravitational potential at the position of a particle is:

$$\Phi(\mathbf{r}_i) = G \sum_{j}^{N} m_j \phi(\mathbf{r}_i - \mathbf{r}_j, \epsilon_i) , \tag{2.94}$$

where ϕ is the form of the contribution of the gravitational potential of each of the particles and ϵ_i is the gravitational softening length (Springel 2010). Then, the total gravitational potential energy of the system of particles is:

$$E = \frac{G}{2} \sum_i \sum_j m_i m_j \phi(\mathbf{r}_i - \mathbf{r}_j, \epsilon_i) \,, \tag{2.95}$$

and the Lagrangian becomes:

$$L = \sum_i^N \left(\frac{1}{2} m_i \mathbf{v}_i^2 - m_i u_i \right) - \frac{G}{2} \sum_i \sum j m_i m_j \phi(\mathbf{r}_i - \mathbf{r}_j, \epsilon_i) \,. \tag{2.96}$$

The resulting acceleration due to the gravitational forces is (Springel 2010):

$$m_i \mathbf{g}_i = - \sum_j^N G m_i m_j \frac{\mathbf{r}_{ij}}{r_{ij}} \frac{[\phi'(r_{ij}, \epsilon_i) + \phi'(r_{ij}, \epsilon_j)]}{2} - \frac{1}{2} \sum_j^N \sum_k^N G m_j m_k \frac{\partial \phi}{\partial \epsilon} \nabla_i \epsilon_j \,. \tag{2.97}$$

In SPH form, this reduces to (Springel 2010):

$$\begin{aligned} \mathbf{g}_i \quad = \quad & -G \sum_j^N m_j \frac{\mathbf{r}_{ij}}{r_{ij}} \frac{[\phi'(r_{ij}, \epsilon_i) + \phi'(r_{ij}, \epsilon_j)]}{2} \\ & + \frac{G}{2} \sum_j^N \left[\eta_i \nabla_i W_{ij}(h_i) + \eta_j \nabla_i W_{ij}(h_j) \right] \end{aligned} \tag{2.98}$$

where

$$\eta_j = \frac{h_j}{3 \rho_j} f_j \sum_k^N m_k \frac{\partial \phi(\mathbf{r}_{jk}, h_j)}{\partial h} \,. \tag{2.99}$$

This acceleration term is added to equation (2.92) to obtain the complete momentum equation.

Any of the previous SPH formulations require a numerical method for integration of the equations. Due to the Hamiltonian nature of the method, symplectic integrators such as the leap-frog scheme could be used to integrate the motion of the particles. However, for most hydrodynamical applications a second-order method is quite acceptable (Springel 2010). For most applications, the Courant criterion is used to determine the size of the time step:

$$\Delta t_i = C \frac{h_i}{c_i} \,, \tag{2.100}$$

where h_i is the smoothing length, c_i is the local sound speed, and C is a modulation constant such that $C < 1$. Typical values for C are in the range of $0.1 - 0.3$ (e. g. Springel 2010). Particles have individual time steps, and in many implementations, these are arranged in a power-of-two hierarchy of time steps, which makes calculations more efficient for systems with a large dynamic range in timescales (Springel 2010).

2.3.4. Artificial Viscosity

Under certain conditions, shock waves or contact discontinuities are produced in a given flow. The Rankine-Hugoniot conditions show that the specific entropy of the gas always increases at a shock front, which means that the flow can no longer be described as inviscid. For this reason, shocks are not correctly represented by the SPH equations derived from the entropy-conserving formulation of Springel & Hernquist (2002). This problem also appears in other SPH formulations (Monaghan 1992). In order to overcome this, an artificial viscosity is introduced to dissipate the necessary amount of kinetic energy and produce entropy at shocks. As long as the viscosity is introduced consistently, the conservation laws ensure the energy is adequately dissipated at shock fronts (Springel 2010). In this subsection, the concept of artificial viscosity and its general properties are described.

The artificial viscosity term typically is expressed as (Springel 2010)

$$\frac{D\mathbf{v}_i}{Dt} = -\sum_{j=1}^{N} m_j \Pi_{ij} \nabla_i \bar{W}_{ij} \,, \tag{2.101}$$

where $\bar{W}_{ij} = \frac{1}{2}[W_{ij}(h_i) + W_{ij}(h_j)]$ is a symmetric interpolating kernel. If the viscosity tensor Π_{ij} is symmetric with respect to two particles, then the force between the particles will be antisymmetric along the line joining the pair. This property ensures the conservation of linear and angular momenta (Springel 2010). To ensure the conservation of total energy, the work done against the viscosity has to be compensated. In terms of the thermal energy per unit mass, the corresponding equation is (Springel 2010):

$$\frac{Du_i}{Dt}_{\text{visc}} = \frac{1}{2}\sum_{j=1}^{N} m_j \Pi_{ij} (\mathbf{v}_i - \mathbf{v}_j) \cdot \nabla_i \bar{W}_{ij} \,, \tag{2.102}$$

or in terms of entropy,

$$\frac{DA_i}{Dt}_{\text{visc}} = \frac{1}{2}\frac{\gamma - 1}{\rho_i^{\gamma-1}}\sum_{j=1}^{N} m_j \Pi_{ij} (\mathbf{v}_i - \mathbf{v}_j) \cdot \nabla_i \bar{W}_{ij} \,. \tag{2.103}$$

A commonly used version of the artificial viscosity tensor is given by:

$$\Pi_{ij} = \begin{cases} [-\alpha c_{ij}\mu_{ij} + \beta\mu_{ij}^2]/\rho_{ij} & \mathbf{v}_{ij} \cdot \mathbf{r}_{ij} < 0 \\ 0 & \mathbf{v}_{ij} \cdot \mathbf{r}_{ij} > 0 \end{cases} , \tag{2.104}$$

with

$$\mu_{ij} = \frac{h_{ij}\mathbf{v}_{ij} \cdot \mathbf{r}_{ij}}{|\mathbf{r}_{ij}|^2 + \epsilon h_{ij}^2} , \tag{2.105}$$

which was originally introduced by Monaghan & Gingold (1983). In these equations, h_{ij} and ρ_{ij} are the arithmetic means of the smoothing length and the density calculated at the position of the two interacting particles, and c_{ij} is the mean sound speed (Springel 2010). In general, the magnitude of the artificial viscosity is modulated by the parameters α and β. However, in some SPH implementations β is defined such that $\beta = 2\alpha$, and typical values for this parameter are in the range $\alpha \approx 0.5 - 1.0$ (Springel 2005). The parameter $\epsilon \sim 0.01$ is introduced to avoid singularities for very small particle separations, and the quadratic term in μ_{ij} prevents particle penetration in strong shocks. This formulation also ensures that entropy increases at shocks (Springel 2010).

The viscosity tensor in equation (2.104) is consistent with the conservation of momentum. It vanishes for solid body rotation, but not in the case of shear flows. For this reason, the viscosity tensor can be multiplied by the factor $(f_i^{AV} + f_j^{AV})/2$ (Balsara 1995), where:

$$f_i^{AV} = \frac{|\nabla \cdot \mathbf{v}|_i}{|\nabla \cdot \mathbf{v}|_i + |\nabla \times \mathbf{v}|_i} . \tag{2.106}$$

Other alternative viscosity factors have been proposed. An example is the one proposed in Monaghan (1997):

$$\Pi_{ij} = -\frac{\alpha}{2}\frac{v_{ij}^s w_{ij}}{\rho_{ij}} , \tag{2.107}$$

where $v_{ij}^s = c_i + c_j - 3w_{ij}$ is an approximate value of the signal velocity between a pair of particles (i, j), and $w_{ij} = \mathbf{v}_{ij} \cdot \mathbf{r}_{ij}/|\mathbf{r}_{ij}|$ is the projection of the relative velocity onto the separation vector. This equation is identical to equation (2.104) if $\beta = \frac{3}{2}\alpha$ and μ_{ij} is substituted with w_{ij}. The difference between this form and that of equation (2.104) is that the previous one produces strong viscosity for particles with small separations. The force diverges as $1/r_{ij}$ down to the limit set by ϵh_{ij} factor (Springel 2010). As a final comment, some recent SPH implementations have tested schemes of adaptive artificial viscosity (e. g. Merlin et al. 2010). The choice of the viscosity factor will depend on the nature of the problem solved.

Chapter 3

Methodology

In this chapter, the general aspects of the methodology followed in the present work are presented. A summary of the code GADGET-2 is provided in §3.1. A brief review of the methods used to generate the model galaxies used as initial conditions is presented in §3.2. A description of the models used in the present work is provided in §3.3, and it is followed by a summary of the stability tests performed on the models in isolated evolution in §3.3.2. The models used for the satellite galaxy models are introduced in §3.4, and §3.5 describes the orbital parameters used for the galaxies.

3.1. The GADGET-2 Code

Some aspects of the GADGET-2 code (Springel 2005) are described, focusing on some implementation aspects of the gravitational and hydrodynamical calculations, time-step criteria, and parameters relevant for the present work. In this code, dark matter and stellar components are treated as collisionless systems. Gravitational forces are computed with a version of the tree code using a hierarchical multipole expansion, and the gas dynamics is treated with the SPH method, collectively known as TreeSPH algorithm (Hernquist & Katz 1985).

In general, the code models the behaviour of the system in an expanding background Universe following the Friedman-Leamaitre model. The Hamiltonian for the collisionless particles is (Springel 2005):

$$H = \sum_i \frac{\mathbf{p}_i^2}{2m_i a(t)^2} + \frac{1}{2}\sum_{ij} \frac{m_i m_j \phi(\mathbf{x}_i - \mathbf{x}_j)}{a(t)} \tag{3.1}$$

where $a(t)$ is the scale factor, derived from a cosmological model, $\mathbf{p}_i = a^2 m_i \dot{\mathbf{x}}_i$ is the canonical momentum of the i-th particle, $\mathbf{x}_i$ and $\mathbf{x}_j$ are the positions, and m_i and m_j are the masses of the i-th and j-th particles, respectively. The function ϕ represents the functional form of the gravitational potential in terms of particle separation. In this formulation, all coordinates are comoving (Springel 2005).

It is possible to use periodic boundaries for cosmological simulations using GADGET-2. In this case, the density is smoothed in a comoving mesh using the spline interpolating kernel proposed by Monaghan & Lattanzio (1985). The gravitational potential is derived from Poisson's equation using Fourier techniques, and when the scale factor is assumed to be $a(t) = 1$, the interaction potential is reduced to the Keplerian potential $\phi \propto 1/|\mathbf{x}_i - \mathbf{x}_j|$, effectively behaving as a Plummer softened potential modulated by the softening length ϵ (Springel 2005). In the present work, no cosmological expansion is considered, so $a(t) = 1$ and boundary conditions correspond to an isolated system, such that $\phi \to 0$ as $\mathbf{x}_i - \mathbf{x}_j) \to 0$.

Hydrodynamics is treated using the SPH equations outlined in §2.3.3. The adopted artificial viscosity is in the form of equation (2.107), which is described in §2.3.4. Tests have shown that this formulation improves time integration stability as it reduces the occurrence of very large viscous accelerations (Springel 2005). The effect of viscosity is further modulated by the Balsara factor described in §2.3.4. This reduces the spurious transport of angular momentum due to shear flows. The entropy formulation of SPH used in GADGET-2 also allows the adiabatic cooling due to the expansion of the Universe to be treated accurately in cosmological simulations (Springel 2005).

The individual time steps for the gas tracer particles are obtained from a Courant-like condition:

$$\Delta t_i^{hyd} = \frac{Ch_i}{\max(c_i + c_j - 3w_{ij})} = \frac{Ch_i}{v_{ij}^{\text{sig}}} \tag{3.2}$$

where C is a constant, h_i is the particle's smoothing length, and $w_{ij} = \mathbf{r}_{ij} \cdot \mathbf{v}_{ij}/|\mathbf{r}_{ij}|$, where $\mathbf{r}_{ij}$ and $\mathbf{v}_{ij}$ are the particle separation and relative velocity, respectively. This factor ponders the effect of shocks and high velocity contrasts in the flow, conditions in which particles are approaching each other ($\mathbf{r}_{ij} \cdot \mathbf{v}_{ij} < 0$). For the constant C, the GADGET-2 code has a default value of 0.15. The time step for SPH particles in this code is controlled by defining maximum and minimum limits. The maximum limit should be set in terms of a dynamical timescale, and the code will determine lower time steps for particles that require it. This may be needed, for example, in regions that have a very high density. On the other hand, the minimum time step can be, in principle, set to zero, but the code cannot actually reach this value. However, if the time step does fall to an excessively small value, the computational time of the simulation can grow significantly. This may be inconvenient when planning to simulate an ensemble of N-body simulations, or when the computational power available is limited. Some testing is recommended to find suitable parameters as well as an adequate lower limit for the time step.

The spatial resolution for the stellar and dark matter components is controlled by the gravitational softening length ϵ. However, it is safe to estimate the resolution limit as $\approx 2\epsilon$. In the case of cosmological simulations with GADGET-2, the density is calculated in a mesh using the interpolating function given in equation (2.64), which has an effective smoothing of length of 2.8ϵ. The gas also has a softening length for gravitational force calculation purposes, but the spatial resolution of any features is controlled by the SPH smoothing length h_i. This quantity depends on the concentration of neighbours around a given particle. The code allows to set a minimum limit for h_i when configuring the parameters for a simulation. However, the documentation recommends not to do so as it requires the code to then vary the number of neighbours around particles when interpolating the density. Tests have shown that this increases the noise in the calculations. If needed, this quantity can also be monitored by requiring the code to output the h_i of each particle.

For the gravitational force calculation, GADGET-2 uses a version of the hierarchical tree code of Barnes & Hut (1986). It begins with a cubic root cell around the system of particles that is recursively subdivided in eight smaller nodes until each particle has been isolated in a node. Then the tree is “walked” in order to calculate the gravitational forces on the individual particles. It uses the monopole moments of the gravitational potential in order to calculate long-range forces, which is advantageous in terms of memory consumption. This algorithm is also easily coupled to the SPH method (Springel 2005). For the opening criterion, it uses a definition slightly different to that of the original tree code of Barnes & Hut (1986). For a node of mass M and size l at a distance r is considered for usage if

$$\frac{GM}{r^2}\left(\frac{l}{r}\right)^2 \leq \alpha_{\mathrm{force}}|\mathbf{a}|\,, \tag{3.3}$$

where $|\mathbf{a}|$ is the magnitude of the total acceleration obtained in the previous time step, and α_{force} is a tolerance parameter (Springel 2005). In the GADGET-2 documentation, the suggested value for $\alpha_{\mathrm{force}} = 0.005$. Testing with a value of $\alpha_{\mathrm{force}} = 0.001$ significantly decreases errors associated with force calculation, but the computational cost in time is significant for a reasonable simulation. For this reason, the first value is used in the present work.

As the geometric centre of a node can differ from the centre of mass, the following condition is added to the opening criterion:

$$|r_k - c_k| \leq 0.6l \tag{3.4}$$

where r_k is the magnitude of the position of the particle of interest, and c_k is the geometric centre. This criterion requires that the particle lies outside a box about 20% larger than that of the tree node (Springel 2005).

For the integration of the equations of motion, GADGET-2 uses a scheme of leap-frog integrators. The Hamiltonian in equation (3.1) can be separated in the form $H = H_{kin} + H_{pot}$. The time-evolution operators for each of the parts H_{kin} and H_{pot} can be computed exactly (Springel 2005). According to Quinn et al. (1997), a series of drift and kick operators can be derived:

$$D(\Delta t) : \begin{cases} \mathbf{p}_i \to \mathbf{p}_i \\ \mathbf{x}_i \to \mathbf{x}_i + \frac{\mathbf{p}_i}{m_i}\Delta t \end{cases}, \tag{3.5}$$

$$K(\Delta t) : \begin{cases} \mathbf{x}_i \to \mathbf{x}_i \\ \mathbf{p}_i \to \mathbf{p}_i + \frac{\mathbf{f}_i}{m_i}\Delta t \end{cases}, \tag{3.6}$$

where $\mathbf{f}_i$ is the force on the particle. These operators are symplectic because they are exact solutions to the canonical transformations generated by the corresponding Hamiltonians (Springel 2005). Following the idea of operator splitting, an approximate time evolution operator can be derived:

$$U(\Delta t) = D\left(\frac{\Delta t}{2}\right) K(\Delta t) D\left(\frac{\Delta t}{2}\right) \text{ or } U(\Delta t) = K\left(\frac{\Delta t}{2}\right) D(\Delta t) K\left(\frac{\Delta t}{2}\right). \tag{3.7}$$

These operators correspond to the drift-kick-drift and kick-drift-kick leapfrog integrators, which are symplectic (Springel 2005). Given the large range of densities in a typical simulation, it is best to have a scheme that assigns individual time steps according to local conditions of a given particle. This improves the computational efficiency of the integration scheme, but from a formal point of view, it is not possible to produce a symplectic integration because the potential part of the Hamiltonian is not separable (Springel 2005). However, it is possible to separate the long-range part of the force from the short-range terms and construct a time evolution operator U that includes a subdivision of the time step. This amounts to giving long-range kicks every Δt and short-range kicks in smaller intervals within Δt (Springel 2005):

$$U(\Delta t) = K_{lr}\left(\frac{\Delta t}{2}\right)\left[K_{sr}\left(\frac{\Delta t}{2m}\right) D_{sr}\left(\frac{\Delta t}{m}\right) K_{sr}\left(\frac{\Delta t}{2m}\right)\right]^m K_{lr}\left(\frac{\Delta t}{2}\right). \tag{3.8}$$

In the normal integration mode of GADGET-2, which is the one used in this work, a global time step is defined. Then, smaller steps are power of two divisions of the global step. Particles can move to smaller time steps, but movements to a higher step have to be done every second step. This scheme provides synchronisation with the higher time step hierarchy and is adequate to minimise the required number of particle drifts and tree constructions (Springel 2005). The criterion used to chose the time step for the stellar and dark matter components is:

$$\Delta t = \min\left[\Delta t_{\max}, \sqrt{\frac{2\eta\epsilon}{|\mathbf{a}|}}\right] . \tag{3.9}$$

The value of η is defined at the beginning of the simulation. Typical values are in the order of 10^{-1}. Tests show that these adaptive time scheme produces good results following a kick-drift-kick sequence (Springel 2005). For the gas particles, the time step is defined following the condition of equation (3.2).

3.2. Building the Model Galaxies

Several different schemes to build model galaxies are available in the literature (e. g Hernquist (1993), Kuijken & Dubinski (1995), Widrow & Dubinski (2005); some of them have been summarised in §2.1.2). The present work uses the method developed by McMillan & Dehnen (2007) to initialise the collisionless components of a disc galaxy. The general steps of this method are the following:

1. An initial N-body sampling of the spherically symmetric components of the galaxy, such as the halo and the bulge, are generated in the presence of the monopole term of the potential of the desired disc.

2. The N-body system is evolved by growing the non-monopole terms of the disc potential adiabatically in an N-body simulation in order to give time for the halo and bulge particles to relax in the new potential.

3. Set the disc component with an N-body sampling of the desired stellar disc.

3.2.1. Spheroidal Components of the galaxy

The model galaxy in this work is constructed self-consistently using the methods of McMillan & Dehnen (2007) as implemented in the code `mkgalaxy`, which is available in the *The Stellar Dynamics Toolbox* NEMO (Teuben 1995). In this scheme, the spherically symmetric components of the galaxy are generated following the scheme proposed by Cuddeford (1991), which is an extension of the Osipkov (1979) and Merritt (1985) models. The proposed distribution function has the form:

$$f(\mathcal{E}, L) = L^{2\alpha} f_0(Q)\,, \tag{3.10}$$

where $Q = \mathcal{E} - \frac{L^2}{2r_a^2}$, and $\mathcal{E} = \Psi - \frac{1}{2}v^2$, which is defined as the relative energy of the particle. Here $\Psi = -\Phi$, where Φ is the gravitational potential, L is the angular momentum, and r_a is the anisotropy radius. The parameter α satisfies $\alpha > -1$ and f is such that $f(Q < 0) = 0$. The distribution function is related to the mass density by an Abel integral equation of the form:

$$f_0(Q) = \frac{\sin\left[(n - \frac{1}{2} - \alpha)\pi\right]}{\pi\lambda(\alpha)\eta(\alpha)} \frac{d}{dQ} \int_0^Q \frac{d^n \rho_{red}}{d\Psi^n} \frac{d\Psi}{(Q - \Psi)^{\alpha + \frac{3}{2} - n}}\,, \tag{3.11}$$

where n is the largest integer satisfying $n \leq \alpha + \frac{3}{2}$. The reduced density is given by (McMillan & Dehnen 2007):

$$\rho_{red} = \frac{1}{r^{2\alpha}} \left[1 + \left(\frac{r}{r_\alpha} \right)^2 \right]^{\alpha+1} \rho \,, \tag{3.12}$$

The functions η and λ are given by (McMillan & Dehnen 2007):

$$\eta(\alpha) = \begin{cases} (\alpha + \frac{1}{2})(\alpha - \frac{1}{2})...(\alpha + \frac{3}{2} - n) & \text{if } \alpha > \frac{-1}{2} \\ 1 & \text{if } -1 < \alpha \leq -\frac{1}{2} \end{cases} \,, \tag{3.13}$$

and

$$\lambda(\alpha) = 2^{\alpha+\frac{3}{2}} \pi^{\frac{3}{2}} \frac{\Gamma(\alpha+1)}{\Gamma(\alpha+\frac{3}{2})} \,. \tag{3.14}$$

This distribution function produces a spherically symmetric system. The velocity distribution is modulated by the anisotropy parameter β given by:

$$\beta(r) = 1 - \left(\frac{\sigma_\theta}{\sigma_r} \right)^2 = \frac{r^2 - \alpha r_a^2}{r^2 + r_a^2} \,. \tag{3.15}$$

If $\alpha = 0$, it is reduced to the Osipkov-Merrit model. If $r_a \to \infty$, the anisotropy of the system is the same at all radii, and $\beta = -\alpha$. This formulation does not assume a Maxwellian velocity distribution at any point, and it is restricted to systems with spherical symmetry ($\Psi = \Psi(r)$, $\rho = \rho(r)$), with physically realistic distribution functions $f_0(Q) > 0$. It can be generalised to include larger spherically symmetric systems within one N-body system (McMillan & Dehnen 2007).

The spherical components are constructed with the following radial density profile (McMillan & Dehnen 2007):

$$\rho_s(r) = \frac{CT(r/r_t)}{x^{\gamma_0} \left(x^\eta + 1 \right)^{(\gamma_\infty - \gamma_0)/\eta}} \,, \tag{3.16}$$

where $x = \sqrt{r^2 + r_c^2}/r_s$. The truncation function is given by

$$T(z) = \begin{cases} \operatorname{sech}(z) = \frac{2}{e^z + e^{-z}} & \text{if } r_t > 0 \\ \frac{2}{\operatorname{sech}(z) + \operatorname{sech}^{-1}(z)} & \text{if } r_t < 0 \end{cases} \,. \tag{3.17}$$

The required parameters are: the total mass M of the system, which determines the normalisation constant C, the inner and outer logarithmic density slopes: γ_0 and γ_∞, the transition strength between inner and outer power-law η, the core radius r_c, and the scale radius r_s and the truncation radius r_t, which defines the form of $T(z)$. The last three parameters should satisfy $0 \leq r_c < r_s < r_t \leq \infty$. The number of bodies N in the spheroid also needs to be specified. The positions of the particles are obtained using the inversion of the cumulative mass profile method (McMillan & Dehnen 2007).

The general idea of the inversion of the cumulative mass profile method can be understood by viewing the integrated mass function of the profile

$$M(< r) = \int_0^{2\pi} \mathrm{d}\,\phi \int_0^{\pi} \sin\theta \,\mathrm{d}\theta \int_0^{r} \rho(r) r^2 \,\mathrm{d}r \,, \tag{3.18}$$

as a cumulative distribution function (CDF). Equation (3.18) can be normalised by dividing by the total mass, so that the integral converges to 1 as $r \to \infty$, provided that the profile decays with radius fast enough or some form of truncation is introduced. By treating the integrated mass function as a CDF, the density profile can be interpreted as a probability density such that the probability of finding a particle in a given element of volume in spherical coordinates is proportional to $\rho(r) \sin\theta \, r^2 \, \delta r \, \delta\theta \, \delta\phi$. Although a profile with spherical symmetry has been used, the angular coordinates are not necessarily initialised from uniform distributions. The correct equations for sampling the coordinates considering only a spherically symmetric distribution are derived in the following steps. The three integrals in equation (3.18) can be interpreted as normalised CDFs for each of the coordinates r, ϕ, and θ. It can be seen that the ϕ coordinate can be initialised from a uniform distribution between 0 and 2π, but this is not true for θ beacuse of the $\sin\theta$ factor in the volume element. By treating the integrals as CDFs for each coordinate, the following equations are obtained:

$$\Phi = \frac{1}{2\pi} \int_0^{\phi} \mathrm{d}\phi' = \frac{\phi}{2\pi} \,, \tag{3.19}$$

where the $1/2\pi$ factor is a normalisation constant, and $0 \leq \phi \leq 2\pi$.

$$\Theta = \frac{1}{2} \int_0^{\theta} \sin\theta' \,\mathrm{d}\theta' = \frac{1}{2}(1 - \cos\theta) \,, \tag{3.20}$$

where the $1/2$ factor is a normalisation constant, and $0 \leq \theta \leq \pi$.

$$R = C \int_0^{r} \rho(r) r^2 \mathrm{d}r' \,. \tag{3.21}$$

where C is a normalisation constant, and $0 \leq r \leq \infty$.

Solving equation (3.19) and (3.20) for ϕ and θ yields

$$\phi = 2\pi\Phi \,, \tag{3.22}$$

and

$$\theta = \cos^{-1}(1 - 2\Theta)\,. \tag{3.23}$$

Values for ϕ and θ can be obtained from using a random number generator to sample Φ and Θ between 0 and 1, and using these two equations to calculate the corresponding coordinates. Equation (3.22) corresponds to a uniform distribution of ϕ between 0 and 2π, which is a result of using a density profile independent of ϕ. However, as Equation (3.23) shows, θ coordinates cannot be sampled from a uniform distribution in θ because of the $\sin\theta$ factor in the definition of a differential volume in spherical coordinates. In the case of the radial coordinate r, if the integrand in equation (3.21) has an analytic antiderivative, it may be possible to solve an equation for r in terms of R. The vaue for r can then be obtained from sampling R between 0 and 1 in a uniform random generator. This method is also described in Hut & Makino (2009). This formalism can also be extended to axisymmetric distribution by obtaining the relevant equations in terms of cylindrical coordinates. For more complicated distributions, other Monte Carlo sampling methods may be adequate; see for example Fishman (2006).

The velocity space is sampled by defining a set of pseudo-elliptical coordinates (u, η) in velocity space, such that the radial component is $v_r = u\cos\eta$, and the tangential component is $v_t = u(1 + (r/r_a)^2)^{-1/2}\sin\eta$. u and η are sampled from the distributions $p(\eta)\sin^{1+2\alpha}\eta$ and $p(u) = u^{2+2\alpha} f_0(\Psi - 1/2u^2)$. The second equation is sampled using the rejection method (McMillan & Dehnen 2007). As indicated before, the spherical initial conditions are generated in the presence of the monopole part of the disc potential.

3.2.2. Stellar Disc

In the code `mkgalaxy`, once the spheroidal components have been generated, these are adjusted to the presence of the full disc potential by running a N-Body simulation using `gyrfalcON` (Dehnen 2000). This code is also available in the NEMO toolbox (Teuben 1995) [1]. This simulation takes the spheroidal components as initial conditions, and the potential of the disc is slowly changed from the monopole term to the full potential.

In order to avoid the drift of the N-body distribution, it has to be symmetrised. This means that for every body with phase-space coordinates $\mathbf{w} = (\mathbf{x}, \mathbf{v})$ there is another one at $-\mathbf{w}$. This is performed with the program `symmetrize`, which arranges the bodies in pairs such that $\mathbf{w}_{2i+1} = -\mathbf{w}_{2i}$, and does so by doubling the total number of bodies. This process is repeated after every block-step in the simulation (McMillan & Dehnen 2007).

---

[1] For additional information on the codes `mkgalaxy` and `gyrfalcON`, please refer to the documentation available with the NEMO distribution at: `http://carma.astro.umd.edu/nemo/`, where a detailed explanation of the numerical procedures, the implementation, and suggested input parameters are presented.

The final step is to populate the disc with particles, which has a density profile given by [2]:

$$\rho(R,z) = \frac{1}{2z_0}\Sigma_0 \exp\left(-\frac{R}{R_D}\right)\text{sech}^2\left(\frac{z}{z_0}\right)\,, \tag{3.24}$$

where R is the galactocentric radius, z is the vertical distance, R_D is the radial scale length, and z_0 is the vertical scale height. The total disc mass is given by $M_d = 2\pi R_d^2\Sigma_0$, which defines the value of the central surface density Σ_0. In this model, R_D, z_0, and M_d are free parameters.

The method of McMillan & Dehnen (2007) has a target radial velocity dispersion in the plane $\sigma_R(R, z=0)$ determined by the Toomre parameter Q, and the scale length R_σ of the radial velocity dispersion function. The Toomre parameter $Q(R)$ (Toomre 1964) is given by:

$$Q(R) = \frac{\sigma_R(R)\kappa(R)}{3.36G\Sigma(R)}\,, \tag{3.25}$$

where $\kappa(R)$ is the epicyclic frequency, and $\Sigma(R)$ is the surface density. The epicyclic frequency κ is given by

$$\kappa(R)^2 = R\frac{d\Omega^2}{dR} + 4\Omega^2\,, \tag{3.26}$$

where Ω is the angular frequency of the orbit, defined by

$$\Omega^2(R) = \frac{v_c^2(R)}{R^2} = \frac{1}{R}\frac{d\Phi}{dR}\,. \tag{3.27}$$

If $R_\sigma > 0$, then the radial velocity dispersion follows an exponential profile

$$\sigma_R(R, z=0) = \sigma_0 \exp\left(-\frac{R}{R_\sigma}\right)\,, \tag{3.28}$$

where R_σ is the scale length of the $\sigma_R(R)$ profile. Note that for this choice of parameters, the normalisation constant σ_0 is determined by the condition that $Q(R_\sigma) = Q_0$, where Q_0 is a free parameter defined by the user in `mkgalaxy`. With this definition, care must be taken if the user wishes to specify the value of $Q(R_\odot)$, where $R_\odot$ is the solar radius, to build a model.

Another option is to set $R_\sigma = 0$, which defines a target velocity dispersion such that Q is constant at all radii, $Q(R) = Q_0$. With this choice of parameters, the radial velocity dispersion is given by

$$\sigma_R(R) = \left(\frac{3.36G\Sigma(R)}{\kappa(R)}\right)Q(R),\,. \tag{3.29}$$

---

[2] This profile is typically assumed because it adequately fits the observed thensity profiles in spiral galaxies (e. g Binney & Tremaine 2008, Sparke & Gallagher 2007)

For the vertical velocity distribution, the vertical velocity dispersion σ_z is such that $\sigma_z^2 = \pi G \Sigma(R) z_0$, where $\Sigma(R)$ is the disc surface density. This means that regions with higher density have a higher vertical velocity dispersion. The vertical profile corresponds to an isothermal sheet.

The algorithm for sampling the positions and velocities of the particles are described in Dehnen (1999) and McMillan & Dehnen (2007). It samples orbits in energy and angular momentum, and an average number of bodies per orbit is defined. This method produces a disc having $\Sigma(R)$ and $\sigma_R(R)$ profiles very similar to those targeted, but not identical. Warmer models may be of interest in theoretical works were the formation of a bar is to be avoided. However, in this case the iteration of particle positions required to obtain a final surface density close to the target becomes more difficult, and produces density profiles that deviate slightly from the exponential profile (McMillan & Dehnen 2007). This point is reviewed in the context of the models used in the present work in §3.3.

3.2.3. Gas Disc

There is no unique method to add a gaseous component to a disc galaxy (e. g. Wang et al. 2010). The method of McMillan & Dehnen (2007) does not consider a gaseous component for a galaxy. In the case of a gas, the collisional term in the Boltzmann equation becomes important, which makes the calculation of a distribution function a very elaborate problem. For this reason, different approaches have been developed in order to initialise a gaseous component. One approach is to obtain the density distribution that satisfies hydrostatic equilibrium in the vertical direction and rotational support in the radial direction. Such schemes have been developed by (e. g. Springel et al. 2005, Wang et al. 2010, Rodríguez-González et al. 2011).

A second approach is to initialise the gas disc with a density distribution and circular velocity similar to that of the disc, and it is allowed to relax in the potential of the entire galaxy. This approach has been implemented in the simulations of Mihos & Hernquist (1994), and of Hernquist & Mihos (1995) where the gas was distributed with a radial scale similar to the stars but with the vertical scale as a function of radius. In both examples, the gas is assumed to follow an isothermal equation of state with $T = 10^4$ K. Another method also been used in the simulations of Springel (2000) where the gas has an initial density profile similar to the stellar disc, an azimuthal velocity component given by the local circular velocity. In this scheme the internal energy per unit mass has an initial value proportional to the vertical velocity dispersion, and changes in the course of the simulation since cooling and heating mechanisms are included. Another example of this scheme is the work of Dobbs et al. (2010), where the gas is assumed to follow the isothermal equation of state.

In the present thesis, a scheme following the second approach described above is used. This is suitable as the present work focuses on the large scale motions of the gas and not on local processes such as shocks. The initial gas disc SPH particles are distributed following a density profile similar to that of the stellar disc, only displaced within a softening length of the stellar particles. It is assumed to follow an isothermal equation of state, meaning that any cooling or heating processes are balanced in a very short time scale. For the gas disc to be in rotational support, the effect of the pressure must be considered (Wang et al. 2010). For an ideal isothermal gas, the equation of state is given by

$$P = \left(\frac{k_B T}{\mu m_p}\right) \rho \,, \tag{3.30}$$

where k_B is the Boltzmann constant, T is the temperature of the gas, μ is the mean molecular weight, and m_p is the proton mass. This defines the sound speed c_s as:

$$c_s = \sqrt{\frac{k_B T}{\mu m_p}} \,, \tag{3.31}$$

and equation (3.30) can be rewritten as $P = c_s^2 \rho$. For an ideal gas, given the internal energy per unit mass u, the pressure can be written as $P = (\gamma - 1)\rho u$ where γ is the ratio of specific heats, and ρ is the density of the gas.

The momentum equation in cylindrical coordinates, with rotational support yields:

$$\frac{v_c^2(R)}{R} = \frac{1}{\rho}\frac{\partial P}{\partial R} + \frac{\partial \Phi}{\partial R} \,, \tag{3.32}$$

given the isothermal equation of state, this means that:

$$\frac{v_c^2(R)}{R} = \frac{1}{\rho}\left(\gamma - 1\right) u \frac{\partial \rho}{\partial R} + \frac{\partial \Phi}{\partial R} \,. \tag{3.33}$$

Multyplying by R and defining $v_c'^2 = R\frac{\partial \Phi}{\partial R}$, the above equation can be rewritten as:

$$v_c^2(R) = v_c'^2 + \left(\gamma - 1\right) u \frac{R}{\rho}\frac{\partial \rho}{\partial R} \,, \tag{3.34}$$

In Wang et al. (2010), the second term is:

$$v_P^2 = \left(\gamma - 1\right) u \frac{\partial \ln \rho}{\partial \ln R} \,. \tag{3.35}$$

In equation (3.34), v_c' is the circular velocity defined by the potential of the mass distribution of the galaxy. However, the momentum equation shows that gas parcels are affected by the pressure gradient in the galaxy; $v_p'^2$ accounts precisely for this effect. On the plane of the galaxy ($z = 0$), the density gradient is negative, therefore v_p^2 is a negative term. This means that the circular velocity of the gas is lower than the circular velocity given only by the potential. This effect is understood from the fact that, due to the negative pressure gradient, there is an outward force on the gas parcels that acts against the pull of gravity. Consequently, gas parcels must have a lower circular velocity in order to stay on a circular orbit. In practice, the correction by v_p^2 may be small. However, Wang et al. (2010) mention that it is important in order to define stable initial conditions for the gas. For an initial exponential disc, equation (3.35) reduces to

$$v_P^2 = -(\gamma - 1)u\left(\frac{R}{R_D}\right) . \tag{3.36}$$

For neutral hydrogen at $T = 10^4$ K, this term amounts to $\sqrt{|v_P^2|} \sim 10$ km s^{-1}. The last equation shows that the correction becomes important at the outer parts of the disc, where the gas is less bound to the disc. Not including the effect of pressure may produce a spurious radial growth as gas parcels move to larger orbits when initialised when considering the circular velocity without the v_P^2 term. This term is included in the initial conditions used in this work.

3.3. Disc Galaxy Models

3.3.1. Model Parameters

The primary galaxy has physical parameters similar to the Milky Way as described in Klypin et al. (2002). It consists of a Navarro-Frenk-White (NFW) (Navarro et al. 1996) dark matter halo, a stellar and gas disc, and a bulge.

The dark matter halo has a mass of $M_h = 10^{12} M_\odot$, and the density follows a NFW profile. This corresponds to an inner slope $\gamma_0 = 1$, an outer slope $\gamma_\infty = 3$, and a transition parameter $\eta = 1$ in equation (3.16). Ths scale length is $r_s = 21$ kpc. Because this profile falls as $1/r^3$ at long distances, the integrated mass grows logarithmically. For this reason, a value of $r_{cut} = 210$ kpc is used in the truncation function given in equation (3.17), which allows the mass of the halo to converge to a finite value. The stellar disc has a density profile given in equation (3.24) with a radial scale length $R_D = 3.5$ kpc, a vertical scale length of $z_D = 0.35$ kpc, and a total mass of $M_d = 4.167 \times 10^{10} M_\odot$. A gas disc with a mass of 10% of the stellar disc is included, and it has an initial distribution similar to that of the stellar disc. The gas temperature was set to $T = 8 \times 10^3$ K. This is in the range of temperatures that correspond to the warm component of the ISM for typical abundances (e. g. Lequeux 2005, Draine 2011, Kwok 2007). The central bulge follows a Hernquist profile (Hernquist 1990), corresponding to an inner slope of $\gamma_0 = 1$, an outer slope of $\gamma_\infty = 4$, and a transition parameter of $\eta = 1$. The mass of this profile converges as $r \to \infty$. The bulge has a total mass of $8.33 \times 10^9 M_\odot$, and a scale radius of $a = 0.7$ kpc. The rotation curve for this model is shown in Figure 3.1. A system of units where $G = 1$ is used, such that the mass unit $u_m = 10^{10} M_\odot$, the length unit is $u_l = 1.0$ kpc, the unit velocity is $u_v = 207.49$ km s^{-1}, and the unit time is $u_t = 4.7$ Myr. In this model, the circular velocity at $R_\odot = 8$ kpc defines an orbital period of $\tau \approx 51 u_t \approx 241$ Myr.

It is also necessary to specify a Toomre Q parameter for the stellar disc. Since the models of McMillan & Dehnen (2007) can generate model galaxies with constant Q, initial conditions satisfying this property are chosen. Two galaxy models are defined: Model A, with $Q = 3.0$, and Model B, with $Q = 1.5$. The first value generates a non-barred galaxy model, and the second one produces a galaxy in which a bar is formed after a few orbital periods of isolated evolution.

It has been shown that bars can produce inflows of gas in disc galaxies. According to simulations by Athanassoula (1994), bars can produce steady flows of gas due to the formation of shocks, and the highest inflow is produced during the formation of the bar. For these reasons, in a barred galaxy it becomes difficult to isolate the effects from the perturbation of the infalling satellite from those of the bar. This problem motivates a model that avoids the formation of a bar such as Model A. Although a galaxy with $Q = 3.0$ may be a rather unrealistic representation, it does produce a model lacking a bar that may be representative of bar-less galaxies such as S0s, and other early-type discs not showing prominent spiral features. The simulations with Model B are also conducted in order to study the response of a barred galaxy to the satellite. The physical properties of the model galaxies are summarised in table 3.1, and some stability tests are described in §3.3.2. [3]

For the model galaxies described, the number of particles in the dark matter halo is$N_h = 10^6$; in the stellar and gas disc it is $N_d = N_g = 500\,000$, and the number of particles in the bulge is $N_b = 10\,000$. The softening lengths of the particles have been defined such that the accelerations between particles of different components are similar at the softening length. The values obtained are for the halo $\epsilon_h = 0.121$ kpc, for the gas and stellar discs $\epsilon_d = \epsilon_g = 0.035$ kpc, and for the bulge $\epsilon_b = 0.110$ kpc. As a final comment of this section, for the simulations with the interacting galaxy, the initial condition for both Model A and B corresponds to the isolated galaxy after four orbital periods of isolated evolution. In this case, the vertical scale length of the gas is approximately half the initial value, corresponding to a $z_g \approx 0.15$ kpc.

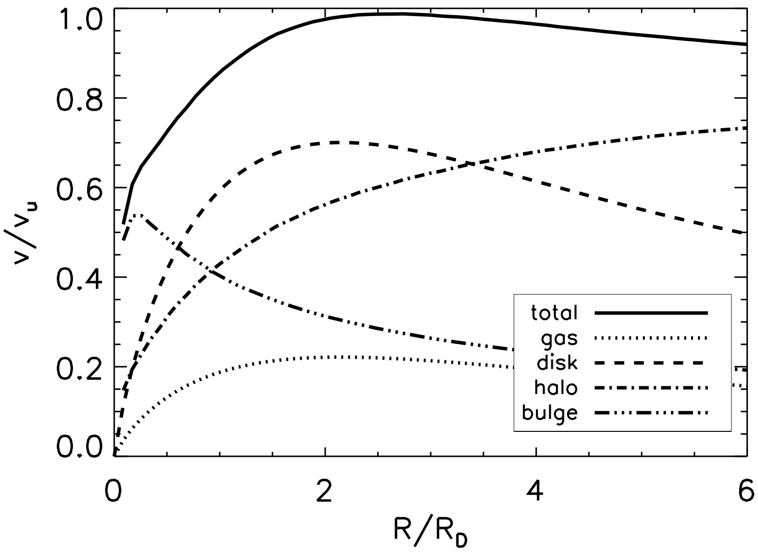

Figure 3.1: The rotation curve of the model galaxy showing the contribution of the dark matter halo, disc, bulge, and gaseous component. The horizontal axis is normalised to the radial scale length R_D, and the vertical axis to the unit velocity u_v.

---

[3] The author is grateful to Prof. F. Combes for stimulating discussions on barred and non-barred galaxies, and galaxy simulations in general.

Table 3.1: Parameters of the Primary Galaxy Models

Component	Property	Model A	Model B
Halo			
	Truncation	sech(r/r_{cut})	sech(r/r_{cut})
	M_h	$10^{12}M_\odot$	$10^{12}M_\odot$
	r_{core}	0.0	0.0
	r_{scale}	$6R_D$	$6R_D$
	r_{cut}	$60R_D$	$60R_D$
	N_h	10^6	10^6
	ϵ_h	0.121 kpc	0.121 kpc
Disc			
	M_d	$4.167 \times 10^{10}M_\odot$	$4.167 \times 10^{10}M_\odot$
	R_d	3.5 kpc	3.5 kpc
	z_d	0.350 kpc	0.350 kpc
	$Q(R)$	*3.0*	*1.5*
	N_d	500000	500000
	ϵ_d	0.035 kpc	0.035 kpc
Gas Disc			
	M_g	$0.1M_d$	$0.1M_d$
	R_g	$\approx R_d$	$\approx R_d$
	z_g	$\approx z_d$	$\approx z_d$
	N_g	500000	500000
	ϵ_g	0.035 kpc	0.035 kpc
Bulge			
	M_b	$8.333 \times 10^9M_\odot$	$8.333 \times 10^9M_\odot$
	a_b	0.700 kpc	0.700 kpc
	N_b	10000	10000
	ϵ_b	0.110 kpc	0.110 kpc

3.3.2. Isolated Evolution

Figure 3.2 plots the radial surface density profiles of the stellar and gaseous components for the initial condition, and after 4 and 8 orbital periods τ [4] of isolated evolution. In Model A (upper panel of Figure 3.2), both the gas and stellar discs remain relatively stable during 8τ. Because the gas is not initialised in a strict hydrostatic equilibrium condition, and due to the higher velocity dispersion in the central regions of the disc, dissipation by the artificial viscosity may be producing the central cusp observed after 8 orbital periods. In spite of this effect, the gas generally maintains the initial density profile and radial scale. The stellar component of Model A practically shows no variations in density, which is expected from the high Q value used.

In the simulation of Model B (lower panel of Figure 3.2), the formation of the bar produces a final density profile with some differences with respect to the initial stellar and gas profiles. In the gas density profile, the surface density at $R \approx R_D$ falls with respect to the initial value, but it remains comparable to the initial profile at larger radii. This change can be explained by the fact that the bar produces gas flows to the central region. The formation of the bar is also evident in the stellar profile as a cusp forms in the central region of the disc. The difference between the initial profile and that obtained after 4 orbital periods is produced by the formation of the bar. The profiles are shown in Figure 3.4. However, the profile produced after 8τ has a behaviour as a function of radius similar to the profile at $t = 4\tau$. The gas surface density at $R > 3R_D$, the region where the infalling satellite will be initially disturbing the disc, remains stable during isolated evolution.

Figures 3.3 and 3.4 show the projected surface density maps, of the gas and stars respectively, on the $x - y$ and $x - z$ planes for both models at 4 and 8 orbital periods of isolated evolution. In the case of Model A (panels (a) and (b)), both the gas and stellar components are stable during the course of the simulation. Although some diffuse structure developed in the gaseous component, it does not have a significant effect, as it will be shown in the following discussion. Regarding Model B, the bar clearly appears in the snapshot at 4 orbital periods, but its strength has decreased slightly by the end of the simulation. Spiral structure is visible in the stellar component during the simulation. In the case of the gaseous component (panels (c) and (d)), a spiral structure is clearly visible in both snapshots. Some spurious clumps have formed in the course of the simulation. A brief discussion on this matter is given in §3.3.3.

A quantity of interest in this study is the integrated mass function of the gas normalised

---

[4] τ is the orbital period at $R_\odot$, corresponding to ≈ 240 Myr.

to the total gas mass M_g, which is formally defined as:

$$\mu_g(< R) = \frac{M(< R)}{M_g} = \frac{1}{M_g}\int_0^{2\pi}\int_0^{R} \Sigma(R', \phi')R' \, \mathrm{dR'd}\phi' \tag{3.37}$$

In practice, this is calculated by dividing the disc in rings, and adding the mass inside each ring. This is then divided by the total mass of gas initially in the disc. The function $\mu_g(< R)$ is plotted for Model A (upper panel) and Model B (lower panel) in Figure 3.6 every two orbital periods from $t = 0$ up to $t = 8\tau$. For Model A, the plot shows that the integrated mass remains quite stable during isolated evolution. A small increase is observed for $R < 0.5R_D$ which is consistent with the increase in central density observed in Figure 3.2. Slight differences are observed with respect to the initial condition that may be attributed to the relaxation of the gas in the galactic potential. Nevertheless, the profile is very stable during isolated evolution.

For Model B, the presence of the bar does produce gas flows during isolated evolution, as shown in the lower panel of Figure 3.2. The inflow appears to be higher at the region $R < R_D$, in the interval between the beginning of the simulation and 4τ (where τ is the orbital period). This period corresponds to the interval when the bar forms, which explains the sudden increase in mass. After 4 orbital periods, gas continues to flow, but does so at a lower rate. In the simulations including the satellite, the resulting $\mu_g(< R)$ function will be compared with that of isolated evolution for both models A and B in order to assess if any significant change in the mass distribution is produced by the infalling satellite.

The values of $\mu(< R)$ at three fixed radii were also calculated as a function of time. These are chosen as $R = 1$, 3.5, and 8 kpc, corresponding to $R \approx 0.3R_D$, R_D, and $2.3R_D$. The behaviour of $\mu(< R)$ as a function of time measures the average gas flow in the radial direction. Figure 3.7 plots this function for the simulations of Model A (upper panel) and Model B (lower panel). In Model A, some oscillations are apparent between $t = 2\tau$ and $t = 4\tau$. After that, the mass distribution seems to be reasonably stable at all radii after 4 orbital periods. This result is important for comparing with the simulations including the infalling satellite. For Model B, there is also a period of relaxation up to $\approx 2 - 3$ orbital periods. After 3 orbital periods, the mass enclosed within $0.28R_D$ and R_D grows at a steady rate, which is expected from the presence of a bar. It is noted that $0.28R_D$ is ≈ 28 times the softening length of the disc, and ≈ 10 times the softening of the halo. This is well above the $\approx 2\epsilon$ limit (where ϵ is the gravitational softening length).

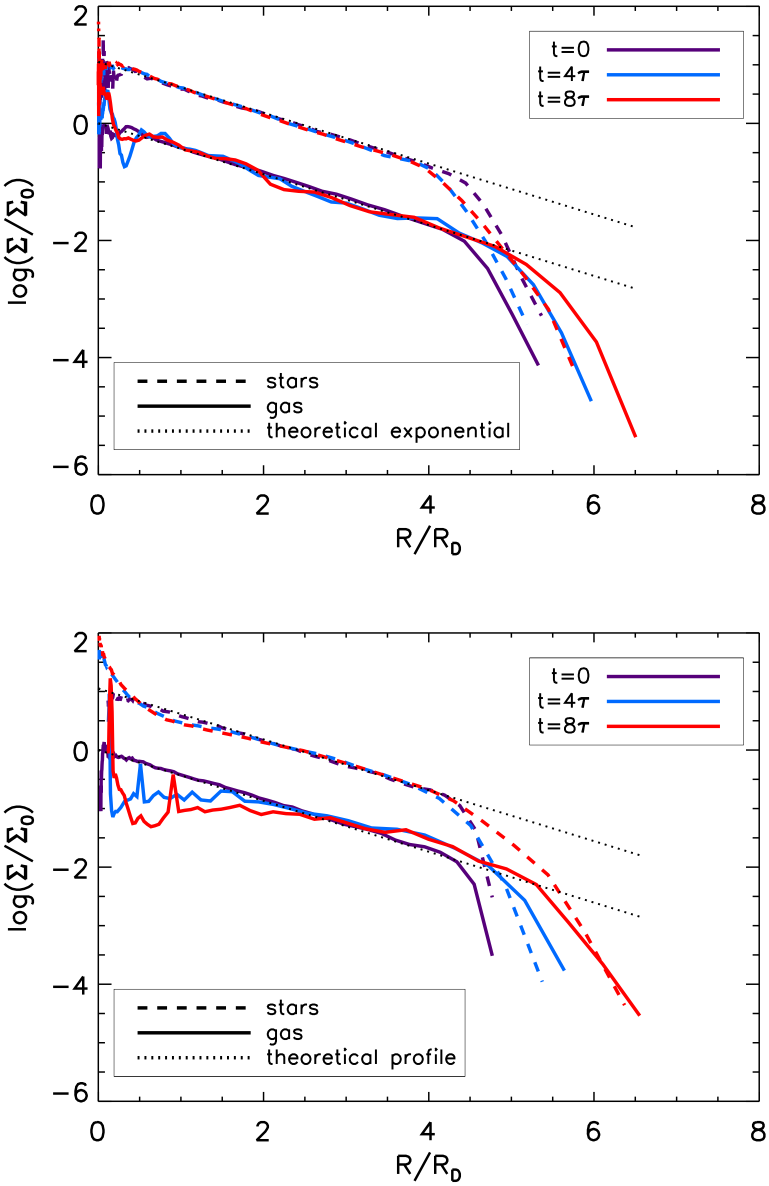

Figure 3.2: Gas (solid line) and stellar (dashed line) surface density profiles for the initial condition, and at $t = 4\tau$ and $t = 8\tau$. The upper panel corresponds to Model A, and the lower panel to Model B.

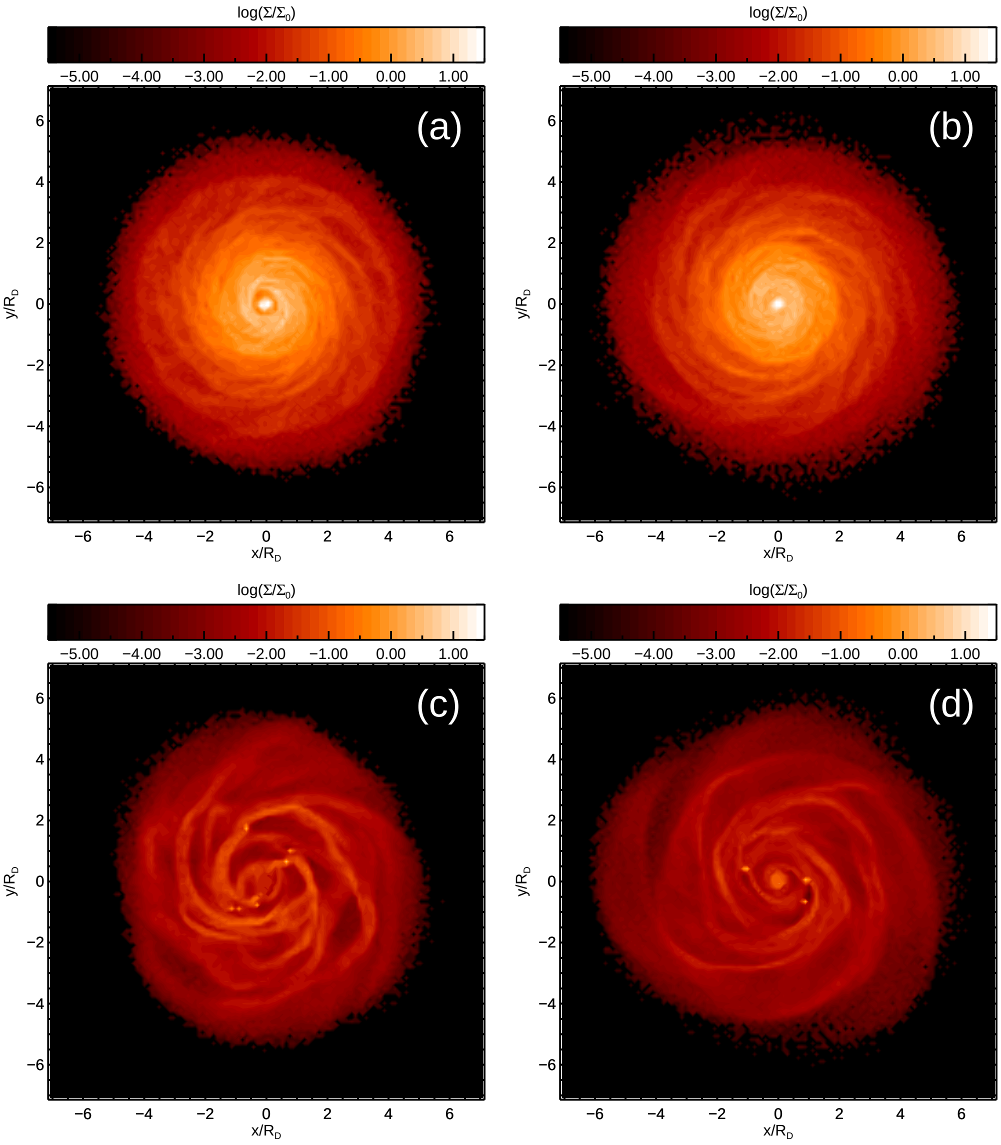

Figure 3.3: Gas surface density maps for Model A at 4τ (a) and 8τ (b), and for Model B (c) and (d) at the same times.

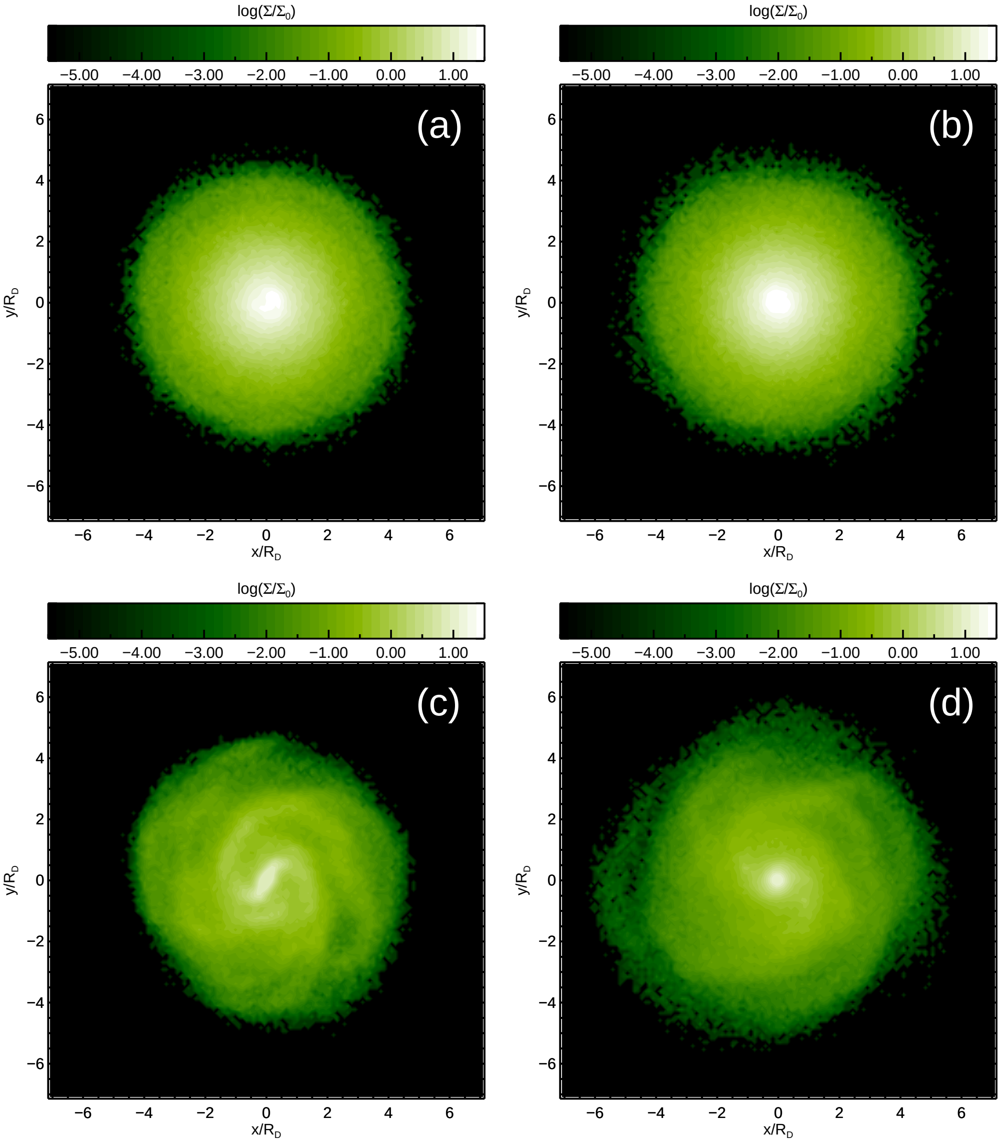

Figure 3.4: Stellar surface density maps for Model A at 4τ (a) and 8τ (b), and for Model B (c) and (d) at the same times.

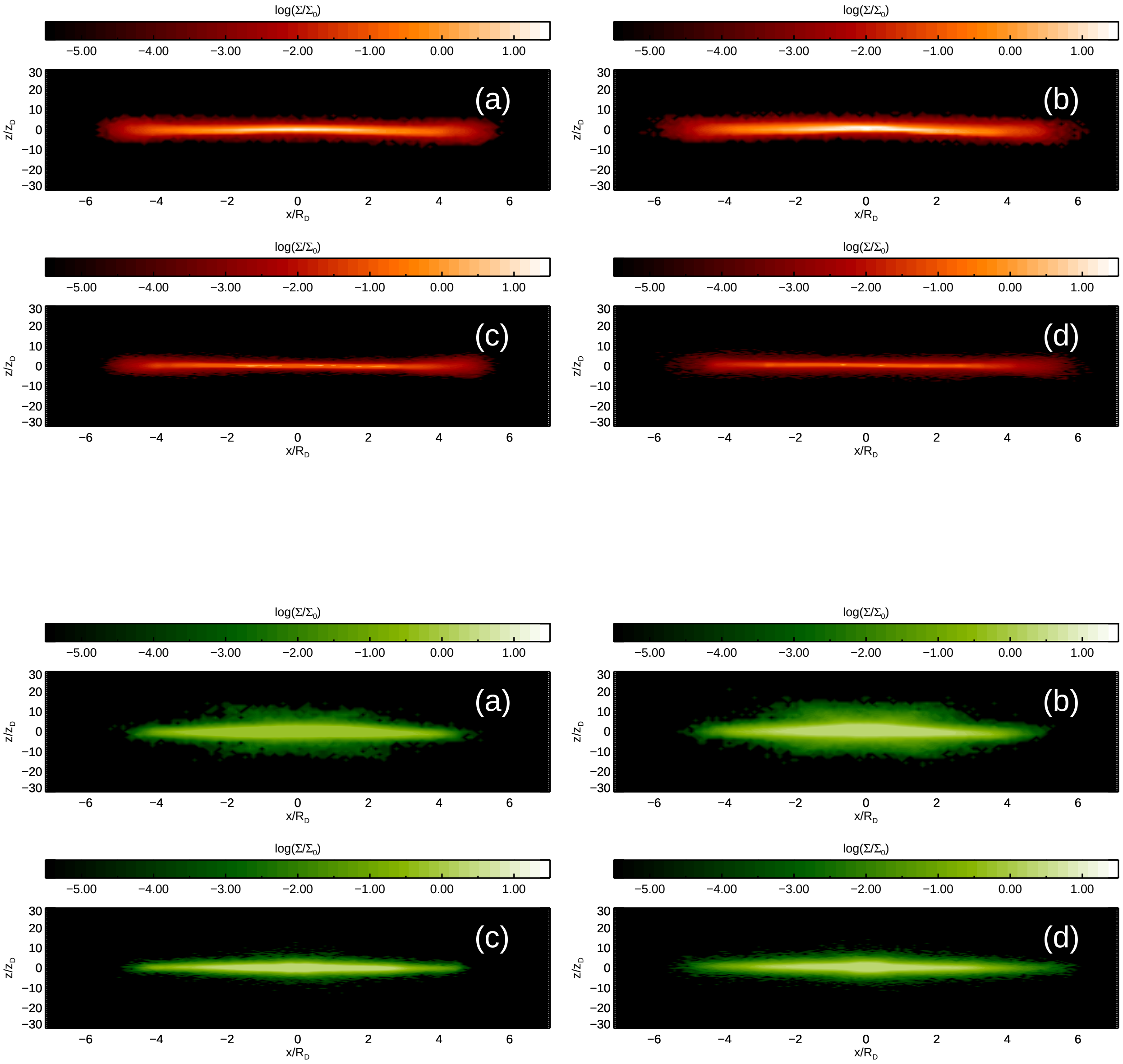

Figure 3.5: In the four upper panels, gas surface density maps in the vertical direction for Model A at 4τ (a) and 8τ (b), and for Model B (c) and (d) at the same times. In the four lower panels, stellar surface density maps in the vertical direction for Model A at 4τ (a) and 8τ (b), and for Model B (c) and (d) at the same times.

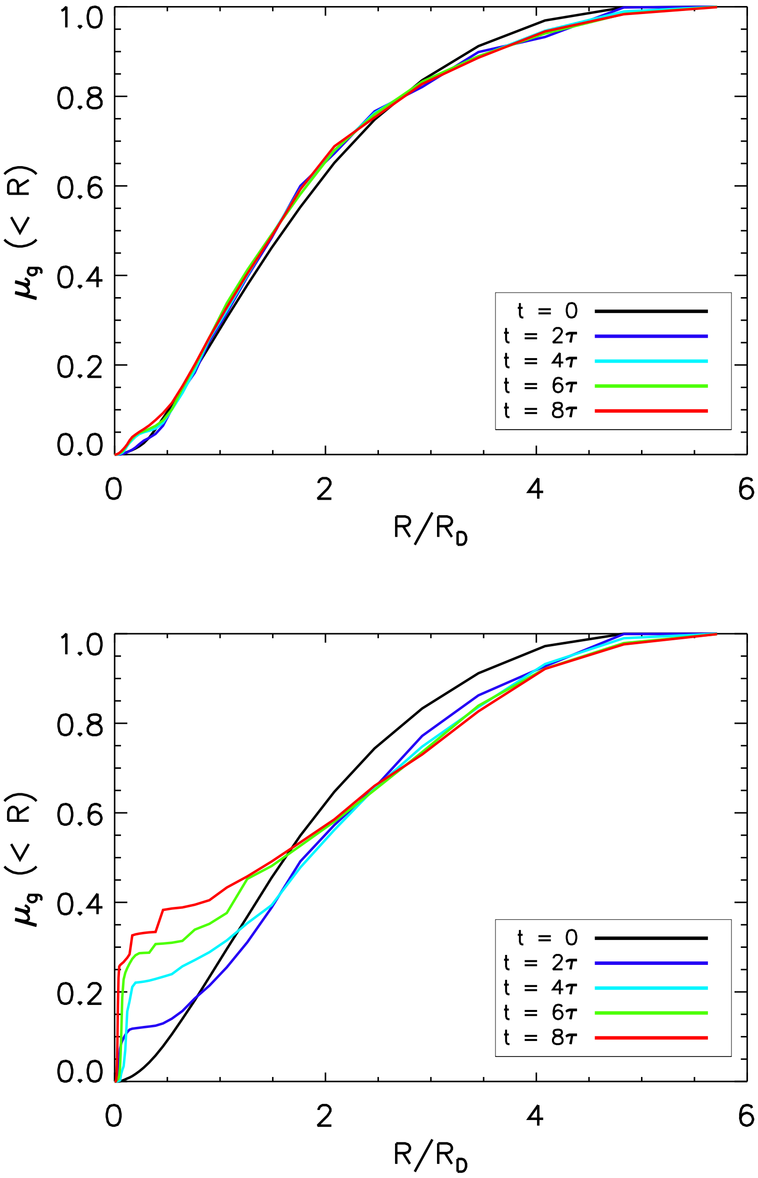

Figure 3.6: Integrated gas mass fraction at several times for Model A (upper panel) and Model B (lower panel).

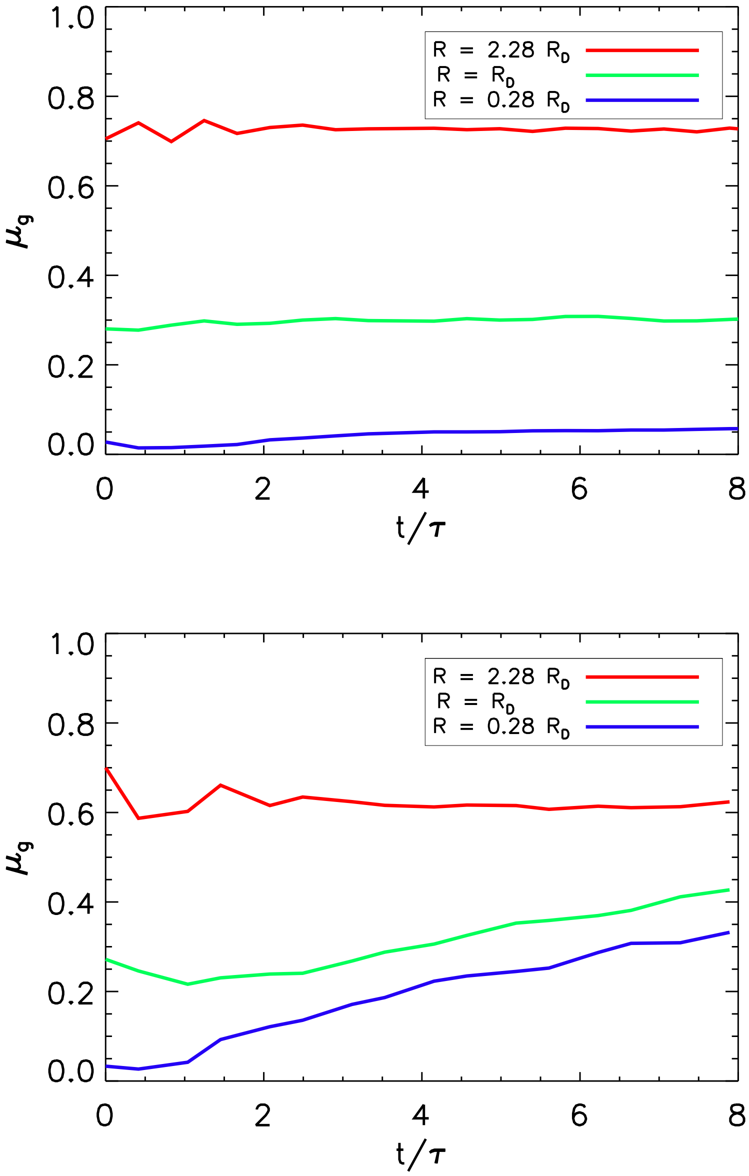

Figure 3.7: The integrated gas mass fraction at $R = 0.28R_D$ (blue line), R_D (green line), and $2.28R_D$ (red line) for Model A (upper panel) and Model B (lower panel).

3.3.3. Artificial Viscostiy Tests with the Barred Galaxy Model

The artificial viscosity used in the SPH formulation of §2.3.4 is consistent with the conservation of momentum . However, some spurious numerical effects may appear, specially in zones where there are high density contrasts. In order to explore to what extent the value of the α parameter affects the evolution of the gaseous component, Model B is tested using values of $\alpha = 0.00,\ 0.25,\ 0.50,\ 0.75$. Figure 3.8 shows the final radial gas surface density profiles, and figure 3.9 shows plots of the enclosed mass fraction of gas $\mu_g(< R)$ at the three fixed radii as a function of time.

The four final radial surface density profiles show a similar tendency. Although there are different fluctuations in each profile, specially at the inner regions, the general behaviour of the profile is similar. This shows that the effect of changing the artificial viscosity is not readily visible in the radial density profiles. However, given the statistical nature of N-body simulations, further tests should be performed with different random samplings of the initial conditions in order to obtain reasonable statistics. Additionally, in order to interpret gas density profiles, the effect of using a finite number of SPH particles to sample the gas should also be taken into account.

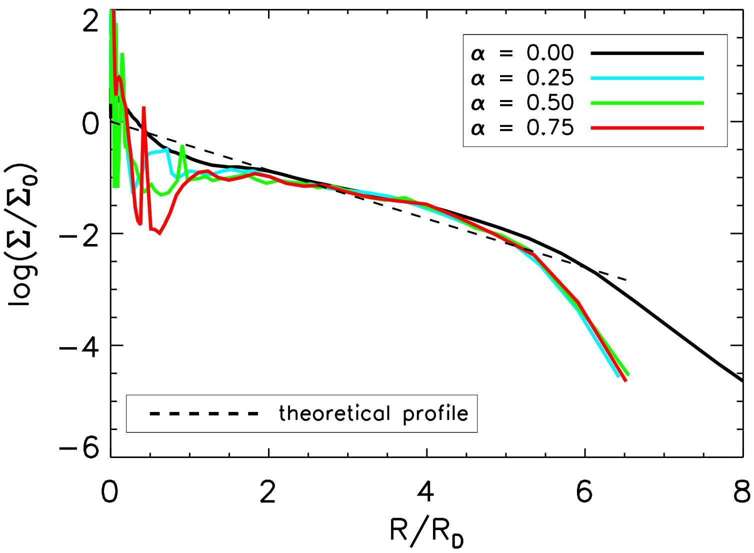

Figure 3.8: The radial gas surface density profiles for simulations of Model B in isolated evolution using different artificial viscosity values are plotted for $t = 8\tau$.

The plots of $\mu(R)$ in Figure 3.9 show that there is an important difference between setting the artificial viscosity to a value $\alpha > 0$, and setting it as $\alpha = 0$. For the latter case, a certain inflow of gas is produced due to the formation of the bar, but it quickly decreases. The mass distribution appears to be quite stable for the rest of the simulation. However, when a value of $\alpha > 0$ is chosen, there is a significant difference with respect to the case with no viscosity. After the initial period of relaxation and formation of the bar, a stable inflow of gas is maintained at $R \approx 0.3R_D$ and at $R \approx R_D$, which is consistent with other studies of flows around bars (e. g. Athanassoula 1994). Figure 3.9 shows that, when $\alpha = 0.25$, flows at $R \approx 0.3R_D$ and at $R \approx R_D$ decrease after $\approx 6\tau$ orbital periods. For higher viscosity values, the $\alpha = 0.75$ simulation shows a slightly higher mass fraction at $R \approx 0.3R_D$ than that of the other simulations. However, at higher radii, the change between the simulation with $\alpha = 0.5$ and the one with 0.75 is unnoticeable. There are no significant differences in the integrated mass fraction at $R = 2.28R_D$ for the three simulations with $\alpha > 0$.

Appropriate values of artificial viscosity should be chosen when strong shocks are present in the flow. Notwithstanding, given the resolution and amount of tracer particles used in these simulations, shocks may not be adequately resolved at small scales, in addition to the fact that SPH is not a good method to follow shocks in detail. However, since the focus of the present work is to study large scale motions of gas, these tests show that the value of α does not have a strong effect as long as it is > 0. Based on these results and that suggested α values in the SPH literature are around $0.5 - 1.0$, a value of $\alpha = 0.5$ is chosen for the simulations including the infalling satellite.

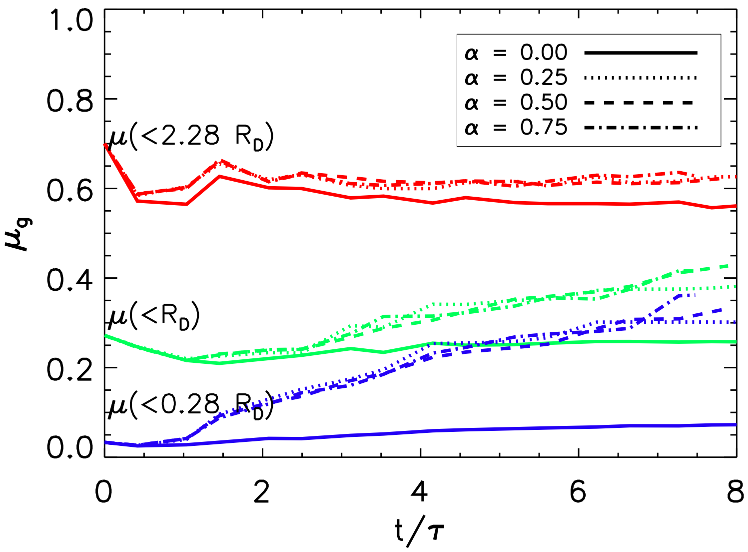

Figure 3.9: The value of $\mu(> R)$ as a function of time is plotted for simulations of Model B using different values of artificial viscosity.

3.4. Satellite Galaxy Models

3.4.1. Overview of the studies and modelling of dwarf galaxies

The study of the density profiles of dwarf galaxies is difficult from an observational point of view due to the low surface brightness of these objects, which limits the study to nearby objects as, for example, the satellites of the Milky Way, and other objects in the Local Group. Small systems such as dwarf spheroidal (dSph) galaxies contain small amounts of stars and gas, and kinematic measurements suggest that these are dominated by dark matter. The density profile of this component can be inferred from fitting models to the kinematic properties, making it an important point of comparison with predictions of cosmological models (e. g Mo et al. 2010, Sparke & Gallagher 2007). Cosmological simulations consistent with the ΛCDM scenario by Navarro et al. (1996) find that dark matter haloes follow a density profile with a cuspy profile. Simulations by Fukushige & Makino (1997) find that $\rho \propto r^{-2}$, and Moore et al. (1998) find $\rho \propto r^{-1.4}$, supporting the cuspy profile model. On the other hand, simulations by Springel et al. (2008) and Navarro et al. (2010), show that the density profile of dark matter haloes is better represented by a Einasto profile, which is shallower than the NFW profile.

Although most observational studies have been restricted to members of the Local Group, many have been able to infer some properties of the density profiles through the analysis of the kinematics. Swaters et al. (2003) used spectroscopic observations of a sample of 15 dwarf galaxies to obtain their rotation curves, and infer the dark matter distribution from best-fit models. About 75% is consistent with cuspy ΛCDM haloes, and only 25 % of the sample is inconsistent with cuspy NFW profile. The study shows that for an inner density profile given by $\rho \propto r^{-\alpha}$, the parameter α is in the range between 0 and 1. The study concludes that most of the galaxies in the sample are better fitted by haloes with shallow or constant density core profiles.

Gentile et al. (2005) studied the particular case of galaxy DDO 47 as it has good HI observations, and it has a very regular velocity field. They obtained the rotation curve, and they infer a dark matter density fitted by the cored Burkert (1995) model, given by

$$\rho(r) = \frac{\rho_0}{(1 + r/r_0)\,(1 + (r/r_0)^2)}\,, \tag{3.38}$$

where ρ_0 is the central density, and r_0 is the core radius.

A study by de Blok et al. (2008) obtains the rotation curves of 19 galaxies from the HI Nearby Galaxy Survey (THINGS). The study concludes that for more massive disc-dominated galaxies, both cusp and core models fit adequately the observations. However, for low-mass galaxies, it is found that a core-dominated halo is preferred over a cusp-like halo. The work of Battaglia et al. (2008) obtains kinematic data of the Sculptor dSph galaxy from spectroscopic observations. A cored halo model, with a core radius of 0.5 kpc and $M(< 1.8\text{kpc}) = (3.4 \pm 0.7) \times 10^8 M_\odot$ fits well the kinematics. A NFW profile also provides a reasonable fit with $M(< 1.8\text{kpc}) = (2.2^{1.0}_{-0.7}) \times 10^8 M_\odot$, and a concentration of $c = 20$. However, it poorly fits the data when a metal-rich stellar population is included.

Walker & Peñarrubia (2011) developed a method to obtain the logarithmic slope $\Gamma = \mathrm{d}\log M(r)/\mathrm{d}\log r$ of the integrated mass function $M(r)$. Using observations from the Magellan/Clay Telescope at Las Campanas Observatory with the MMFS instrument, they find for the Fornax and Sculptor dSph galaxies slopes of $\Gamma = 2.61^{0.43}_{-0.77}$ and $\Gamma = 2.95^{0.51}_{-0.93}$, respectively. This results are indicative of density profiles with a core.

On the other hand, Breddels & Helmi (2013) test if NFW and Einasto profiles can fit the dark matter profiles inferred for the Fornax, Sculptor, Coma, and Sextans dSph galaxies, and conclude that no particular model is significantly preferred. The four galaxies are consistent with either a NFW, a Einasto, or a cored profile. It was found that Sextans shows a slight preference for cored models. However, a recent study by Adams et al. (2014) fits the derived profiles of dSphs in the Local Group to a density profile of the form

$$\rho(r) = \frac{\rho_0}{(r/r_s)^\gamma \left[1 + r/r_s\right]^{3-\gamma}} \,. \tag{3.39}$$

The study finds an average $\gamma = 0.67 \pm 0.10$, which is shallower than the NFW profile ($\gamma = 1$). Although there is still some debate on whether the dwarf satellites have core-like or cuspy density profiles, several observational studies support a core model.

From a theoretical point of view, the works of Kazantzidis et al. (2008) and Kazantzidis et al. (2009) find from cosmological simulations that substructures in the mass range of $M \approx 10^{10} M_\odot$ have a density profile similar to the Hernquist model. This profile has an inner slope equal to a NFW profile $\gamma = 1$, but the outer slope is 4, thus falling more rapidly with distance. Lokas et al. (2010) study the final stellar properties of dwarf spheroidal galaxies produced by the morphological transformation induced by the tidal interaction of a discy dwarf on an eccentric orbit around a galaxy similar to the Milky Way. They conclude that the more evolved systems are prolate spheroids with little rotation, and that the final density distribution of stars can be modelled by a simple modification of the Plummer profile. A recent work by Vera-Ciro et al. (2013) analyses the substructure of around Milky Way-type haloes in the Aquarius simulation and concludes that their density profiles are more consistent with an Einasto profile than a NFW.

3.4.2. Model Satellites

For the present work, a Plummer profile (e. g. Plummer 1911) is chosen for the model satellites. This is motivated by the fact that it has a mass converging to a finite value as $r \to \infty$, and It has a cored density profile. This property is consistent with the inferred properties of dwarf satellites described previously. It has a density profile given by:

$$\rho(r) = \frac{\rho_0}{(1 + (r/a)^2)^{5/2}}\,, \tag{3.40}$$

where $\rho_0 = 3M/(4\pi a^3)$ is the central density, a is the scale radius. The N-body models are constructed with the `mkplummer` tool provided in the NEMO package (Teuben 1995). The initial positions are obtained from sampling the density profile, and the initial velocities are generated by sampling the distribution function. It is assumed that the density and velocity distributions are isotropic, so the distribution function can be written in the form (e. g. Binney & Tremaine 2008):

$$f(\mathcal{E}) \propto \mathcal{E}^{7/2}\,, \tag{3.41}$$

where $\mathcal{E} = \Psi - \frac{1}{2}v^2$, $\Psi = -\Phi$, where Φ is the gravitational potential, and v is the velocity. This distribution function can be derived using the Eddington inversion equation. For a detailed derivation, refer to Binney & Tremaine (2008); and for a detailed derivation using the Plummer profile, see Hut & Makino (2009). Two models are constructed with masses of $M = 6 \times 10^9 M_\odot$ and $M = 1.2 \times 10^{10} M_\odot$, from this point onwards, named Satellite 1 and Satellite 2, respectively.

The central density of the satellite is chosen such that the average density within the half-mass radius of the satellite is comparable to the average density of the central regions of the disc. For a Plummer sphere, the half-mass radius is $R_{1/2} \approx 1.305a$. Therefore, the average density within a volume surrounded by this radius is:

$$\rho_{sat} = \frac{1/2\, M_s}{4/3\pi R^3_{S_{1/2}}} = \frac{3M_s}{8\pi R^3_{S_{1/2}}}\,, \tag{3.42}$$

where ρ_{sat} is the average density, M_s is the mass, $R_{S_{1/2}}$ is the half-mass radius of the satellite.

The average density of the disc can be defined as:

$$\bar{\rho}_D = \frac{M(< R)}{\Delta V}\,, \tag{3.43}$$

where $M(< R)$ is the mass integrated up to a given radius, and ΔV is a cylinder of radius R and height h enclosing that area. For the present work, the mass up to the half-mass radius of the disc $R_{D_{1/2}}$ is considered. For an exponential density profile, $R_{D_{1/2}} \approx 1.678 R_D$, where R_D is the disc scale length. To define the volume of the cylinder a height of $h = 2z_D$ is assumed, meaning that only mass between $-z_D$ and z_D is considered. This is warranted by the fact that at z_d the density has fallen to ≈ 0.4 of the central value. Thus, the average disc density can be approximated by:

$$\bar{\rho}_D \approx \frac{1/2\, M_D}{2\pi R_{D_{1/2}}^2\, z_D} \approx \frac{M_D}{4\pi R_{D_{1/2}}^2\, z_D}\,. \tag{3.44}$$

By combining ρ_{sat} and $\bar{\rho}_D$, a relation for the scale radius of the satellite in terms of the average disc density is obtained:

$$\frac{3M_s}{8\pi R_{S_{1/2}}^3} = \bar{\rho}_D\,, \tag{3.45}$$

then, solving for $R_{S_{1/2}}$ gives

$$R_{S_{1/2}} = \left(\frac{3M_s}{8\pi\bar{\rho}_D}\right)^{1/3}\,. \tag{3.46}$$

For a Plummer sphere, $R_{S_{1/2}} = 1.305a$, and substituting in the equation above gives

$$a \approx 0.377 \left(\frac{M_s}{\bar{\rho}_D}\right)^{1/3}\,, \tag{3.47}$$

For a satellite with $M_s = 6 \times 10^9 M_\odot$ (Satellite 1) this relation gives a scale radius of $a \approx 1.0$ kpc, and $M_s = 1.2 \times 10^{10} M_\odot$ (Satellite 2) gives $a \approx 1.3$ kpc. These values are used to generate the N-body representations used in the present work. The number of particles used is $N_s = 72000$. The softening length of the satellite is set equal to that of the non-collisional particles of the disc, which is 0.035 kpc. The properties of the satellites are summarised in Table 3.2.

Table 3.2: Satellite Properties

Satellite	M [5]	a (kpc)	ϵ (kpc)
1	0.6	1.0	0.035
2	1.2	1.3	0.035

---

[5] Masses have been scaled to code units: $10^{10} M_\odot$

Tests of a Model Satellite with Gas

Several observational studies show that dSph have a low gas content. Cosmological simulations by Sawala et al. (2012), study to what extent subhaloes capable of hosting dwarf galaxies retain a certain fraction of gas at the present epoch ($z = 0$). They conclude that satellites with a mass $M > 6 \times 10^9 M_\odot$ can retain a fraction of gas in the range of a $1 - 10\%$. Other simulations such as those by Revaz et al. (2009) also include a gaseous component in modelling the chemical evolution of spheroidal galaxies. As some dwarf galaxies may retain a small fraction of gas, this motivates the use of a model satellite including a gaseous component in studies of their interaction with other galaxies.

Common approximations for the gaseous component are to assume that either it is in virial equilibrium (e. g. Revaz et al. 2009) or in hydrostatic balance. In the first case, an order of magnitude of the gas temperature can be obtained assuming that the thermal energy is comparable to the gravitational potential energy of the system. Assuming that the gas is neutral hydrogen, this means that

$$\frac{GM}{a} \approx \frac{3}{2}\frac{k_B T}{m_\mathrm{H}}\,, \tag{3.48}$$

where G is the gravitational constant, M is the total mass of the system, a is the scale radius of the system, k_B is the Boltzmann constant, T is the temperature, and m_H is the hydrogen mass. For a satellite with $M = 6 \times 10^9 M_\odot$ (it is assumed that the gas fraction is in the order of a few percent, thus the mass of the satellite is dominated by its collisionless components: stars and dark matter), and a scale radius of $a = 1$ kpc, equation (3.48) yields $T \approx 2 \times 10^6$ K, which may be rather unrealistic for a dSph galaxy. Revaz et al. (2009) find, for model galaxies with pseudo-isothermal profiles and masses in the range $M \sim 10^8 M_\odot$, a virial temperature $T \sim 10^5 - 10^6$ K.

A more general approach is to derive the required gas density profile from the hydrostatic balance equation and the Poisson equation. This allows to specify the temperature of the system with more freedom. The total density of the galaxy is $\rho_t = \rho_{nc} + \rho_{gas}$, where ρ_{nc} corresponds to a collisonless component, and ρ_{gas} is the gas density. Then, the Poisson equation becomes

$$\nabla^2 \Phi = 4\pi G(\rho_{nc} + \rho_{gas})\,, \tag{3.49}$$

where Φ is the total potential of the system. Because the system is spherically symmetric, it can be expressed as

$$\frac{1}{r^2}\frac{\mathrm{d}}{\mathrm{d}r}\left(r^2 \frac{\mathrm{d}\Phi}{\mathrm{d}r}\right) = 4\pi G(\rho_{nc} + \rho_{gas})\,. \tag{3.50}$$

Assuming an isothermal gas $P = \rho c_s^2$, and that the system does not have a temperature profile $T(r)$, the hydrostatic balance equation for this spherically symmetric system is

$$\frac{\mathrm{d}\Phi}{\mathrm{d}r} = -\frac{c_s^2}{\rho_{gas}}\frac{\mathrm{d}\rho_{gas}}{\mathrm{d}r}\,. \tag{3.51}$$

The problem to be solved is to find the gas density profile that satisfies hydrostatic equilibrium within a spherical distribution of collisionless particles. In this case, ρ_{nc} is not an unknown variable, and it is assumed to follow a Plummer profile. Therefore, equations (3.50) and (3.51) form a system of equations where the unknowns are the total potential Φ, and ρ_{gas}.

The hydrostatic balance is then easily integrated to:

$$\rho_{gas} = \rho_{0\,gas} e^{-(\Phi(r)-\Phi(0))/c_s^2}\,. \tag{3.52}$$

Substituting this in the Poisson equation then yields:

$$\frac{1}{r^2}\frac{\mathrm{d}}{\mathrm{d}r}\left(r^2\frac{\mathrm{d}\Phi}{\mathrm{d}r}\right) = 4\pi G(\rho_{nc} + \rho_{0gas} e^{-(\Phi-\Phi(0))/c_s^2})\,. \tag{3.53}$$

This is a non-linear second order ordinary differential equation where the solution is the potential function $\Phi(r)$. The solution must satisfy $d\Phi/dr(0) = 0$ as the force at the centre of a spherical mass distribution is zero. The value $\Phi(0)$ can be set to any numerical value because adding a constant to the potential does not change the form of the potential. What affects the gas distribution is the potential depth $\Delta\Phi = \Phi(r) - \Phi(0)$ that appears in equation (3.52).

As $r \to \infty$, $\Delta\Phi$ is finite, corresponding to the potential depth of the gas and the non-collisional component. This implies that $\rho(r \to \infty)$ has a constant value, and the resulting gas profile has to be truncated for the total mass to converge. This constant density at large radii may be interpreted in the context of an isothermal gas in thermodynamic equilibrium (e. g. isothermal atmospheres). Because the gas has constant temperature at all radii, it has the same specific internal energy at all points, and its constituent atoms have the same velocity distribution. Then, at larger radii, more atoms have enough energy to escape from the system. Additionally, at infinity $d\Phi/dr = 0$, thus a constant density background satisfies hydrostatic equilibrium.

This isothermal model is a simple approximation. The equation (3.53) can be expanded to

$$\frac{\mathrm{d}^2\Phi}{\mathrm{d}r^2} + \frac{2}{r}\frac{\mathrm{d}\Phi}{\mathrm{d}r} = 4\pi G(\rho_{nc} + \rho_{0gas} e^{-(\Phi-\Phi(0))/c_s^2})\,. \tag{3.54}$$

which has a singularity at $r = 0$ in the second term. For a physical solution, the density has a maximum at $r = 0$, and the potential has a minimum at this point due to the condition

$d\Phi/dr(0) = 0$.

The system of equations can also be combined to obtain in terms of density:

$$\frac{\mathrm{d}^2\rho_{gas}}{\mathrm{d}r^2} + \left(\frac{2}{r} - \frac{1}{\rho_{gas}}\frac{\partial\rho_{gas}}{\partial r}\right)\frac{\partial\rho_{gas}}{\partial r} + \frac{4\pi G}{c_s^2}(\rho_{gas}^2 + \rho_{nc}\rho_{gas}) = 0\,, \tag{3.55}$$

This equation also presents a singularity at $r = 0$. Either way, this example shows that trying to include a gaseous component is not an easy task. A solution could be obtained using a power series method or a numerical method that takes care of the $\frac{1}{r}$ coefficient. However, as it will be shown in the following paragraphs, neglecting the self-gravity of the gas, and solving the hydrostatic equilibrium equation assuming that the gas settles in a Plummer potential yields a rather compact gas density profile. This approximate solution allows to derive some properties of the gas distribution in a quantitative way.

By substituting the Plummer potential

$$\Phi(r) = -\frac{GM}{a}\frac{1}{(1 + (r/a)^2)^{1/2}}\,, \tag{3.56}$$

where M is the mass of the object, and a is the scale radius, in equation (3.51), it can be shown that

$$\int_{\rho_g(0)}^{\rho_g(r)} \frac{d\rho_g}{\rho_g} = \frac{1}{c_s^2}\frac{GM}{a}\int_0^r \frac{(r/a)}{\left(1 + (r/a)^2\right)^{3/2}}\mathrm{d}r\,. \tag{3.57}$$

Integration leads to the density profile

$$\rho(r) = \rho(0)\exp\left[\frac{1}{c_s^2}\frac{GM}{a}\left(1 - \frac{1}{\left(1 + (r/a)^2\right)^{1/2}}\right)\right] \tag{3.58}$$

where c_s is the isothermal sound speed. This approximation is valid for systems with very low gas mass fractions, where the potential of the system is dominated by the dark matter and stellar components. The derived profile as well as the Plummer density profile are shown in Figure 3.10 for several gas temperatures. The gas density was calculated assuming that the satellite has $M = 6.0 \times 10^9 M_\odot$, a scale radius $a = 1.0$ kpc. Profiles with temperatures $T = 10^4, 10^5$, and 10^6 K are plotted. Figure 3.10 shows that, when using an isothermal equation of state, very compact density profiles can result at low temperatures. The scale radius R_g of this profiles can be estimated by finding from equation (3.58) the radius at which the density has fallen by a factor $1/e$. After some algebraic manipulation, it can be shown that this radius is:

$$R_g = a\sqrt{\frac{q}{1-q}} \tag{3.59}$$

where $q = c_s^2(a/GM)$. For $T = 10^4$ K, $R_g = 0.057$ kpc, for $T = 10^5$ K, $R_g = 0.182$ kpc, and for $T = 10^6$ K, $R_G = 0.686$ kpc with the mass and scale radius used above. Simulating such systems would require softening lengths several factors smaller than these values.

The solution with $T = 10^6$ K shows a profile that is rather unrealistic for a galaxy. The constant density behaviour at large radii in the solution to the system of equations described above is a consequence of using an isothermal temperature profile. In this approximation, the self-gravity of the gas has been neglected, so the potential energy of the system is dominated by the non-gaseous components. This is the temperature in which the internal energy of the gas is comparable to the potential energy of the system, according to the estimation of equation (3.48).

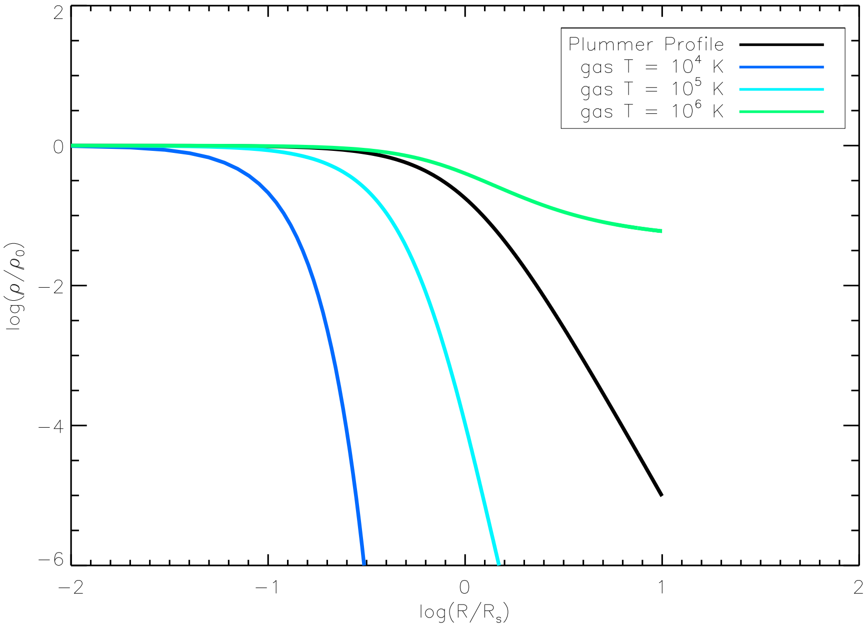

Figure 3.10: Analytic gas density profiles for an isothermal gas with $T = 10^4$ K (blue line), 10^5 K (light blue line), and 10^6 K (green line) in hydrostatic balance within a Plummer potential with $M = 6.0 \times 10^9 M_\odot$ and $a \approx 1.0$ kpc. The black line corresponds to the Plumer density profile for the same mass and scale radius parameters.

Some numerical tests have been performed distributing gas and a collisionless component following an initial Plummer profile with the collisionless component having a mass of $M = 6.0 \times 10^9 M_\odot$, and a scale radius of $a \approx 1.0$ kpc. The gas is allowed to relax in the potential of the system. Two gas fractions were tested: 1 and 10%. Preliminary tests were performed with 20000 collisionless particles, and 20000 gas particles in GADGET-2. The gas quickly settles in a very compact region in approximately 0.3 Gyr. After this time, the simulation required very small time steps $\Delta t \sim 10^2 - 10^3$ yr, making the integration costly in terms of computational time. The results are shown in Figures 3.11 and 3.12. This number of particles may be more prone to be affected by relaxation effects. However, similar tests with 72000 particles in each component showed no significant improvement.

Another test was performed using a pseudo-isothermal profile using 72000 collisionless particles and 72000 gas particles. The collisionless profile was generated using the `mkhalo` procedure in NEMO (Teuben 1995). The gas was distributed following a similar profile and allowed to relax in this potential. The use of this profile was motivated by its smaller slope, which allows for a more extended gas distribution. It is noted that a similar profile was used in Revaz et al. (2009) in a study of dwarf galaxies. The mass and scale radius are the same as those for the Plummer test. In this simulations, the gas concentrates at the central region, but it is relatively stable for about 700 Myr. The initial and final density profiles are shown in Figure 3.13. Although a dense core forms, the plot shows that more gas is present at distances up to a scale radius. In this case, the core is not as dense as that formed in the simulations using a Plummer potential. Nevertheless, due to the dense central region, small time steps are required to follow the central region adequately.

Because of the difficulties presented in initialising a gaseous component in the model dwarf galaxy, having a constant temperature profile and an isothermal equation of state, only collisionless models will be used. The gas distributions derived may not be representative of a dwarf satellite, and require additional computational time to follow the dynamics of the central parts of the satellite adequately. These models could be improved by including a temperature profile $T(r)$ in the hydrostatic balance equation. However, this complicates the model as it is necessary to specify a temperature profile to initialise satellite in addition to the density profile. Another option is to use a different equation of state, but this would also change the host galaxy models. [6]

---

[6] The author is grateful to Y. Revaz, P. Jablonka, and V. Springel for stimulating discussions on models of spherical galaxies with a gaseous component.

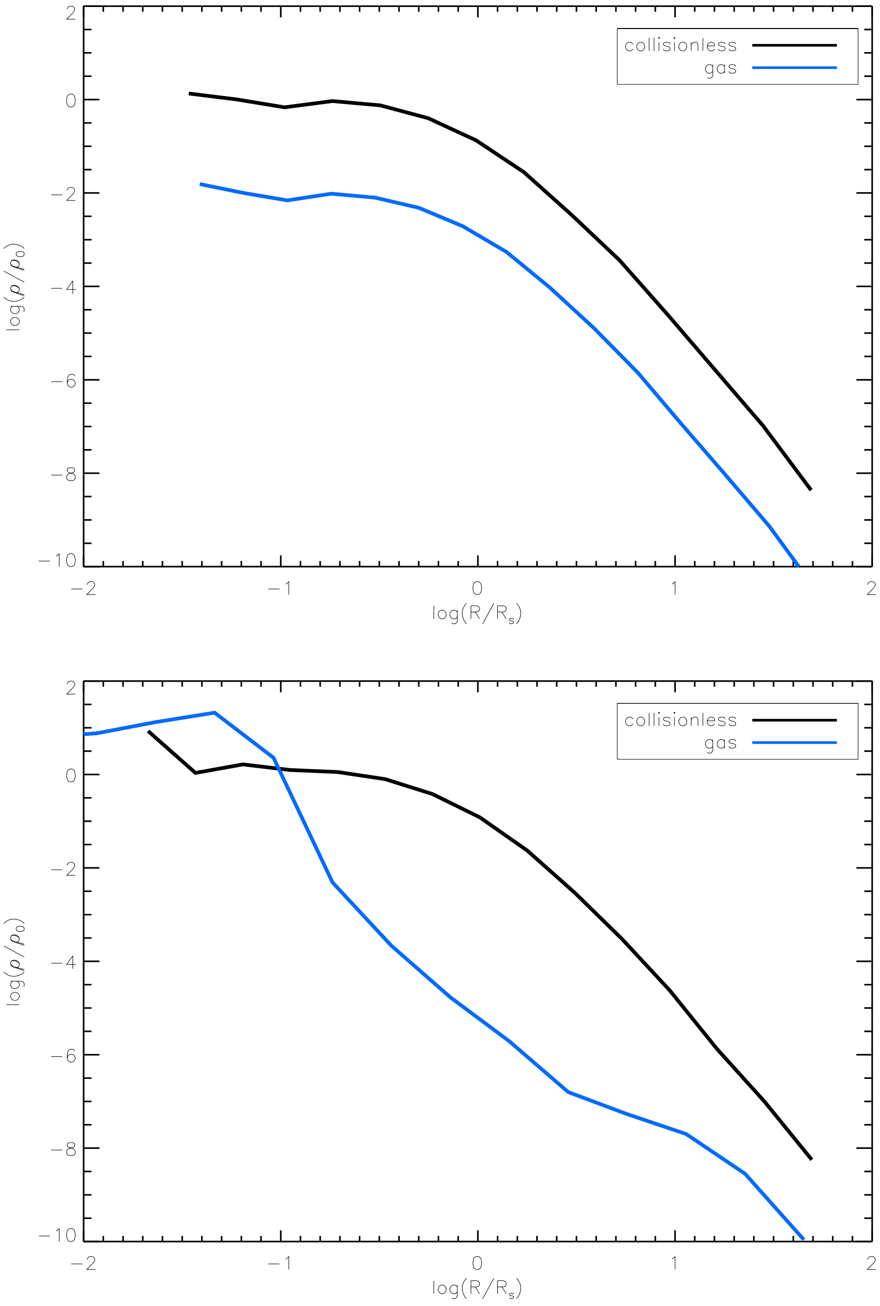

Figure 3.11: The top panel shows the initial gas and collisionless component densities following a Plummer profile. The bottom panel shows the distribution after 0.3 Gyr. The gas fraction is 1% of the satellite's mass.

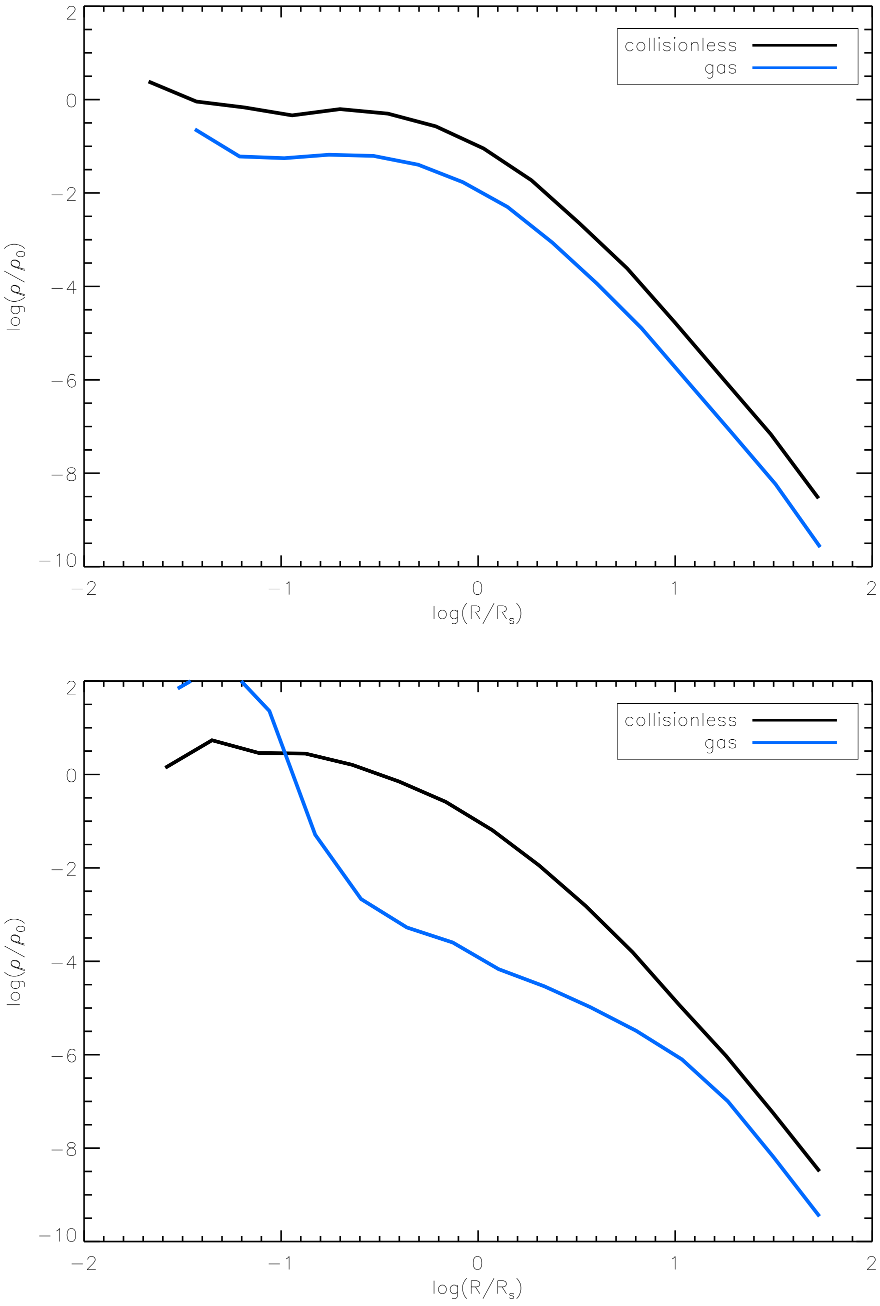

Figure 3.12: The top panel shows the initial gas and collisionless component densities following a Plummer profile. The bottom panel shows the distribution after 0.3 Gyr. The gas fraction is 10% of the satellite's mass.

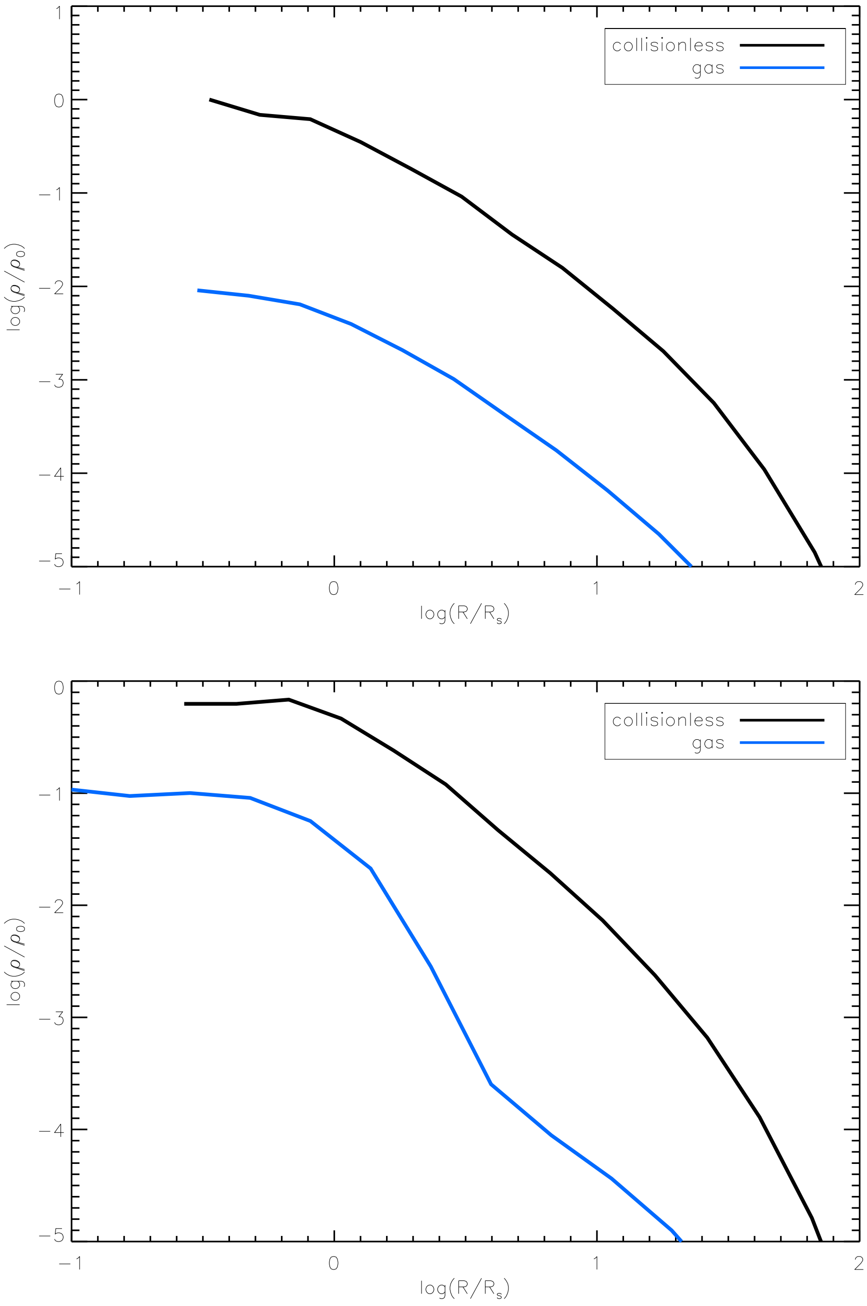

Figure 3.13: The top panel shows the initial gas and collisionless component densities following a pseudo-isothermal profile. The bottom panel shows the distribution after about 700 Myr. The gas fraction is 10% of the satellite's mass.

3.5. Simulations of the Interacting Galaxies

3.5.1. Choice of Orbital Parameters

According to cosmological simulations, there is a distribution for the orbital parameters of infalling satellites; see for example Moore et al. (1999), Benson (2005), Khchfar & Burkert (2006), Wetzel (2011). A detailed analysis of the parameter space would require large amounts of computational time. For this reason, a set of relatively simple orbital configurations is chosen in order to explore the effects of small satellites in the mass ranges described above. In order to study the trends of the dynamical effects of the interaction, some studies choose circular orbits as first approximations (e. g. Mihos & Hernquist 1994, Hernquist & Mihos 1995, Chang 2008). It is expected that dynamical friction can circularise the orbit of an infalling satellite, but the process may be rather slow (e. g. Hashimoto et al. 2003).

Other works have explored more eccentric orbits as in, for example, Bekki & Freeman (2003), Moore et al. (1999), Velazquez & White (1999), and Villalobos & Helmi (2007). Moore et al. (1999) find in cosmological simulations that many satellites fall in an orbit with a pericentre to apocentre ratio of 1:6. Many of these works focus on the dynamical aspects of the interaction of the satellite with a disc galaxy, and its observable consequences in a controlled numerical experiment. Some works such as Kazantzidis et al. (2008) and Kazantzidis et al. (2009) explore orbits derived from cosmological simulations, but still use a controlled set of orbits to explore the dynamical effects on the host.

For the present work, the selected orbits are two circular orbits with initial radii $R_i = 3R_D$ and $R_i = 6R_D$, with an initial inclination $i = 30°$, and a coplanar orbit with pericentre at $R = R_D$. In all cases, both prograde and retrograde orbits are considered. The circular orbits are motivated by the fact that they produce an encounter in which the satellite arrives with a velocity comparable to that of the circular velocity of the disc. Hernquist & Mihos (1995) have explored the case with $R_i = 6R_D$ and $i = 30°$, but only considering the prograde case with a satellite with a slightly larger mass ratio. The present work explores this orbit, but also includes retrograde cases and a smaller initial radii. The coplanar orbit allows the study of an extreme case in which the satellite is disturbing the host galaxy. It is interesting to compare how the prograde case compares with the retrograde case. Retrograde orbits have been relatively unexplored because the slower decay of the orbit requires more computational time to follow the satellite until it reaches the inner disc (e. g. Hernquist & Mihos 1995) and because of their high relative velocity with respect to disc rotation, these are expected to have less damage than prograde orbits.

These orbits have been chosen because they are extreme cases that give a measure of the upper limits of the effects that can be produced in the primary galaxy. Additionally, as these circular orbits have been studied in the previous works, the results obtained in the present work can be compared with previous works. It is noted that the satellites are initialised in orbits quite close to the host galaxy, which may affect the orbital distribution of the orbits of stars in the host and introduce some spurious effects, as mentioned in, for example, Kazantzidis et al. (2008) and Kazantzidis et al. (2009). However, obtaining a distribution function for the disc that considers the presence of the potential of the satellite is not an easy task in terms of the CBE. Some works, such as Kazantzidis et al. (2008) and Kazantzidis et al. (2009) use schemes that adiabatically introduce the potential of the infalling satellite before introducing the N-body representation in a point close to the primary galaxy. However, in such schemes, the mass loss due to stripping by dynamical friction may not be adequately represented.

The approximate paths of the orbits mentioned above are shown in Figure 3.14, 3.15, and 3.16. These are obtained using a fourth order Runge-Kutta method with adaptive time step. The primary galaxy is represented by a NFW dark matter density profile, a Miyamoto-Nagai disc, and a central bulge. The effect of dynamical friction can be included by choosing one of the following schemes: a constant dynamical friction, or it is possible to choose between the adaptive schemes of Hashimoto et al. (2003), and Zentner & Bullock (2003).

Table 3.3: Orbit Initial Conditions

Orbit	x	y	z [7]	v_x	v_y	v_z [8]	i
1	0.0	9.09	5.25	±197.81[9]	0.0	0.0	30°
2	0.0	18.19	10.50	±195.30	0.0	0.0	30°
3	19.40	0.42	0.0	-21.96	±65.55 [10]	0.0	0°

---

[7] Positions are in kpc.

[8] Velocities are in $\mathrm{km\,s^{-1}}$.

[9] Negative velocities are prograde, and positive velocities are retrograde orbits.

[10] The positive velocity is the prograde orbit; the negative is the retrograde orbit.

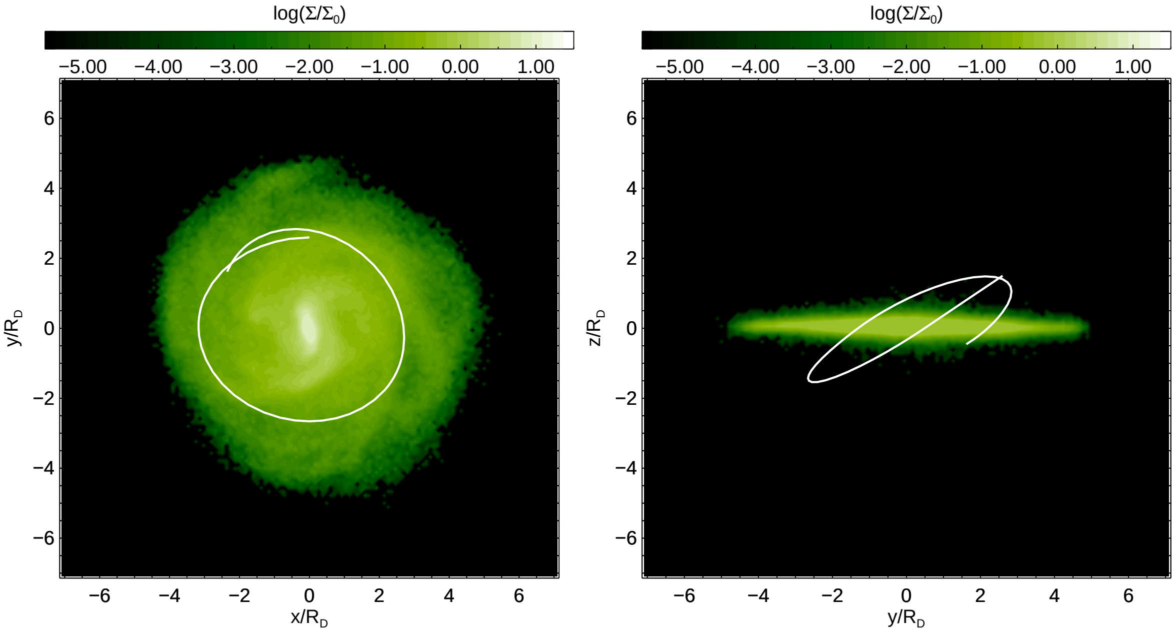

Figure 3.14: Projection of Orbit 1 in the horizontal (left panel) and vertical (right panel) planes.

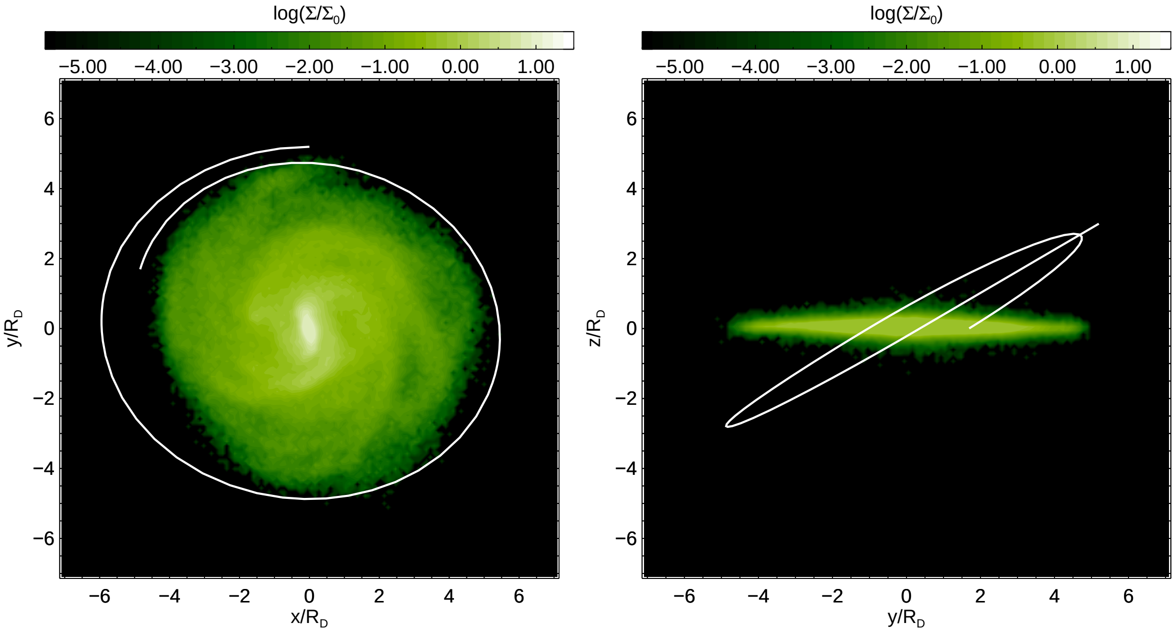

Figure 3.15: Projection of Orbit 2 in the horizontal (left panel) and vertical (right panel) planes.

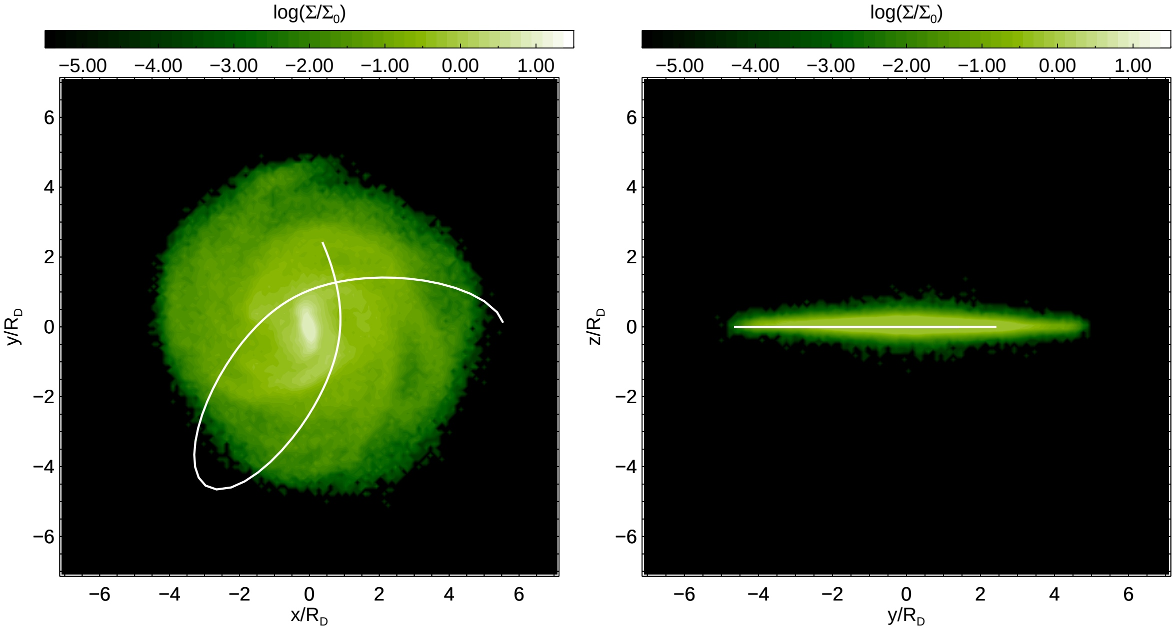

Figure 3.16: Projection of Orbit 3 in the horizontal (left panel) and vertical (right panel) planes.

3.5.2. Summary of Simulation Parameters

For all the simulations performed, the parameters of the Tree code algorithm for the gravitational force calculation in GADGET-2 have been set to the following values: the opening criterion is set at $\theta = 0.7$, and the tolerance parameter in equation (3.3) of §3.1 is set to $\alpha_{force} = 0.005$. The effect of this parameter was tested using one of the model satellites of the previous section, using 72000 particles. The satellite was allowed to evolve for 1 Gyr in isolated evolution. Values of $\alpha = 0.005, 0.0025, 0.001, 0.0001$ were used to measure its effect in terms of the conservation of energy, drift of the centre of mass, and computational time. The results are summarised in Table 3.4. This table shows that reducing α_{force} by a factor of 5 improves energy conservation by $\approx 70\%$, at the cost of almost doubling the computational time. The test with $\alpha_{force} = 0.001$ shows that the error in energy falls by nearly an order of magnitude, but the computational time increases by a factor of $\approx 4.4\%$. In terms of the centre of mass drift, although not shown in Table 3.4, reducing the force tolerance parameter by a factor of 5, reduces drift by $\approx 85\%$. Setting $\alpha_{force} = 0.005$, and reducing the time step in half, does not produce a significant difference in improving conservation of energy or reducing drift, but increases the computational cost by a factor of two.

Due to the large number of particles and the computational time required to repeat the simulations of the model satellite described in the preceding paragraph, it was not possible to repeat such detailed tests with Models A and B. The isolated evolution tests described in §3.3.2 were performed using $\alpha_{force} = 0.005$, and including hydrodynamics with $\alpha_{visc} = 0.5$. In both Models A and B, the drift of the centre of mass was within the 2ϵ limit. For Model A, the magnitude of the displacement was about 50% lower than that of Model B. The larger number of particles of the galaxy $N \approx 2 \times 10^6$ contributes in reducing the relaxation effects that are observed with the tests using the Plummer model, which has only $N = 72000$. These tests were performed with a time step range of $\Delta t = 0.005 - 0.5$, corresponding to $0.024 - 2.35$ Myrs. For Model A, the fractional error in conservation of energy during isolated evolution is $\approx 0.08\%$ both at $t = 4\tau$ and $t = 8\tau$. For Model B, the fractional error is $\approx 0.37\%$ at $t = 4\tau$, and $\approx 0.63\%$ at $t = 8\tau$. For Model A, the computational time was between 3 and 4 days. However, for Model B, this increased to approximately 18 days. Both simulations were performed with 16 CPUs. Due to the number of simulations planned and the number of particles involved, the values of $\alpha_{force} = 0.005$, artificial viscosity $\alpha_{visc} = 0.5$ were chosen.

A total of 12 simulations considering the effect of the satellite are performed per model host galaxy, amounting to 24 simulations. Some preliminary tests have been performed with time step intervals of $\Delta t = 0.07 - 0.5$, and $\Delta t = 0.05 - 0.5$ to see if higher time steps could be used. However, in many cases this results in a conservation of energy fractional error $> 1\%$. A time step range of $\Delta t = 0.01 - 0.5$ was tested. Results show that energy errors are $< 1\%$. With this choice of parameters, computational time is in the range of 20 - 30 days per simulation. The simulations requiring the highest computational times are those of prograde Orbit 2, and of Orbit 3. The minimum time step was chosen as 0.01 and not 0.005 as in the isolated evolution tests. This was motivated by the fact that tests with a Plummer satellite and the galaxy showed that reducing the time step by a factor of two does not produce a significant improvement in energy, but does increase by about a factor of two the computational cost.

The simulations were performed in three different servers: two TYAN-FT48 computers with 48 AMD Opteron 800 MHz CPUs and 256 GB of RAM each; another TYAN-FT48 with 64 AMD Opteron 2.1 Ghz processors and 256 GB of RAM; and a Supermicro AS-2042 with 64 AMD 1.4 GHz CPUs and 128 GB of RAM.

Table 3.4: Force Calculation Error Tests

α_{force}	t_{comp} (s)	$\Delta E(\%)$
0.005	16537.89	0.3
0.0025	22675.31	0.1
0.001	29894.71	0.08
0.0001	73310.34	0.02

Table 3.5: Summary of the Simulation Parameters

Gravitational Force Calculation		Time integration		SPH	
θ	0.7	η	0.01	$N_{neighbours}$	64
α_{force}	0.005	Δt_{min}	0.01	ΔN	± 2
ϵ_h	0.121 kpc	Δt_{max}	0.5	α_{visc}	0.5
ϵ_d	0.035 kpc			$C_{courant}$	0.15
ϵ_g	0.035 kpc				
ϵ_b	0.110 kpc				

Chapter 4

Results

In this chapter, the results of the simulations described in the previous chapter are presented. In §4.1, a qualitative description of the morphological features induced by the interaction of these minor satellites with their host galaxies is given. In §4.2, the resulting gas mass distribution after the interaction is presented. In §4.3, the behaviour as a function of time of the enclosed mass within three fixed radii is presented as a measure of the gas flow rate induced by the interaction.

4.1. Morphological Features

Examples of the morphological features induced by the interacting satellite are shown in this section. To visualise the morphology of the galaxy, surface density maps are calculated in a two-dimensional mesh enclosing the galaxy. The surface density is calculated for every cell by dividing the mass inside the cell by its area. All the figures in this section are presented in the following general scheme: panels (a) and (b) show the isolated and perturbed galaxies, respectively, for Model A; panels (c) and (d) show the same information but for Model B. The approximate position of the satellite is represented by a white dot, which corresponds to the centre of mass of the particles within a sphere that contains initially $\approx 10\%$ of the mass of the satellite. Testing shows that this procedure traces the surviving core of the satellite after some passages as long as it has not been significantly disrupted or accreted.

Figures 4.1 and 4.2 show the resulting density maps at $t = 0.6\tau$ for the gaseous and stellar components, respectively, for the satellite with $M = 0.6$ (Satellite 1) engaging in a prograde encounter following Orbit 1 ($R_i = 3R_D$, $i = 30°$). The snapshots correspond to a time $\approx 0.3\tau$ after the first passage. Figures 4.3 and 4.4 (in pages 111 and 111) correspond to the same time, but for the satellite with $M = 1.2$ (Satellite 2). The satellite with $M = 0.6$ induces the formation of a spiral arm which is evident in Model A, as seen in panel (b) of Figure 4.1

(see page 109). However, this feature is not so apparent in the barred galaxy (panel (d) of the same figure). A slight disturbance is evident in the stellar density maps; see panels (b) and (d) of Figure 4.2 in page 110. In the simulations with the more massive satellite, the arm pattern in the gaseous component appears to be more enhanced in Model A, as shown in in panel (b) of Figure 4.3 in page 111. This feature is also more evident in Model B, shown in panel (d) of the same figure, as compared to the simulation with the less massive satellite. Additionally, the shape of the galaxy has become slightly oval for both models, and the perturbation is more evident in the stellar density map. It is slightly more noticeable for Model B in Figure 4.4 in page 112. Although more snapshots are not included, as the satellite is accreted and the system evolves, a tightly wound spiral pattern remains in the gas at the end of the simulation.

The density maps resulting from the simulation with Satellite 1 having the orbital parameters of Orbit 1 in a retrograde sense are shown in Figures 4.5 and 4.6, in pages 113 and 114, which correspond to $t \approx 1.17\tau$. For Satellite 2, these are shown in Figures 4.7 and 4.8, in pages 115 and 116, respectively, corresponding to $t \approx 1.0\tau$. In the simulations of Model A with Satellite 1, a low-density region forms in the lower side of the gaseous component of the galaxy resembling the shape of a “crescent moon”. This feature is less visible in the stellar component of this model. In the case of the barred galaxy (Model B), this effect is barley visible in the gas density, and a slightly asymmetric spiral arm pattern is seen in the stellar component. In the simulations with Satellite 2, the perturbation is more evident in the gaseous components of both models. The stellar component of Model A now shows a low density region corresponding to the same area where this disturbance occurs in the gas. In the case of Model B, it is possible to see that the low-density region forms in the III quadrant of the image, just below an arm. The overall spiral pattern has been disturbed with respect to that seen in the isolated galaxy. The disc morphology remains perturbed in the remainder of the simulation.

Orbit 2 ($R_i = 6R_D$, $i = 30°$) produces the most noticeable and impressive morphological features. The following description focuses on the features observed slightly after 2.5τ after the beginning of the simulation, which corresponds to the satellite having passed two times through the plane of the disc. The gas and stellar density maps for the simulation with Satellite 1 are shown in Figures 4.9 and 4.10, in pages 117 and 118, respectively. The same maps for the simulation with Satellite 2 are shown in Figures 4.11 and 4.12, in pages 119 and 120, respectively. In the case of the simulation with Satellite 1, a spiral pattern resembling a grand design galaxy is produced in the gaseous component of both Models A and B, with two large tails extending beyond the edge of the original isolated galaxy are produced. In the stellar components, the pattern is more evident in Model B than in Model A. With the more massive satellite, the distribution of gas is significantly disturbed in both model galaxies. However, a spiral pattern is still visible in the stellar component, specially in Model B. It can be seen that the the gas is tracing the over-densities in the stellar component. By the end of the simulation, the galaxy has been significantly disturbed in both models, but it still retains the overall structure of a disc. With Satellite 1, some tails extend up to $R \approx 7R_D$ in both models at the end of the simulation, and this resut is not very different for Satellite 2.

For the retrograde case of Orbit 2, the gas and stellar density maps are presented in Figures 4.9 and 4.10, in pages 117 and 118, respectively, for the simulations with Satellite 1; and in Figures 4.11 and 4.12, in pages 119 and 120, respectively, for the simulations with Satellite 2. These snapshots correspond to approximately 4τ after the beginning of the simulation. The least massive satellite induces no significant disturbance. However, the interaction with the second satellite produces more evident features. In both models A and B, there is a cut in the density distribution at the III quadrant side of the galaxy. This is also visible in the stellar component of both models. During the course of the simulation, regardless of the model of the primary galaxy, the satellite spends more time disturbing the rim of the galaxy because the orbital decay is slower. Figure 4.11 shows that doubling the mass of the satellite produces a stronger effect on the disc. However, panel (d) of the same figure shows that it appears to be lower in the barred galaxy. The effect of a more massive satellite is also noticeable when comparing the stellar density maps in Figures 4.10 and 4.12.

The results for the simulations with Orbit 3 ($R_{peri} = R_D$, $i = 0°$) in a prograde sense are shown in Figures 4.17 and 4.18 for Satellite 1 (see pages 125 and 126, respectively), and in Figures 4.19 and 4.20 for Satellite 2 (see pages 127 and 128, respectively). For both satellites, the response of the gaseous component bears some resemblance with that of the prograde case of Orbit 1. However, the morphology is rather more asymmetric. It is also different in the sense that a very low density trail forms in front of the high-density induced arm. It is evident that the more massive satellite is introducing a stronger perturbation since the centre of the galaxy appears more disturbed and a more evident trail of lower density is left behind the satellite. In the stellar component of Model A, the effect of the less massive satellite is not easily discernible, but a rather asymmetric pattern is visible in stellar component. For Model B, both satellites destroy the spiral pattern of the original isolated system. The morphology of the stellar component also bears some resemblance with the first passage of the satellite in Orbit 1 (Figures 4.2 and 4.4).

Finally, the density maps resulting from the retrograde simulations of Orbit 3 are shown in Figures 4.21 and 4.22 for Satellite 1 (see pages 129 and 130), and in Figures 4.23 and 4.24 for Satellite 2 (see pages 131 and 132). A characteristic feature of this orbit is that it produces the arm pattern seen in the upper part of the disturbed galaxies shown in panels (b) and (d) of Figures 4.21 and 4.22. This pattern is formed as the satellite passes through the disc and produces a perturbation in the gas density, as it rotates with the galaxy, the pattern shown is produced. This feature is visible in both the gaseous and stellar components. Another visible feature in the gas disc is a low density region, nearly coincident with the position of the satellite. As the mass of the satellite is increased, the size of the region increases. Although noise is present when treating low density regions due to the finite number of particles, the fact that it becomes more evident when doubling the mass of the satellite suggests that the more massive satellite is indeed producing a stronger effect.

Table 4.1: Index the Figures of the Morphological Features discussed in this section

Orbit	Prograde		Retrograde	
	$M_s = 0.6$	$M_s = 1.2$	$M_s = 0.6$	$M_s = 1.2$
Orbit 1 Gas	P. 109	P. 111	P. 113	P. 115
Orbit 1 Stars	P. 110	P. 112	P. 114	P. 116
Orbit 2 Gas	P. 117	P. 119	P. 121	P. 123
Orbit 2 Stars	P. 118	P. 120	P. 122	P. 124
Orbit 3 Gas	P. 125	P. 127	P. 129	P. 131
Orbit 3 Stars	P. 126	P. 128	P. 130	P. 132

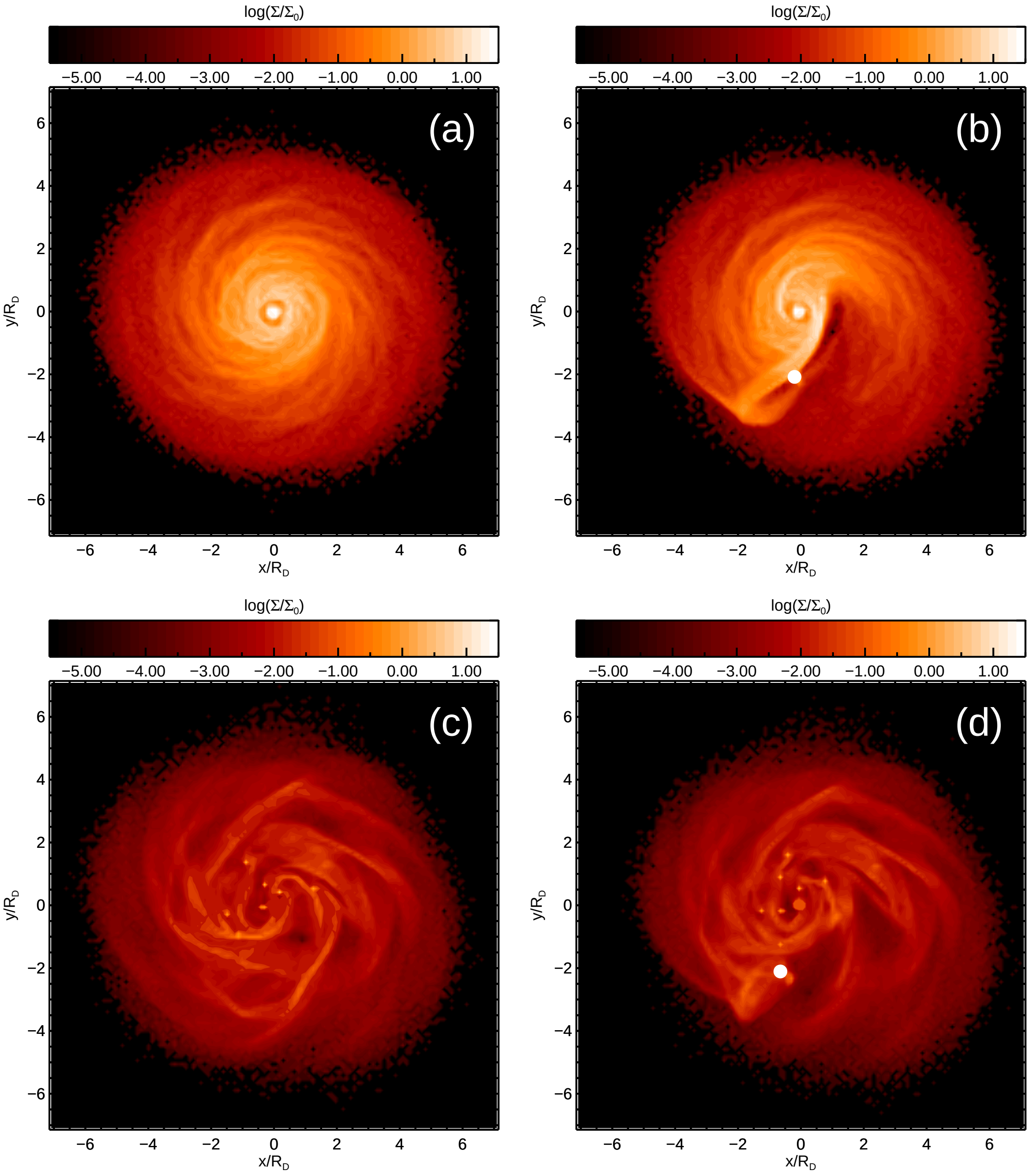

Figure 4.1: Gas surface density for the simulation with prograde Orbit 1 ($R_i = 3R_D, i = 30°$) with the satellite with $M = 0.6$. Panels (a) and (b) correspond to the isolated and the disturbed Model A. Panels (c) and (d) correspond to the same information for Model B. All snapshots correspond to $t = 0.59\tau$.

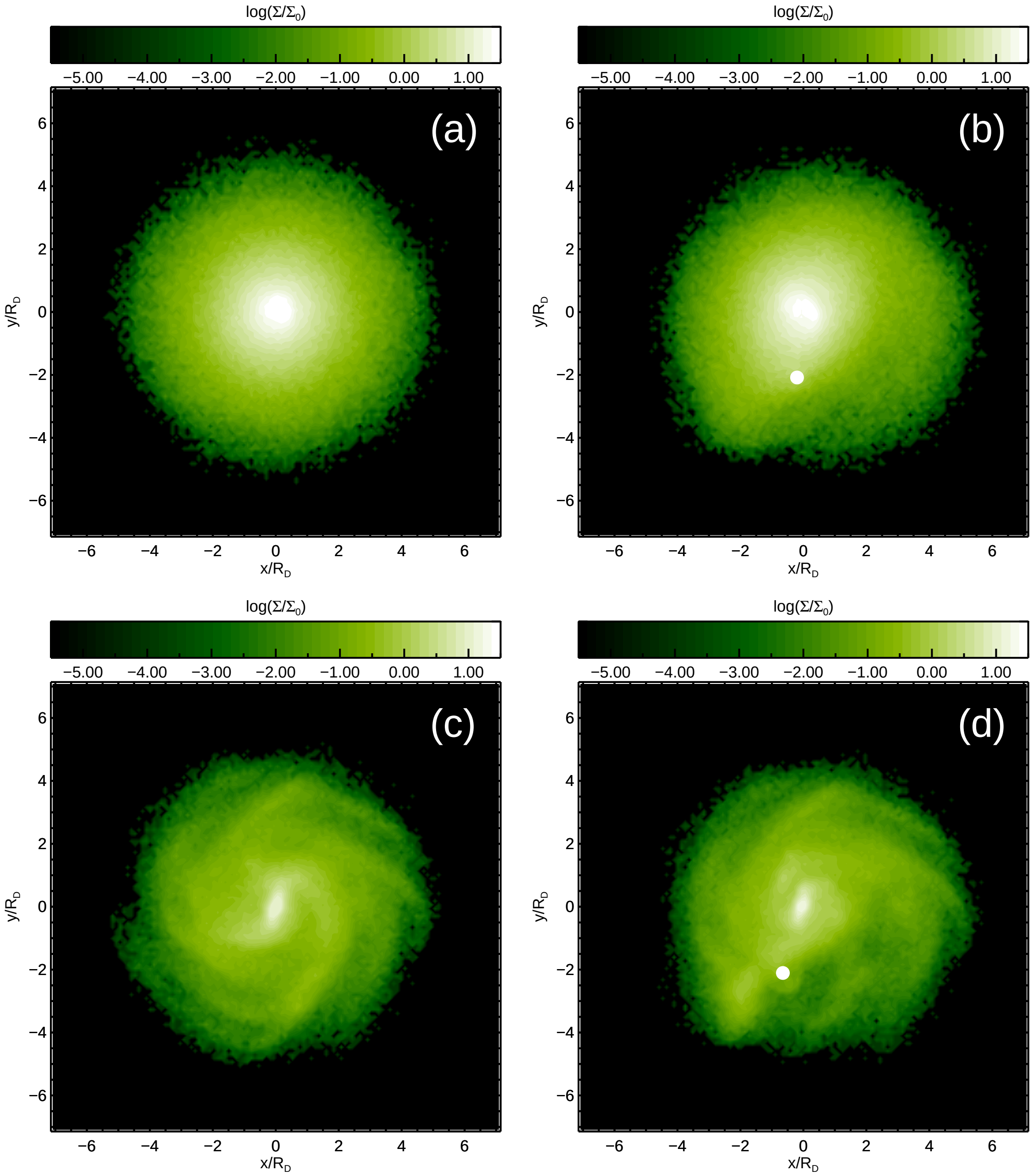

Figure 4.2: Stellar surface density for the simulation with prograde Orbit 1 ($R_i = 3R_D, i = 30°$) with the satellite with $M = 0.6$. Panels (a) and (b) correspond to the isolated and the disturbed Model A. Panels (c) and (d) correspond to the same information for Model B. All snapshots correspond to $t = 0.59\tau$.

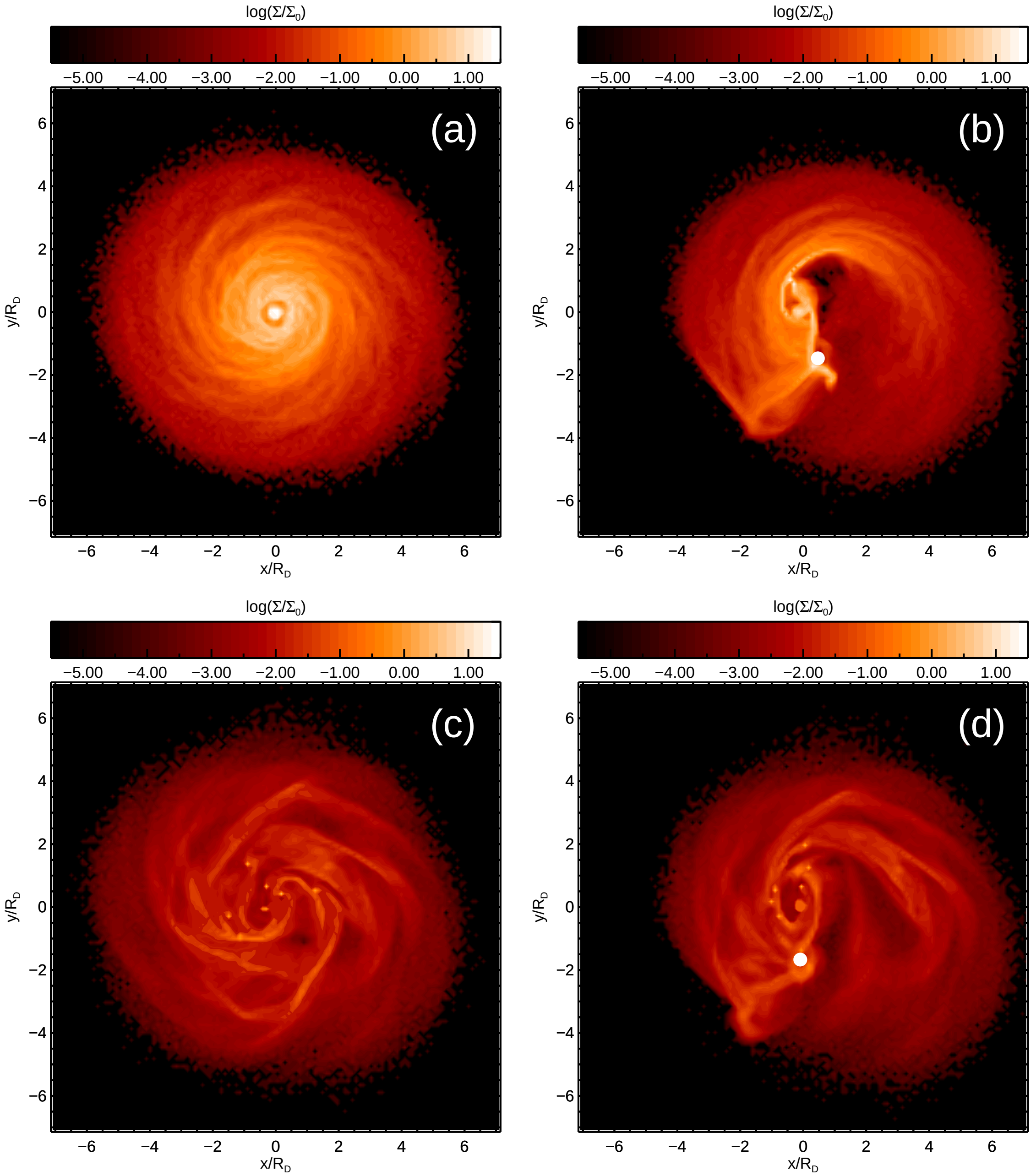

Figure 4.3: Gas surface density for the simulation with prograde Orbit 1 ($R_i = 3R_D, i = 30°$) with the satellite with $M = 1.2$. Panels (a) and (b) correspond to the isolated and the disturbed Model A. Panels (c) and (d) correspond to the same information for Model B. All snapshots correspond to $t = 0.59\tau$.

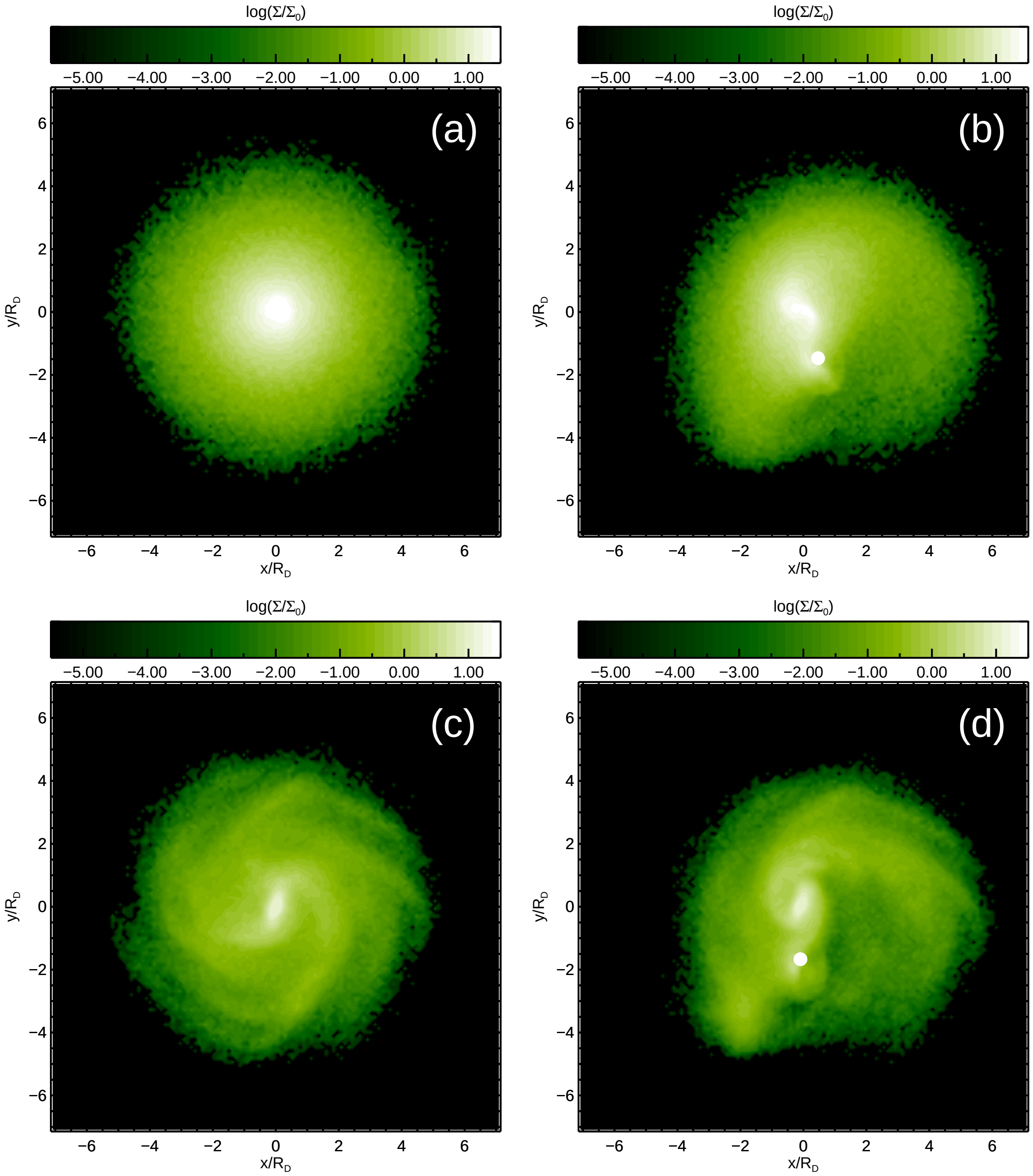

Figure 4.4: Stellar surface density for the simulation with prograde Orbit 1 ($R_i = 3R_D, i = 30°$) with the satellite with $M = 1.2$. Panels (a) and (b) correspond to the isolated and the disturbed Model A. Panels (c) and (d) correspond to the same information for Model B. All snapshots correspond to $t = 0.59\tau$.

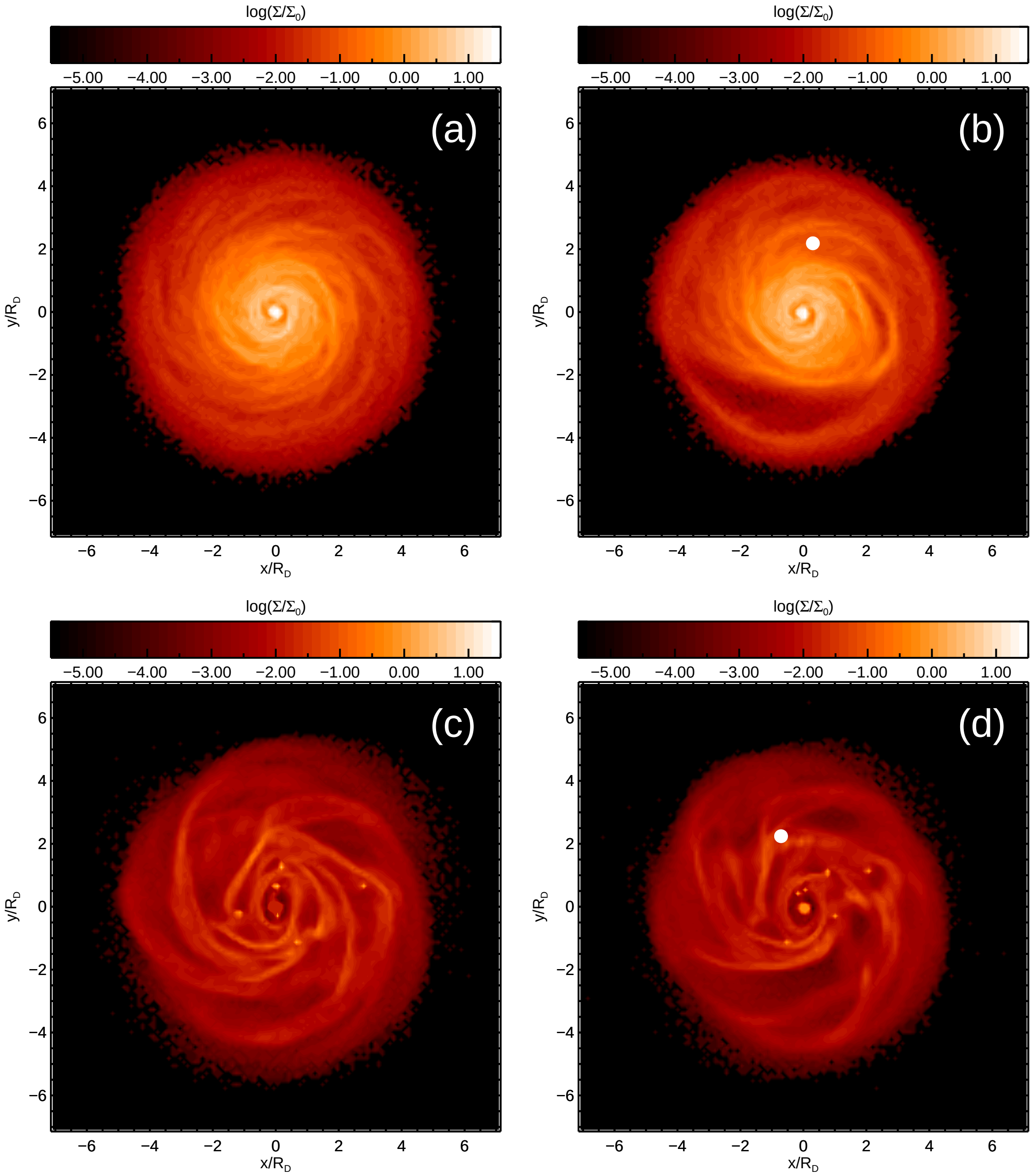

Figure 4.5: Gas surface density for the simulation with retrograde Orbit 1 ($R_i = 3R_D, i = 30°$) with the satellite with $M = 0.6$. Panels (a) and (b) correspond to the isolated and the disturbed Model A. Panels (c) and (d) correspond to the same information for Model B. All snapshots correspond to $t = 1.18\tau$.

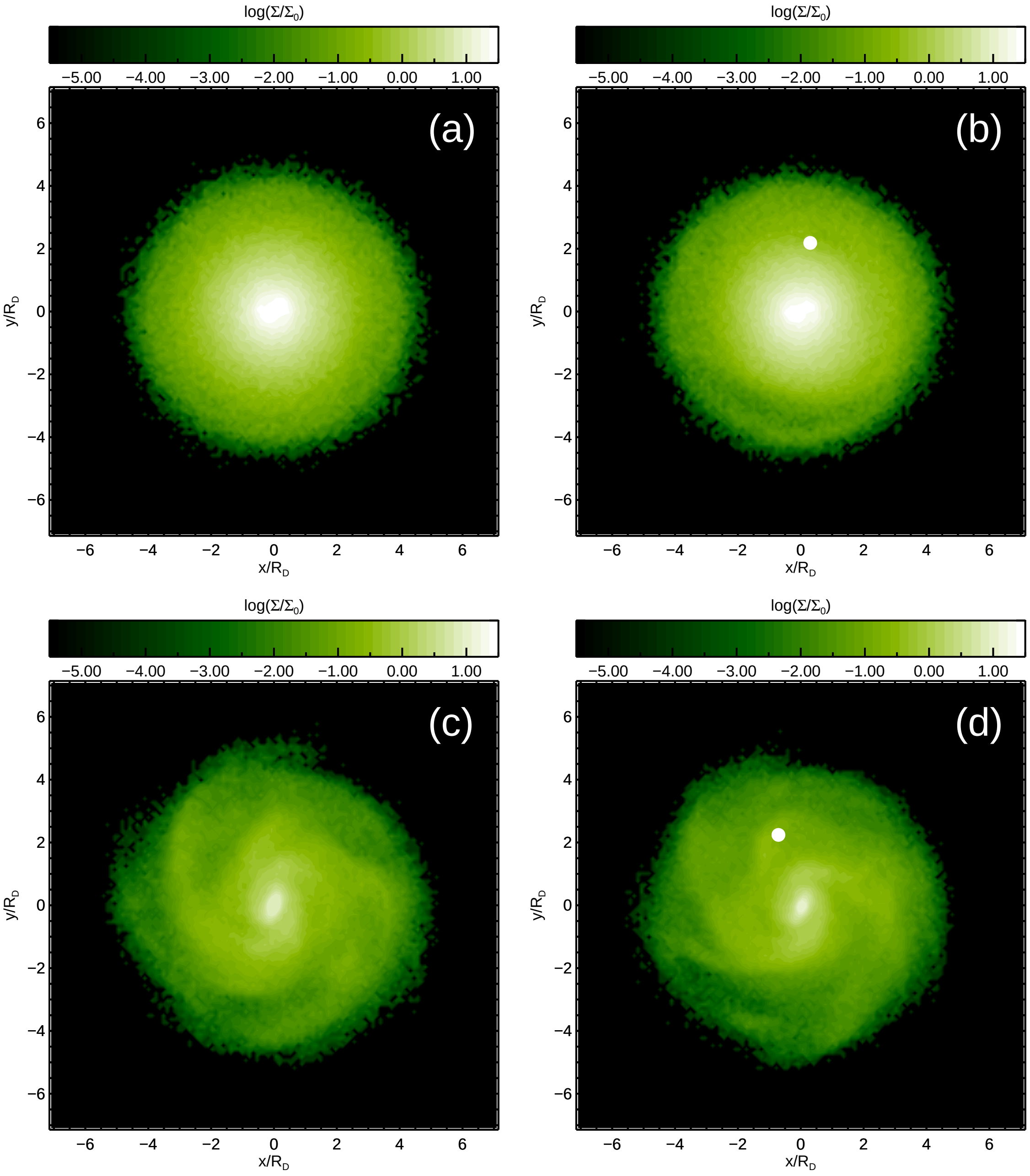

Figure 4.6: Stellar surface density for the simulation with retrograde Orbit 1 ($R_i = 3R_D, i = 30°$) with the satellite with $M = 0.6$. Panels (a) and (b) correspond to the isolated and the disturbed Model A. Panels (c) and (d) correspond to the same information for Model B. All snapshots correspond to $t = 1.18\tau$.

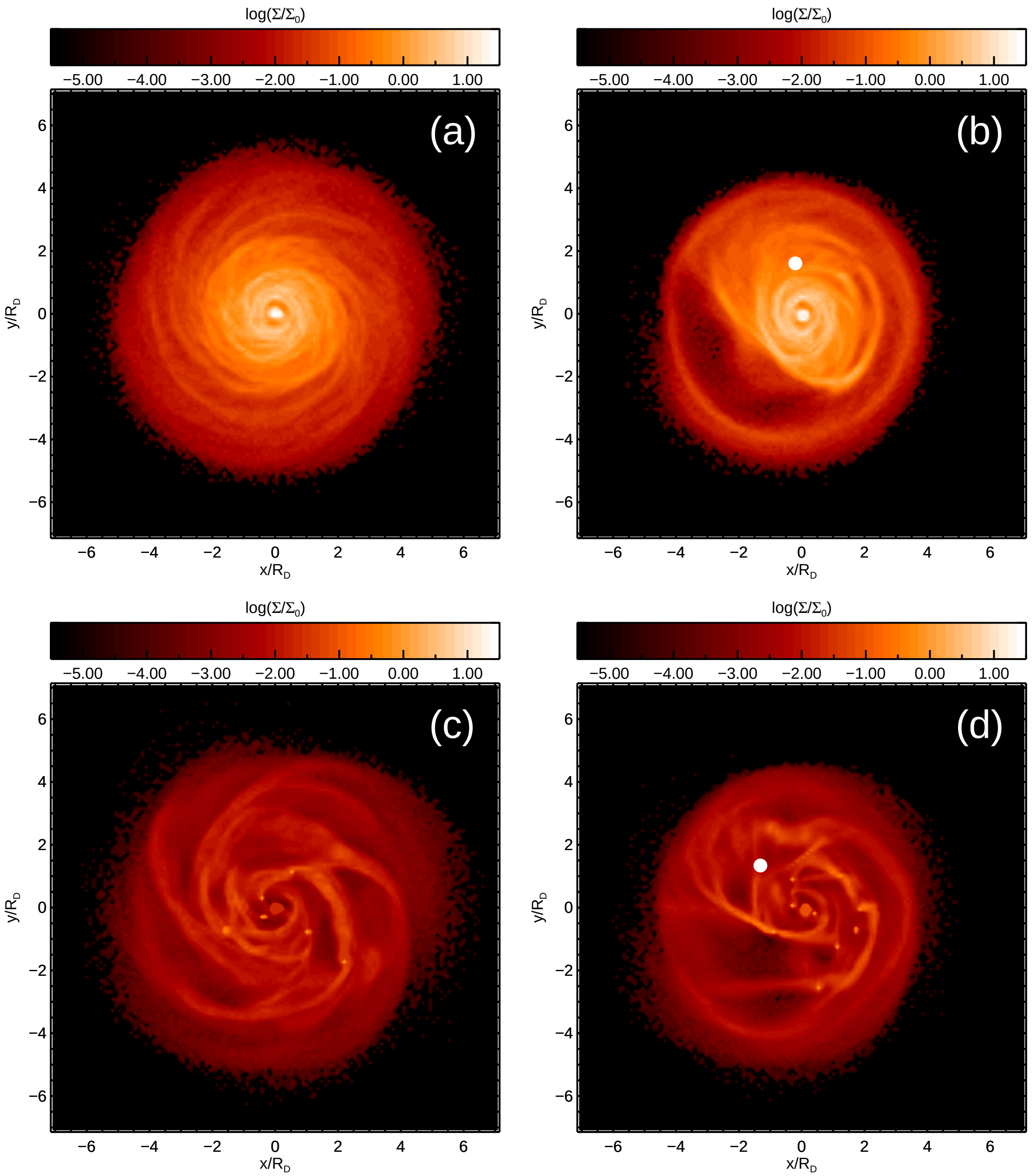

Figure 4.7: Gas surface density for the simulation with retrograde Orbit 1 ($R_i = 3R_D, i = 30°$) with the satellite with $M = 1.2$. Panels (a) and (b) correspond to the isolated and the disturbed Model A. Panels (c) and (d) correspond to the same information for Model B. All snapshots correspond to $t = 1.18\tau$.

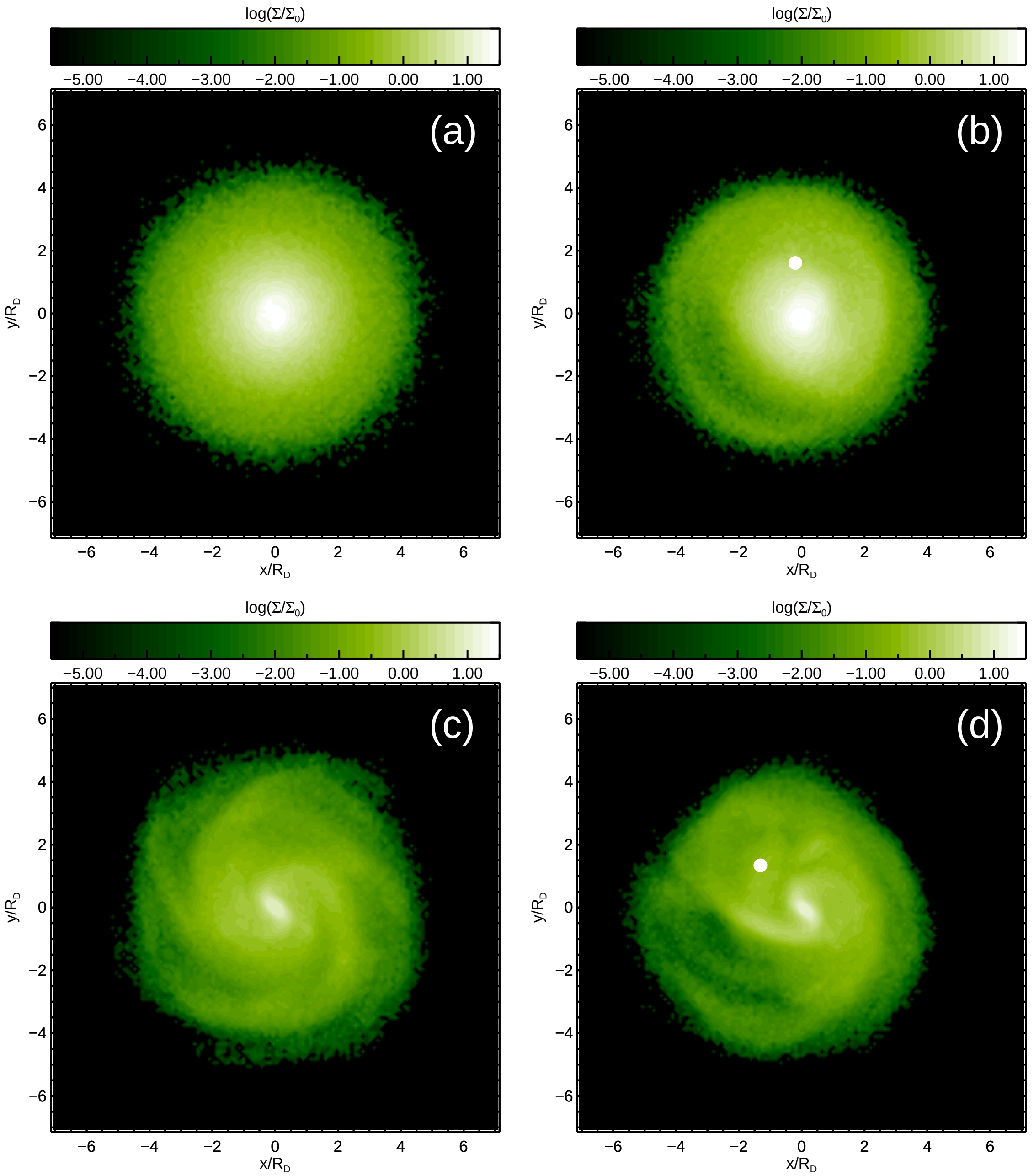

Figure 4.8: Stellar surface density for the simulation with retrograde Orbit 1 ($R_i = 3R_D, i = 30°$) with the satellite with $M = 1.2$. Panels (a) and (b) correspond to the isolated and the disturbed Model A. Panels (c) and (d) correspond to the same information for Model B. All snapshots correspond to $t = 1.18\tau$.

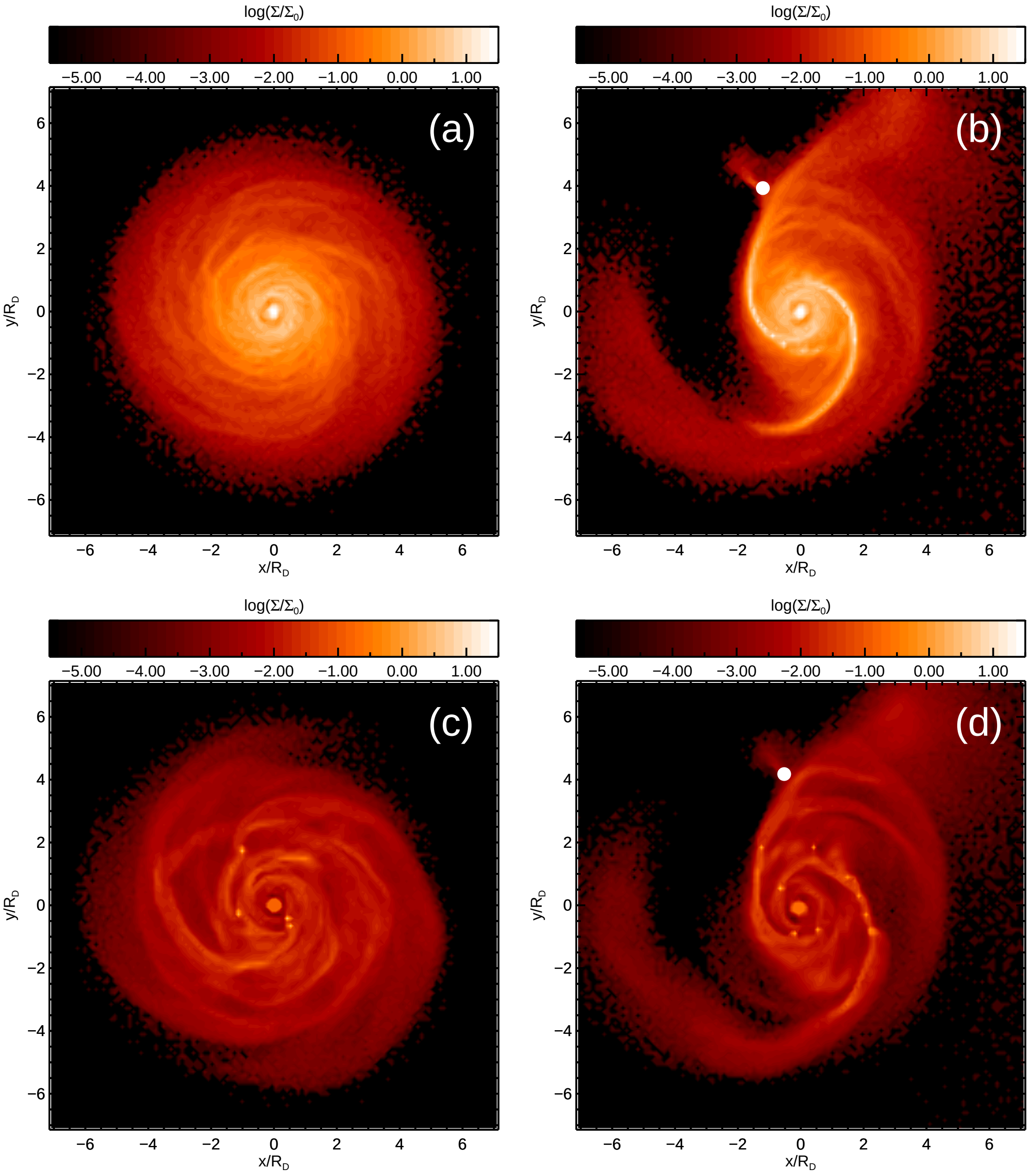

Figure 4.9: Gas surface density for the simulation with prograde Orbit 2 ($R_i = 6R_D, i = 30°$) with the satellite with $M = 0.6$. Panels (a) and (b) correspond to the isolated and the disturbed Model A. Panels (c) and (d) correspond to the same information for Model B. All snapshots correspond to $t = 2.55\tau$.

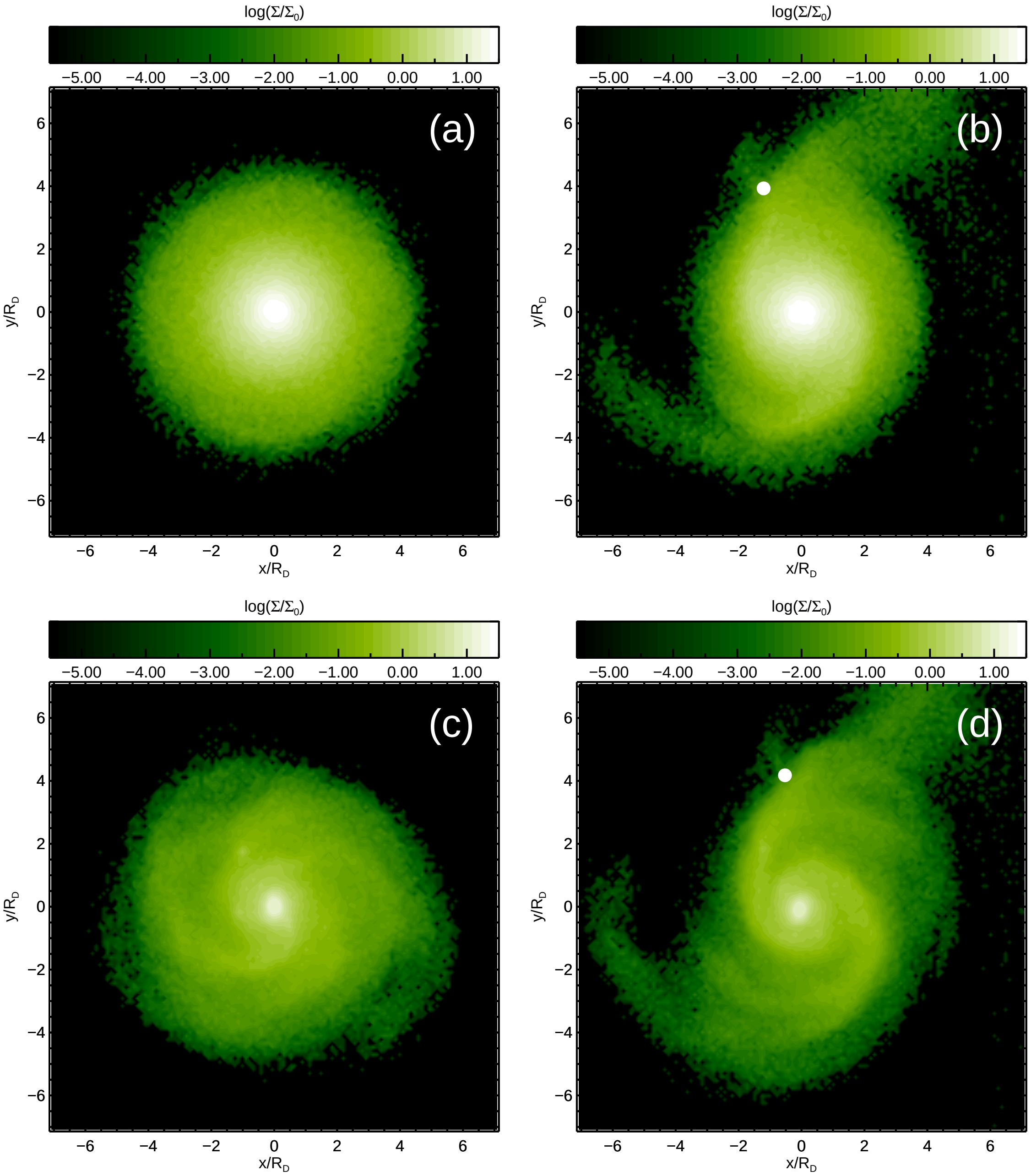

Figure 4.10: Stellar surface density for the simulation with prograde Orbit 2 ($R_i = 6R_D, i = 30°$) with the satellite with $M = 0.6$. Panels (a) and (b) correspond to the isolated and the disturbed Model A. Panels (c) and (d) correspond to the same information for Model B. All snapshots correspond to $t = 2.55\tau$.

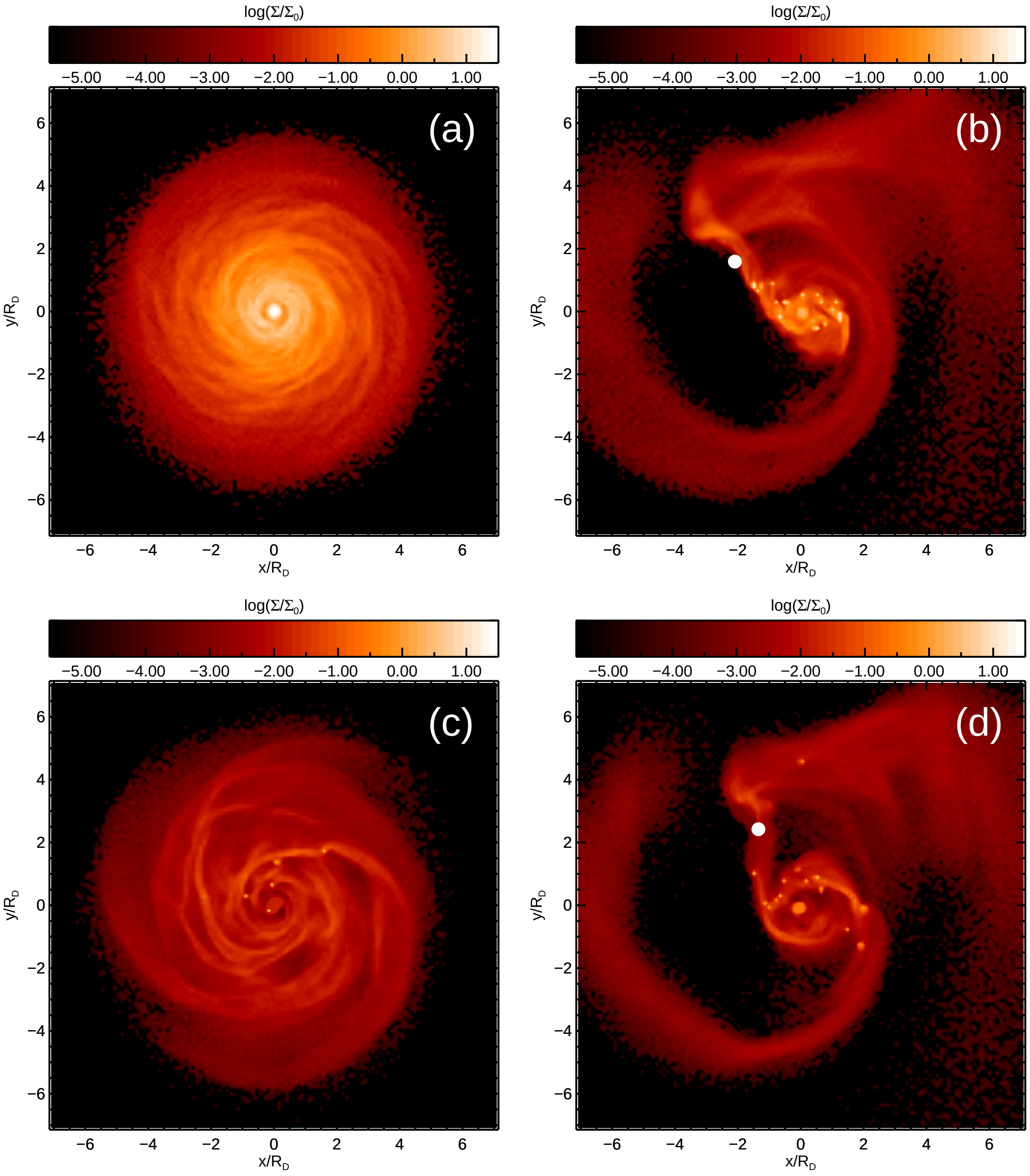

Figure 4.11: Gas surface density for the simulation with prograde Orbit 2 ($R_i = 6R_D, i = 30°$) with the satellite with $M = 1.2$. Panels (a) and (b) correspond to the isolated and the disturbed Model A. Panels (c) and (d) correspond to the same information for Model B. All snapshots correspond to $t = 2.35\tau$.

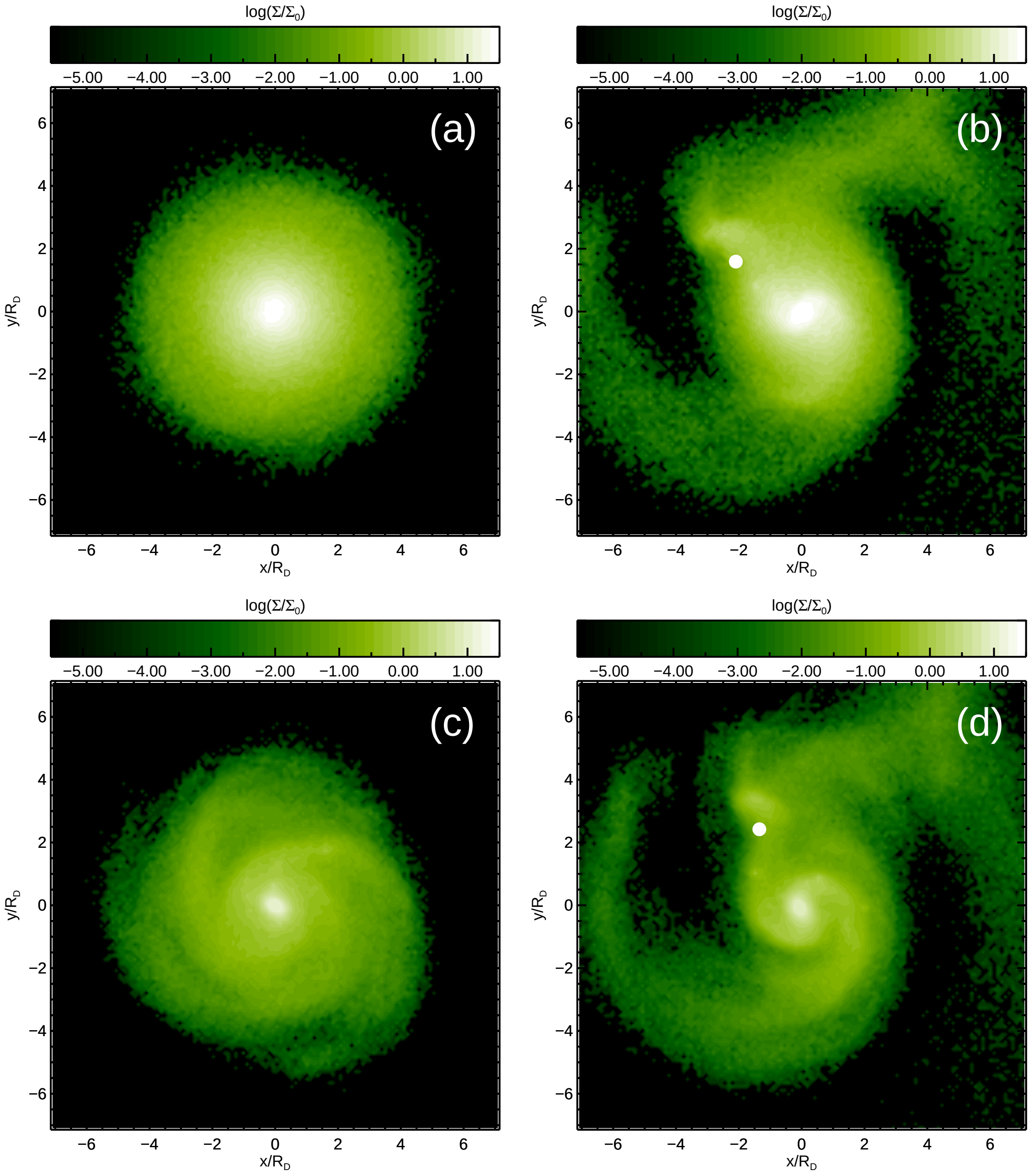

Figure 4.12: Stellar surface density for the simulation with prograde Orbit 2 ($R_i = 6R_D, i = 30°$) with the satellite with $M = 1.2$. Panels (a) and (b) correspond to the isolated and the disturbed Model A. Panels (c) and (d) correspond to the same information for Model B. All snapshots correspond to $t = 2.35\tau$.

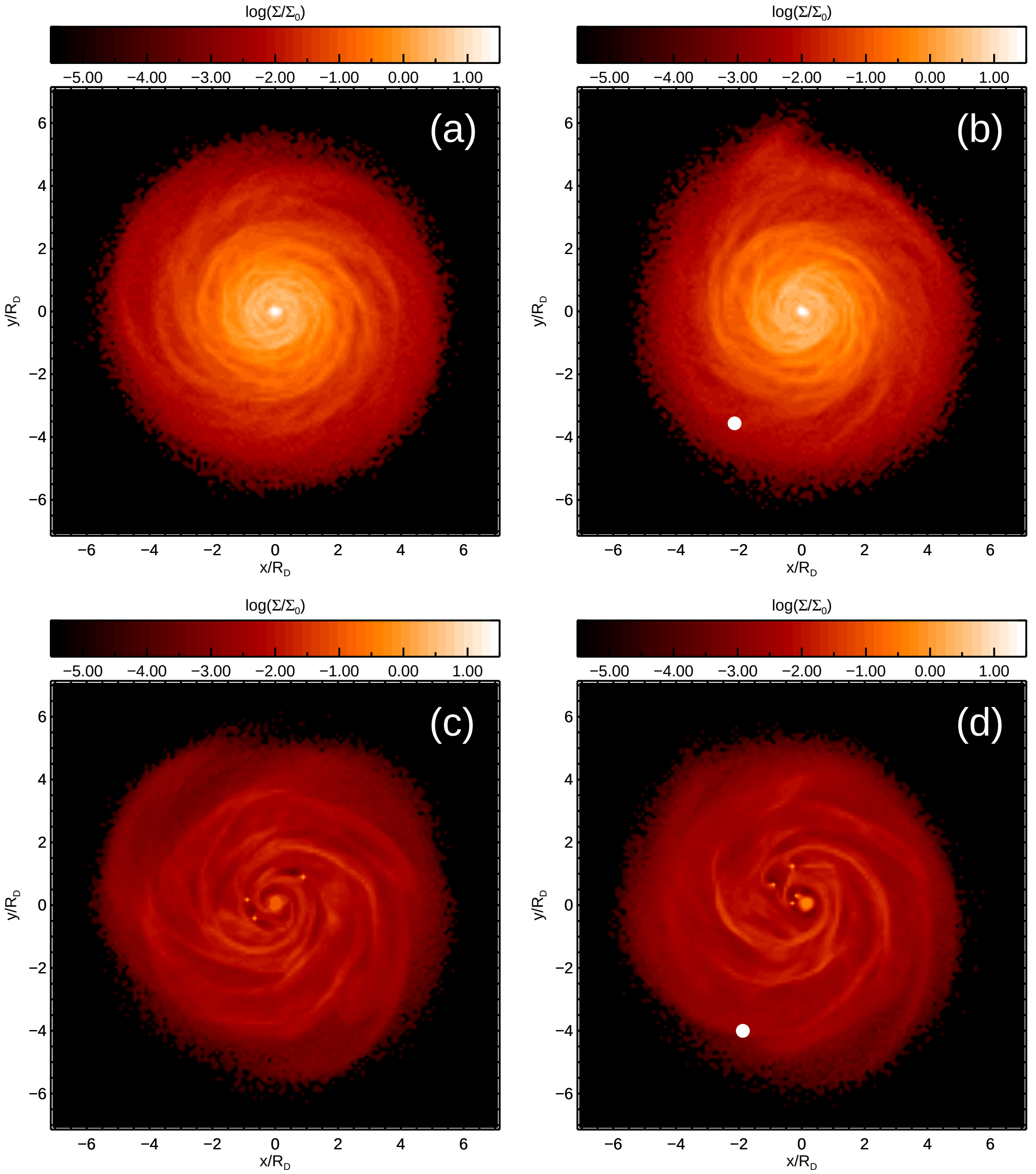

Figure 4.13: Gas surface density for the simulation with retrograde Orbit 2 ($R_i = 6R_D, i = 30°$) with the satellite with $M = 0.6$. Panels (a) and (b) correspond to the isolated and the disturbed Model A. Panels (c) and (d) correspond to the same information for Model B. All snapshots correspond to $t = 3.92\tau$.

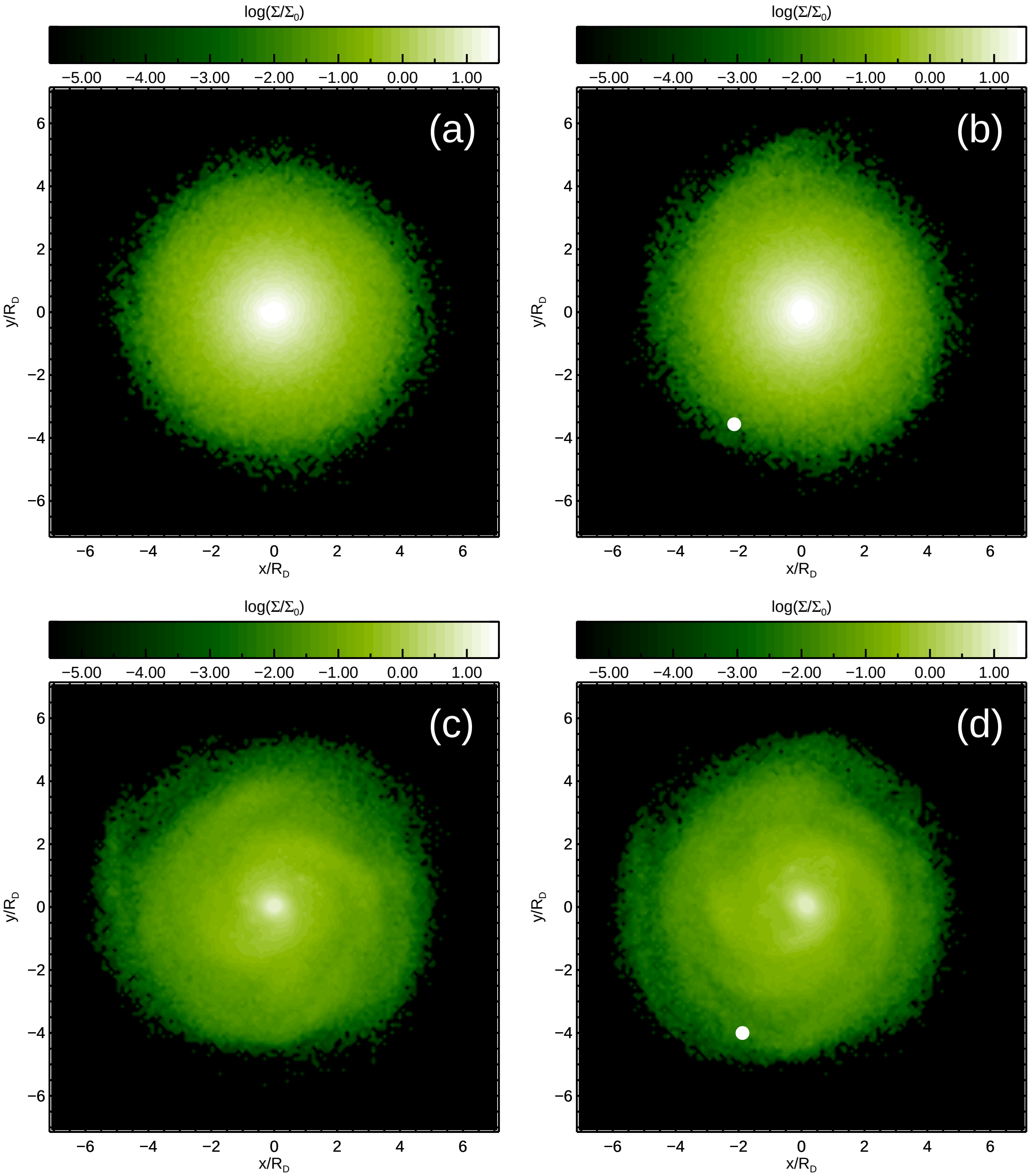

Figure 4.14: Stellar surface density for the simulation with retrograde Orbit 2 ($R_i = 6R_D, i = 30°$) with the satellite with $M = 0.6$. Panels (a) and (b) correspond to the isolated and the disturbed Model A. Panels (c) and (d) correspond to the same information for Model B. All snapshots correspond to $t = 3.92\tau$.

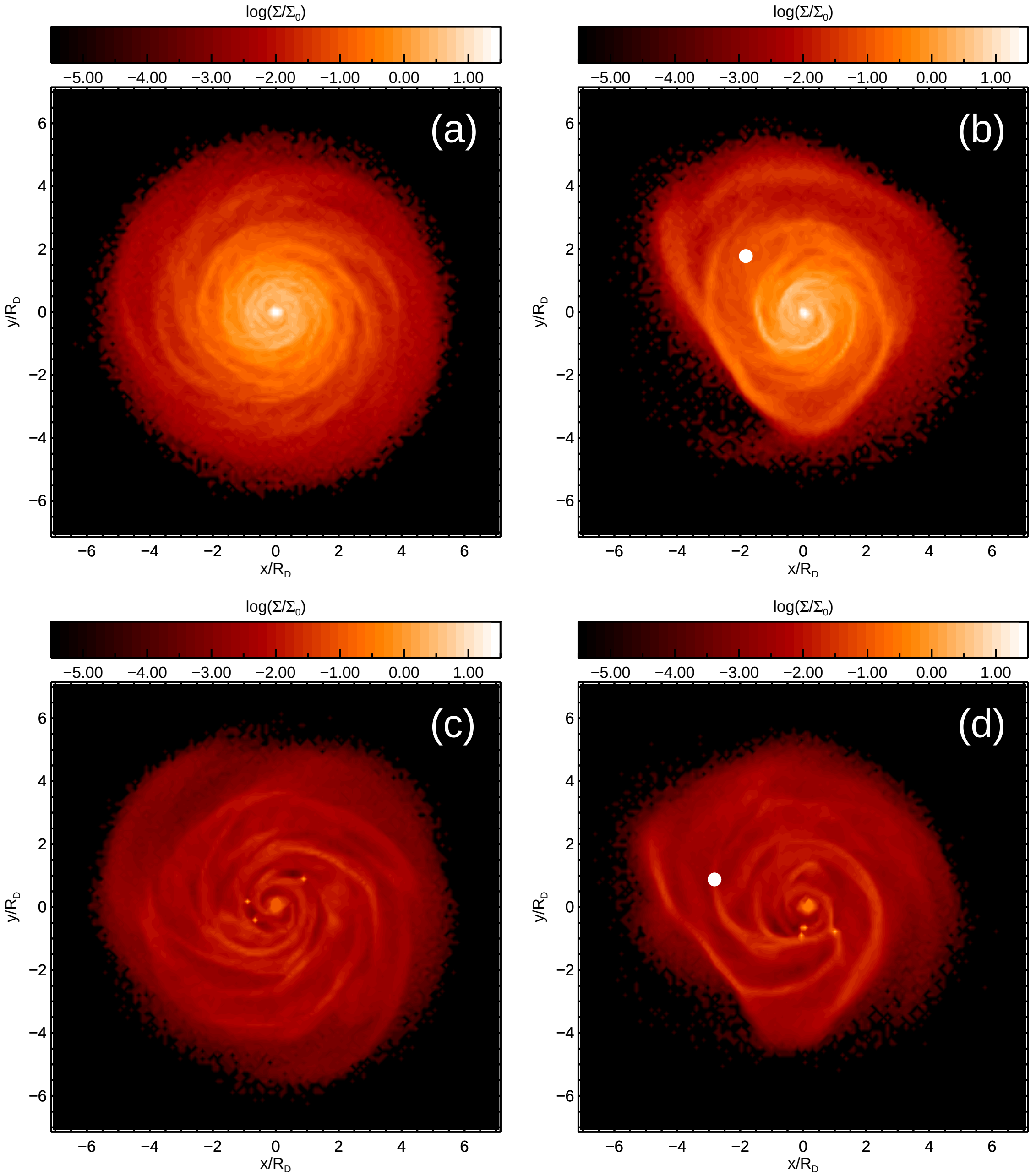

Figure 4.15: Gas surface density for the simulation with retrograde Orbit 2 ($R_i = 6R_D, i = 30°$) with the satellite with $M = 1.2$. Panels (a) and (b) correspond to the isolated and the disturbed Model A. Panels (c) and (d) correspond to the same information for Model B. All snapshots correspond to $t = 3.92\tau$.

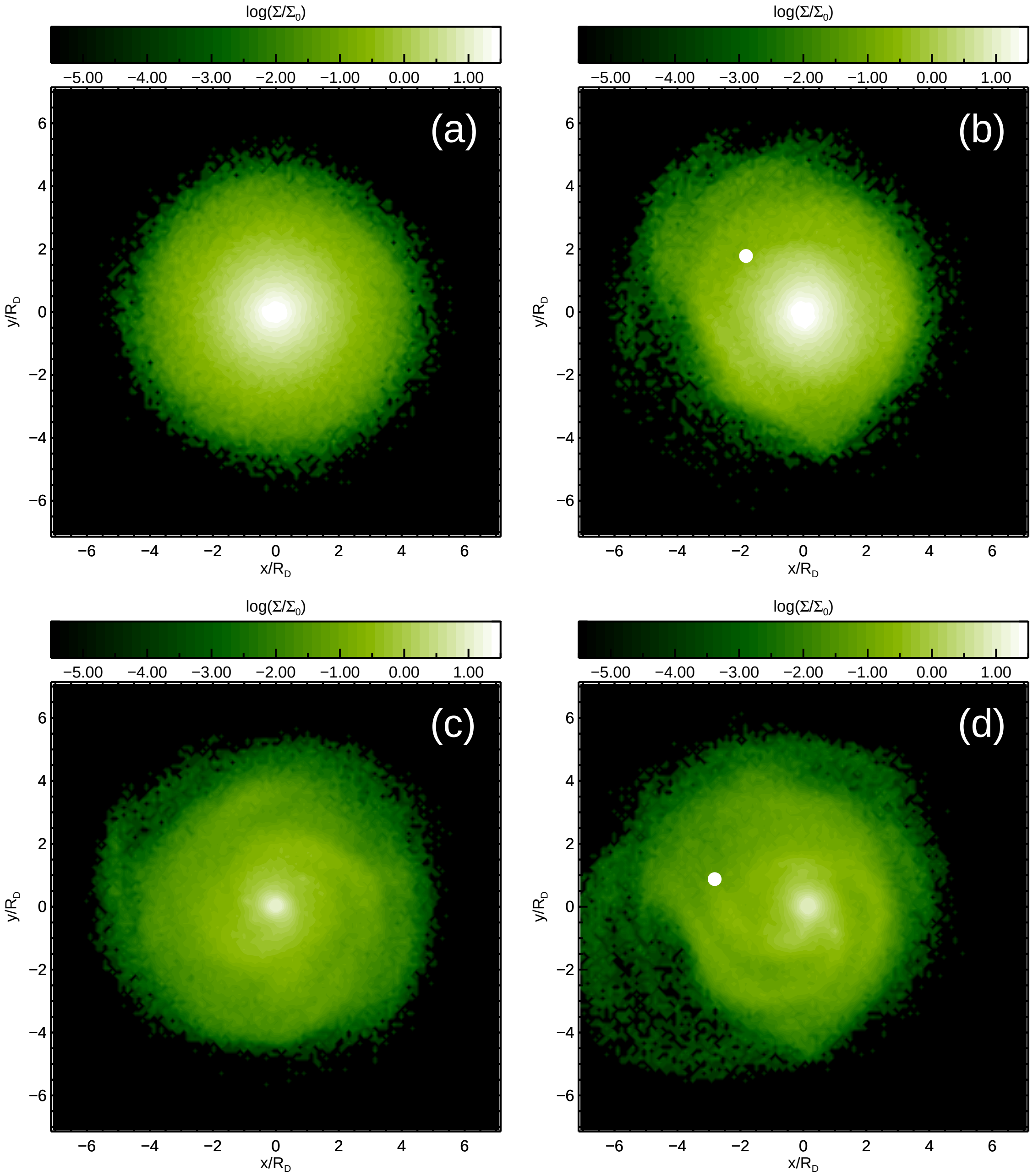

Figure 4.16: Stellar surface density for the simulation with retrograde Orbit 2 ($R_i = 6R_D, i = 30°$) with the satellite with $M = 1.2$. Panels (a) and (b) correspond to the isolated and the disturbed Model A. Panels (c) and (d) correspond to the same information for Model B. All snapshots correspond to $t = 3.92\tau$.

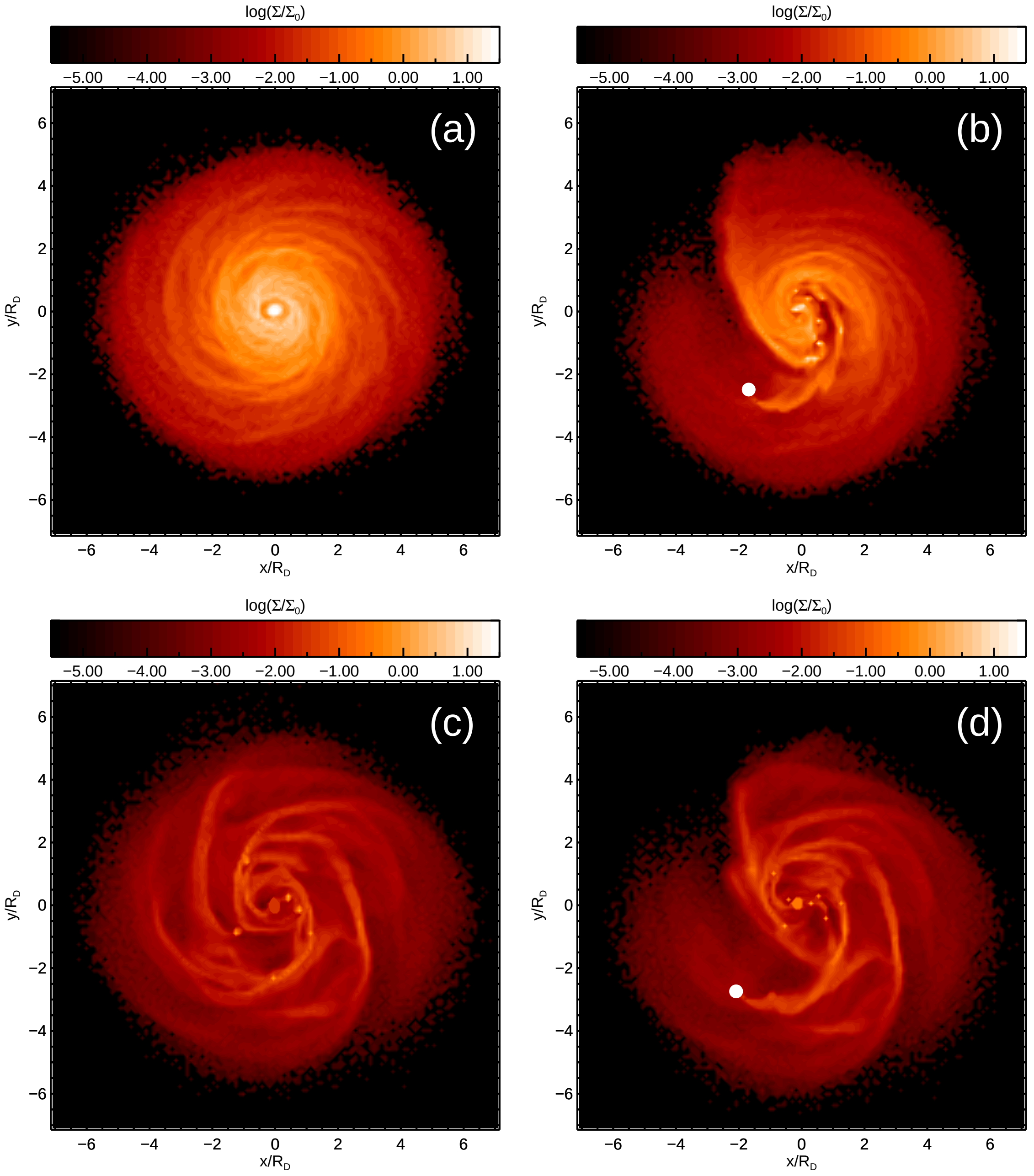

Figure 4.17: Gas surface density for the simulation with prograde Orbit 3 ($R_{peri} = R_D, i = 0°$) with the satellite with $M = 0.6$. Panels (a) and (b) correspond to the isolated and the disturbed Model A. Panels (c) and (d) correspond to the same information for Model B. All snapshots correspond to $t = 0.78\tau$.

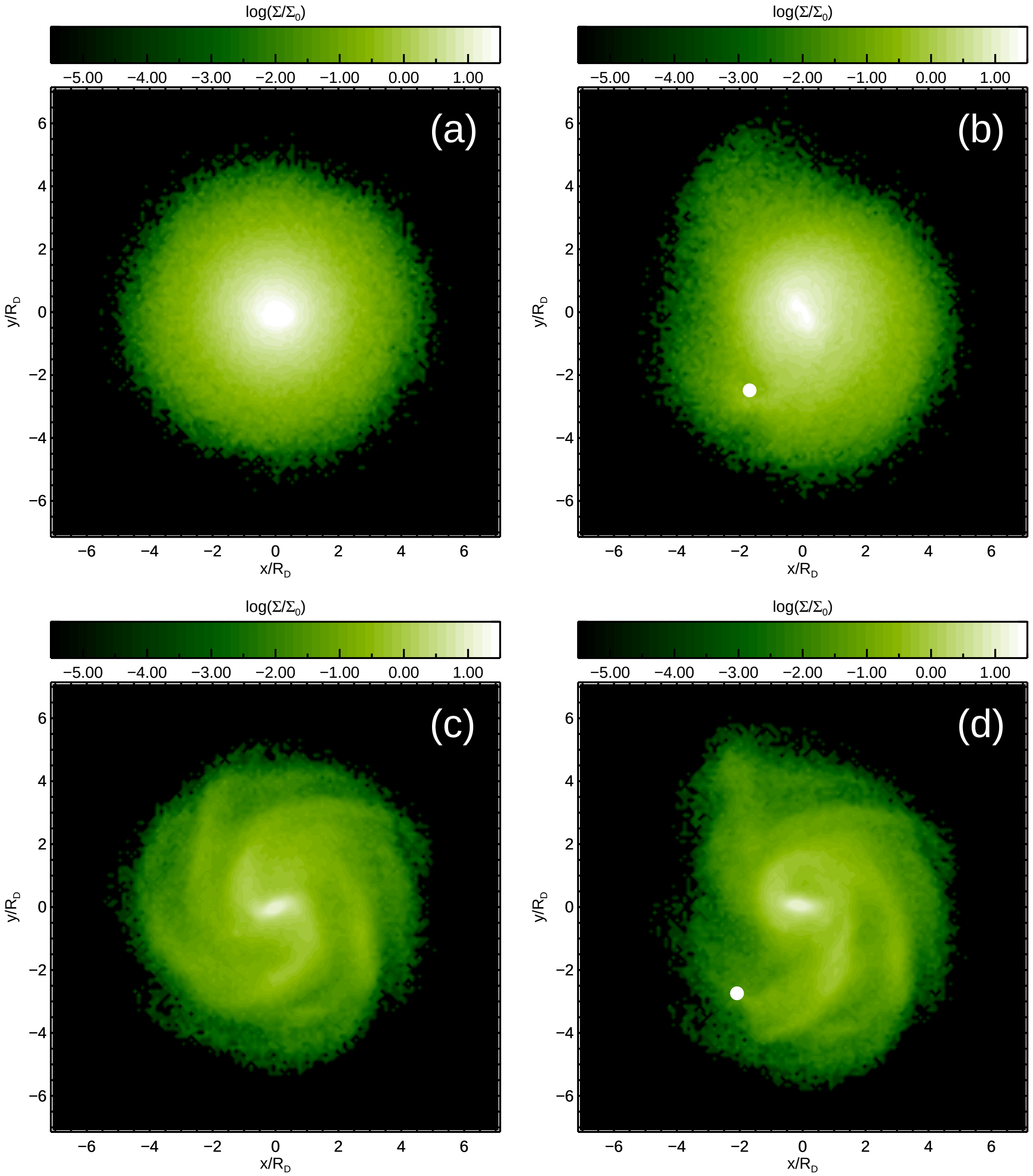

Figure 4.18: Stellar surface density for the simulation with prograde Orbit 3 ($R_{peri} = R_D, i = 0°$) with the satellite with $M = 0.6$. Panels (a) and (b) correspond to the isolated and the disturbed Model A. Panels (c) and (d) correspond to the same information for Model B. All snapshots correspond to $t = 0.78\tau$.

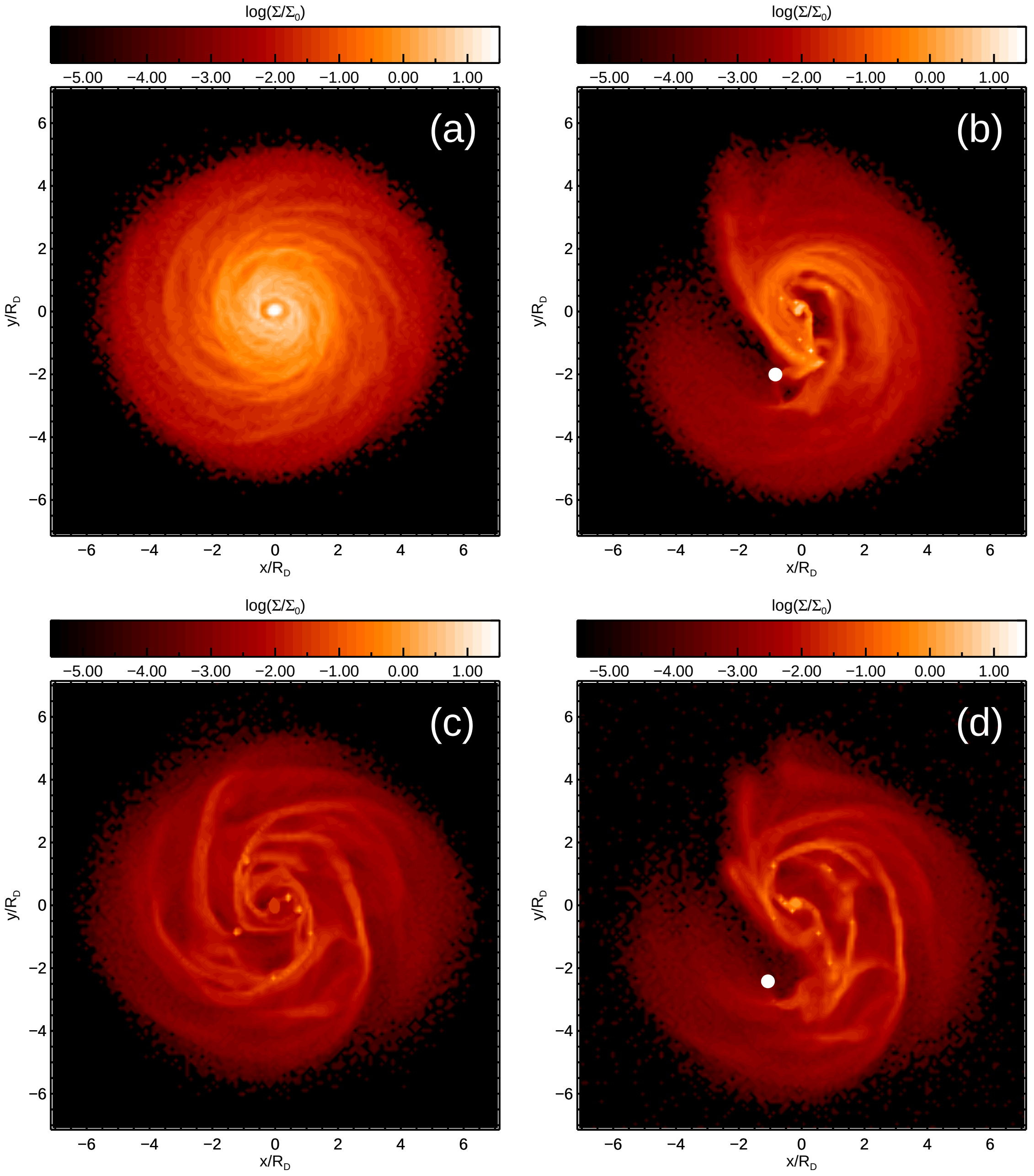

Figure 4.19: Gas surface density for the simulation with prograde Orbit 3 ($R_{peri} = R_D, i = 0°$) with the satellite with $M = 1.2$. Panels (a) and (b) correspond to the isolated and the disturbed Model A. Panels (c) and (d) correspond to the same information for Model B. All snapshots correspond to $t = 0.78\tau$.

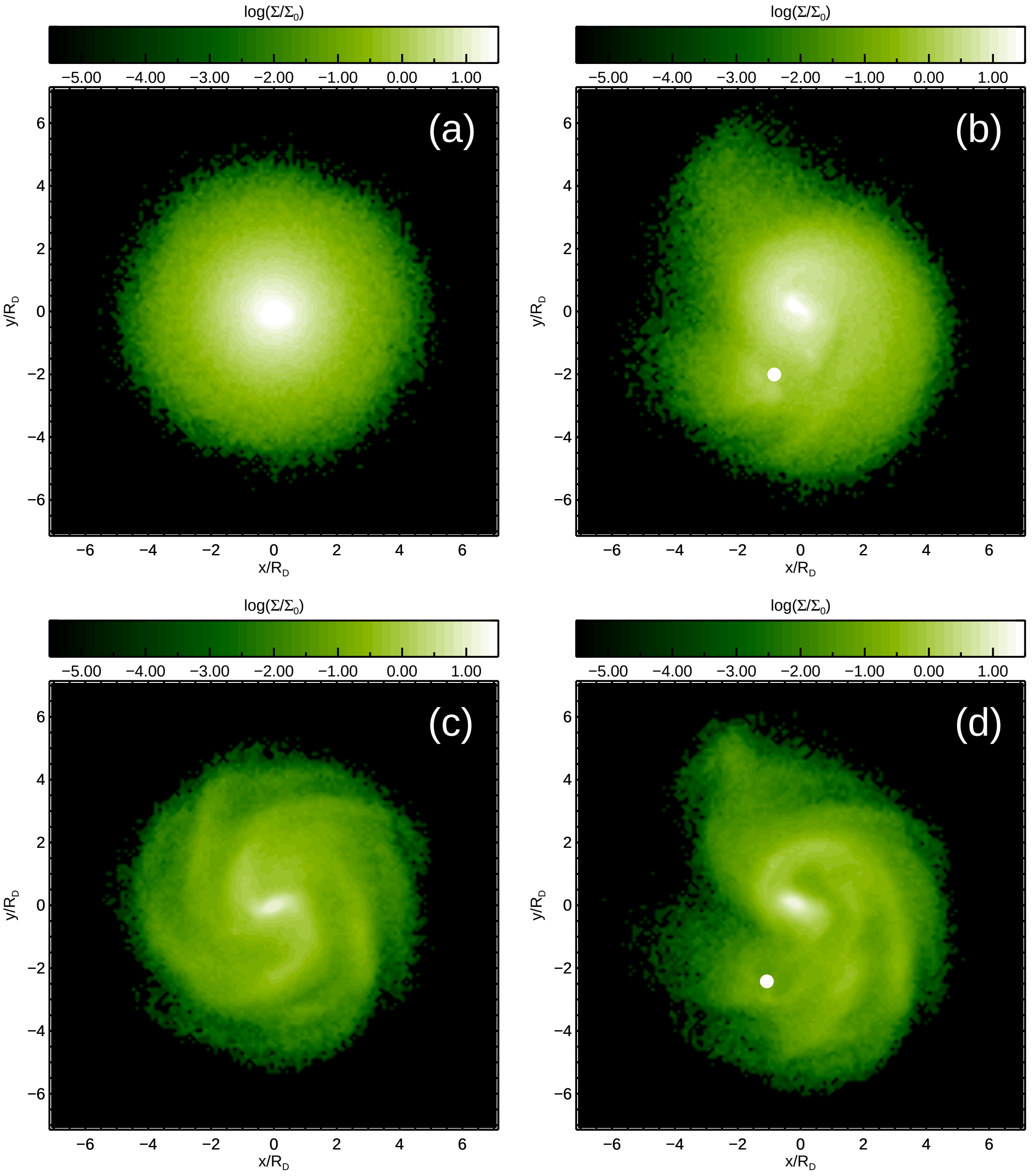

Figure 4.20: Stellar surface density for the simulation with prograde Orbit 3 ($R_{peri} = R_D, i = 0°$) with the satellite with $M = 1.2$. Panels (a) and (b) correspond to the isolated and the disturbed Model A. Panels (c) and (d) correspond to the same information for Model B. All snapshots correspond to $t = 0.78\tau$.

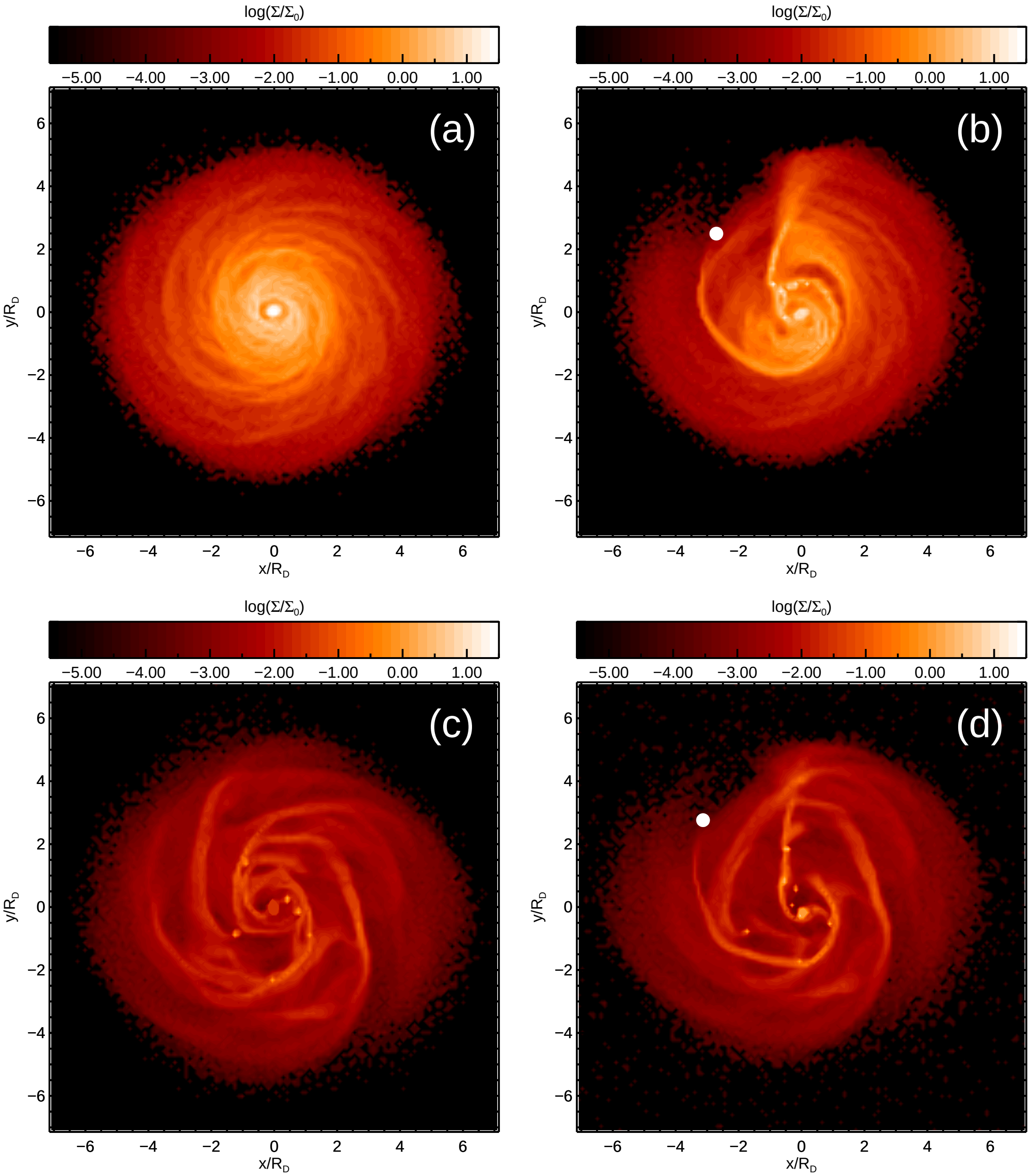

Figure 4.21: Gas surface density for the simulation with retrograde Orbit 3 ($R_{peri} = R_D, i = 0°$) with the satellite with $M = 0.6$. Panels (a) and (b) correspond to the isolated and the disturbed Model A. Panels (c) and (d) correspond to the same information for Model B. All snapshots correspond to $t = 0.78\tau$.

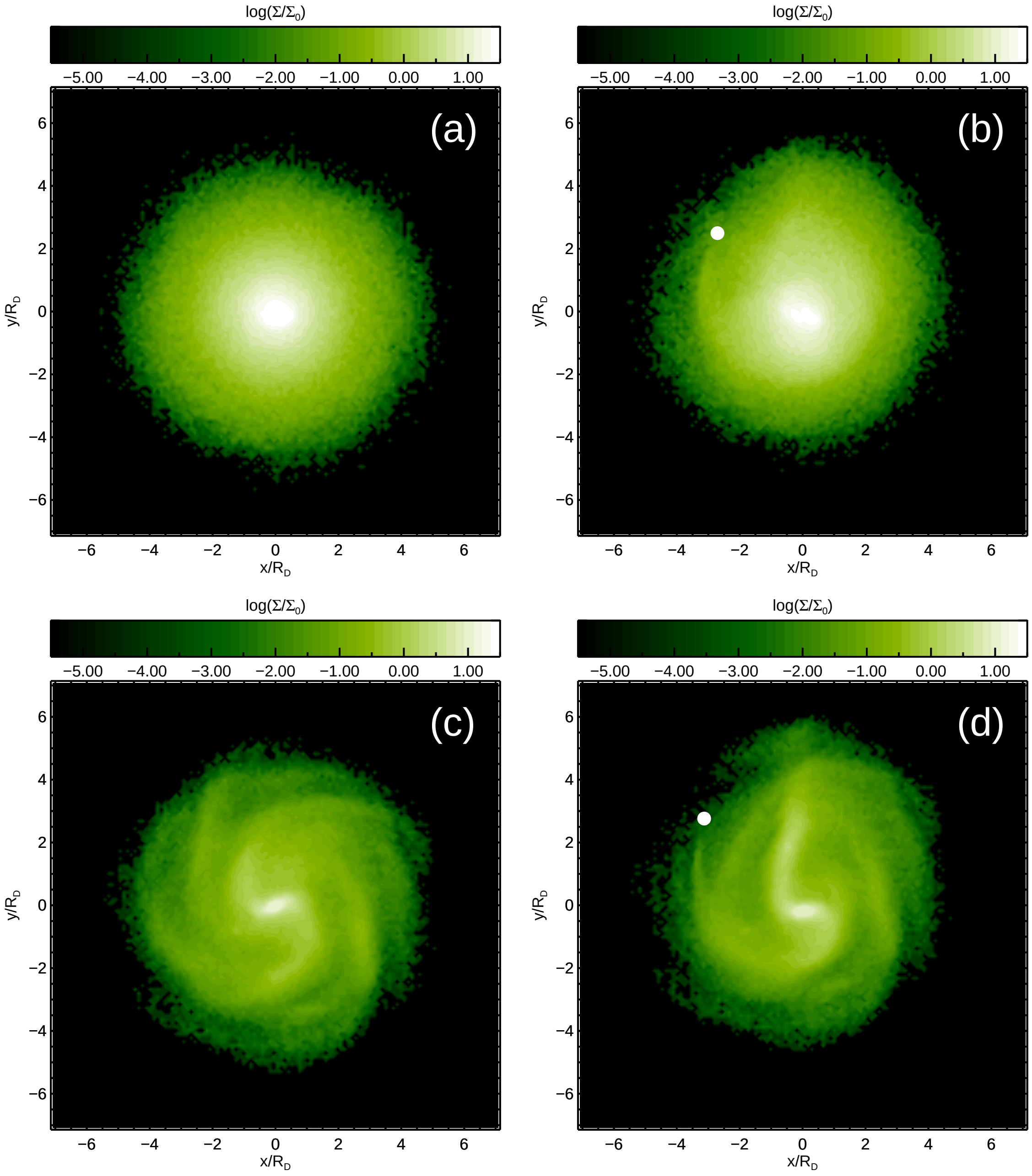

Figure 4.22: Stellar surface density for the simulation with retrograde Orbit 3 ($R_{peri} = R_D, i = 0°$) with the satellite with $M = 0.6$. Panels (a) and (b) correspond to the isolated and the disturbed Model A. Panels (c) and (d) correspond to the same information for Model B. All snapshots correspond to $t = 0.78\tau$.

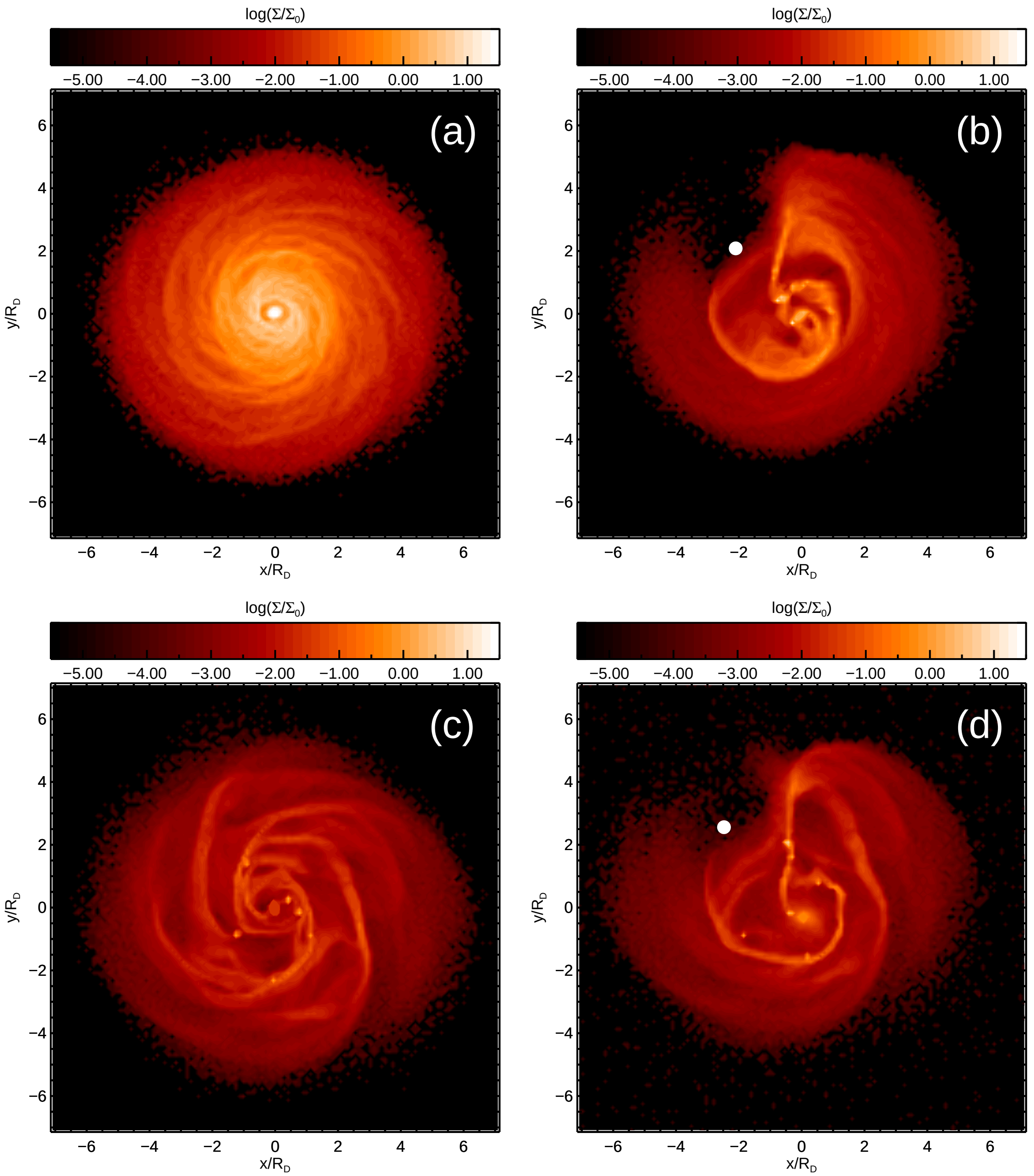

Figure 4.23: Gas surface density for the simulation with retrograde Orbit 3 ($R_{peri} = R_D, i = 0°$) with the satellite with $M = 1.2$. Panels (a) and (b) correspond to the isolated and the disturbed Model A. Panels (c) and (d) correspond to the same information for Model B. All snapshots correspond to $t = 0.78\tau$.

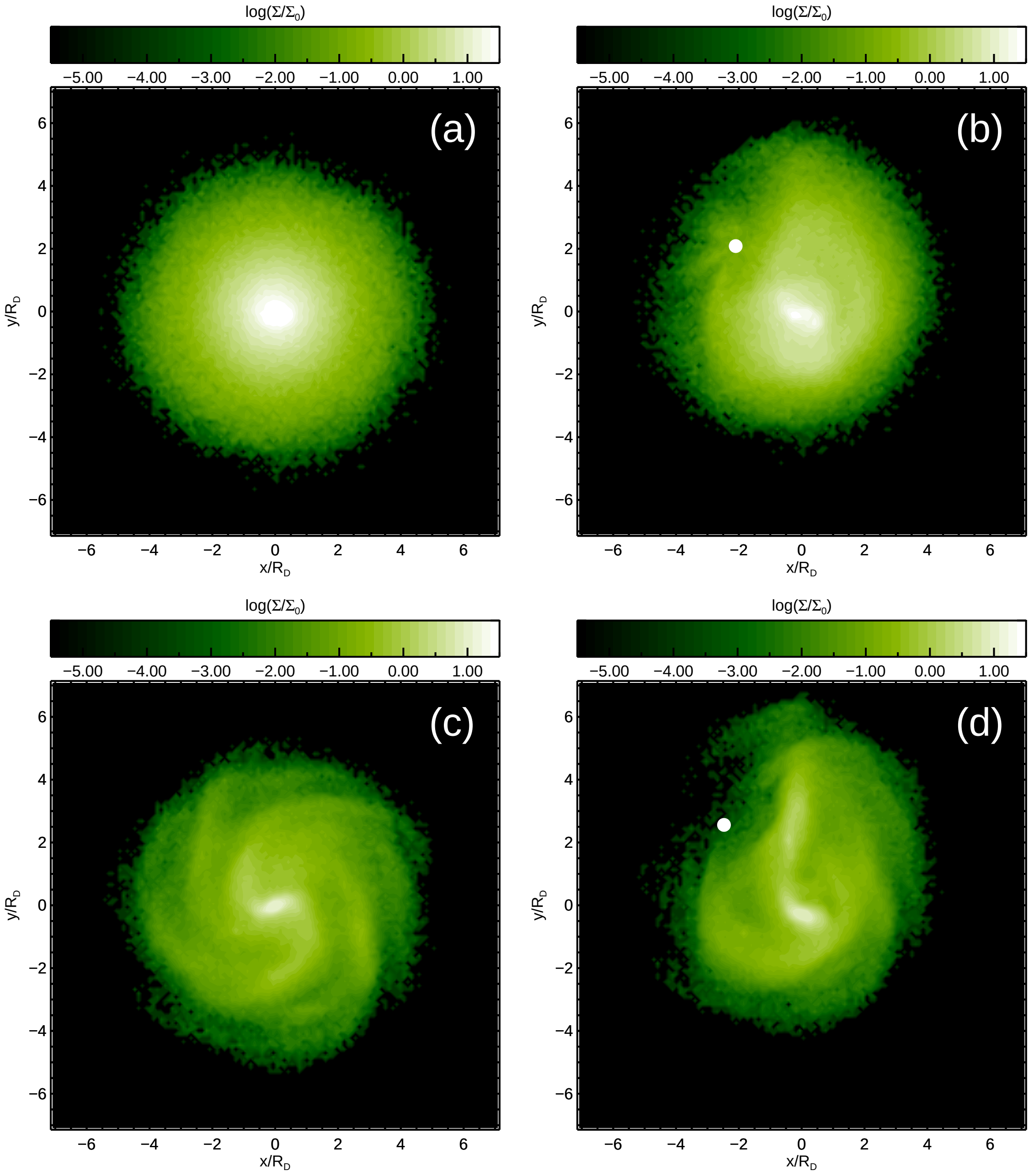

Figure 4.24: Stellar surface density for the simulation with retrograde Orbit 3 ($R_{peri} = R_D, i = 0°$) with the satellite with $M = 1.2$. Panels (a) and (b) correspond to the isolated and the disturbed Model A. Panels (c) and (d) correspond to the same information for Model B. All snapshots correspond to $t = 0.78\tau$.

4.2. Distribution of Gas Mass

In order to study the effect of the interacting satellite in moving significant amounts of gas in the disc of the host galaxy, the distribution of gas mass at the end of the simulation is computed. This is done by obtaining the cumulative mass function $M(< R)$ as described in §3.3.2. As this is defined in terms of the galactocentric radius, the inclination of the host galaxy produced by the interaction with the satellite introduces a variation in the function $M(< R)$. If the disc has an inclination i, the radius on the disc plane is R, and the projected radius is $R_p = R\cos i$, then the difference $R - R_p = R(1 - \cos i)$. Therefore, the fractional error introduced is: $\delta R/R = 1 - \cos i$. For inclinations of 10° and 15°, the variation is of ≈ 1.5 and 3.4 %, respectively, and the error becomes apparent at large radii. For this reason, the principal axes of the moment of inertia were calculated using only the particles of the gas and stellar discs, and the system was rotated to that frame. Particles within a radius of $\approx 4R_D$ were considered to avoid the effect of tails induced by the satellite. The purpose of this procedure is to measure the gas distribution in a plane approximately coincident with the plane of the disc. Testing of this procedure showed that the disc was correctly rotated, and the difference between the corrected and original calculations was not discernible in the $\mu_g(< R_D)$. Small differences were observed only in the retrograde orbits with $R_i = 6R_D$, which produces a significant inclination of the primary's disc. Nevertheless, the results presented in this section and in §4.3 are calculated in the frame of the principal axes.

For the prograde encounter with Model A following Orbit 1 ($R_i = 3R_D$, $i = 30^\circ$), the final gas mass distribution, defined as $\mu_g(< R) = M(< R)/M_g$, is shown in the left panel of Figure 4.25. The gas fraction up to R_D increases to ≈ 34 % of the total gas mass, compared to the ≈ 30 % value of the isolated case. At radii larger than about $1.5R_D$, the final $\mu_g(< R)$ falls slightly with respect to the isolated case, which means that some gas is moving to higher orbits. This can be attributed to energy and momentum transferred by the satellite during its first passages. In general, there is not much difference in the distribution produced by the two satellites. At low radii, the distribution for the satellite with $M_s = 1.2$ (Satellite 2) is about 8 % lower than that of the satellite with $M_s = 0.6$ (Satellite 1).

In the retrograde case of this encounter, the left panel of Figure 4.25 shows that Satellite 2 produces a noticeable change in the mass distribution as it is slightly higher than that of isolated evolution. This is an interesting result showing that gas is moving radially inwards in the entire disc, but it is not reaching the central regions as it happens in the prograde case. The form of the final $\mu_g(< R)$ profile is similar in shape to that of the isolated case but with a steeper slope. The effect of Satellite 1 is almost indiscernible from the final distribution in isolated evolution.

For Orbit 2 ($R_i = 6R_D$, $i = 30°$), the results for a prograde encounter with Model A are shown in the left panel of Figure 4.26, which shows that there is a marked difference between the final distribution of Satellite 1 and that of Satellite 2. The most massive satellite, Satellite 2, is driving a significant amount of gas to the central regions of the host. At $R = R_D$, the gas fraction within this radius is about 63% of the total gas mass, which represents an increase of approximately a factor of 2 with respect to isolated evolution. For the less massive satellite, although gas is moved to the inner regions, the process appears to be less efficient. At $R = R_D$, the gas fraction is $\approx 36\%$ of the total gas mass, which is about 10% more with respect to isolated evolution. However, at $R = 2R_D$, the final distribution increases $\approx 14\%$ with respect to the isolated case. Both distributions fall with respect to the distribution in isolated evolution at larger radii $R > 2R_D$, implying that gas is also being driven to higher radii by the interaction with the satellite. Since the satellite first disturbs the outer, less dense, and less bound regions of the galaxy, particles can be driven to higher orbits as the satellite passes through this regions, which may explain the distribution at large radii.

The final mass distributions for the retrograde encounters of Orbit 2 are shown in the right panel of Figure 4.26. There is no difference between the final distribution induced by the satellite and that of isolated evolution. Also, there is no difference between the distribution produced by Satellite 1 and that by Satellite 2. As this orbit takes more time to decay, it remains for a longer period disturbing only the rim of the disc. Therefore, no significant effects are produced in the gas mass distribution of the galaxy.

In the case of the simulations with Orbit 3 ($R_p = R_D$, $i = 30°$, the final gas mass distributions $\mu_g(< R)$) are shown in Figure 4.27. The left panel shows the results of the prograde orbit and the right shows those of the retrograde orbit. Both prograde and retrograde orbits produce final mass distributions with a higher mass fraction in the inner regions of the disc. For the prograde case (left panel of Figure 4.27), results are showing that Satellite 2 is driving a slightly higher amount of gas to the central regions than Satellite 1. At $R = R_D$, the enclosed mass in the simulation with Satellite 1 is approximately 42% higher than that of the isolated case, and in the simulation with Satellite 2, it is about 58% higher than in isolated evolution. For the retrograde case, the final distributions are similar for both satellites. Satellite 1 produces an increase in the enclosed mass at $R = R_D$ of $\approx 52\%$, and Satellite 2 produces an increase of about $\approx 60\%$.

In the case of Model B, a prograde encounter of a satellite in Orbit 1 produces the final distributions shown in the left panel of Figure 4.28. Qualitatively, there is no significant difference between the distribution of the interacting pair and that of isolated evolution. Calculating the difference of $\mu_g(< R)$ with respect to the distribution in isolated evolution at

$R = R_D$ shows that there is a slight decrease of $\approx 4\%$ for the simulations of both satellites. For the retrograde case (Figure 4.28, left panel), both satellites appear to be producing certain inflows as the mass distribution becomes steeper. This is more evident for Satellite 2. At $R = R_D$, the integrated mass fraction is about 2% higher for Satellite 1, and about 8% for Satellite 2 with respect to isolated evolution. The difference for the first satellite is practically negligible. However, the second satellite introduces a noticeable effect. Repeating the same calculation at $R = 2R_D$ shows that the integrated mass is $\approx 13\%$ higher for the simulation with the second satellite. This results are consistent with those obtained with Model A.

For the encounters of satellites in Orbit 2 with Model B, the left panel of Figure 4.28 shows the final gas mass distributions for a prograde orbit. In this case, it is evident that Satellite 2 ($M = 1.2$) drives a significantly higher amount of gas to the central regions, than Satellite 1 ($M = 0.6$). At $R = R_D$, the integrated gas mass fraction μ_g for the simulation with Satellte 1 is approximately 3% higher than that of the isolated case, and at $R = 2R_D$, the distribution is 10% higher. For the more massive satellite, at $R = R_D$, μ_g is about 44% higher than in the isolated case. At this point, the integrated gas mass fraction is approximately 60% of the total mass of the galaxy. At $R = 2R_D$ the integrated mass is similar to that in the simulation with the less massive satellite. At radii larger than $2R_D$, the mass distribution falls with respect to the isolated case due to the fact that gas is moved to larger orbits. For the retrograde case, shown in the right panel of Figure 4.28, results show that the satellite is not introducing any effect distinguishable from isolated evolution. For both satellites, the final distribution at $R = R_D$ is only about 1% higher with respect to isolated evolution, which is a negligible difference. These results are consistent with the simulations with Model A.

Finally, for the simulations of Orbit 3 with Model B, the final gas mass distributions are shown in Figure 4.30. Both prograde and retrograde orbits produce final mass distributions that show that gas is moving to the inner parts of the galaxy. The effect seems not to be strongly dependent on the mass of the satellite. For the prograde orbit (left panel), at $R = R_D$, the final integrated mass is approximately 21% higher for the simulation with Satellite 1, and about 8% higher than isolated evolution for Satellite 2. The difference between both distributions becomes practically negligible at higher radii. At $R = 2R_D$, both distributions are about 16% higher than that of isolated evolution. For the retrograde case (right panel of Figure 4.30), the final distributions of both satellites are similar. At $R = R_D$, the integrated gas mass increased approximately 10% with respect to the final distribution in isolated evolution.

Table 4.2 summarises the difference between the cumulative mass at R_D for the final mass distribution of the disturbed galaxy and that for the isolated distribution. This measures how much mass was gained from the outer parts of the galaxy due to the effect of the perturbation. The difference between the prograde and retrograde cases is clear for the inclined orbits (Orbits 1 and 2). The prograde orbits are able to drive a higher amount of gas than the retrograde ones. The strongest effect is produced by the prograde cases of Orbit 2, which appears to depend on the mass of the satellite. In the case of Orbit 3, both prograde and retrograde orientations are able to drive gas to within $R < R_D$. The difference between a prograde and retrograde orbit is not significant, and it appears to be weakly dependent on the mass of the satellite.

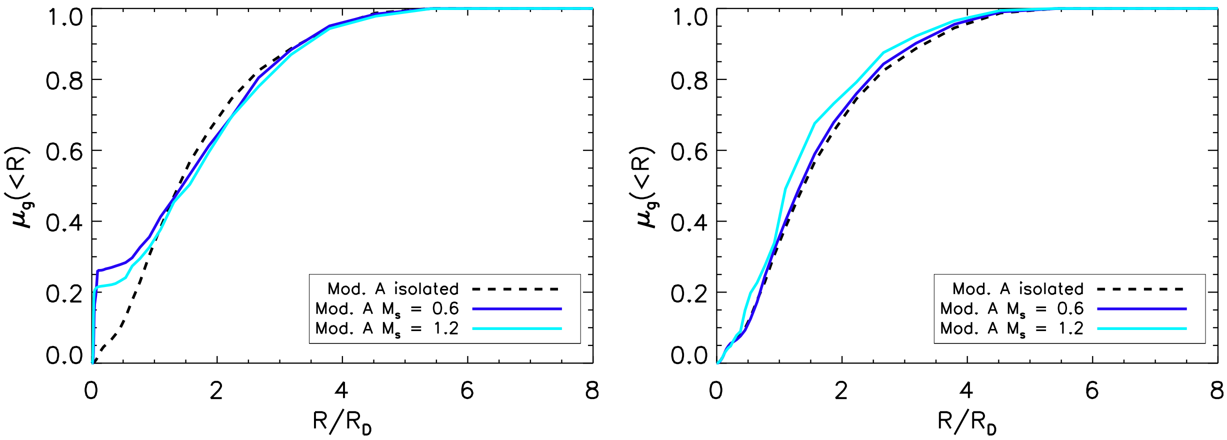

Figure 4.25: Final integrated mass fraction of the simulations of Model A with Orbit 1. The left panel corresponds to the prograde orbit and the right panel corresponds to the retrograde orbit.

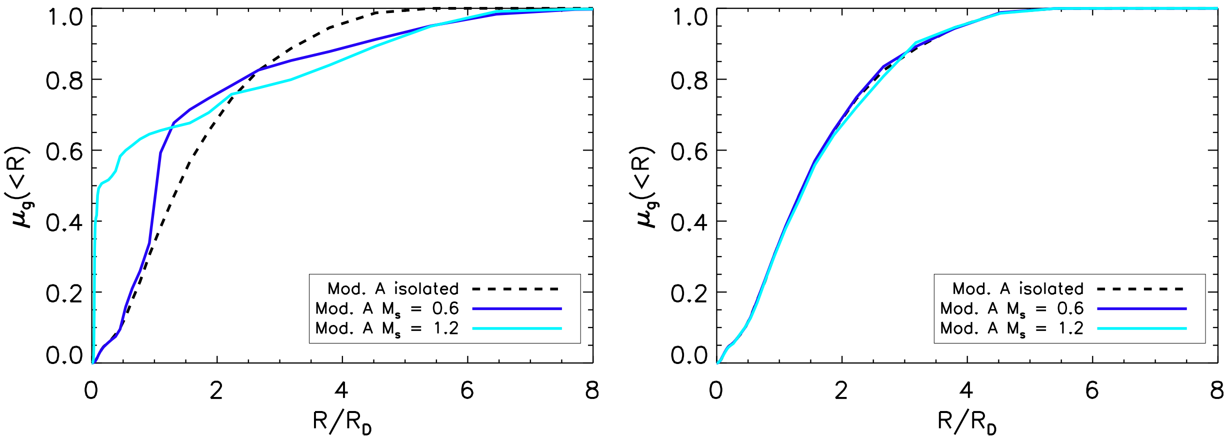

Figure 4.26: Final integrated mass fraction of the simulations of Model A with Orbit 2. The left panel corresponds to the prograde orbit and the right panel corresponds to the retrograde orbit.

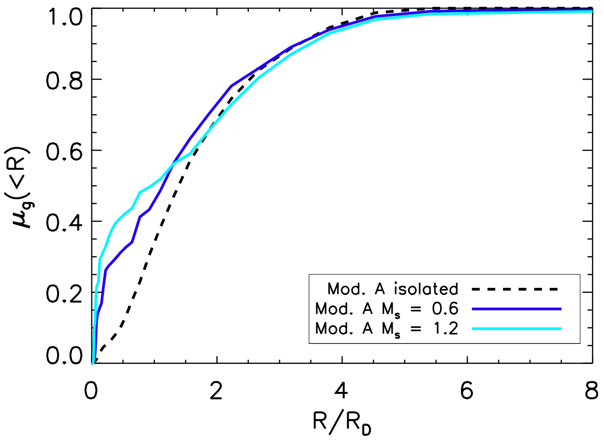

Figure 4.27: Final integrated mass fraction of the simulations of Model A with Orbit 3. The left panel corresponds to the prograde orbit and the right panel corresponds to the retrograde orbit.

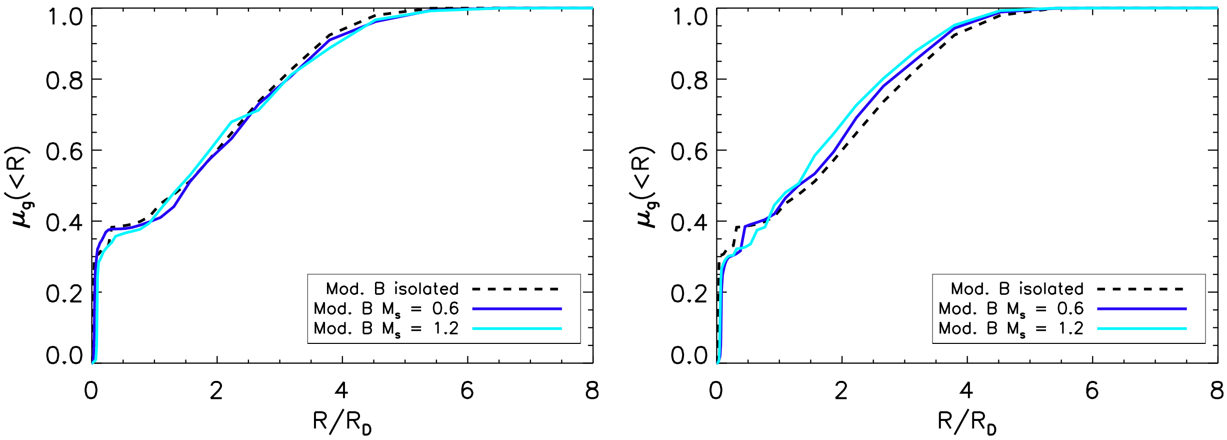

Figure 4.28: Final integrated mass fraction of the simulations of Model B with Orbit 1. The left panel corresponds to the prograde orbit and the right panel corresponds to the retrograde orbit.

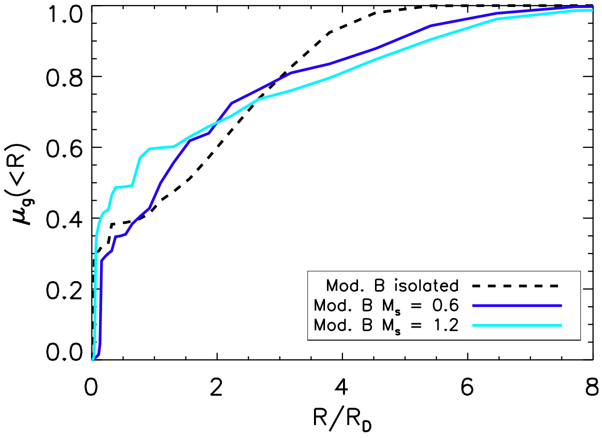

Figure 4.29: Final integrated mass fraction of the simulations of Model B with Orbit 2. The left panel corresponds to the prograde orbit and the right panel corresponds to the retrograde orbit.

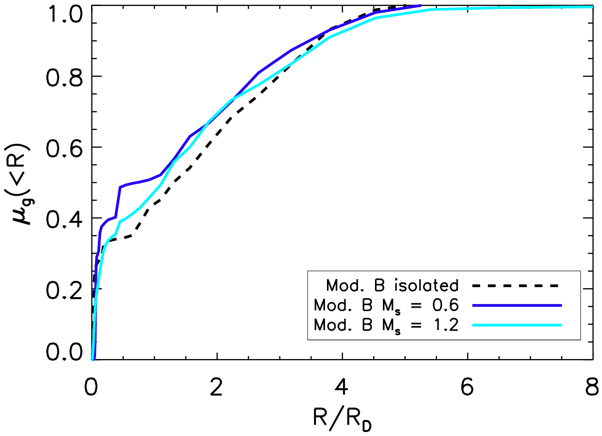

Figure 4.30: Final integrated mass fraction of the simulations of Model B with Orbit 3. The left panel corresponds to the prograde orbit and the right panel corresponds to the retrograde orbit.

Table 4.2: Mass difference between the perturbed and isolated distributions at $R = R_D$

Orbit	Prograde		Retrograde	
	$M_s = 0.6$	$M_s = 1.2$	$M_s = 0.6$	$M_s = 1.2$
Mod. A Orbit 1	0.023	0.010	0.007	0.016
Mod. A Orbit 2	0.015	0.152	0.000	-0.001 [1]
Mod. A Orbit 3	0.057	0.079	0.071	0.082
Mod. B Orbit 1	0.038	0.036	0.048	0.059
Mod. B Orbit 2	0.051	0.125	0.039	0.047
Mod. B Orbit 3	0.084	0.058	0.000	0.071

---

[1] In this case, the final gas mass distribution was slightly lower than that of isolated evolution. However, other simulations with a statistically different N-body sampling of the initial conditions should be done to confirm this trend.

4.3. Induced Gas Flows

Model A

The integrated gas mass fraction $\mu_g(< R)$, as defined in §4.2, provides an estimation of the amount of gas accumulated inside a given radius. However, the redistribution of the gas is a gradual process. Therefore, the behaviour of the fraction of gas inside a given radius as a function of time gives an estimation of the average flow rates of gas. The integrated gas mass fraction is estimated as a function of time within $R < 0.28R_D$, and $R < R_D$, which amounts to < 1 kpc and < 3 kpc, when scaled to $R_D = 3.5$ kpc. This is calculated every 0.05 Gyr. The functions for the interacting cases are compared to those of isolated evolution. The results of such calculations are described in this section. First, the results for Model A are described, followed by those for Model B.

For the case of Model A with a satellite in Orbit 1, results are shown in Figure 4.31 for a prograde encounter (left panel) and a retrograde encounter (right panel). For the prograde case, Satellite 1 ($M_s = 0.6$), plotted with a solid line, produces a significant and steady flow to a region with $R < 0.28R_D$. For Satellite 2, plotted with a dashed line, the response appears to be higher at the inner regions. At $R = R_D$, the integrated mass function μ does not show significant variations with respect to that of isolated evolution, implying that a small amount of gas is flowing from larger radii. At $t \approx 0.3\tau$, the disturbance becomes apparent at $R = R_D$. This time coincides with the first passage of the satellite with the disc. After $t \approx 0.7\tau$, the gas flow to $R < 0.28R_D$ becomes apparent, which corresponds to the approximate time that the gas is taking to reach this region. This plot is showing that a significant amount of gas in the galaxy is moving within a region with $R < R_D$, and a small amount is flowing from larger radii. For this encounter, by $t \approx 1.3$ the satellite has practically been accreted by the host. However, gas flows are still evident for a period of 3τ.

For the retrograde case of Orbit 1 (left panel of Figure 4.31), Satellite 1 produces no significant motions of the disc. However, Satellite 2 produces some flows after $t \approx 1.4\tau$. When the satellite follows Orbit 1, it has 4 passages through the disc before finally being accreted. The time when flows appear is nearly coincident with the last passages of the satellite. The behaviour of $\mu(< R)$ shows that gas is flowing to a region $R < R_D$ with the more massive satellite, but no inflows are evident at $R = 0.28R_D$. Any effect from the less massive satellite is indistinguishable from the behaviour in isolated evolution. In this case, it is evident that the more massive satellite is producing a stronger response.

The results for the simulations of a satellite in Orbit 2 and Model A are shown in Figure 4.32. For a retrograde encounter (left panel), the less massive satellite is inducing gas flows that are evident at larger radii. The more massive satellite produces a strong response across the entire galaxy. Gas flows appear at $R = R_D$ at $t \approx 1.7\tau$, which is consistent with the time at which the satellite has a second passage through the disc. At $R = 0.28R_D$, gas starts to flow at this point at $t > 0.3\tau$. For Satellite 1, about 10% of the gas mass passed through R_D in a time scale of approximately 1 orbital period. For Satellite 2, approximately 35% of the gas mass passed through this point in a scale of approximately 1.5τ. In this simulation, the highest rate occurs at $0.28R_D$. Figure 4.32 shows that, although the flow is a gradual process, it does not necessarily occur at a constant rate. For the retrograde simulations of Orbit 2, the plot on the left panel of Figure 4.32 shows that no significant inflows are observed in the inner parts of the galaxy. This is consistent with the fact that the satellite's orbit has not decayed enough to disturb the inner parts of the host system.

Figure 4.33 shows the results for a satellite in Orbit 3 interacting with Model A. The results for a prograde encounter show that both satellites produce inflows of gas in the host galaxy, with the more massive satellite producing a stronger response. A similar tendency is observed for the retrograde encounter. Both the prograde and retrograde encounters are similar in the sense that there is a certain interval where a high inflow rate is produced, followed by a more steady flow. On the other hand, flows in the retrograde case seem to occur at a later time than in the prograde case. The gas flow rate appears to be lower with the smaller satellite. For the prograde encounter, the simulation with Satellite 1 shows that, on average, approximately 20% of the total gas mass flows to the region inside $R < 0.28R_D$ in a timescale of approximately 3.5τ. At $R = R_D$, about 15% of the gas mass flows in a timescale of $\approx 3\tau$. Regarding Satellite 2, the simulation shows that at $R = 0.28R_D$ a fraction of $\approx 25\%$ of the gas mass flows to an inner region in a timescale of $t \approx 2\tau$, and a smaller flow rate is maintained afterwards. Approximately 20% of the gas mass moves to the region inside R_D in a time scale of approximately 1 orbital period. After $t = 2\tau$, no significant flows are visible.

For the retrograde case of a satellite in Orbit 3 with Model A, the gas mass fraction within $0.28R_D$ for the simulation with Satellite 1 changes in a timescale of approximately 2τ, and the amount of gas gained is equivalent to 20% of the total gas mass. At $R = R_D$, a flow rate similar to the prograde case is observed. The more massive satellite produces a stronger response. At $R = 0.28R_D$, the gas fraction begins to grow a approximately 1.3τ. A fraction of about 15% of the gas mass is gained in a scale of $\approx 0.5\tau$, then an additional 5% more is gained in about 2 orbital periods. At $R = R_D$, about 15% is gained in a time scale of approximately 1τ. After this point, mass continues to flow at a lower rate.

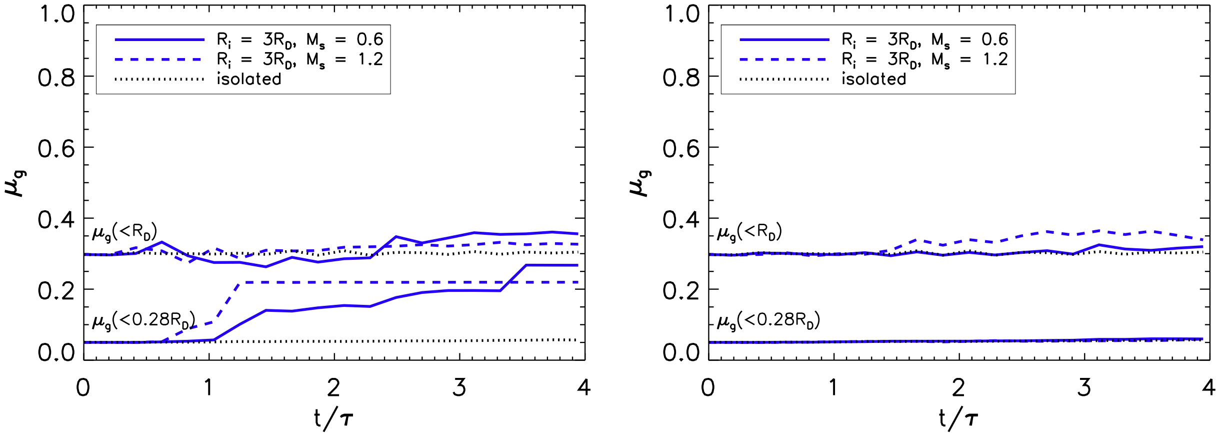

Figure 4.31: Induced gas flows in the simulations of the prograde (left panel) and retrograde (right panel) cases of Orbit 1 with Model A.

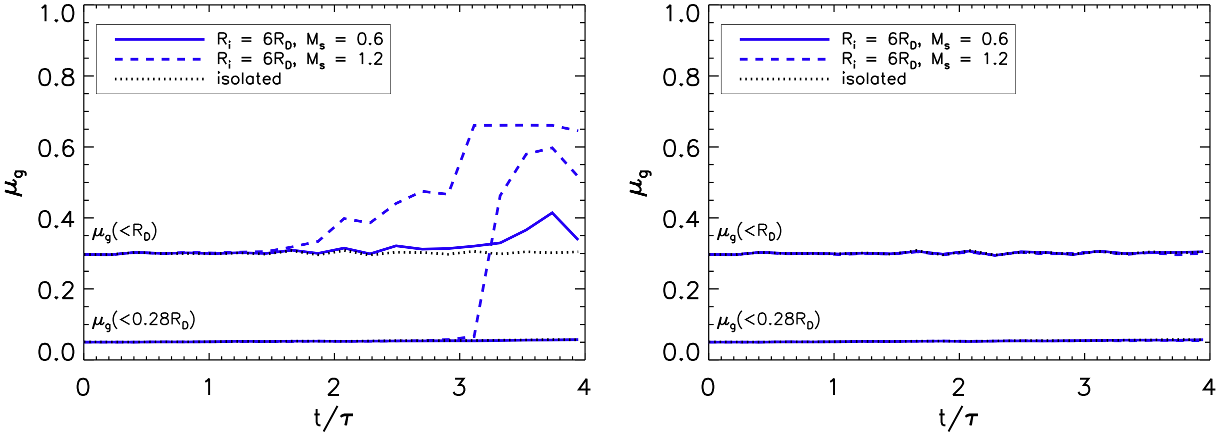

Figure 4.32: Induced gas flows in the simulations of the prograde (left panel) and retrograde (right panel) cases of Orbit 2 with Model A.

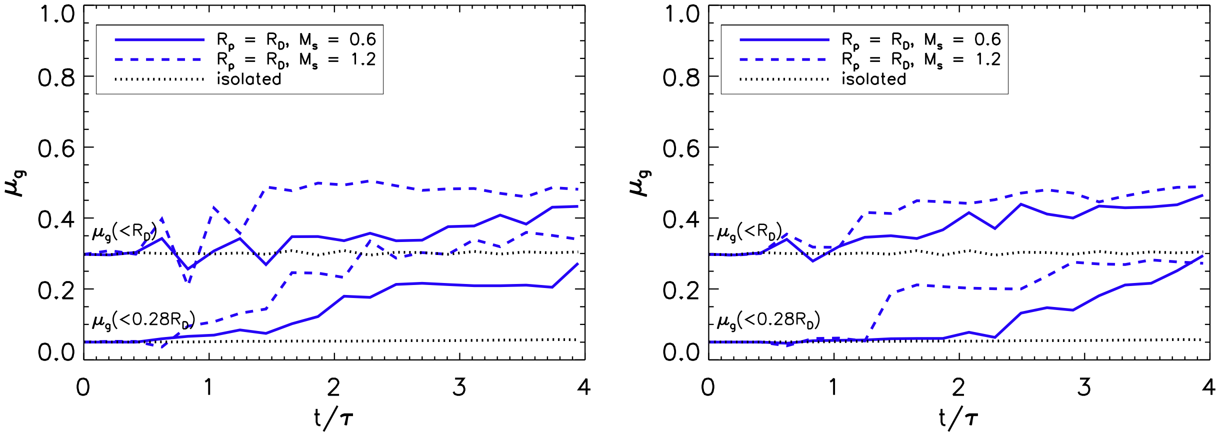

Figure 4.33: Induced gas flows in the simulations of the prograde (left panel) and retrograde (right panel) cases of Orbit 3 with Model A.

Model B

From this point onwards, the results of the simulations with Model B are described. The results for a satellite in Orbit 1 are shown in Figure 4.34, where the left and right panels show the effects of the prograde and retrograde encounters, respectively. Both the prograde and retrograde simulations show similar tendencies. Although a response is visible in both cases with both of the model satellites used, it is difficult to discern any flow different to that of isolated evolution. Additionally, this seems to be weakly dependent on the mass of the satellite. The same simulations with Model A show that this orbit produces small flow rates at $R = R_D$, which may be comparable to those produced by the effect of a bar in an isolated galaxy. At $R = 0.28R_D$, some gain is visible for the less massive satellite in a prograde orbit. When comparing the induced flows with those of isolated evolution, it can be seen that these follow a trend similar to the flows induced by the bar. From a morphological point of view, the prograde encounters produce a significant disturbance in the morphology, but it is possible that the perturbation is not strong enough to produce flows that overtake those of the bar.

For the simulations of a satellite in Orbit 2 and Model B, the results are shown in Figure 4.35. In the prograde case, the simulation with Satellite 1 shows a response not very different from that of isolated evolution. However, the simulation with Satellite 2 does show an evident response after approximately $t = 2\tau$ as there is gas flowing through a ring at $R = R_D$. At $R = 0.28R_D$, gas starts to flow after $t = 3\tau$. The fact that gas starts to flow at this region about 1 orbital period after it begins at larger radii, shows that gas is migrating from external regions to internal places of the disc. At $R = R_D$, a fraction of approximately 15% of the gas of the galaxy is passing through this point. At the inner ring with $R = 0.28R_D$, a fraction of approximately 10% of the gas of the galaxy moves inward in a timescale of $\approx 0.3\tau$. In the retrograde case, no significant response is observed, which is expected from the fact that the satellite's orbit has not decayed enough to disturb the inner regions of the host.

In the case of Orbit 3, both prograde and retrograde orbits produce noticeable gas flows in the host. These results are shown in Figure 4.36. Gas flows are produced in the retrograde case regardless of the mass of the satellite. For Satellite 1, the flow rate at $R = 0.28R_D$ is not significantly different from that of isolated evolution, but at $R = R_D$, a significant difference with respect to isolated evolution appears in the last orbital period of the simulation. In a period of approximately 1.2τ, a fraction of approximately 10% of the gas mass of the galaxy has passed to a region inside $< 0.28R_D$. For Satellite 2, the flow rate at $R = 0.28R_D$ is similar to that of isolated evolution. However, at $R = R_D$ the gas fraction starts to increase from $t \approx 0.5\tau$ to $t \approx 1.6\tau$, although some oscillations are visible. After this interval, the integrated mass fraction stays at a nearly constant value. The amount of gas that passed through this point corresponds to approximately 10% of the total gas mass. For the retrograde case, both satellites produce flows different to those of isolated evolution. For Satellite 1, the integrated mass fraction starts to grow after $t \approx 2.5\tau$ at $R = 0.28R_D$. At $R = R_D$, significant flows appear at almost 1 orbital period. The highest rate occurs between $t \approx 0.8\tau$ and $t \approx 1.4\tau$. For the satellite with $M = 1.2$, no significant flows are observed at $R = 0.28R_D$, but some appear at $t \approx 1\tau$. At $R = R_D$, the difference with respect to the flow in isolated evolution is not significant.

From the results described in this section, it is clear that Orbit 2 produces the most important effects and their magnitude depends on the mass of the satellite regardless of the model used for the host galaxy. The prograde cases of Orbit 1 suggest a slightly higher response to the more massive satellite, although it is not conclusive. In the case of Orbit 3, the coplanar orbit, flows are induced regardless of the orientation of the direction of the satellite with respect to the sense of rotation of the disc. In the simulations with Model A, higher flows are produced by the more massive satellite. However, this tendency is not so clear with Model B.

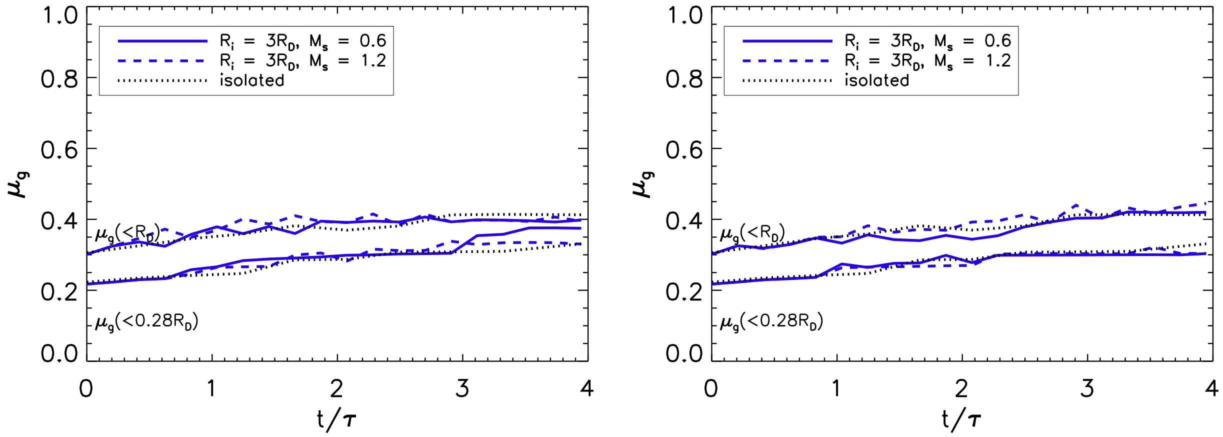

Figure 4.34: Induced gas flows in the simulations of the prograde (left panel) and retrograde (right panel) cases of Orbit 1 with Model B.

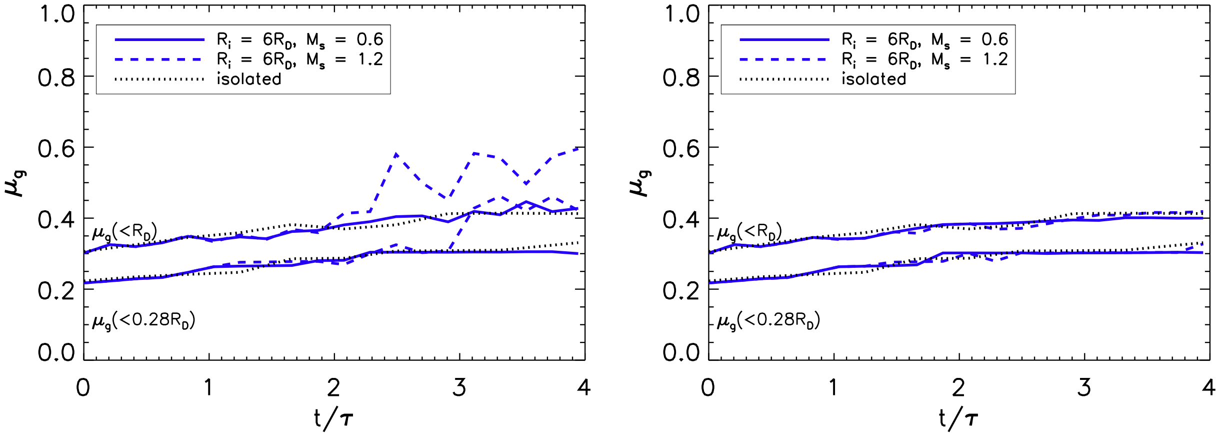

Figure 4.35: Induced gas flows in the simulations of the prograde (left panel) and retrograde (right panel) cases of Orbit 2 with Model B.

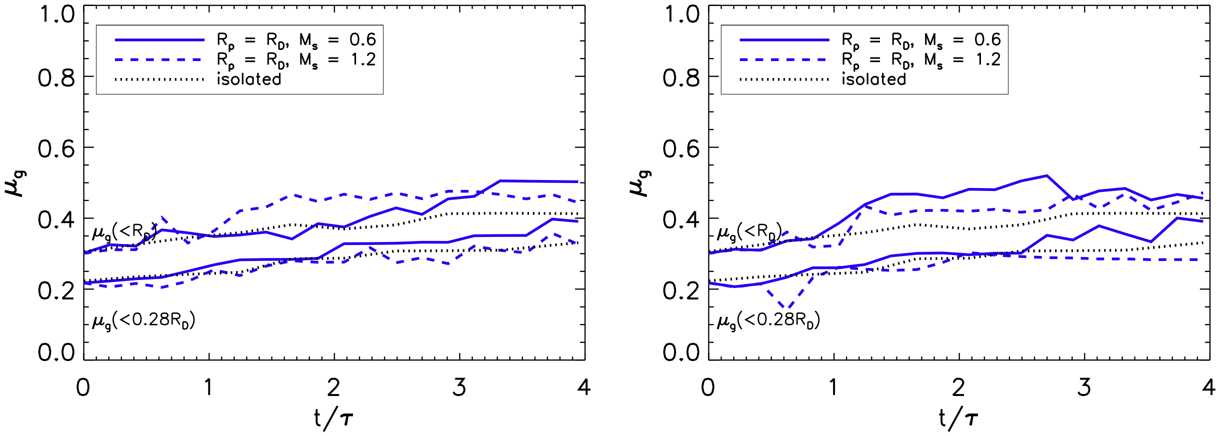

Figure 4.36: Induced gas flows in the simulations of the prograde (left panel) and retrograde (right panel) cases of Orbit 3 with Model B.

Chapter 5

Discussion

In this chapter, a discussion of the results of the preceding section is presented. First, a brief discussion of the morphology is presented, followed by a review of the final gas mass distributions and how does it compare with previous works. Then, a brief discussion regarding the induced flows is given. Finally, the implications of this work in the context of galaxies hosting active galactic nuclei (AGNs) are reviewed.

5.1. Physical Aspects

5.1.1. Morphologies

In terms of morphology, it is clear that prograde orbits produce morphological features that are evident in both the gas and stellar components. These features tend to show a higher density contrast in the gaseous component than in the stellar component. Retrograde orbits can produce a noticeable effect, though it becomes apparent after the satellite has passed several times through the disc.

The morphology of the prograde encounters found here is qualitatively similar to that obtained in Mihos & Hernquist (1994) and Hernquist & Mihos (1995). This would be expected from Orbit 2 ($R_i = 6R_D$, $i = 30°$) since it corresponds to the orbit used in these works. Satellites in prograde orbits are expected to produce higher damage on the disc since the relative velocity of the perturber with respect to disc rotation is low. Therefore, orbits of gas and stars where the satellite is passing can be significantly disturbed as they move slowly with respect to the satellite. The morphology of spiral arms in the stellar component observed in this work are similar to those of other studies of infalling satellites such as Velazquez & White (1999), Kazantzidis et al. (2008), and Kazantzidis et al. (2009). In the present thesis, satellites in the mass range between 6:1000 and ≈3:265 are used, whereas Velazquez

& White (1999) use satellites with mass ratios between ≈1:125 and ≈3:200, and in the works of Kazantzidis et al. (2008) and Kazantzidis et al. (2009), satellites with a mass ratio in the range between ≈1:000 and ≈1:38 are used. These works do not consider hydrodynamical effects.

In a recent work by Chakrabarti et al. (2011), the tidal effect of satellites in the range of 1:3 to 1:100 is studied in order to obtain models that fit the observed gas distributions of galaxies such as M51 and NGC 1512, and to explore to what extent can the mass of an interacting satellite can be inferred from the observed morphology. Chakrabarti et al. (2011) use galaxy models similar to the ones of Springel et al. (2005) and the GADGET-2 code for their simulations. Although they explore a mass range similar to that of the present work, they do not explore the effect of the satellite in terms of radial inflows. The results presented in §4.1 are similar to the morphology observed in the simulations of satellites with a mass ratio of ≈1:100 of Chakrabarti et al. (2011). On the other hand, the simulations of the retrograde orbits of the present work show that the perturbation of the satellite can be strong enough to break the axisymmetry of the disc, but it is sensitive to the mass of the satellite and the inclination with respect to the plane.

Observational studies have shown that many galaxies present *lopsided* distributions of the gaseous and stellar components. Some examples of these works are Baldwin et al. (1979), Beale & Davies (1969), Richter & Sancisi (1994), Rix & Zaritsky (1995), Zaritsky & Rix (1997), and Bournaud et al. (2005). This topic is further reviewed by Jog & Combes (2009). Matthews et al. (1998) show that a fraction of 77% of a sample of late-type galaxies show lopsided HI distributions. Bournaud et al. (2005) show that mergers with a mass ratio ≈1:10 are expected to produce lopsidedness with $m = 1$ and $m = 2$ modes. The present work shows that even less massive satellites are still capable of producing such effects, as shown in §4.1.

5.1.2. Gas Flows

The results presented in §4.2 show that satellites even in the mass range of ≈ 1:100 can produce significant flows in the host galaxy, but it is sensitive to the orbital parameters of the satellite. Additionally, the mass of the satellite was varied in order to explore the effect of a more massive satellite with the same orbital parameters. As mentioned previously, the prograde orbits produce the most noticeable effects on the final integrated gas mass fraction $\mu_g(< R)$ of the host galaxy. In the case of the non-barred galaxy (Model A), the satellite in Orbit 1 ($R_i = 3R_D, i = 30°$), drives gas to the central region of the galaxy and the inner region of the galaxy is clearly disturbed. However, the satellite in Orbit 2 ($R_i = 6R_D, i = 30°$) produces a much stronger effect, and it is also the most sensitive to the mass of the satellite. With the most massive satellite, ≈ 63% of the total gas mass was driven to $R < R_D$, whereas with the less massive satellite, about 35 % of the gas was driven to this region. This difference can be explained by the fact that a satellite in Orbit 1 passes through regions of higher density and gravitationally more bound, thus being more difficult to disturb. This effect as well as the prograde sense of the orbit favours a quick disruption of the satellite, reducing the intensity of the perturbation. In the case of Orbit 2, the satellite first disturbs the outer, less dense, and less bound regions of the galaxy. In addition to this, a stronger spiral pattern is formed in both the gas and stellar components. These non-axisymmetric features produce torques that can remove angular momentum from the gas. In the retrograde cases of Orbit 1 and 2, no significant gas flows are produced.

The prograde case of Orbit 3 ($R_{peri} = R_D, i = 0°$) shows that gas flows are induced, as dynamical effects would have been expected from a prograde orbit. In the simulations with Model A, for the less massive satellite, the final integrated mass fraction at $R = R_D$ is about 40% higher than in isolated evolution; and for the more massive satellite, it is about 58% higher. In the case of Model B, the difference between the final integrated mass fraction at $R = R_D$ is about 20%, and it does not show a dependence on the mass of the satellite. However, it is an interesting result that the retrograde case is also producing flows. In the simulations with Model A, the final integrated mass fraction at $R = R_D$ is about 60% higher with respect to isolated evolution for the less massive satellite; and about 60% higher for the more massive satellite. In the case of Model B (barred galaxy), the final gas mass distributions are similar to those of the simulations of Model A in the sense that they show a similar behaviour as a function of radius, but do not show a clear dependence with the mass of the satellite. The simulations with Model B also show that the retrograde encounter following Orbit 3 produces gas inflows which produce a final gas mass distribution that is about 10% higher than that of isolated evolution. With the satellite in this orbit, the integrated mass fraction at $R = R_D$is about 50% of the mass of the galaxy, with no clear dependence on the mass of the satellite.

In a galaxy with a barred component (Model B), gas inflows are already induced by the presence of the bar. Since Model A avoids the formation of a bar and other non-axisymmetric features, it allows to isolate the effects of the infalling satellite on the host galaxy. The simulations with Model A show that satellites with a mass ratio of ≈1:100 can still produce significant gas inflows in the host galaxy. With the most massive satellite in Orbit 2, approximately 35% of the gas mass passed through $R = R_D$ in a timescale of $t \approx 2.5\tau$. This corresponds to $\approx 1.6 \times 10^9 M_\odot$ in approximately 600 Myr. The interacting satellite induces non-axisymmetric features in the gas which can redistribute the angular momentum of the gas and produce inflows. As the gas concentrates in the spiral arms, it can loose orbital energy through dissipation and shocks can also contribute in removing energy from the gas.

With respect to shocks, although an artificial viscosity term is introduced in SPH to allow the formation of shocks, these may not be adequately represented in the current simulations. Nevertheless, the present work focuses in the large-scale dynamics of the gas, which is adequately modelled in a SPH code. Regarding the effect of non-axisymmetric features, simulations with Model A show that the cases where the most prominent features are observed, correspond to those where the largest inflows were observed. An interesting result is that of the prograde case of Orbit 3, which shows that some particular retrograde orbits can produce discernible gas flows. In this case, approximately 20% of the gas mass was driven to $R < R_D$ during the simulation. This orbit does induce non-axisymmetric features in the disc which may contribute to produce inflows. Moreover, the continuous presence of the satellite in the plane of the disc introduces an additional perturbation in the potential that can disturb the orbits of the gas and contribute to the flows. Although such a fine-tuned coplanar orbit may be rather unlikely, it does show that the cumulative effect of a retrograde orbit is not negligible. The difference between the prograde and retrograde simulations of Orbit 3 are noticeable in the flows at $R = 0.28R_D$. For the first case, about 30% of the gas moves to $R < 0.28R_D$ whereas in the second case, the fraction is slightly more than 20%. From the simulations of Model A, it can be concluded that small satellites can still have a significant dynamical effect on a disc galaxy.

The simulations with Model B show the effect of the infalling satellites within a barred galaxy. The fact that the final gas mass distributions of both the prograde and retrograde cases are similar to those of Model A supports the idea that the induced gas flows are a consequence of the disturbance of these satellites on the host galaxy. However, their evolution as a function of time is different with respect to Model B. The final gas mass distribution for the prograde case of Orbit 1 shows no significant difference to that of isolated evolution. However, the simulations with Model A show that the satellite in this orbit disturbs the gas in the inner parts of the galaxy. In the case of Model B, since the interaction takes place at a moment when the bar has already redistributed the material at the inner regions, a certain fraction of the galaxy's gas is no longer available to be further affected by the satellite. On the other hand, the simulations with Orbit 2 do show that the the interaction is contributing with gas flows. The simulations of Model B in isolated evolution show that the mass fraction at $R \approx 2.28R_D$ stays at $\approx 60\%$ during 8 orbital periods, and the gas disc extends up to about $(5 - 6)R_D$. Therefore, about 40% of the galaxy gas can still be disturbed by a very small infalling satellite at larger radii.

In the case of the simulations with Orbit 3 and Model B, these show that both the prograde and retrograde orbits produce inflows that are somewhat higher than those in isolated evolution. For the prograde orbit, the final gas mass fraction $\mu_g(< R_D)$ is about

20% higher than that of isolated evolution; and for the retrograde, orbit it is about 10% higher. The dependence of the final integrated gas mass fraction on the mass of the satellite is not significant. As seen with Model A, an interesting result is that the retrograde case of Orbit 3 produces noticeable gas inflows in Model B. In this case, slightly less than 10% of the mass of the galaxy moves to a region within $R = R_D$, but at $R = 0.28R_D$ the difference with respect to the flows produced in isolated evolution is not significant. Although the impact of a bar depends on its strength and size, it is clear that it can produce continuous inflows of gas (e. g. Athanassoula 1994). The simulations of the present work suggest that the effect of minor satellites should become important when they disturb the outer parts of a galaxy hosting a bar.

The work of Mihos & Hernquist (1994) (MH94) and Hernquist & Mihos (1995) (HM95) explored the effect of minor mergers as a mechanism for inducing activity in galaxies using a model galaxy with an isothermal dark matter halo, stellar and gas discs, with bulge and no bulge. Their model had $Q(R_\odot) = 1.5$ at the solar radius. These authors indicate that no significant gas flows are observed in isolated evolution, but do not comment in detail the effect of the presence of a bar, making a comparison with their results in this matter rather difficult. In terms of the final gas mass distribution, they obtain that approximately 50% of the gas moves to $R < R_D$ in a bulgeless galaxy, but this decreases to about 35% when the mass of the bulge is 1/3 of the disc's mass. However, it is not clear to what extent the bar has affected the gas flows.

In the present work, a NFW dark matter profile is used, also with stellar and disc components, and a bulge is included in all simulations, corresponding to $\approx 1/5$ of the disc's mass. A model galaxy with a rather high Toomre parameter ($Q = 3$), not explored in previous works, is also used. HM95 use a satellite with a Hernquist profile with $M_s = 0.1M_D$, corresponding to a mass ratio of ≈1:72 with respect to the total mass of their galaxy. In this work, however, satellites with a Plummer profile are used, with masses $M_s \approx 0.13M_d$ and $M_s \approx 0.3M_D$. As previously mentioned, this corresponds to approximate mass ratios of 6:1000 and 3:265, respectively.

Using an orbit similar to that of MH94 and HM95, which is Orbit 2, their results and those found for the less massive satellite in the present work are compared in Table 5.1. The less massive satellite used in the present work corresponds to a smaller mass ratio than that of HM95. The bulge mass of the galaxy models of this work is between the masses used by HM95. Table 5.1 shows that the simulation of Model A has a slightly higher inflow at $R = R_D$ as compared to HM95. The value of the present work is similar to the that of the less massive bulge in HM95. The results of Model B also shows values slightly higher than those of HM95. The final integrated mass functions of Orbit 2 with the less massive satellite are qualitatively similar to those of HM95, and that of Model B shares more similarities in the behaviour as a function of radius. However, the results of the present work show a higher mass fraction at $R = 2R_D$ than in HM95. A marked difference between HM95 and the present work is that the latter uses a dark matter halo, with a NFW halo that is ≈ 3.9 times more massive. A different profile may affect the dynamics of the disc as the orbital families in the central region may change, and a more massive halo implies a deeper potential well. However, the similarity in the results suggests that the details of the halo profile may not be of strong importance for the gas motions at galactic disc scales, in comparison to the total mass of the halo.

Table 5.1: Integrated mass fraction

	No bulge	$M_b = 1/9$	$M_b = 1/3$	$M_b = 1/5$ (non-barred)	$M_b = 1/5$ (barred)
$\mu(< R_D)$	50 %	45 %	35 %	45 %	46 %
$\mu(< 2R_D)$	65 %	65 %	65 %	75 %	67 %

In the present work, a set of retrograde orbits has also been explored. Such cases are relatively unexplored in the literature, as less damage is expected from satellites following these orbits. In the case of inclined orbits such as Orbit 1 and 2, no significant inflows are obtained as it would have been expected from the fact that the relative velocity with respect to the disc is high. However, a coplanar retrograde orbit such as Orbit 3 produces significant flows of gas regardless of the presence of a bar. In the case of Model A, the final gas mass fraction within $R = R_D$ increases about 60% with respect to isolated evolution, with no significant difference between simulation with the less massive satellte and the more massive one. In the case of Model B, the increase is about 12% with no clear difference with respect to the mass of the satelllite. The movement of the small satellite across the galaxy does produce morphological features that break the axisymmetry of the disc. The perturbation of the gravitational potential induced by these density features as well as the continuous presence of the satellite in the plane can maintain a certain mass inflow rate. Although such a fine-tuned orbit may be unlikely for an infalling satellite, it provides an example of a retrograde orbit that produces noticeable effects in the dynamics of the host galaxy. A situation that has not been explored or reported earlier in similar works as this.

In terms of the mass flow rate, the results described in §4.3 show that the rate at which gas flows to the central regions depends on the orbital parameters of the infalling satellite. The differences observed between simulations with different satellite masses suggest some dependence on this parameter. However, it is not possible to find any clear tendency as only a limited sample of the orbital parameter space and the mass range of small satellites has been explored. The integrated gas fraction up to $R = 0.28R_D$ and $R = R_D$ was compared. In the simulations of Model A, it is shown that both satellites, when following Orbit 1 in a prograde sense, disturb the inner region of the galaxy. However, the less massive satellite produces a steady flow rate whereas the more massive satellite produces a rather sudden flow of gas. This is concluded from the difference in the time interval in which the flows take place in Figure 4.31 of §4.3. The gas distribution is disturbed at both $R = R_D$ and $R = 0.28R_D$; nonetheless, there is a delay of approximately $0.5\tau \approx 120$Myr between the moment at which gas starts flowing through $R = R_D$ and that when it flows through $R = 0.28R_D$. The contrast between satellite masses and the mentioned time delay becomes more important for Orbit 2. For the satellite with $M = 0.6$ simulation, gas flows through $R = R_D$ are produced, but it does not appear to be moving down to $R = 0.28R_D$. However, when the satellite's mass is doubled, the gas flow rate at $R = R_D$ is approximately a factor of 2 higher, and the perturbation is able to drive gas down to $R = 0.28R_D$. In this case, the time delay is of $\approx 1.5\tau \approx 360$Myr. For the retrograde cases of these orbits no significant flows are observed.

In the case of Orbit 3, the time delay between the flows starting at $R = R_D$ and at $R = 0.28R_D$ is not as evident as in the previous cases. The final integrated gas fraction at $R = R_D$ only increases with increasing satellite mass by $\approx$10% for Model A. In the rest of the simulations, the dependence on the mass of the satellite is not clear. The more massive satellite produces faster inflows, as it can be seen in Figure 4.33. The amount of displaced gas does not appear to depend significantly on whether the orbit is prograde or retrograde. Although the satellite spends more time in the plane of the galaxy when placed in this orbit, the gas inflow is not as significant as in Orbit 2. It is possible that, since the satellite in Orbit 2 is circular, some resonance effects may be introduce that further enhance gas motions. However, the satellite in Orbit 3 is capable in inducing gas flows to the inner regions of the galaxy ($R < 0.28R_D$) regardless of the mass of the satellite or the orientation of the orbit.

For the simulations of Model B, results that show trends similar to those of Model A are obtained. Because there are flows in isolated evolution due to the bar, the results of these simulations are compared with the changes in integrated mass fraction that occur in isolated evolution. In most cases, it is difficult to see a significant difference between isolated evolution and the disturbed galaxy except for Orbit 2. However, in this orbit, the less massive satellite produces no significant difference with respect to isolated evolution. However, as the mass of the satellite is increased, flows are produced that lead to a final $\mu_g(< R_D)$ about 50% higher than that of isolated evolution. The time delay between the flows starting at $R = R_D$ and at $R = 0.28R_D$ is $\approx \tau \approx 240$ Myr. For this simulation, approximately 20% of the gas mass of the galaxy moved to within $R = R_D$, which corresponds to a mass of $\approx 8.9 \times 10^8 M_\odot$. In the case of Orbit 3, the difference with respect to isolated evolution is smaller than in Orbit 2, and the dependence on the satellite mass is less evident. Nevertheless, the satellite in this orbit is able to produce a flow rate that is about a factor of 2 higher than that of isolated evolution. In spite of the presence of a bar and the bulge, satellites in this orbit induce flows to the central regions of the galaxy regardless of whether the orbit is prograde or not.

The simulations with a non-barred galaxy (Model A) have shown that satellites in the mass range of ≈1:100 can produce significant flows to the central regions of the host. This model allows the study of the effects of the satellite in a system that initially lacks important non-axisymmetric features such as a bar or prominent spiral structure. The result may be sensitive to the orientation of the orbit as well as to the mass of the satellite. The simulation with the less massive satellite shows that gas inflows are produced for all prograde orbits but it is difficult to reach the region within $R = 0.28R_D$, except for the coplanar orbit. Increasing the mass of the satellite by a factor of 2, produces an increase of a factor of ≈ 1.5 in the final integrated gas mass fraction at $R = R_D$ in the case of Orbit 2. Hernquist & Mihos (1995) indicate that it is possible that the presence of a bulge may act as a regulator of the flow by introducing an Inner Lindblad Resonance. However, the galaxy models used include a bulge and there are cases where the final gas mass distribution was similar to the simulation with bulgeless models of HM95.

Model B has allowed to quantify the effects of the satellite in terms of gas motions considering the presence of the bar. The gas distributions show trends similar to those of Model A, supporting the argument that these are a consequence of the perturbation of the disc produced by interaction with the satellite. In the case of Orbit 2, a the fraction of gas within $R = R_D$ is about 45% of the gas of the galaxy for the less massive satellite, and it is about 60% of the gas for the more massive satellite. For the more massive satellite, this corresponds to a difference of 30% with respect to isolated evolution. For Orbit 3, gas reaches the central regions regardless of whether its prograde or retrograde, and the integrated gas fraction is higher than that of isolated evolution. In most cases, gas flows from regions where $R > R_D$ suggesting that the interaction is effective in driving gas from outer regions of the galaxy.

Because the interaction with the satellite induces the formation of features such as arms, these contribute to torques that may remove angular momentum from the gas (e. g. Alexander & Hickox 2012, Hopkins & Quataert 2010, Combes 1994). These torques are important at larger scales (Hopkins & Quataert 2010). Shocks in spiral arms may be another contributing factor (Kim & Kim 2014). Although it is not possible to asses adequately the effect of shocks in this work, it is a physical mechanism that may operate at some scales of the gas disc, and it may contribute to additional flows. When comparing with previous works, the results of the present work suggest that the cusp of the dark matter profile may not have an important effect in the gas flows. The total mass of the halo is a more important parameter, since it affects the depth of the potential well.

5.2. Astronomical Applications

5.2.1. Perturbed Discs

Several isolated galaxies (see for example Karachentsev 1972) show signs of disturbances like lopsidedness. However, there is no evidence of the presence of similar companions in their vicinity. Due to the low surface brightness of dwarf galaxies, It is difficult to determine observationally if they have a population of small satellites. According to the standard galaxy formation scenario (e. g. Mo et al. 2010), a significant population of satellites is expected around galaxies. According to Moore et al. (1999), this implies that galactic discs will have experienced of the order of thousands of minor interactions leading to impulsive shocks and resonant heating. The present work shows that even satellite galaxies, smaller than about the size of the Small Magellanic Cloud, can induce lopsided density distributions in galaxies similar to the Milky Way. Furthermore, their effects may be more appreciable in the HI gas maps of galaxies.

Face-on galaxies sometimes show asymmetries that are not attributable to medium-size satellites, comparable to the Large Magellanic Cloud. An example of such asymmetries can be observed in images of NGC 5230 [1].The results of the present work show that such small satellites around such galaxies may induce these morphological features. Considering that Milky Way-sized haloes may have had an active accretion history, these satellites can still have an impact on these systems.

5.2.2. Active Galactic Nuclei

The present work also has implications in the triggering of nuclear activity in galaxies. In the context of Active Galactic Nuclei (or AGNs), it is widely accepted that mergers are a triggering mechanism for nuclear activity (e. g Alexander & Hickox 2012), but it is not clear from an observational standpoint to what extent minor mergers and perturbations of small satellites can have an impact. Additionally, there is no clear correlation between the presence of an AGN and a bar in the host galaxy (e. g. Beckmann & Shrader 2012). The simulations with Model A may have particular implications in this context.

---

[1] The author is grateful to Dr. Leonel Gutiérrez for pointing this out. Information and images of this galaxy may be obtained from the NED database.

For a galaxy with a weak bar or no bar component, these interactions can be a viable mechanism for inducing important gas flows to the central regions. Other effects such as star formation and feedback should also be considered in a more complete modelling. In the case of barred galaxies, the simulations of Model B indicate that these minor satellites can have an important effect as long as the presence of the bar has not depleted significant amounts of gas. Nevertheless, gas from the outer regions of the galaxy may still be relatively undisturbed and be redistributed by the interaction. Most of the prograde orbits seem favourable for driving gas to the central regions ($R < 0.28R_D$). When scaled to $R_D = 3.5$ kpc, it means that the gas is reaching the inner kpc of the host. When the satellite disturbs the outer parts of the galaxy, it is found that it can take up to $\approx \tau$ for the gas to reach the central regions. This result is relevant in the sense that if these mergers leave transient morphological features, they may dissolve before any activity is triggered in the nuclear region. In the case of the retrograde circular orbits, no flows were obtained, but noticeable morphological effects were apparent, specially with the more massive satellite. Although these orbits may not be relevant in the context of nuclear activity, they may be relevant in triggering activity such as star formation.

As a final comment, it is noted that in some of our simulations, it is found that a gas fraction comparable to 50% of the gas of the galaxy, corresponding to $\approx 2.2 \times 10^9 M_\odot$, ends at the region where $R < R_D$. In the most extreme case (Orbit 2), approximately 35% of the gas moves to within $R < R_D$ from outer regions during the simulation, which corresponds to a mass of $1.5 \times 10^9 M_\odot$. In the simulations of this work, the gas is driven to the central regions of the galaxy in a typical timescale of approximately or greater than 240 Myr. In simulations of gas flows in interacting galaxies, Hopkins & Quataert (2010) find an accretion rate of $\dot{M} \sim 10 M_\odot \, \mathrm{yr}^{-1}$ at scales of 0.1 pc. Analysis of the NUGA sample of active galaxies by Haan et al. (2009) finds for nearby spiral galaxies accretion rates in the range of $0.01 - 50 M_\odot \, \mathrm{yr}^{-1}$ at scales of from 1kpc to 10pc with typical flow timescales of 10^8 years. In a numerical study of fly-by interactions, Montuori et al. (2010) find typical timescales for inflows also in the order of 10^8 years. These are similar to the timescale for the gas flows found in the present work. Assuming a mass flow rate of $\sim 10 M_\odot \, \mathrm{yr}^{-1}$ (e. g. Hopkins & Quataert 2010) in a timescale of 240 Myr, the amount of accreted gas is $2.4 \times 10^9 M_\odot$, which is comparable to the fraction of gas that moves to within $R = R_D$ found in some of the simulations of the present work. The results found in the present thesis may also be relevant in the context of driving star formation activity. According to R. C. Kennicutt (1998), displacing a fraction of up to 50% of the gas of the galaxy may be needed to fuel the star formation observed in some active galaxies.

Chapter 6

Conclusions and Future Work

In the present work, the effects of small satellites in inducing gas flows in a disc galaxy have been explored. The host galaxy consists of a dark matter halo with a Navarro-Frenk-White density profile, stellar and gas discs with an exponential density profile, and a bulge with a Hernquist profile. The satellites have a mass ratio of 0.005 and 0.011 with respect to the total mass of the galaxy, which have been modelled as collisionless systems following a Plummer density profile.

Two model galaxies are considered: a non-barred galaxy (Model A) and a barred galaxy (Model B). Because the presence of a bar induces gas flows and redistributes material in isolated galaxies, a model that lacks such a perturbation is ideal to isolate the perturbation that the infalling satellite generates, motivating the use of Model A. However, there is a significant fraction of galaxies hosting a bar, thus Model B allows to study the effect of such small satellites in the context of these galaxies.

The satellites were placed in three different orbits. The first two orbits are circular with initial radii $R_i = 3R_D$ and $6R_D$, where R_D is the scale length of the disc, and with an initial inclination of $i = 30°$. The third orbit is a coplanar orbit with a pericentre passage at $R = R_D$ and an apocentre at $R \approx 6R_D$. The prograde and retrograde cases of these orbits have been considered. These orbits are chosen because they are extreme cases that give a measure of the upper limits of the effects that can be produced and the disc. The second orbit has also used in previous works, providing a point of comparison of previous results with those obtained in the present work. The two satellite masses, two galaxy models, and the six orbits amounted to a total of 24 simulations of the interacting galaxies.

The main results are summarised as follows:

- In terms of morphology, the prograde circular orbits introduce significant perturbations in the gas and the stellar components of the galaxy. In the case of the retrograde cases, the more massive satellite produces a final asymmetric density distribution. Both prograde and retrograde coplanar orbits introduce noticeable perturbations in the density of the host galaxy. Given the small mass ratios of the satellites, it is an interesting result that these small satellites can still produce observable effects on the disc of the host.

- Satellites with these small mass ratios still produce significant gas flows in the disc of the host. However, it depends on the orientation of the orbit and the mass of the satellite. Simulations with a non-barred galaxy (Model A) show that the induced perturbations and gas flows are an effect of the infalling satellite. The simulations with a barred galaxy (Model B) show that the satellite can still produce gas flows in such a system. The simulations with both models show that the highest inflows are produced by the prograde orbit with $R_i = 6R_D$, $i = 30°$, where a quantity up to $\approx 60\%$ of the gas mass of the galaxy is driven to the region within $R = R_D$. The retrograde circular orbits do not show significant inflows. However, both the coplanar prograde and retrograde orbits are able to produce gas inflows, taking a fraction of $\approx 50\%$ of the gas mass to a region within R_D.

- The integrated mass up to radii of $R = 0.28R_D$ and $R = R_D$ is calculated as a function of time, showing that the mass inflows are not gradual, but are sensitive to the orbit and the mass of the satellite. In the case of the circular orbits, with $R_i = 3R_D$, some gradual flows are produced that are not very sensitive to the mass of the satellite. The orbit with $R_i = 6R_D$ produces very rapid flows, and the response of the gas increases significantly when the mass of the satellite is doubled. Most of the gas flows occur in a time scale of $\sim \tau$, where τ is the orbital period of the galaxy. This orbit disturbs gas that is distributed at larger radii in the galaxy, and flows at $R = R_D$ and $R = 0.28R_D$ are observed. The gas arrives at $R = R_D$ and, after a timescale of $\approx \tau \approx 240$ Myr, it starts to flow down to the innermost region. The response of the galaxy to this orbit is similar in both the non-barred and barred models, and is more sensitive to the mass of the satellite. The simulations with the coplanar orbit show that both satellites produce rather gradual flows regardless of whether the orbit is prograde or retrograde, and it does not depend strongly on the mass of the satellite or the presence of the bar.

- Small satellites with mass ratios in the range $\approx 1 : 100$ can still produce observable distortions in the gas and stellar components of the galaxy. This shows that these minor interactions can be a mechanism that induces lopsidedness and asymmetric distributions in galaxies.

- This work also has shown that small satellites can induce important gas flows to the central regions of a disc galaxy, which is relevant in the context of fuelling active galactic nuclei.

Cosmological simulations, consistent with the ΛCDM model, have shown that many of these small satellites can exist around galaxies similar in mass to the Milky Way. The effect of infalling satellites in a cosmological context has been studied previously considering the stellar component of the host galaxy, but not taking into account hydrodynamical effects. The effect of these small substructures on the gaseous component of disc galaxies has not been explored. Therefore, it is an interesting continuation of this work to make similar simulations with infalling satellites having initial conditions derived from cosmological simulations, in order to asses their effect in terms of gas flows to the central regions of the host. Also, it would be relevant to include the effect of star formation and feedback in these models to study their impact on the induced flows.

Bibliography

S. Aarseth. *Gravitational N-Body Simulations.* Cambridge University Press, 2003.

S. Aarseth. Dynamical evolution of clusters of galaxies, I. *MNRAS*, 126:223, 1963.

J. J. Adams, J. D. Simon, M. H. Fabricius, R. C. E. van den Bosch, J. C. Barentine, R. Bender, K. Gebhardt, G. J. Hill, J. D. Murphy, & R. A. Swaters. Dwarf Galaxy Dark Matter Density Profiles Inferred from Stellar and Gas Kinematics. *MNRAS*, 440:208, 2014.

L. A. Aguilar. El problema de N cuerpos en la astronomía. *Rev. Mex. de Física*, 38:701, 1991.

D. M. Alexander & R .C. Hickox. What drives the growth of black holes? *New Astronomy Reviews*, 407:93, 2012.

H. Arp. *Atlas of Peculiar Galaxies.* California Inst. of Technology, 1966.

E. Athanassoula. The existence and shapes of dust lanes in galactic bars. *MNRAS*, 259:345, 1990.

L. Athanassoula. Gas Dynamics and Star Formation in and around Bars. In *Mass-Transfer Induced Activity in Galaxies*, page 143. Cambridge University Press, 1994.

J. E. Baldwin, D. Lynden-Bell, & R. Sancisi. Lopsided galaxies. *MNRAS*, 193:313, 1979.

D. Balsara. von Neumann stability analysis of smoothed particle hydrodynamics –suggestions for optimal algorithms. *JCoPh*, 121:357, 1995.

J. Barnes. Interactions and Mergers in Galaxy Formation. In *The Formation and Evolution of Galaxies*, page 403. Cambridge University Press, 1994.

J. Barnes. Dynamics of galaxiy interactions. In *Galaxies: Interactions and Induced Star Formation*, page 275. Springer, 1996.

J. Barnes & L. Hernquist. Fueling starburst galaxies with gas-rich mergers. *ApJ*, 370:L65, 1991.

J. Barnes & L. Hernquist. Transformations of Galaxies. II. Gasdynamics in Merging Disk Galaxies. *ApJ*, 471:115, 1996.

J. Barnes & P. Hut. A hierarchical $O(N \log N)$ force-calculation algorithm. *Nature*, 324:446, 1986.

J. Barnes & P. Hut. Error Analysis of a Tree Code. *ApJS*, 70:389, 1989.

J. Barnes & S. D. M. White. Shock Simulation by the Paricle Method SPH. *MNRAS*, 211: 753, 1984.

J. E. Barnes & L. Hernquist. Dynamics of Interacting galaxies. *ARA&A*, 30:705, 1992.

G. Battaglia, A. Helmi, E. Tolstoy, M. Irwin, V. Hill, & P. Jablonka. The Kinematic Status and Mass Content of the Sculptor Dwarf Spheroidal Galaxy. *ApJ*, 681:L13, 2008.

J. S. Beale & R. D. Davies. Neutral Hydrogen Asymmetry in the Galaxy M101 as Evidence for Tidal Effects. *Nature*, 193:313, 1969.

V. Beckmann & C. Shrader. *Actice Galactic Nuclei*. Wiley-VCH, 2012.

K. Bekki & K. C. Freeman. Formation of ω Centauri from an ancient nucleated dwarf galaxy in the young Galactic disc. *MNRAS*, 346:L11, 2003.

A. J. Benson. Orbital parameters of infalling dark matter substructures. *MNRAS*, 634:551, 2005.

A. J. Benson. Galaxy formation theory. *Physics Reports*, 495:33, 2010.

G. Bertin. *Dynamics of Galaxies*. Cambridge University Press, 2000.

J. Binney & S. Tremaine. *Galacyic Dynamics*. Princeton University Press, 2008.

F. Bournaud, F. Combes, C. J. Jog, & I. Puerari. Lopsided spiral galaxies: evidence for gas accretion. *A&A*, 438:507, 2005.

M. A. Breddels & A. Helmi. Model comparison of the dark matter profiles of Fornax, Sculptor, Carina, and Sextans? *A&A*, 558:A35, 2013.

J. S. Bullock, K. R. Stewart, M. Kaplinghat, E. J. Tollerud, & J. Wolf. Stealth galaxies in the halo of the Milky Way. *ApJ*, 717:1043, 2010.

A. Burkert. The Structure of Dark Matter Halos in Dwarf Galaxies. *ApJL*, 477:L25, 1995.

G. Carraro, C. Lia, & C. Chiosi. Galaxy formation and evolution - I. The Padua tree-sph code (pd-sph). *MNRAS*, 297:1021, 1998.

S. Chakrabarti, F. Bigiel, P. Chang, & L. Blitz. Finding Dwarf Galaxies from Their Tidal Imprints. *ApJ*, 743:35, 2011.

P. Chang. Gas Shepherding by an Infalling Satellite. *ApJ*, 684:236, 2008.

C. Clarke & R. Carswell. *Principles of Astrophysical Fluid Dynamics.* Cambridge University Press, 2007.

F. Combes. How Galaxies Accrete Mass and Evolve: Spiral Waves and Bars, Warps, and Polar Rings. In *The Formation and Evolution of Galaxies*, page 317. Cambridge University Press, 1994.

P. Cuddeford. An analytic inversion for anisotropic spherical galaxies. *MNRAS*, 414:253, 1991.

W. J. G. de Blok, F. Walter, E. Brinks, C. Trachternach, S-H. Oh, & R. C. Kennicutt Jr. High-Resolution Rotation Curves and Galaxy Mass Models from THINGS. *AJ*, 136:2648, 2008.

G. de Vaucouleurs. Classification and Morphology of External Galaxies. *Handbuch der Physik*, 53:275, 1959.

W. Dehnen. Simple Distribution Functions for Stellar Disks. *AJ*, 118:1201, 1999.

W. Dehnen. A Very Fast and Momentum-conserving Tree Code. *ApJ*, 536:L39, 2000.

C. L. Dobbs, C. Theis, J. E. Pringle, & M. R. Bate. Simulations of the grand design galaxy M51: a case study for analysing the tidally induced spiral structure. *MNRAS*, 403:625, 2010.

D. Donnelly & E. Rogers. Symplectic Integrators: An Introduction. *Am. J. Phys.*, 73:938, 2005.

B. T. Draine. *Physics of the Interstellar and Intergalactic Medium.* Princeton University Press, 2011.

G. S. Fishman. *A First Course in Monte Carlo.* Thomson, 2006.

T. Fukushige & J. Makino. On the Origin of Cusps in Dark Matter Halos. *ApJL*, 477:L9, 1997.

G. Gentile, A. Burkert, P. Salucci, U. Klein, & F. Walter. The Dwarf Galaxy DDO 47 as a Dark Matter Laboratroy: Testinc Cusps Hiding in Triaxial Halos. *ApJL*, 634:L145, 2005.

R. A. Gingold & J. J. Monaghan. Smoothed particle hydrodynamics: theory and application to non-spherical stars. *MNRAS*, 181:375, 1977.

Qi Guo, S. D. M. White, M. Boylan-Kolchin, G. De Lucia, G. Jauffmann, G. Lemson, C. Li, V. Springel, & S. Weinmann. From dwarf spheroidals to cD galaxies: simulating the galaxy population in a ΛCDM cosmology. *MNRAS*, 740:101, 2011.

S. Haan, E. Schinnerer, E. Emsellem, S. García-Burrillo, F. Combes, C. G. Mundell, & H. W. Rix. The dynamical and chemical evolution of dwarf spheroidal galaxies. *A&A*, 501:189, 2009.

Y. Hashimoto, Y. Funato, & J. Makino. To Circularize or Not To Circularize?-Orbital Evolution of Satellite Galaxies. *ApJ*, 582:196, 2003.

D. Heggie & P. Hut. *The Gravitational Million-Body Problem: A Multidisciplinaty Approach to Star Cluster Dynamics*. Cambridge University Press, 2003.

L. Hernquist. N-body Realizations of Compound Galaxies. *ApJS*, 86:389, 1993.

L. Hernquist. Performance characteristics of tree codes. *ApJS*, 64:715, 1987.

L. Hernquist. An Analytical Model for Spherical Galaxies and Bulges. *ApJ*, 356:359, 1990.

L. Hernquist & N. Katz. TREESPH - A unification of SPH with the hierarchical tree method. *ApJS*, 149:135, 1985.

L. Hernquist & J. C. Mihos. Excitation of activity in galaxies by minor mergers. *ApJ*, 448: 41, 1995.

P. F. Hopkins & E. Quataert. How do massive black holes get their gas? *MNRAS*, 407:1529, 2010.

F. Hoyle & W. A. Fowler. On the nature of strong radio sources. *MNRAS*, 125:169, 1963.

P. Hut & J. Makino. The Art of Computational Science: The Kali Code, 2009. URL `http://www.artcompsci.org/kali/vol/plummer/volume9.pdf`.

P. Hut, J. Makino, & S. McMillan. Building a better leapfrog. *ApJL*, 443:L93, 1995.

A. Jenkins, C. S. Frenk, S. D. M. White, J. M. Colberg, S. Cole., A. E. Evrard, H. M. P. Couchman, & N. Yoshida. The mass function of dark matter haloes. *MNRAS*, 321:372, 2001.

C. J. Jog & F. Combes. Lopsided Spiral Galaxies. *Physics Reports*, 471:75, 2009.

I. D. Karachentsev. Catalogue of isolated pairs of galaxies in the northern hemisphere. *Soobshch. Spets. Astrofiz. Obs.*, Vyp. 7:92, 1972.

G. Kauffman, S. D. M White, & B. Guiderdoni. N-body Realizations of Compound Galaxies. *MNRAS*, 264:201, 1993.

S. Kazantzidis, J. Magorrian, & B. Moore. Generating Equilibrium Dark Matter Halos: Inadequacies of the Local Maxwellian Approximation. *ApJ*, 601:37, 2004.

S. Kazantzidis, J. S. Bullock, A. R. Zentner, A. V. Kravtsov, & L. A. Moustakas. Cold Dark Matter Substructure and Galactic Disks. I. Morphological Signatures of Hierarchical Satellite Accretion. *ApJ*, 688:254, 2008.

S. Kazantzidis, A. R. Zentner, A. V. Kravtsov, J. S. Bullock, & V. P. Debattista. Cold Dark Matter Substructure and Galactic Disks. II. Dynamical Effects of Hierarchical Satellite Accretion. *ApJ*, 700:1896, 2009.

S. Khchfar & A. Burkert. Orbital parameters of merging dark matter halos. *A&A*, 445:603, 2006.

Y. Kim & W.-T. Kim. Gaseous spiral structure and mass drift in spiral galaxies. *MNRAS*, 440:208, 2014.

I. R. King. The structure of star clusters. III. Some simple dymamical models. *ApJ*, 71:64, 1966.

I. R. King. Basic Galacyic Dynamics. In *The Milky Way as a Galaxy*, page 117. University Science Books, 1989.

H. Kinoshita, H. Yoshida, & H. Nakai. Symplectic Integrators and their Application to Dynamical Astronomy. *Celestial Mechanics and Dynamical Astronomy*, 50:59, 1990.

A. Klypin, A. V. Kravtsov, O. Valenzuela, & F. Prada. Where are the missing satellites? *ApJ*, 522:82, 1999.

A. Klypin, H. Zhao, & R. Somerville. ΛCDM-based Models for the Milky Way and M31. I. Dynamical Models. *ApJ*, 573:597, 2002.

K. Kuijken & J. Dubinski. Nearly self-consistent disc-bulge-halo models for galaxies. *MNRAS*, 277:1341, 1995.

S. Kwok. *Physics and Chemistry of the Interstellar Medium.* University Science Books, 2007.

J. Lequeux. *The Interstellar Medium.* Springer-Verlag, 2005.

E. L. Lokas, S. Kazantzidis, J. Klimentowski, L. Mater, & S. Callegari. The Stellar Structure and Kinematics of Dwarf Spheroidal Galaxies Formed by Tidal Stirring. *ApJ*, 708:1032, 2010.

L. B. Lucy. A numerical approach to the testing of the fission hypothesis. *AJ*, 181:1013, 1977.

J. Makino. Vectorization of a Treecode. *JCoPh*, 87:148, 1990.

L. D. Matthews, W. van Driel, & J. S. Gallagher III. High-Resolution, High Signal-to-Noise, Global HI Spectra of Southern, Extreme Late-Type Spiral Galaxies. *AJ*, 116:2196, 1998.

P. J. McMillan & W. Dehnen. Initial conditions for disc galaxies. *MNRAS*, 378:541, 2007.

E. Merlin, U. Buonomo, T. Grassi, L. Piovan, & C. Chiosi. EvoL: the new Padova Tree-SPH parallel code for cosmological simulations. I. Basic code: gravity and hydrodynamics. *A&A*, 513:A36, 2010.

E. Merlin, C. Chiosi, L. Piovan, T. Grassi, U. Buonomo, & F. La Barbera. Formation and evolution of early-type galaxies - III. Dependence of the star formation history on the total mass and initial overdensity. *MNRAS*, 427:1530, 2012.

D. Merritt. Distribution functions for spherical galaxies. *MNRAS*, 214:25, 1985.

J. C. Mihos & L. Hernquist. Triggering of starbursts in galaxies by minor mergers. *ApJ*, 425: L13, 1994.

S. Mikkola. A comparison of initially bound and unbound three-body systems. *MNRAS*, 223:757, 1989.

S. Mikkola & J. Hietarinta. A numerical investigation of the one-dimensional Newtonian three-body problem. *Celestial Mechanics and Dynamical Astronomy*, 46:1, 1989.

H. Mo, F. van den Bosch, & S. D. M. White. *Galaxy Formation and Evolution.* Cambridge University Press, 2010.

J. J. Monaghan. Smoothed Particle Hydrodynamics. *ARA&A*, 30:543, 1992.

J. J. Monaghan. SPH and Riemann Solvers. *JCoPh*, 136:298, 1997.

J. J. Monaghan & R. A. Gingold. Shock Simulation by the Paricle Method SPH. *JCoPh*, 52: 135, 1983.

J. J. Monaghan & J. C. Lattanzio. A refined particle method for astrophysical problems. *A&A*, 149:135, 1985.

M. Montuori, P. Di Matteo, M. D. Lehnert, F. Combes, & B. Semelin. The dilution peak, metallicity evolution, and dating of galaxy interactions and mergers. *A&A*, 518:A56, 2010.

B. Moore, F. Governato, T. Quinn, J. Stadel, & G. Lake. Resolving the Structure of Cold Dark Matter Halos. *ApJL*, 499:L5, 1998.

B. Moore, S. Ghigna, F. Governato, G. Lake, T. Quinn, J. Stadel, & P. Tozzi. Dark matter substructure within galactic halos. *ApJ*, 524:L19, 1999.

J. F. Navarro, C. Frenk, & S. D. M. White. The Structure of Cold Dark Matter Halos. *ApJ*, 462:462, 1996.

J. F. Navarro, A. Ludlow, V. Springel, J. Wang, M. Vogelsberger, S. D. M. White, A. Jenkins, & C. S. Frenk an A. Helmi. The diversity and similarity of simulated cold dark matter haloes. *MNRAS*, 402:21, 2010.

M. Noguchi. Gas dynamics in interacting disc galaxies – Fuelling of nuclei by induced by bars. *A&A*, 203:259, 1988.

L. P. Osipkov. Spherical systems of gravitating bodies with an ellipsoidal velocity distribution. *Pis ma Astronomicheskii Zhurnal*, 5:77, 1979.

B. Phookun & L. G. Mundy. NGC 4654: A Virgo cluster spiral interacting with the intracluster medium. *ApJ*, 453:154, 1995.

H. C. Plummer. On the problem of distribution in globular star clusters. *MNRAS*, 71:460, 1911.

W. H. Press & P. Schechter. Formation of Galaxies and Clusters by Self-Similar Gravitational Condensation. *ApJ*, 187:425, 1974.

T. Quinn, N. Katz, J. Stadel, & G. Lake. Time stepping N-body simulations. *preprint astro-pj/9710043*, 1997.

Jr. R. C. Kennicutt. Star Formation in Galaxies Along the Hubble Sequence. *ARA&A*, 36: 189, 1998.

Y. Revaz, P. Jablonka, T. Sawala, V. Hill, B. Letarte, M. Irwin, G. Battaglia, A. Helmi, M. D. Shetrone, E. Tolstoy, & K. A. Venn. The dynamical and chemical evolution of dwarf spheroidal galaxies. *A&A*, 501:189, 2009.

O. G. Richter & R. Sancisi. Asymmetries in disk galaxies. How often? How strong? *A&A*, 290L:L9, 1994.

H.-W. Rix & D. Zaritsky. Nonaxisymmetric Structures in the Stellar Disks of Galaxies. *ApJ*, 447:82, 1995.

A. Rodríguez-González, A. Esquivel, A. C. Raga, & P. Colín. Mass and metal ejection efficiency in disk galaxies driven by young stellar clusters of nuclear starburst. *RevMexAA*, 742:113, 2011.

P. Saha & S. Tremaine. Long-term planetary integration with individual time steps. *AJ*, 108:1962, 1994.

E. E. Salpeter. Accretion of interstellar matter by massive objects. *ApJ*, 140:796, 1964.

A. Sandage & J. Bedke. *Atlas of Galaxies.* Scientific and Technical Information Division – NASA, 1988.

A. Sandage & J. Bedke. *The Carnegie Atlas of Galaxies.* Carnegie Institution, 1994.

A. Sandage, M. Sandage, & J. Kristian. *Galaxies and the Universe.* University of Chicago Press, 1975.

T. Sawala, C. Scannapieco, & S. D. M. White. Local Group dwarf galaxies: nature and nurture. *MNRAS*, 420:1714, 2012.

M. Schwarzchild. A numerical model for a triaxial stellar system in dynamical equilibrium. *ApJ*, 232:236, 1979.

M. Schwarzchild. Self-consistent models for galactic halos. *ApJ*, 409:563, 1993.

C. K. Seyfert. Nuclear Emission in Spiral Nebulae. *ApJ*, 97:28, 1943.

I. Shlosman, M. C. Begelman, & J. Frank. The fuelling of active galactic nuclei. *Nature*, 345: 679, 1990.

F. H. Shu. Models of Partially Relaxed Stellar Disks. *ApJ*, 158:505, 1969.

L. Sparke & J. Gallagher. *Galaxies in the Universe*. Cambridge University Press, 2007.

V. Springel. The cosmological simulation code GADGET-2. *ARA&A*, 364:1105, 2005.

V. Springel. Smoothed Particle Hydrodynamics in Astrophysics. *ARA&A*, 48:391, 2010.

V. Springel. Modelling star formation and feedback in simulations of interacting galaxies. *MNRAS*, 312:859, 2000.

V. Springel & L. Hernquist. Cosmological smoothed particle hydrodynamics simulations: the entropy equation. *MNRAS*, 333:649, 2002.

V. Springel & S. D. M. White. Tidal tails in cold dark matter cosmologies. *MNRAS*, 307: 162, 1999.

V. Springel, N. Yoshida, & S. D. M. White. GADGET: a code for collisionless and gasdynamical cosmological simulations. *New Astronomy*, 6:79, 2001.

V. Springel, T. Di Mattero, & L. Hernquist. Modelling feedback from stars and black holes in galaxy mergers. *MNRAS*, 361:776, 2005.

V. Springel, J. Wang, M. Vogelsberger, A. Ludlow, A. Jenkins, A. Helmi, J. F. Navarro, C. S. Frenk, & S. D. M. White. The Aquarius Project: the subhaloes of galactic haloes. *MNRAS*, 391:1685, 2008.

R. A. Swaters, B. F. Madore, F. C. van den Bosch, & M. Balcells. The Central Mass Distribution in Dwarf and Low Surface Brightness Galaxies. *ApJ*, 583:732, 2003.

D. Syer & S. Tremaine. Made-to-measure N-body systems. *MNRAS*, 282:223, 1996.

P. J. Teuben. The Stellar Dynamics Toolbox NEMO. In *Astronomical Data Analysis Software and Systems IV*, 77, page 398. PASP Conference Series, 1995.

A. Toomre. On the gravitational stability of a disk of stars. *ApJ*, 139:1217, 1964.

H. Velazquez & S. D. M. White. Sinking satellites and the heating of galaxy discs. *MNRAS*, 304:254, 1999.

C. A. Vera-Ciro, A. Helmi, E. Starkenburg, & M. A. Breddels. Not too big, not too small: the dark haloes of the dwarf spheroidals in the Milky Way. *MNRAS*, 428:1696, 2013.

A. Villalobos & A. Helmi. Simulations of minor mergers - I. General properties of thick discs. *MNRAS*, 391:1806, 2007.

M. G. Walker & J. Peñarrubia. A Method for Measuring (slopes of) the Mass Profiles of Dwarf Spheroidal Galaxies. *ApJ*, 742:20, 2011.

H. Wang, R. S. Klessen, C. P. Dullemond, F. C. van den Bosch, & B. Fuchs. Equilibrium intialization and stability of three-dimensional gas discs. *MNRAS*, 407:705, 2010.

D. W. Weedman. High-Velocity Gas Motions in Galactic Nuclei. *ApJ*, 159:405, 1970.

A. R. Wetzel. On the orbits of infalling satellite haloes. *MNRAS*, 412:49, 2011.

S. D. M. White & M. Rees. Core condensation in heavy haloes - A two-stage theory for galaxy formation and clustering. *MNRAS*, 183:341, 1978.

L. Widrow & J. Dubinski. Equilibrium Disk-Bulge-Halo Models for the Milky Way and Andromeda Galaxies. *ApJ*, 631:838, 2005.

L. Woltjer. Emission Nuclei in Galaxies. *ApJ*, 130:38, 1959.

H. Yoshida. Construction of higher order symplectic integrators. *Phys. Lett. A*, 150:262, 1990.

D. Zaritsky & H. W. Rix. Lopsided Spiral Galaxies and a Limit on the Galaxy Accretion Rate. *ApJ*, 477:118, 1997.

Y. B. Zel'Dovich & I. D. Novikov. . *Sov. Phys. Dok.*, 9:246, 1964.

A. R. Zentner & J. S. Bullock. Halo Substructure and the Power Spectrum. *ApJ*, 346:49, 2003.